School of Civil and Mechanical Engineering

Folded Sandwich Protective Structures against Blast and Impact Loads

Zhejian Li

This thesis is presented for the Degree of
Doctor of Philosophy
of
Curtin University

August 2019

Declaration

To the best of my knowledge and belief this thesis contains no material previously published by any other person except where due acknowledgment has been made.

This thesis contains no material which has been accepted for the award of any other degree or diploma in any university.

Signature:

Date:

Abstract

In this thesis, novel folded truncated pyramid structures and a bi-directional load-self-cancelling square dome structure are proposed as the core of light-weight protective sandwich structures to resist blast and impact loads. Analytical derivations, numerical simulations, quasi-static and dynamic crushing tests are carried out to examine the dynamic crushing behaviours and energy absorption capacities of various designs for developing the best-performing core structures for blast and impact load resistance.

The single-layer folded truncated pyramid structures with three different base shapes including triangle, square and pentagon are firstly proposed. The specimens with these single-layer truncated triangle, square, and pentagon pyramid (i.e. TTP, TSP and TPP) structures are folded from pre-cut aluminium thin sheets. Quasi-static crushing tests are carried out and numerical simulations are conducted using FEA software LS-DYNA. Truncated square pyramid (TSP) folded structure shows superior crushing behaviour with low initial peak force and high crushing resistance as compared to TTP, TPP and Miura-type foldcore. The blast mitigation capacity of sacrificial cladding with single-layer TSP folded structure as core is then evaluated. Enhanced blast mitigation capacities are observed when compared to conventional claddings including honeycomb and aluminium foam. Analytical model is also developed for quick design based on blast loading scenarios and cladding properties. Rigid polyurethane (PU) foam and expanded polystyrene (EPS) foam infills are then considered for further improvement in blast mitigation and energy absorption capacities of sacrificial cladding with single-layer TSP folded structure as core.

To experimentally verify the dynamic crushing behaviour of the proposed folded TSP folded structure and the feasibility of potential applications of such structure in real life, numerous experimental studies are carried out. Multi-layered TSP and TTP sandwich structures are proposed with reusable set-up where the number of layer could be adjusted according to the applied loading for better protection. Multi-layered folded structures with different configurations of foam infills and with graded foam infills are dynamically tested. The results demonstrate high energy absorption capability of multi-layer TSP and TTP folded structures and significant enhancement in energy

absorption with foam infills and graded foam configurations under dynamic loading, indicating great potential of these multi-layered folded structures as energy absorbers.

Apart from the folded structure, a bi-directional load-self-cancelling blast resistant panel as a new structural form is also proposed and numerically investigated. Owing to the two-way symmetrical arch design, the reaction force at boundary along the out-of-plane direction is greatly reduced. Blast loading transmitted along the arch is partially cancelled out at the intersection of the arches. This new panel design could be used as blast resistant door to greatly reduce the reaction force provided by the frame in the blast event.

Acknowledgement

I would like to take this opportunity to express my sincere gratitude and deep regards to my supervisors Prof. Hong Hao and Dr. Wensu Chen for their exemplary guidance, endless patience and wisdom. Their guidance has been important throughout my PhD studies.

Secondly, I would like to thank my parents. There were some hard times and difficult decisions to make during my PhD study. Thank you for the encouragements and support throughout the years.

I would like to thank Prof. Zhong You and his PhD students from the University of Oxford for having me at the Deployable Structure research group as a visiting scholar. I would like to thank Curtin University for sponsoring me for this visiting with the HDR student mobility scholarship. I would also like to thank Curtin University Civil and Mechanical Engineering Lab for helping me in manufacturing some of the specimens of folded structures and related machining.

I sincerely thank all of the members from my research centre, Centre for Infrastructural Monitoring and Protection (CIMP) at Curtin University. I would like to thank especially the following colleagues for their assistance throughout my study: Cheng Yuan, Minghong Li, Huawei Li, Zhixing Li, Feng Shi. I thank final year project student Ms. Samantha Tyson from Curtin University for helping me prepare the testing specimens. Thanks go to the collaborators, Dr. Jian Cui, Prof. Yanchao Shi from Tianjin University for helping out the dynamic testing. I thank the assistance provided by Ms. Xiaochen Yang from Motion Structure Lab at Tianjin University for the 3D DIC surface flatness analysis of the proposed folded structure.

Last, I would like to thank my friends, Peng Yuan, Chao Duan, Christopher Bahr and his funny face. I would also like to thank Amy, Helena, Katrina, Rose, Salman, Wenjing, Zaq from UWA outdoor club for the paddling trips and scuba diving we have done together.

Zhejian Li

June, 2019

List of Publications

This thesis is assembled by accepted and submitted publications, which form the individual chapters and are listed below.

Chapter 3

Li Z, Chen W, Hao H. Crushing behaviours of folded kirigami structure with square dome shape. International Journal of Impact Engineering. 2018;115:94-105.

DOI: 10.1016/j.ijimpeng.2018.01.013

Chapter 4

Li Z, Chen W, Hao H. Numerical study of open-top truncated pyramid folded structures with interconnected side walls against flatwise crushing. Thin-Walled Structures. 2018;132:537-48.

DOI: 10.1016/j.tws.2018.08.023

Chapter 5

Li Z, Chen W, Hao H. Blast mitigation performance of cladding using Square Dome-shape Kirigami folded structure as core. International Journal of Mechanical Sciences. 2018;145:83-95.

DOI: 10.1016/j.ijmecsci.2018.06.035

Chapter 6

Li Z, Chen W, Hao H. Numerical study of blast mitigation performance of folded structure with foam infill. Structures. 2019;20:581-93.

DOI: 10.1016/j.istruc.2019.06.012

Chapter 7

Li Z, Chen W, Hao H, Cui J, Shi Y. Experimental study of multi-layer folded truncated structures under dynamic crushing. International Journal of Impact Engineering. 2019;131:111-22.

DOI: 10.1016/j.ijimpeng.2019.05.010

Chapter 8

Li Z, Chen W, Hao H. Dynamic crushing and energy absorption of foam filled multi-layer folded structures: Experimental and numerical study. International Journal of Impact Engineering. 2019;133:103341.

DOI: 10.1016/j.ijimpeng.2019.103341

Chapter 9

Li Z, Chen W, Hao H. Functionally graded truncated square pyramid folded structures with foam filler under dynamic crushing, Composites Part B. 2019:177:107410.

DOI: 10.1016/j.compositesb.2019.107410

Chapter 10

Li Z, Chen W, Hao H. Numerical study of sandwich panel with a new bi-directional Load-Self-Cancelling (LSC) core under blast loading. Thin-Walled Structures. 2018;127:90-101.

DOI: 10.1016/j.tws.2018.02.003

List of Relevant Additional Publications

Journal paper

Li Z, Chen W, Hao H. Mechanical properties of carbon foams under quasi-static and dynamic loading. International Journal of Mechanical Sciences. 2019: 105039

DOI: 10.1016/j.ijmecsci.2019.105039

Conference papers

Li Z, Chen W, Hao H. Crushing behaviour of multi-layered kirigami structure under different loading rates. 10th International Symposium on Impact Engineering; 2019, Gmunden, Austria.

Li Z, Chen W, Hao H. Blast resistant performance of cladding with folded open-top truncated pyramid structures as core. 7th International Meeting on Origami in Science, Mathematics, and Education; 2018, Oxford, UK.

Li Z, Chen W, Hao H. Quasi-static crushing behaviours of folded open-top truncated pyramid structures with interconnected side walls. 7th International Meeting on Origami in Science, Mathematics, and Education; 2018, Oxford, UK.

Li Z, Chen W, Hao H, editors. Cladding blast mitigation performance of folded truncated square pyramid with infilled aluminium foam as core. 5th International Conference on Protective Structures; 2018, Poznan, Poland.

Hao H, **Li Z**, Chen W. Performance of sandwich panel with square dome shape folded kirigami core under blast loading. 13th International Conference on Steel, Space and Composite Structures; 2018, Perth, Australia. **Keynote**

Li Z, Chen W, Hao H. Blast resistant performance of multi-layer square dome shape kirigami folded structure. 6th International Conference on Design and Analysis of Protective Structures; 2018, Melbourne, Australia.

Li Z, Chen W, Hao H. Numerical study of folded dome shape aluminium structure against flatwise crushing. 12th International Conference on Shock & Impact Loads on Structures; 2017, Singapore.

Statement of Contribution of Others

The work presented in this thesis was primarily designed, numerically simulated, experimentally executed, analysed and written by the first author (Zhejian Li) of the individual manuscripts. Contributions by others are described as follows. The signed contribution forms are attached in the appendix.

Chapter 3 to Chapter 6

Prof. Hong Hao and Dr. Wensu Chen revised and edited the manuscript, provided intellectual input towards data processing, analysis, and discussion of the results. Mr. Cheng Yuan helped with the Direct Image Correlation (DIC) analysis of the material testing. Dr. Pinghe Ni helped with the curve fittings. Civil and Mechanical Engineering Lab helped machining and manufacturing some specimens and set-ups. The financial support was provided by Australian Research Council DECRA project (DE160101116).

Chapter 7

Prof. Hong Hao and Dr. Wensu Chen revised and edited the manuscript, provided intellectual input towards data processing, analysis, and planning of the dynamic tests. Dr. Jian Cui and Prof. Yanchao Shi from Tianjin University assisted with the dynamic testing set-up, data recording, and control settings. Ms. Samantha Tyson from Curtin University assisted with the specimen preparation and preliminary data processing. Civil and Mechanical Engineering Lab helped with some machining and manufacturing. Ms. Xiaochen Yang from Motion Structure Lab at Tianjin University helped with surface flatness analysis of specimens. The financial support was provided by Australian Research Council DECRA project (DE160101116).

Chapter 8

Prof. Hong Hao and Dr. Wensu Chen revised and edited the manuscript, provided intellectual input towards data processing, analysis, and planning of the dynamic tests. Ms. Samantha Tyson from Curtin University assisted with the specimen preparation and preliminary data processing. Civil and Mechanical Engineering Lab helped with some machining and manufacturing. The financial support was provided by Australian Research Council DECRA project (DE160101116).

Chapter 9

Prof. Hong Hao and Dr. Wensu Chen revised and edited the manuscript, provided intellectual input towards data processing, analysis, and planning of the dynamic tests. Ms. Samantha Tyson from Curtin University assisted with the specimen preparation and preliminary data processing. Civil and Mechanical Engineering Lab helped with some machining and manufacturing. Ms. Xiaochen Yang from Motion Structure Lab at Tianjin University helped with surface flatness analysis of specimens. The financial support was provided by Australian Research Council DECRA project (DE160101116).

Chapter 10

Prof. Hong Hao and Dr. Wensu Chen helped with defining of the scope of this study. They both revised and edited the manuscript, provided intellectual input towards data processing, analysis. The financial support was provided by Australian Research Council DECRA project (DE160101116).

Table of Contents

1. Introduction

1.1 Background

Blast and impact protection for structure, equipment and personnel is becoming more and more important in recent years due to the increasing number of accidental explosion events as well as terrorist activities (1). Owing to their lightweight and high energy absorption capability, sandwich structures have been widely used as protective structure against dynamic loads such as blast and impact (2).

Sandwich structures have been widely used as energy absorbers in applications such as impact attenuator (3), vehicle crash box (4), safety bumper (5), helmet (6) and sacrificial cladding (7-10). These types of energy absorbing structures usually consist of a cellular crushable core which is sandwiched between two plates and fixed in front of the protected structure. Under dynamic loading such as impact or blast, the crushable core undergoes large plastic deformation under a constant low stress absorbing a large amount of energy. The peak force transmitted to the structure is greatly reduced. Conventional crushable cores including honeycomb (11-17), polymeric (18-20) and aluminium foam (7, 21-30) have been extensively investigated. However, these conventional sandwich structures have their drawbacks for the purpose of energy absorption as discussed in chapter 2.3 and 2.4.

1.2 Objectives

The objective of this study is to develop new forms of sandwich structures with ideal crushing behaviours and high energy absorption capabilities under dynamic loads. To achieve effective blast and impact mitigation, the new forms of structures should yield a uniform crushing response throughout deformation, with low fluctuation in crushing resistance and low initial peak force. It is also ideal for the structure to have a high specific energy absorption and possibly a reusable set-up. For the development of this new panel, a thorough understanding of current structural forms used in sandwich structures is required, this includes the characteristics of dynamic crushing response of typical sandwich structure under dynamic loading and the contributing factors.

Numerical analysis is firstly conducted for designing, parametric study, and evaluation of dynamic response under impact and blast loads. Experiments are carried out for

further verification and examination of the dynamic crushing behaviour of the proposed folded structures. Their crushing responses, energy absorption capacities and blast mitigation performance are evaluated and compared with the existing folded structures and common sandwich structures such as foam and honeycomb.

To further improve the crushing resistance of the proposed folded structures, the alternatives such as adding foam fillers are considered in this study. As wall thickness is often limited by the folding process, to further increase the crushing resistance and energy absorption of folded structures, alternatives other than increasing the wall thickness shall be considered. The effects of material, shapes and graded configuration of the foam filler are also investigated in this study.

1.3 Research Outline

This thesis comprises eleven chapters. The contents of nine chapters following the induction and literature review are described as follows:

Chapter 3 presents numerical analysis of the proposed truncated square pyramid structures. The aim of the study is to examine the crushing behaviour of the proposed TSP foldcore, as interconnected sidewalls of the foldcore lead to more constraints of the structure under crushing and result in higher crushing resistance. Single sheet fabrication can be also achieved for the proposed foldcore. The calibrated numerical model is used for conducting dynamic crushing analysis of the proposed TSP structures with different geometric configurations including slope angle, open/close top, and base size. The comparison with one of the best performing kirigami cube strip foldcore is also included.

Chapter 4 presents experimental and numerical analysis of truncated pyramid structures with different base shapes, i.e. triangle, square and pentagon. The quasi-static crushing tests of all three foldcores (TTP, TSP, TPP) are firstly carried out on the base plates with boundary constraints. Numerical models are developed and verified with test data. Dynamic crushing analysis is then carried out under two boundary conditions, i.e. simple supported and fixed boundary. The effects of base shapes, boundary conditions, crushing speeds on damage mode and load-displacement responses are compared among the proposed foldcores. Miura-type foldcore is also numerically simulated as benchmark for three proposed foldcores.

Chapter 5 presents numerical study of blast mitigation of sacrificial cladding with TSP folded structure as core. The blast mitigation capabilities of TSP foldcore are compared with two conventional cladding cores, honeycomb and aluminium foam, under various blast intensities. Parameters such as peak transmitted force, centre displacement and energy absorption are used as criteria for the evaluation of blast mitigation performance. Single degree of freedom analysis is also carried out based on the previous studies. Design formulae and charts are developed for designing the suitable cladding configurations based on mechanical properties of the cladding and the imposed blast load.

Chapter 6 presents numerical study of blast mitigation performance of foam filled TSP folded structure. The quasi-static crushing tests of rigid polyurethane (PU) foam filled TSP foldcore are firstly conducted. Two different shapes of foam fillers are considered. The foam-wall interaction effect is also verified by comparing the crushing resistances of foam filled TSP foldcore and two components (foam and TSP core) crushed separately. The calibrated numerical model based on these crushing test results is then used for blast mitigation of TSP foldcore with the proposed foam filler.

Chapter 7 presents experimental study of three-layer TSP and TTP folded structures under various dynamic loading conditions. A reusable multi-layer set-up is developed and manufactured as no fixing is required between the foldcore and interlayer plates which is different from many conventional sandwich structures. The crushing behaviours are experimentally verified with low fluctuation, low initial peak force and less sensitive to loading rate as comparing to other current sandwich structures. The differences between TSP and TTP foldcores are compared, and the influence of cell wall thickness is also investigated.

Chapter 8 presents experimental and numerical study of foam filled multi-layer TSP kirigami structure under dynamic loading. A total of five foam infill configurations are studied, which include the effects of foam material, foam density and foam shapes on dynamic crushing behaviour of multi-layer folded structures. These include three densities of cubic expanded polystyrene (EPS) foams and two shapes of rigid polyurethane (PU) foams. Numerical studies are carried out along with test data for investigating the effect of five different foam filler configurations on damage mode, crushing response and energy absorption of the structures.

Chapter 9 presents experimental study of functionally graded foam filled multi-layer TSP kirigami structures under different dynamic loading conditions. Two series of foam fillers are inserted inside the multi-layer TSP folded structures, one by varying the foam filler density and the other by varying the foam shapes to create different functionally graded structures. Their collapsing order, damage mode, load-displacement responses are analysed under two loading rates. Significant influences on crushing behaviours are shown with respect to loading rate and graded configurations.

Chapter 10 presents numerical study of a new bi-directional load-self-cancelling (LSC) panel under blast load. It is proposed as a new type of blast resistant panel with low weight and high performance. It is designed to significantly reduce the force transmitted to the support of the panel, owing to the two-way symmetrical arches. Different LSC panels are also included as benchmark for comparison.

Chapter 11 summarizes the findings in this study, as well as some future works.

2. Literature review

2.1 Overview

This chapter presents a literature review of the previous and current studies of sandwich protective panels. The literature review includes five parts: 1. Impulsive loadings; 2. Ideal energy absorber; 3. Sandwich structures; 4. Folded structures, and 5. Methodology.

2.2 Impulsive loadings

Both blast and impact loadings are often considered as impulsive loadings which have characteristics of short duration and large amplitude. Under high speed dynamic loading conditions, inertial effect and material strain rate effect become important factors for the crushing behaviour of structures (2). In a blast event, a shock wave is produced by the rapid expansion of detonation products. The shock wave can be characterized by very short duration in the order of mili-second and high pressure up to 100 MPa. A typical free-field pressure-time history of blast wave is shown in Figure 2-1 (31). Two phases can be observed, where the negative phase of blast loading is often neglected in designing protective structures due to its low pressure and impulse (7). The typical blast loading can be characterized with a very sharp increase of pressure reaching the peak pressure P_{SO} followed by a decaying process back to ambient pressure P_O after the positive duration t_o.

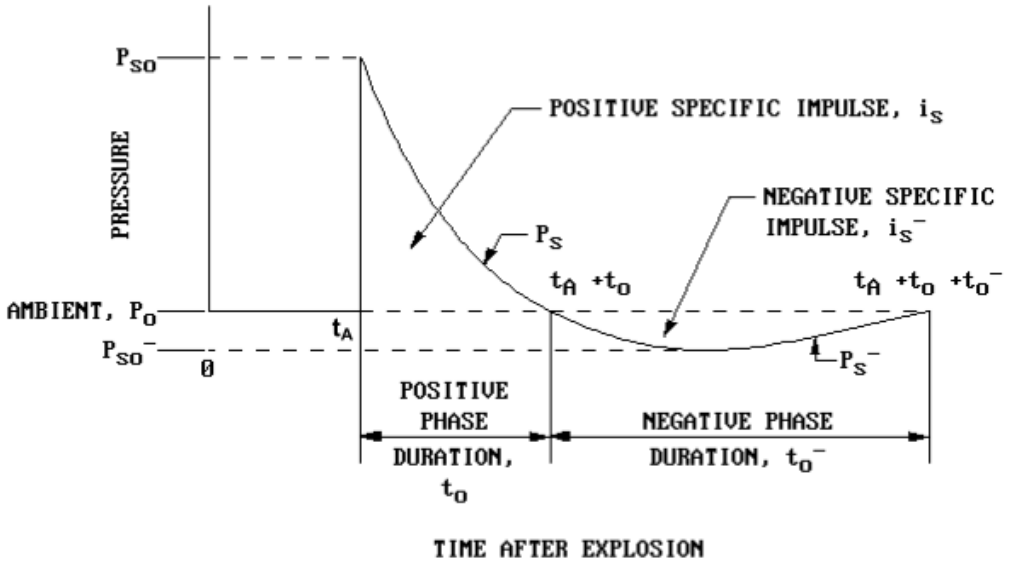

Figure 2-1. Free-field pressure-time history (31)

Design guide Unified Facilities Criteria UFC 3-340-02 (31), correlates the blast parameters such as amplitude of blast loading and scaled distance. Scaled distance, *Z*, is used and described as follows:

$$Z = \frac{R}{W^{1/3}} \qquad (2\text{-}1)$$

where *R* is the stand-off distance, i.e., the distance from centre of explosive source in meters, and *W* is the equivalent TNT charge mass in kilograms.

2.3 Ideal energy absorber

General principles of ideal energy absorber are summarized by Lu and Yu (2) as follows:

- Irreversible energy conversion
- Constant and restricted reaction force
- Long stroke
- Stable and repeatable deformation mode
- Light weight and high specific energy absorption capacity
- Low cost and easy installation

The energy absorber should be able to irreversibly convert the input kinetic energy into inelastic energy. If the input kinetic energy is converted into reversible energy such as elastic energy, potential subsequent damage may be caused to the protected structure and protected personnel once the absorber reaches its maximum capacity. The reaction force throughout deformation should be kept under the threshold value for protection. In some cases, maximum stress or acceleration is used for the evaluation of energy absorbers, where stress and accelerations can be calculated by using reaction force, related mass and area of contact (32). Furthermore, the energy absorber should have enough crushable distance in order to absorb a large amount of energy during impact or blast loadings, as the energy absorbed is equal to crushing distance times the reaction force. Uniform and stable deformation mode is also desired regardless of the loading rates. Other factors such as cost, weight and easy for installation should be also considered for designing an energy absorber. For instance, a crash box which connects the vehicle bumper and chassis is widely used in the

automotive industry, it undergoes large deformation and absorbs energy under collision. Many methods such as introduced dents, pre-folds or stamped out patterns on the original square thin-walled tubular structures (33, 34) were developed to reduce the peak force while maintaining the deformation mode during the crushing.

With the protection of energy absorbers, the protected structure experiences greatly reduced transmitted force under extreme loadings such as blast and high speed impact (18, 35). This is because that the crushing resistance of the energy absorbing structure is often much lower compared to the peak load of the blast or impact loads. Under blast and impact loads, the crushable energy absorber undergoes large deformation, therefore prolong the loading duration and reduce the peak force transmitted to the protected structure. For example, blast mitigation capabilities of sacrificial cladding with different thicknesses of rigid polyurethane (PU) foam are experimentally studied by Ousji et al (18). As shown in Figure 2-2, compared to the case without any energy absorbing sacrificial cladding (blue line), the pressure transmitted to the protected structure is greatly reduced for the cases with 30 and 50 mm thick PU foam (cyan and purple lines) as an energy absorber. Furthermore, the duration of the transmitted pressure is largely prolonged compared to the case without any protection.

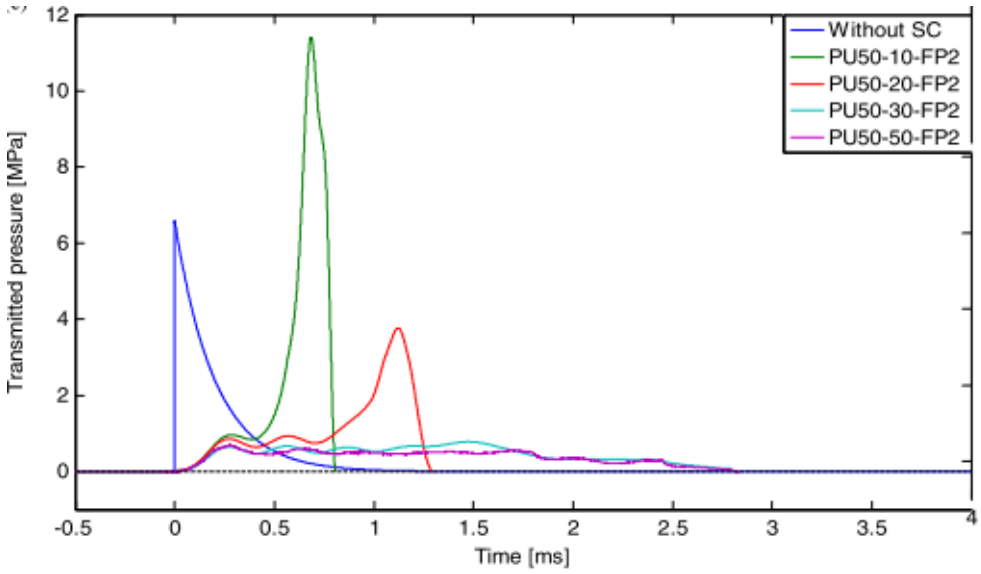

Figure 2-2. Transmitted pressure to the structure protected by the sacrificial cladding of PU foam with thicknesses of 10, 20, 30 and 50 mm under blast loading (18)

To achieve effective protection, energy absorbers should be carefully selected. In some cases, energy absorber could lead to more severe damage to the protected structure than the case without any protection (35), as a result of the densification of

the energy absorber before the end of the loading is reached. The energy absorber becomes very strong and hard to deform. Once the structure is fully compacted and the crushing resistance increases drastically, which is also referred as the densification stage. With the ongoing loading, the already compacted energy absorber can impact the protected structure and lead to a large increase in transmitted force. For example, as shown in Figure 2-2, for sacrificial cladding with 10 and 20 mm thickness of PU foam (red and green lines), the pressure transmitted to the protected structure drastically increases towards the end portion of the curves, and the transmitted pressure for the 10 mm PU foam protected case even exceeds the case without any protection. Therefore, in order to achieve maximum protection and avoid further damage to the protected structure, the energy absorber needs to be carefully designed according to the specific loading case.

2.4 Sandwich structures

Sandwich structures usually consist of a cellular core and two skin plates, therefore achieving light weight and high strength to weight ratio. Sandwich structures have been widely used in the aerospace (36), aviation (37), automotive (5, 38), and naval industries (21). Different topologies and materials of the cores have been extensively investigated, these include honeycomb (12, 13), lattice (39, 40), corrugated (41-43), dome (44, 45), eggbox (46, 47), auxetic (48, 49), metallic and polymeric foams (20, 24, 25, 27). A sketch of different sandwich core topologies is shown in Figure 2-3 (50).

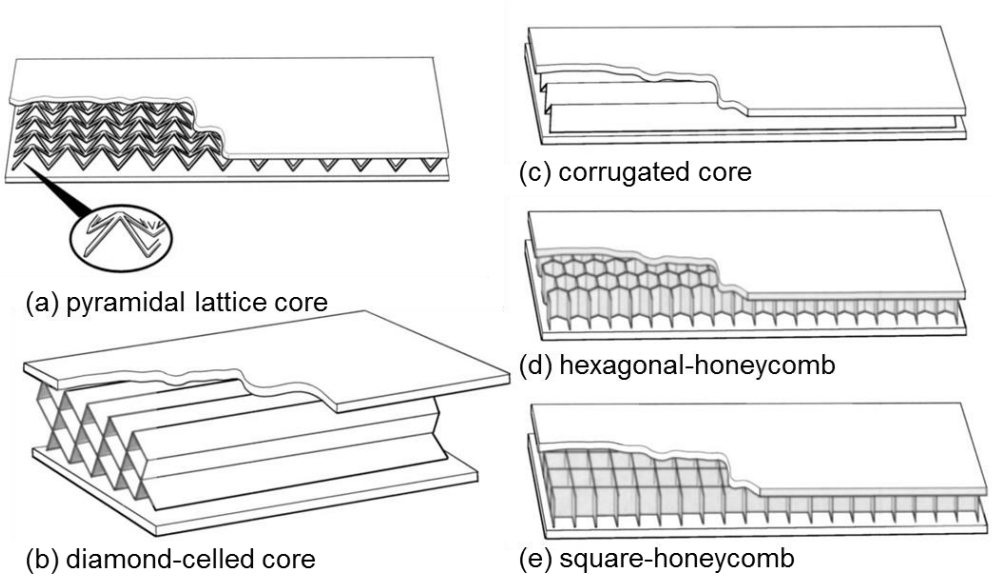

Figure 2-3. Sketch of different sandwich core topologies (50)

2.4.1 Sandwich structures as energy absorbers

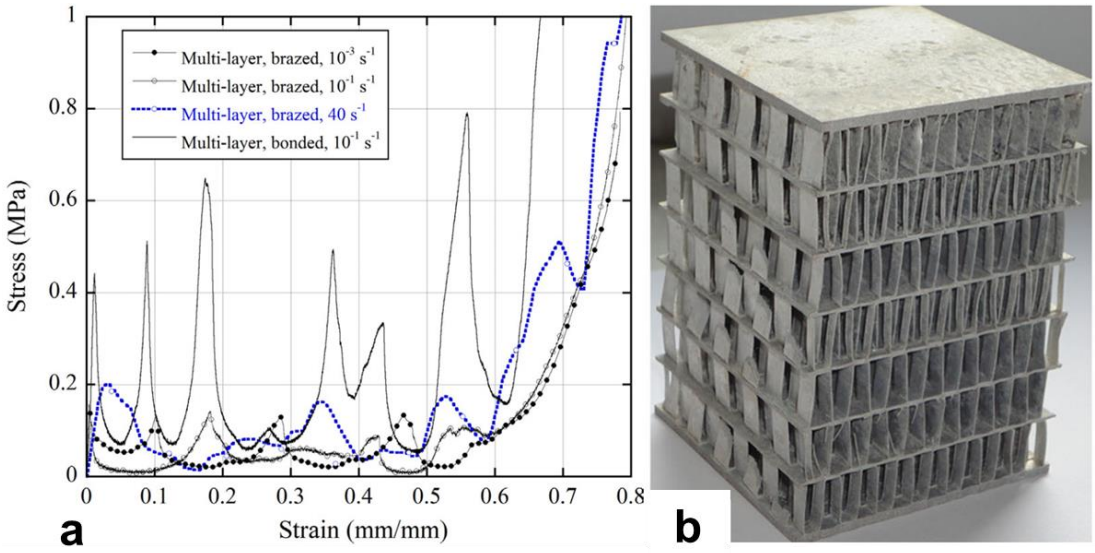

Figure 2-4. (a) Stress-strain curves of multi-layer corrugated sandwich structure under different strain rates and bonding conditions between layers; (b) specimen of sandwich structure (43)

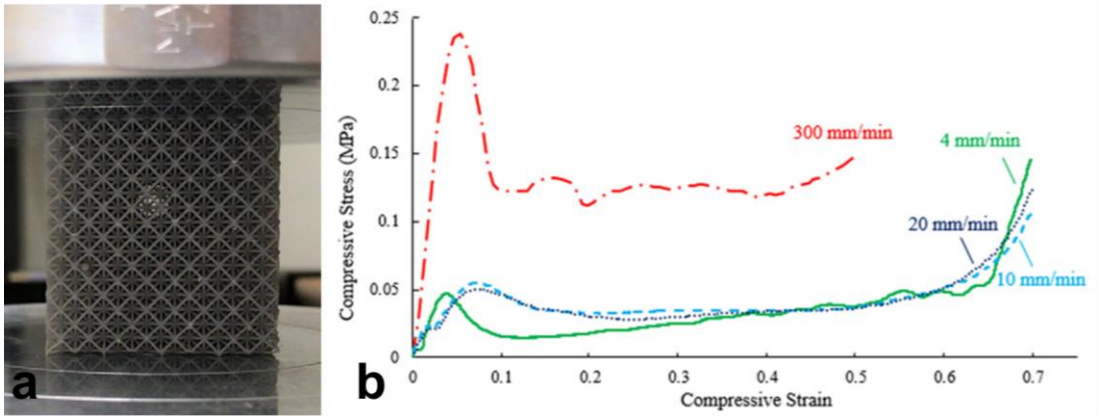

Figure 2-5. (a) Specimen of 3D printed lattice structure; (b) Stress-strain curves of the lattice structure under different crushing speed (51)

Many studies suggest that under dynamic loading, conventional sandwich structures such as honeycomb (17, 52), corrugated (43) and lattice (51, 53) have an inconsistent crushing behaviour with a sudden rise in initial peak crushing resistance and large fluctuation in resistance during crushing, which may not be ideal for the application as energy absorption under high loading rate as discussed above (2). For example, the crushing response of a multi-layer corrugated sandwich structure is shown in Figure 2-4 (43), significant fluctuation in crushing resistance is shown where the peak stress can be several times higher than the average crushing resistance. A similar increase of

initial crushing resistance can be observed in Figure 2-5 for a 3D printed polymer based lattice structure under increasing crushing speeds (51).

Metallic and polymeric foams have uniform deformation process with a long plateau stage of crushing resistance. However, most of the stochastic foams have bending dominated deformation (54), which results in a lower crushing resistance than stretching dominated cellular structures of the same density (26). Some topologies of sandwich structures were created to improve the energy absorption capability as compared with foam materials of similar materials and densities. Aluminium egg box structure was developed to have a foam-like uniform crushing behaviour while achieving a higher specific energy absorption than the foam material counterparts (46). However, its crushing resistance was only slightly higher than the foam of similar densities.

2.4.2 Sandwich structures as blast resistant panel

Accidental explosion and terrorist activities have been increasing around the globe in recent years, more than half of the terrorist activities were related to bombing attacks (55-57). As protection of life and infrastructure from bomb attacks, blast resistant panels have been widely used across military, commercial and industrial applications (58-60). Blast-resistant doors as an example of such panels are used at the entrances of shelters and ammunition storage magazines. The traditional blast resistant doors are often designed as a solid panel of great weight which leads to poor operational performance and high costs (61). The ideal characteristics of a blast resistant panel should be lightweight while capable of resisting blast loads. In some applications such as blast resistant door, the deformation of the panel is required to be limited to ensure the operable condition after the blast. This is different from an energy absorber as discussed in the previous section, where large deformation is desired for energy absorbing purpose.

Various blast resistant panels have been developed. The performances of sandwich structures with different forms, materials and topologies have been comprehensively reviewed (54, 62, 63). Forms of sandwich structure core include honeycomb, corrugate, metallic foam, lattice and functionally graded core. The superior performance of sandwich structures under dynamic loading has been demonstrated via both numerical simulations and experimental tests (7, 19, 64-69). Curved sandwich

panel with aluminium foam as core also demonstrated superior performance over the equivalent flat sandwich panel and solid plate against blast loading (70-73). Most of these studies focused on the energy absorption and the deformation of the panel after the blast, the investigations on blast load transferred to the supports were limited.

In practice, supports of the structural panel also need to be properly designed and protected because damage to the support may lead to the complete failure of the panel structure. In this regard, a uni-directional multi-arch panel was proposed (61, 74). As shown in Figure 2-6, this innovative design makes use of the unique property of the arch structure form that transfers a certain amount of load applying onto the arch to the supports. In this case, loads in the opposite directions at the intersections of adjacent arches would cancel each other, leading to reductions of the net loads to the supports of the structural panel. Both numerical simulations and experimental tests verified the effectiveness of the uni-directional multi-arch panel in resisting blast and impact loads (61, 74). Detailed discussions on the designs and performances of uni-directional multi-arch panels subjected to blast and impact loads can be found in the references (61, 74, 75). However, some limitations of using this uni-directional panel were also identified. It cancelled loads only in one direction, hence its effectiveness in load-cancellation was effective in one direction only. Therefore, further improvement can be achieved by implementing load-cancellation along other directions using the designed geometry of the structure.

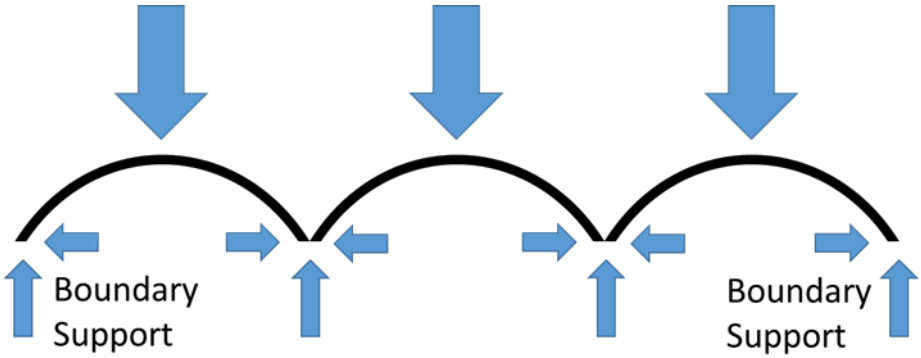

Figure 2-6. Mechanism of load-self-cancelling structure with multi-arch geometry (76)

2.5 Folded structures

In recent decades, folded structures (77, 78) were developed and used as cores of energy absorbing sandwich structures. As one of the most commonly used folded structures in sandwich panels, Miura-type origami foldcore was proposed in 1972 for

space craft solar panel deployment (79) and has been intensively investigated as the cores of sandwich structures recently. It is a type of rigid foldable origami pattern consisting of repeating tessellated shapes, as shown in Figure 2-7 (a), and is made from an unbroken sheet folded along creases without stretching or twisting of the panels. Miura-type foldcore offers advantages such as continuous fabrication and open ventilation channel design which allows moisture and heat to escape as compared to conventional honeycomb sandwich structures (80). In terms of crushing resistance, however, Miura-type origami foldcore is not comparable to the conventional honeycomb core of similar density (81). Furthermore, the failure mode of plate buckling is also observed on Miura-type core under the out-of-plane impact, leading to a non-uniform collapse. As shown in Figure 2-7 (b) , it also has a high initial peak force followed by a significant force reduction (82), which is a drawback for being used as an energy absorber for structure protection.

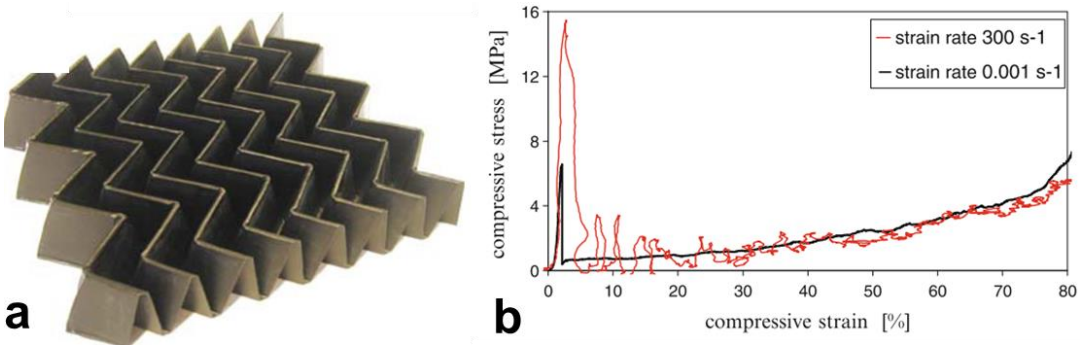

Figure 2-7. (a) Rigid foldable Miura-type foldcore made of CFRP (80); (b) Compressive stress-strain curves of Miura-type foldcore made of CFRP under different strain rates (82)

To increase the crushing resistance and achieve a more uniform crushing resistance of the folded structure, curved-crease foldcores were proposed (81, 83). Different from the standard Miura-type foldcore, curved-crease foldcores are folded along curves instead of segments of straight lines, as shown in Figure 2-8 (84, 85). Due to the higher buckling resistance provided by the curved faces of the foldcore, it had a higher energy-absorption capacity as compared with straight-crease foldcore or Miura-type, and slightly lower crushing resistance capacity than honeycombs in terms of average crushing stress (84). However, the curved-crease foldcore has a more uniform failure response and a lower ratio of initial peak stress to average stress when compared with honeycomb structure, due to less constraints for each unit cell.

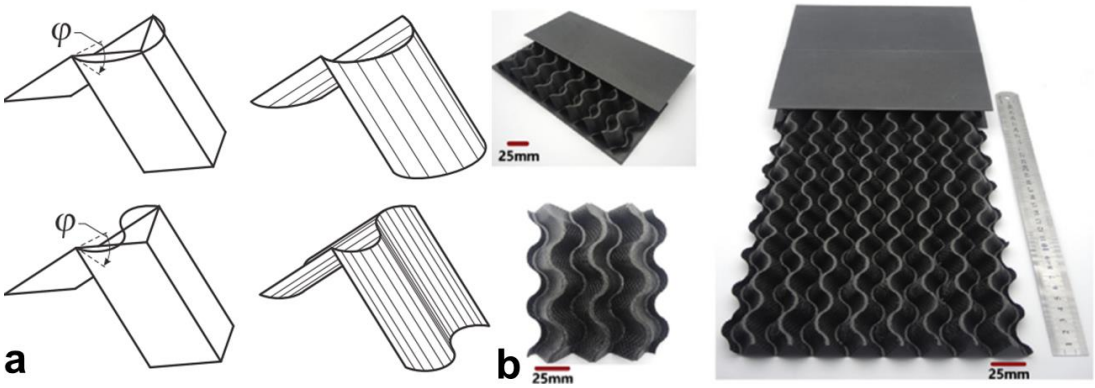

Figure 2-8. (a) Unit cells of two types of curved-crease foldcore based on Miura-type (84); (b) a curved-crease foldcore sandwich panel made of CFRP (85)

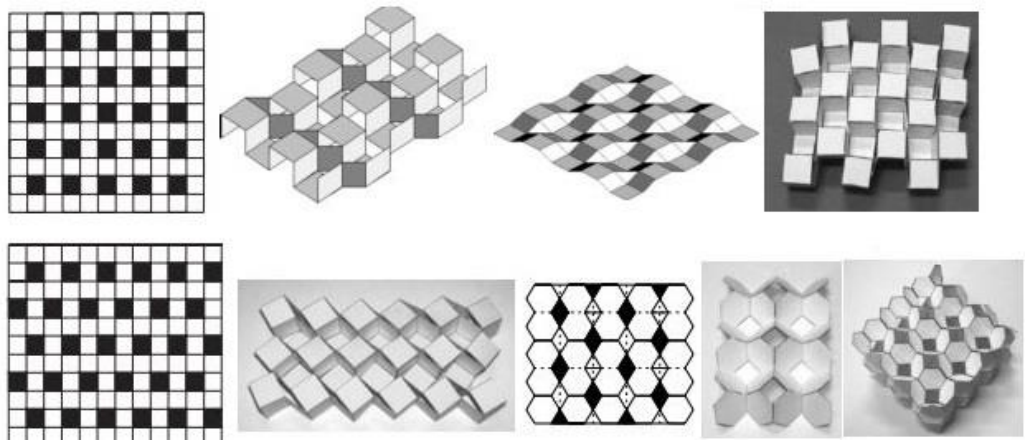

Figure 2-9. Examples of existing kirigami structure, black shades are the cut out of sheet material (86)

Crushing behaviours of Kirigami foldcore have been recently studied as well (87), an examples are shown in Figure 2-9 and Figure 2-10 (86, 87). The sheet of kirigami structure can be cut, stamped or punched prior to folding, therefore achieving more complex geometry and potentially increasing their crushing resistance capacity. Up to 74% rise in average crushing stress is achieved for cube strip kirigami foldcore under quasi-static crushing comparing to the standard Miura-type origami foldcore and a comparable crushing resistance to honeycomb structure (87).

However, unlike other folded structures, the best performing kirigami structures, including both cube strip and diamond strip kirigami foldcores (87), cannot be fabricated using single sheet material. Multiple sheet strips are required to be folded individually and placed for the fabrication of a single panel. Furthermore, in many of the existing kirigami folded structures in Figure 2-9 and Figure 2-10 (86, 87), not all vertical faces are connected with adjacent faces. Some obvious gaps between adjacent

vertical faces are marked out in red lines as shown in Figure 2-10. Further improvements in crushing resistance and energy absorption are expected for folded structure with connected vertical faces due to additional constraints under out-of-plane crushing. However, by simply connecting the adjacent vertical faces of cube strip kirigami foldcore shown in Figure 2-10 (b), the foldcore becomes a square honeycomb structure. The square honeycomb structure has a non-uniform collapsing with a high initial peak force and the crushing resistance becomes very sensitive to loading rate due to the inertial stabilization provided by the sidewalls (17), which may not be ideal as an energy absorber.

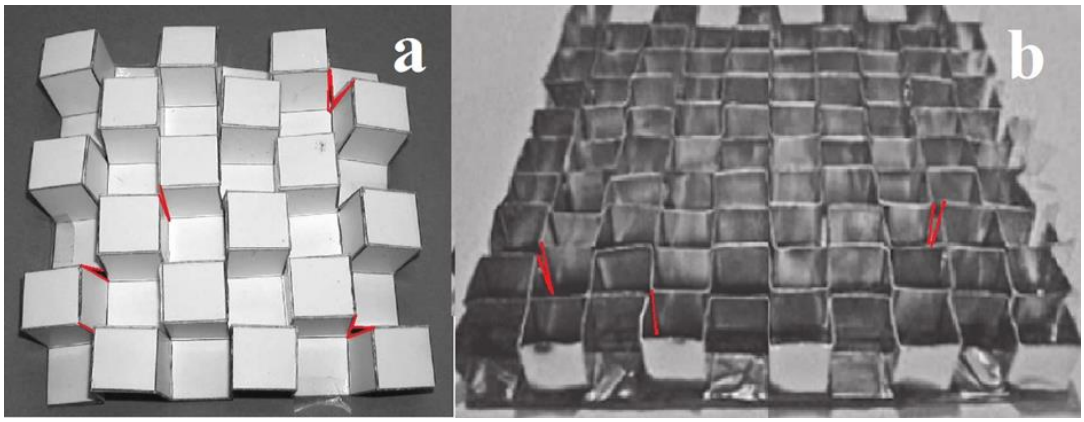

Figure 2-10. Unconstrained adjacent vertical faces (a) cube foldcore (86) (b) cube strip foldcore (87)

2.6 Foam filled tubes and sandwich structures

Tubes and columns are studied for their crushing behaviours under various loading rates since these structures are relatively cheap and efficient for energy absorbing (88-94). However, the crushing resistance of the thin-walled tubes fluctuates during the deformation, and often have a high initial peak force (34, 94). As mentioned in chapter 2.4.1, various foam materials are used as energy absorber due to its lightweight and uniform deformation process with nearly constant load (27). The foam materials including polymeric foams (95, 96) and aluminium foams (97-99) are inserted into the thin-walled tubes to enhance the crushing stability and the energy absorption capacities of the structures. In terms of specific energy absorption, the aluminium foam filler was found to be preferable to thickening the wall of the columns, and a closed-form solution of the average crushing force was developed for foam-filled square columns (97). As shown in Figure 2-11 (b), the crushing force of foam filled

column is much greater than the sum of crushing force of the standalone column and the foam filler. The foam-wall interaction effect leads to significant increase in average crushing force and energy absorption of the structures (99). For instance, it was found that the foam-wall interaction effect for column structures contribute to 80%, 140% and 180% of the compressive strength of the standalone foam fillers for single, double and triple cell column structures respectively (98).

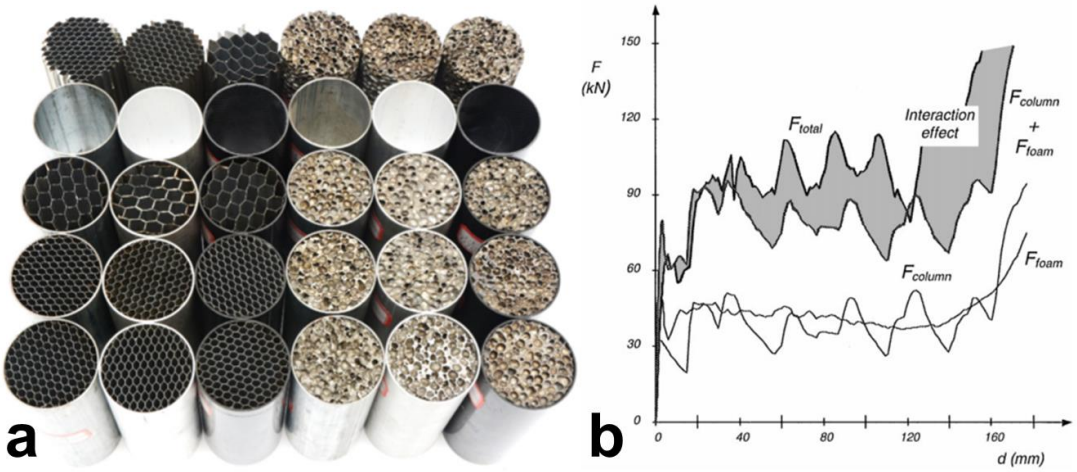

Figure 2-11. (a) Examples of aluminium foam and honeycomb filled tubes (100); (b) Interaction effect between foam infill and column wall (99)

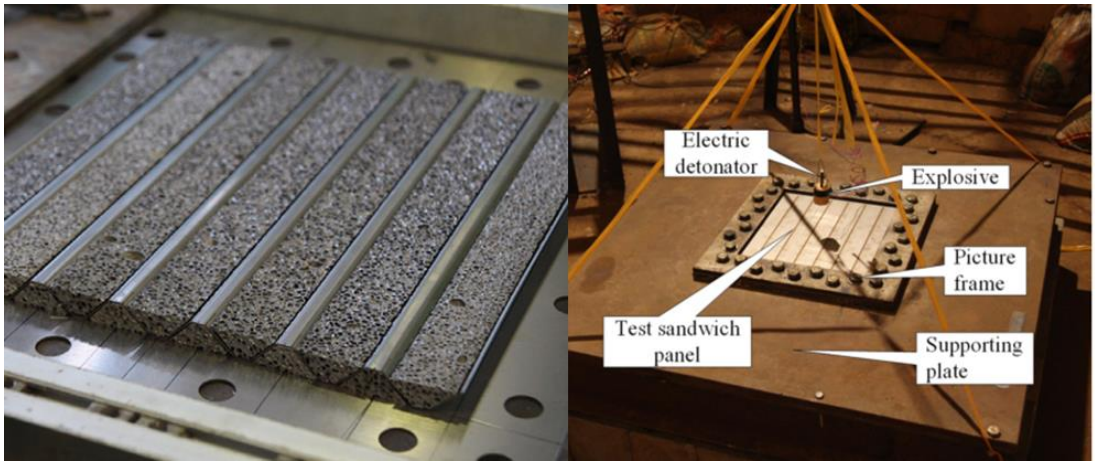

Figure 2-12. Aluminium foam filled corrugated core of a sandwich panel and its blast test setup (101)

Apart from thin-walled tubes and columns, the foam materials are filled in the core of many sandwich structures as shown in Figure 2-12 and Figure 2-13, these include corrugated panel (101-103), eggbox core (104), pyramidal lattice core (105), energy absorption connectors (106, 107) and corrugated sandwich cylindrical shell (108). These foam filled sandwich structures are investigated under various loading

conditions such as quasi-static bending and crushing, dynamic impacting and blast loadings. Change in damage modes and enhancement in structure performance can be observed for all these structures with foam fillers. Therefore, the lightweight foam filler can be used as an effective way to increase the energy absorption of the sandwich structures, especially for the structures with large surface area in the core for a greater foam-wall interaction effect.

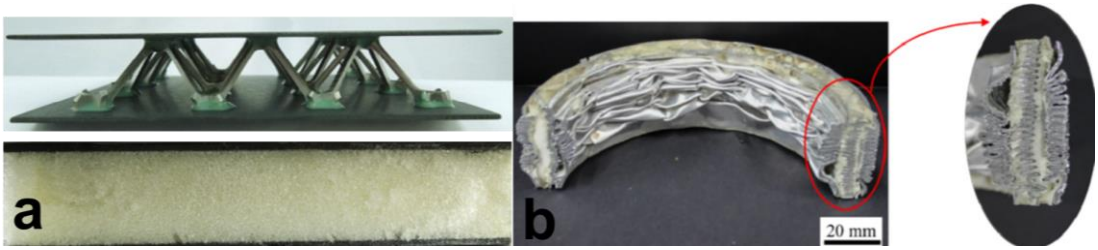

Figure 2-13. (a) Sandwich panel with polyurethane foam filled pyramidal lattice truss core (105); (b) Damage mode of a polymethacrylimid (PMI) foam filled corrugated sandwich cylindrical shell (108)

2.7 Investigation methods for dynamic loading

2.7.1 Experimental investigations

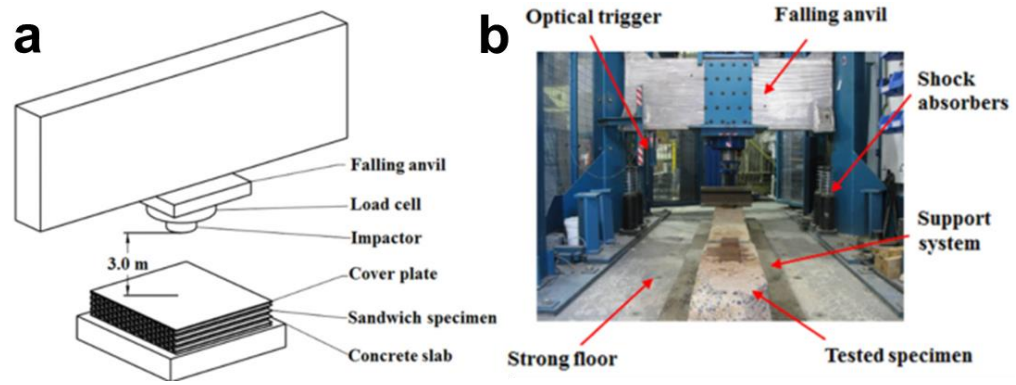

Figure 2-14. Drop weight test of an auxetic panel: (a) schematic diagram; (b) test facility (49)

There are numerous techniques such as gas gun (39), Split Hopkinson Pressure Bar (SHPB) (11), drop weight (49) and pendulum (2) to apply impact loads on structures. A drop weight testing facility is shown in Figure 2-14. These testing facilities can simulate the impact loads. However, due to the mechanism of drop weight and pendulum impact, the loading rate may vary throughout the deformation of the tested structures. To apply a constant impacting speed, high speed testing machine is used. For instance, INSTRON VHS 160/100-20 uses servo-hydraulic and control

technologies to provide relatively constant loading speed throughout the deformation of the tested structures for dynamic tensile (109) and compressive testings (110, 111).

Ballistic pendulum systems are widely used for free air blast test, these include two-cable pendulum (7, 112) and four-cable pendulum (113, 114). As the tested structure is attached on the pendulum and placed in front of the charge, the blast loading applied on the tested structure causes the rotation or translation of the pendulum. The imparted impulse from the blast can be measured, according to the rotational angle or oscillation amplitude of the pendulum. An example of a two-cable pendulum and its mechanism is shown in Figure 2-15.

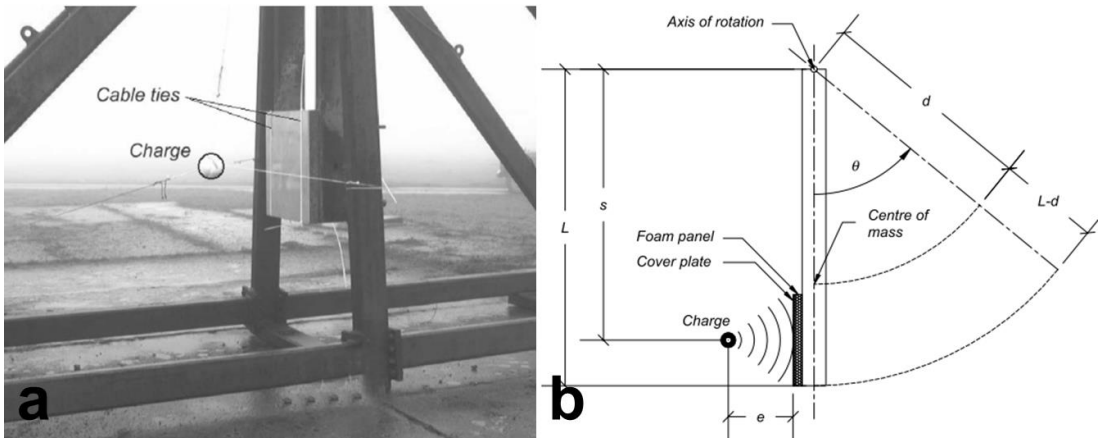

Figure 2-15. (a) Pendulum set up for blast test; (b) simplified illustration of the blast-loaded pendulum (7)

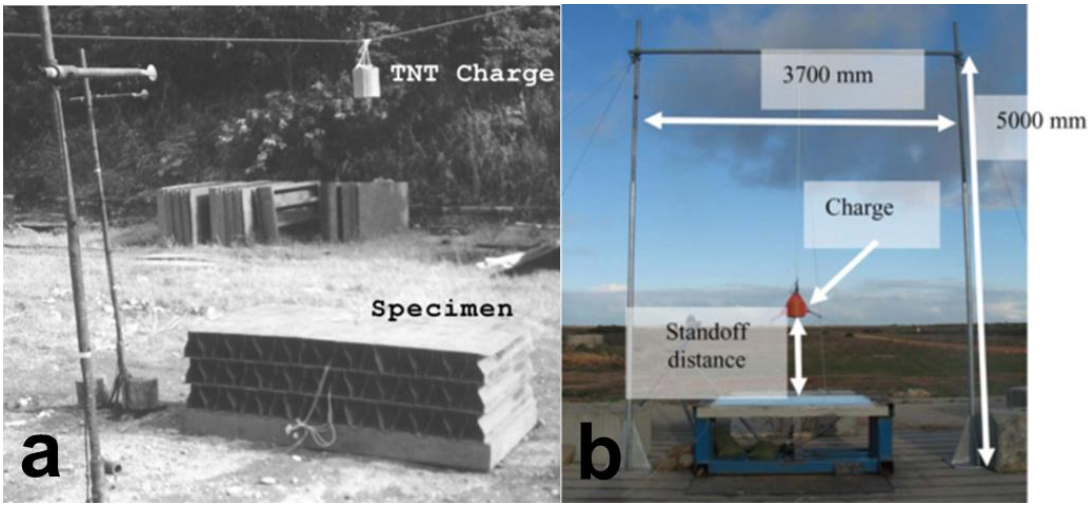

Figure 2-16. (a) Blast test of layered sacrificial cladding (115); (b) blast test of aluminium foam as cladding (116)

Other arrangement include placing specimens on a rigid support and tested under blast loadings (49, 115). Sensors including accelerometer, displacement transducer and

pressure sensor are often used in these tests to measure and record the relevant parameters, such as over pressure, acceleration and displacement. In some studies of blast mitigation performance of sacrificial claddings, the cladding structures were placed on a simply supported concrete beam or slab (116, 117). The blast mitigation performances were evaluated by comparing the final deformation of the protected concrete structure with other referenced tests. Examples of these two cases are shown in Figure 2-16, where a structure is placed on a rigid concrete block and an end-supported concrete slab, respectively. However, the blast loading exerted on the structure may not be uniform in these tests, due to the short stand-off distance. The shock tube is used by some researchers to generate more uniform blast loads (18, 118, 119). Furthermore, to evaluate the reduction in peak force transmitted to the structure with and without any protective cladding, load cells were placed in-between the protective cladding and the rigid support. Recorded force-time histories were then compared and evaluated to examine the blast mitigation capability of the tested cladding structures. Examples of the shock tube tests and the transmitted force measuring set-up are shown in Figure 2-17 and Figure 2-18, where relatively uniform pressure distributions were generated on the different locations of the panels (18, 118, 119).

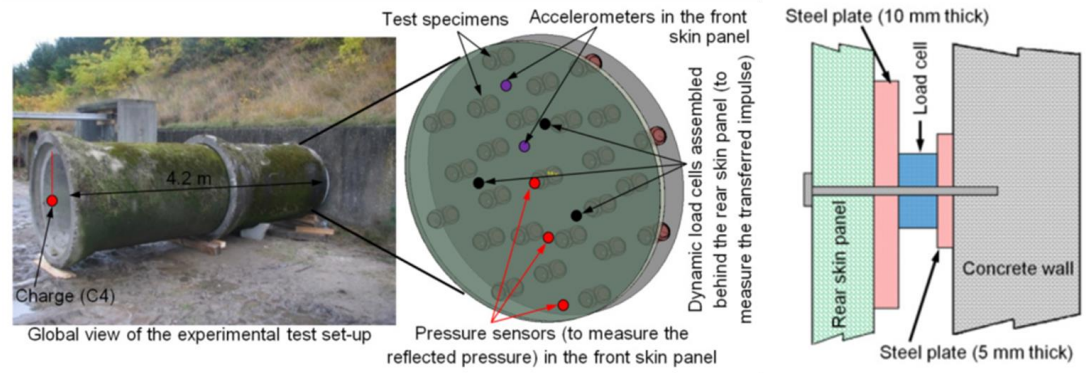

Figure 2-17. Experiment setup of the shock tube blast test of cladding with empty cans and the load cell setup (118)

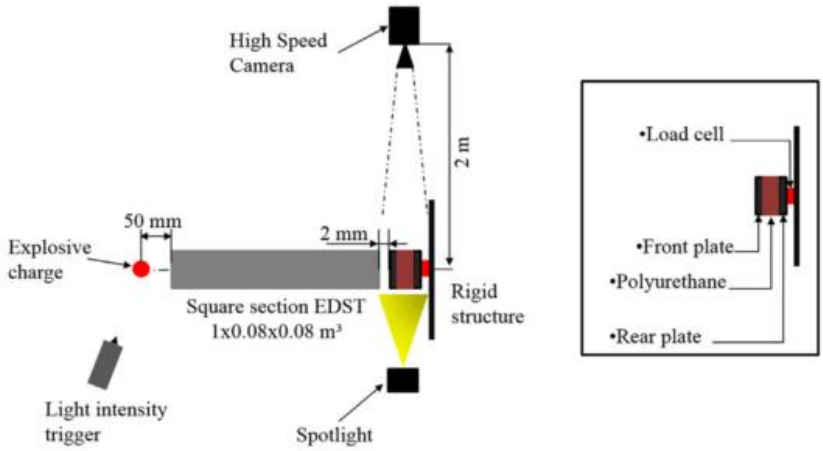

Figure 2-18. Schematic graph of explosive driven shock tube blast test of sacrificial cladding with PU foam and the load cell setup (18, 119)

Other techniques are applied for simulating intensive impulsive loading without using any explosive. Radford et al (120) used metal foam projectile impacting on the structures to simulate blast loading. The pressure transient is found to be independent of dynamic impedance of the impacted structure, which indicates that the metal foam projectile can be used as a convenient experimental tool for testing the shock resistance of structures. Chen and Hao (74) used a pendulum impacting system with a striker plate and an airbag to simulate uniform blast loadings onto the clamped sandwich panel. For each loading, the pendulum impacted on a thick stiffened striker plate. The impulsive loading was then uniformly transferred from the striker plate to the clamped specimen via a confined airbag placed between the striker plate and the clamped specimen. As shown in Figure 2-19, Remennikov et al (121) developed an Advanced Blast Simulator (ABS) using an oxy-acetylene gas mix as driver to simulate blast loads with up to 350 kPa of overpressure.

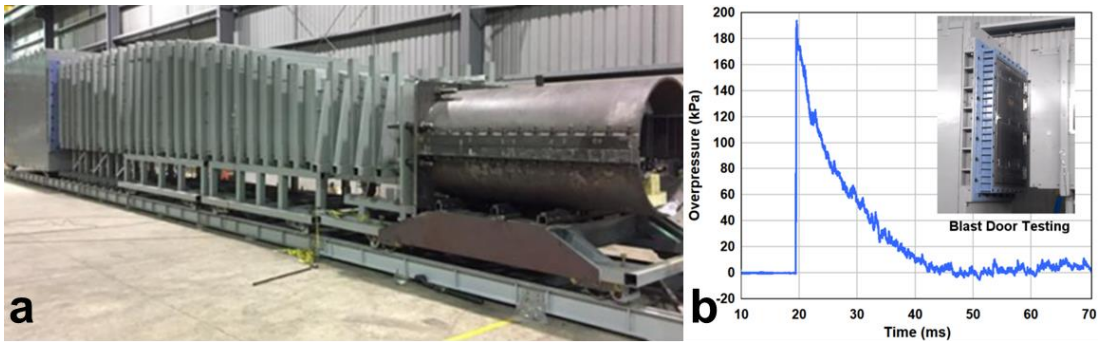

Figure 2-19. (a) Advanced Blast Simulator (ABS) configuration; (b) Testing of a blast door (121)

2.7.2 Numerical simulations

It is noted that conducting experimental tests can be extremely expensive, dangerous and may take a long time to prepare. Furthermore, reproducibility of blast and impact tests can lead to inconsistent results due to the uncertainties involved in the blast and impact. Stress/strain distribution and wave propagation can be hard to measure. These shortcomings can be eliminated by conducting numerical simulations. Commercial finite element software packages such as LS-DYNA and ABAQUS are often used to simulate tests for investigation of structural responses. Loading conditions, geometric parameters and boundary conditions can be easily changed in the numerical models and more detailed results can be extracted. Parametric studies can be conducted in numerical simulations, much quicker and cheaper than actual tests. However, the numerical model must be verified carefully with actual testing data to ensure an accurate result.

In the commercial FE software LS-DYNA, blast load can be simulated in two ways: modelling the charge as a material with Arbitrary-Lagrangian-Eulerian (ALE) algorithm (65, 73, 122, 123) or defining blast loads with functions (61, 124, 125). For the first method, the charge is modelled as a material with Jones-Wilkins-Lee equation of state (EOS) which describes the relationship between pressure, the local density and the local energy (65, 73). The explosive expands significantly to the air domain and interacts with the structures using the ALE algorithm, which is a hybrid algorithm between Lagrangian and Eulerian algorithm. Shock wave interaction and reflection can be simulated using this method. However, the computational cost can be very expensive. Blast load can also be predicted empirically based on testing data. Blast pressure prediction program CONWEP, which is based on empirical relations derived from testing data, is incorporated into LS-DYNA with the keyword *LOAD BLAST ENHANCED (61). The pressure is calculated as follows:

$$P(\tau) = P_r \cos^2\theta + P_i\left(1 + \cos^2\theta - 2\cos\theta\right) \qquad (2\text{-}2)$$

where *Pr* is the reflected pressure, *Pi* is the incident pressure and θ is the angle of incidence. The computational time is greatly reduced with this method. However, it is worth noting that localised impulsive load cannot be simulated and the wave-reflection is not considered by this method.

Foam materials can be modelled with *MAT CRUSHABLE FOAM (65, 126, 127), the mechanical properties such as yield strength, Poisson's ratio, density, and stress-strain curve can be defined. The elastic-plastic material models *MAT PLASTIC KINEMATIC and *MAT PIECEWISE LINEAR PLASTICITY are often used for modelling metal materials (59, 65, 73). *MAT PLASTIC KINEMATIC is commonly used for modelling metals with bi-linear elastic-plastic constitutive relationship and isotropic or kinematic hardening plasticity which is defined by a hardening parameter β, where β equals to 1, representing isotropic hardening, is used. The material strain rate effect is also considered by applying Cowper-Symonds model in LS-DYNA which is defined as follows (128).

$$\frac{\sigma_d}{\sigma_s} = 1 + \left(\frac{\dot{\varepsilon}}{C}\right)^{\frac{1}{p}} \qquad (2\text{-}3)$$

where σ_d is the dynamic yield stress at plastic strain rate $\dot{\varepsilon}$, σ_s is the static yield stress. Strain rate parameters C and P are Cowper and Symonds constants. *MAT PIECEWISE LINEAR PLASTICITY is an elasto-plastic material with an stress-strain curve and the strain rate dependency can be defined (129). The stress-strain curve can be defined by the measured data of material. Three formulations including Cowper-Symonds with deviatoric strain rate, scale yield stress and viscoplastic formulation can be chosen for strain rate effects (129).

2.8 Summary

In this chapter, the information regarding dynamic impulsive loadings, energy absorption, related sandwich structures, folded structures and methodology are briefly discussed. From the literature review, some research gaps are presented below.

To mitigate the damage of impulsive loadings including blast and impact, two types of protective sandwich structures can be applied. The first type is used as an energy absorber. The desired mechanical properties of these energy absorbing sandwich structure include low initial peak force, consistent crushing resistance throughout the deformation of the structure and low sensitivity to loading rate. Most of the conventional sandwich structures have a high strength to weight ratio. Their dynamic responses, however, are not ideal to be used as energy absorbing devices.

Characteristics such as high initial peak force, fluctuation in crushing resistance and highly sensitive to loading rates are often presented for these conventional sandwich structures. Most of the current energy absorbing structures including egg box and aluminium foam have good dynamic responses but their energy absorption capacity is often low and can be further improved. Folded structures have gained some attention recently, as complex geometry could be achieved using sheet material and has the potential to be used as an energy absorber. New forms of folded structures may be developed with inter-connected adjacent vertical faces to achieve a higher crushing resistance while maintaining the uniform crushing behaviour and low sensitivity to loading rates.

For the second type of protective sandwich structures to resist the intensive blast loadings, the structure must be strong enough to survive the intensive loadings. Most of the existing research, however, only focus on the sandwich structure itself. For the case of blast resistant door panel, the damage caused at the door frame could be crucial as well. New bi-directional load-self-cancelling sandwich structure could be investigated to reduce the reaction force from the support and reduce the damage caused in the event of an explosion.

In terms of investigation methods, both experimental techniques and numerical simulations are reviewed. A wide range of experimental facilities are developed by researchers, and are able to generate desired dynamic loads. However, these experimental tests could be very expensive. FEA software LS-DYNA, is used by many researchers for these non-linear dynamic analysis of structures. It has been proven that verified numerical models could provide accurate and detailed results for structural analysis.

Chapter 3. Truncated square pyramid (TSP) folded structure with interconnected sidewalls

The related work in this chapter has been published in International Journal of Impact Engineering.

Li Z, Chen W, Hao H. Crushing behaviours of folded kirigami structure with square dome shape. International Journal of Impact Engineering. 2018;115:94-105. DOI: doi.org/10.1016/j.ijimpeng.2018.01.013

3.1 Introduction

In this chapter, a new rigid kirigami foldcore with tessellated truncated square pyramid (TSP) is proposed. The proposed TSP pattern is inspired by a combination of bi-directional load-self-cancelling square dome structure (76) and the kirigami patterns by Fathers et al (87). Finite element analysis software LS-DYNA is employed to analyse peak stress, average stress, energy absorption and densification strain of different foldcores. A numerical model of a foldcore with cube strip kirigami pattern under flatwise quasi-static crushing is firstly constructed and calibrated by comparing its generated stress-strain curves with the existing experimental data. The calibrated numerical model is then used to perform numerical simulations of the responses of the proposed TSP folded structures. The proposed foldcores are compared with the cube strip kirigami structure, which has already demonstrated superior energy absorption capacity over other origami foldcores from the previous studies (84, 87). In addition, various dynamic loading rates are applied on the proposed foldcores to investigate the effect of strain rate on structural response and energy absorption capacity of these foldcores.

3.2 Numerical model validation

Finite element software LS-DYNA is used for numerical simulation. Experimental data of the cube strip kirigami foldcore under quasi-static flatwise crushing by Fathers et al (87) is used for model calibration. The accuracy and reliability of the numerical model is examined by comparing the stress-strain curves. Folding configuration of kirigami cube strip foldcore is shown in Figure 3-1. Each row of cube strip is folded from a single strip of aluminium sheet and foldcore is then glued to the base plate. No

connection or glue is placed between each row of cube strip. Each unit cell of cube strip foldcore consists of four 10 mm by 10 mm square faces and has a dimension of 20 mm by 10 mm by 10 mm in length, width and height, respectively. In the previous study, the strips are folded from aluminium 1100 alloy sheet with a thickness of 0.15 mm, which gives foldcore a volumetric density of ρ_v=3%.

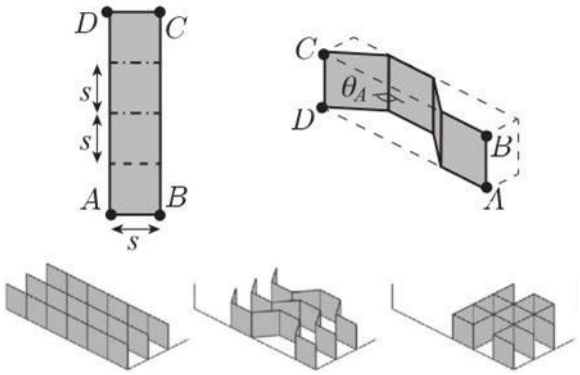

Figure 3-1. Crease pattern and folded configuration of kirigami foldcore with cube strip (87)

3.2.1 Numerical model

A numerical model is built with one folded unit cell as shown in Figure 3-2 (a). To verify the numerical model, it is similar to the numerical analysis in the previous study (87). The foldcore unit cell is modelled by using default Belytschko-Tsay type shell elements, as shown in Figure 3-2. An isotropic hardening material model *MAT_024 PIECEWISE LINEAR PLASTICITY is used for the material. The material properties and true plastic stress-strain data for the sample material are listed in Table 3-1 and Table 3-2, respectively. The unit cell is fixed onto a rigid plate by constraining the bottom edges of the cell. The sample is then flatwise crushed till around strain ε=0.8 by another rigid plate from top with a constant crushing speed of 0.05 m/s. It should be noted that computational cost for explicit simulation by using experimental quasi-static loading speed (1mm/min) is too expensive, in this chapter the crushing speed of 0.05 m/s is adopted because it was found sufficient to ensure quasi-static conditions in the simulation (87). Top rigid crushing plate is set to have only one-degree of freedom in vertical direction, which simulates flatwise crushing experiment. The self-contact of the foldcore is modelled by the keyword *CONTACT AUTOMATIC SINGLE SURFACE. The contacts between foldcore and top/bottom plates are modelled by *CONTACT AUTOMATIC NODES TO SURFACE. Friction

coefficient of 0.25 from the cube strip foldcore study (87) is used for the contact interactions. Figure 3-2 (b/c/d/e) show the numerical models of the proposed unit cells, together with the folded unit cell shown in Figure 3-2 (a) used for model validation.

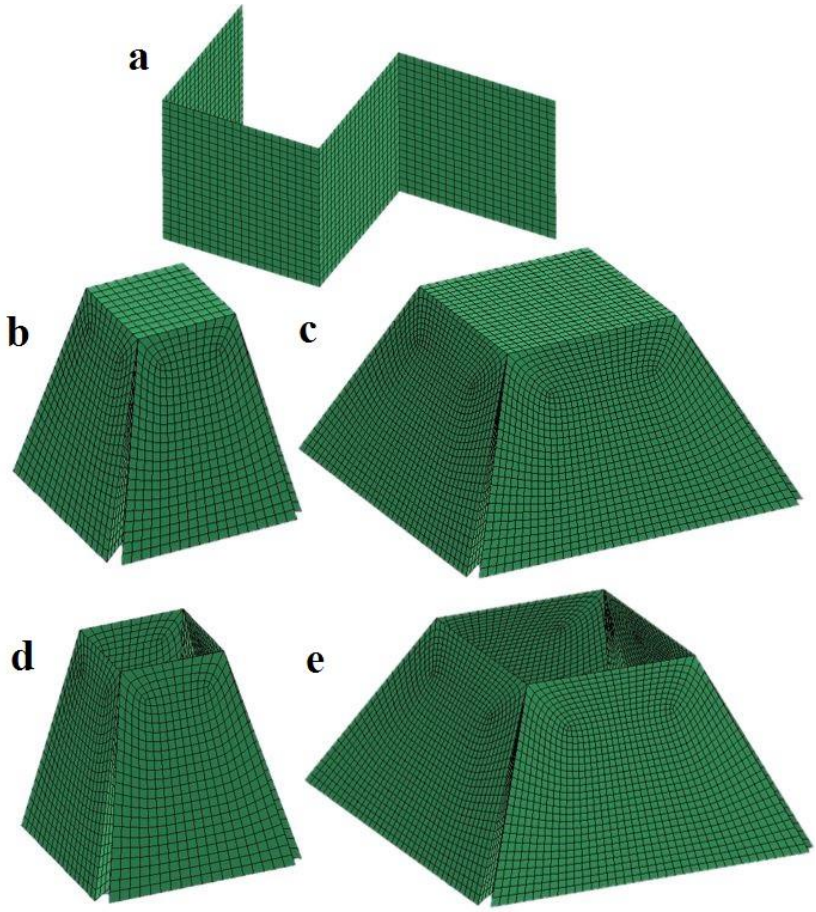

Figure 3-2. Single unit cell with mesh size of 0.5 mm, (a) kirigami cube strip foldcore, (b) 10 mm closed top TSP foldcore, (c) 20 mm closed top TSP foldcore, (d) 10 mm open top TSP foldcore, (e) 20 mm open top TSP foldcore

Table 3-1. Material properties of Aluminium 1100 alloy (81)

Parameter	**Young's modulus (GPa)**	**Poisson's ratio**	**Yield stress (MPa)**	**Density (kg/m^3)**
Value	69	0.33	23.9	2710

Table 3-2. True plastic stress-strain data of Aluminium 1100 alloy from experiment (87)

Strain	0	0.007	0.019	0.048	0.106	0.183	0.260
Stress (MPa)	23.9	38.4	51.9	67.8	83.6	96.1	105.8

3.2.2 Mesh convergence test

As an important factor for determining both the computational cost and simulation accuracy, mesh size convergence tests are carried out with four element sizes of 1 mm, 0.5 mm, 0.25 mm and 0.125 mm. Stress is calculated from the reaction force of crushing a foldcore unit cell and its base area, i.e., 10 mm by 20 mm for cube strip foldcore. As shown in Figure 2-10 (b), the top edges of each unit cell of the tested foldcore are not all on the exact same elevated level, due to manufacturing error. The 0.5 mm manufacturing imperfection, which is equal to 5% strain for this 10 mm high foldcore, was considered in the numerical simulations conducted by Fathers et al (87). However, the imperfection is removed to simplify the simulation in the mesh convergence tests of this chapter. The average stress of a unit cell is calculated using base area of 20 mm by 10 mm.

The results of the mesh convergence test are shown in Figure 3-3. No obvious difference in the peak stress and the flowing stress obtained with these four different mesh sizes. However, mesh size has significant effect on the densification stage. Numerical result of using 1 mm mesh yields a much smaller densification strain and higher stress. The other three mesh sizes (0.5 mm, 0.25 mm, 0.125 mm) generate similar results and a good agreement is obtained comparing with the experimental and numerical data given in (87). Therefore, 0.5 mm mesh size is used in the subsequent simulations.

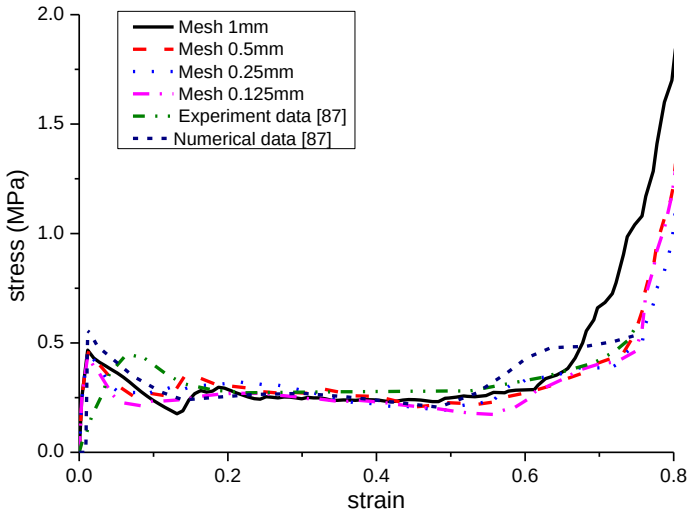

Figure 3-3. Stress-strain curves of cube strip foldcore with different mesh sizes and comparison with the experimental and numerical data in (87)

It is noted that the initial stiffness, i.e., the slope before the initial peak stress corresponding to the experimental data in (87) is smaller than the numerical result. This is caused by the variation of core height of the sample induced by the folding process in preparing the testing samples. Other than that, the comparison demonstrates the numerical model yields good predictions of the performance of a foldcore. It should be noted that the initial imperfection of the foldcore, which is probably inevitable in practice, is not considered in the present analysis since it does not affect the performance of the foldcore in terms of the initial peak stress, plastic flow and densification process.

3.3 Geometries of TSP foldcore

The traditional kirigami folded cube pattern (86) and kirigami cube strip pattern (87) previously studied have one drawback. Adjacent vertical faces of each unit cell of the foldcore are not constrained. There is no vertical constraint as no connection exists between each row of folded cube strip. Similarly, vertical connections only exist on some vertical faces of folded cube structure. Folding process of cube pattern is shown in Figure 2-10 (b), and some of the obvious loose edges for both foldcores are marked out in red shown in Figure 2-10. This might be one of the main causes for the inferiority of cube strip foldcore as compared to the square honeycomb with the same unit cell configuration in terms of crushing resistance.

To improve the crushing resistance of the structure, the adjacent faces on the proposed foldcores are designed to be connected. This is achieved by adding triangular interconnections between two adjacent sidewalls of the folded core, as shown in Figure 3-4 (b) (d). These interconnections provide extra supports for out-of-plane loading. To properly represent the near-fully-folded configuration in reality, slight gap of 0.5 mm is assumed in the numerical models, also shown in Figure 3-4 (d). The folding creases are marked in continuous line in Figure 3-4 (a). The only cut-out requirement for folding is the octagon shape in the centre of four adjacent unit cells. For the structure with open top, the smaller squares in the centre of each unit cell are cut out and then the sheet is folded in the same way as the TSP structures with closed top.

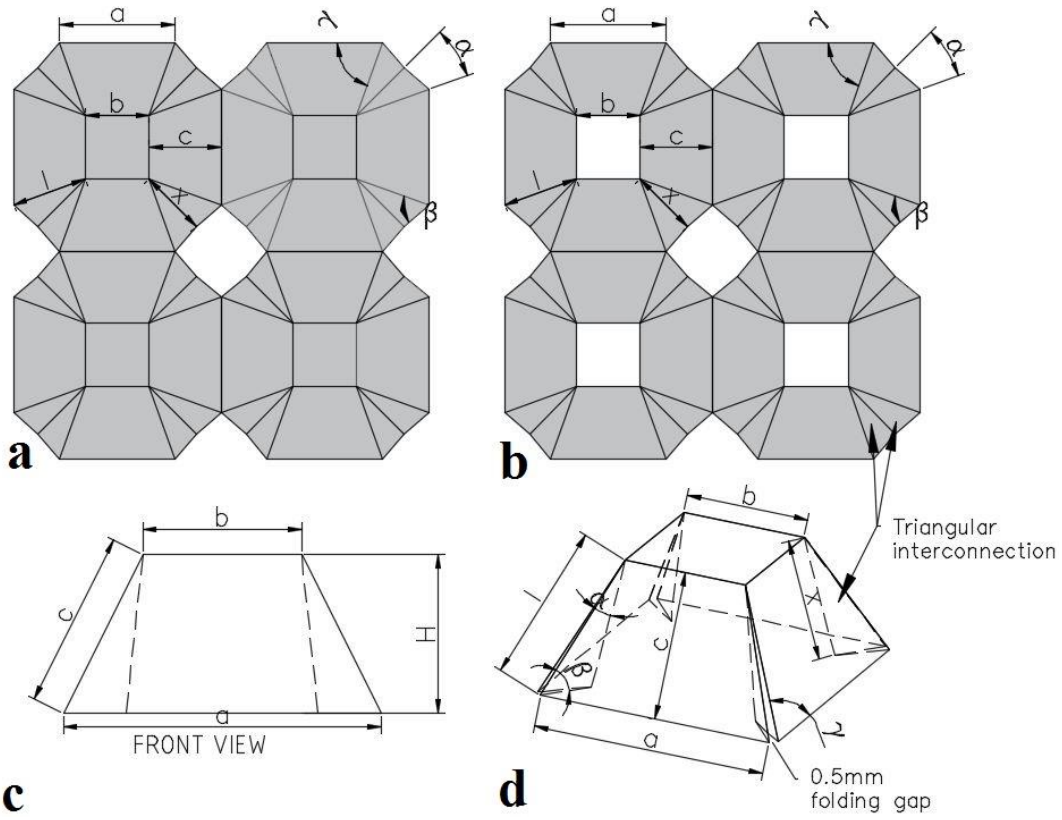

Figure 3-4. (a) Crease pattern of closed top TSP foldcore; (b) Crease pattern of open-top TSP foldcore; (c) front view of a unit cell of TSP foldcore; (d) isometric view of folding configurations of TSP foldcore

The added sidewall interconnections constrain the dimension of the foldcore. The top angle of triangular interconnection i.e. alpha α, is restricted by the top and base square length, *a*, *b*, and the height of the truncated pyramid, *H* as shown Figure 3-4 (c). The volumetric density ρ_v, is kept constant as 3% throughout this chapter. Accordingly, the thickness of the foldcore t is modified based on the calculated surface areas of each core. For the proposed TSP foldcore, the shape of the unit cell and the interconnections of sidewalls are determined by three parameters, i.e. *a*, *b*, *H*. Other geometry parameters shown in Figure 3-4 can be determined by these three parameters as follows:

$$c=\sqrt{(\frac{a-b}{2})^2+H^2}\ ;\ l=\sqrt{(\frac{a-b}{2})^2+c^2}\ ;\ \gamma=arctan\left(\frac{2c}{a-b}\right);\alpha=\gamma-\frac{\pi}{4}\ ;$$

$$\beta=arccos\left(\frac{\sqrt{2}a-\sqrt{2}b}{2l}\right);\ x=\frac{sin\beta\cdot l}{sin\left(\pi-\alpha-\beta\right)};$$

The total surface area for each closed top unit cell

$$A = b^2 + 4 \times \frac{1}{2} c(a+b) + 8 \times \frac{1}{2} sin\alpha \cdot xl \ ;$$

The total surface area for each open-top unit cell $= 4 \times \frac{1}{2} c(a+b) + 8 \times \frac{1}{2} sin\alpha \cdot xl$;

The relative density, or volumetric density, $\rho_v = \frac{A \cdot t}{a^2 H}$.

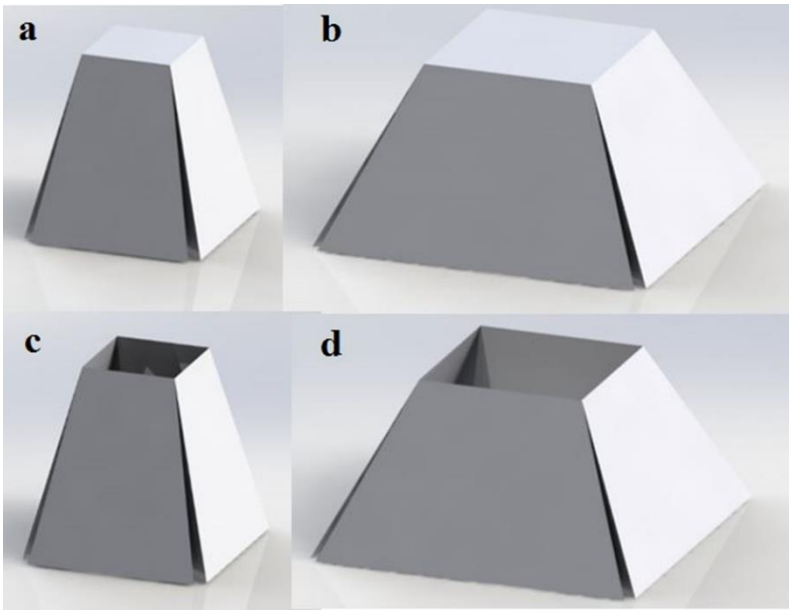

Figure 3-5. Four configurations of folded truncated pyramids, (a) TSP10-CT; (b) TSP20-CT; (c) TSP10-OT; (d) TSP20-OT

Two types of kirigami foldcores with truncated square pyramid, each with two different base dimensions are investigated in this chapter. One type of foldcore is TSP with top face and another type is the same truncated pyramid but without top face. The top face of each unit cell can be removed as it provides little contribution to energy absorption in flatwise crushing of the foldcore. Height, *H*, is set as 10 mm for all the four TSP foldcores. For the 10 mm closed top TSP foldcore, *a*=10 mm, *b*=5 mm and *t*=0.055 mm to achieve a 3% relative volumetric density. For the 10 mm open-top TSP foldcore, *t* is calculated to be 0.057 mm. For the TSP foldcore with the base size of 20 mm, the thickness of the wall is calculated to be 0.13 mm and 0.147 mm, for the closed and open top foldcores, respectively. These foldcores are denoted as TSP10-CT, TSP10-OT, TSP20-CT, TSP20-OT, which define the base length a (10 mm or 20 mm)

and the closed or open top on the foldcores. The illustrations of four configurations of foldcores are shown in Figure 3-5.

3.4 Quasi-static flatwise crushing

Structural responses of quasi-static flatwise crushing of four types of foldcores are obtained from numerical simulations and compared with the calibrated cube strip foldcore. Average plateau stress, σ_{ave}, densification strain, ε_D, and peak stress, σ_{peak}, are used for analysis and evaluation of the foldcores. The stress-strain curves are calculated from the force-time (P-T) curves obtained from the numerical simulations, where the vertical reaction forces are exerted on the rigid crushing plate under a constant speed (v). Stress, σ, is equal to the reaction force divided by the base area instead of top area, given as $\sigma = \frac{P}{a^2}$, since stress calculated from base area can better describe the crushing of sandwich structure where array of truncated pyramids are folded as core. Strain is calculated using the product of time and crushing speed divided by the overall height of the foldcore, given as $\varepsilon = \frac{vT}{H}$, where T is the time since the beginning of crushing.

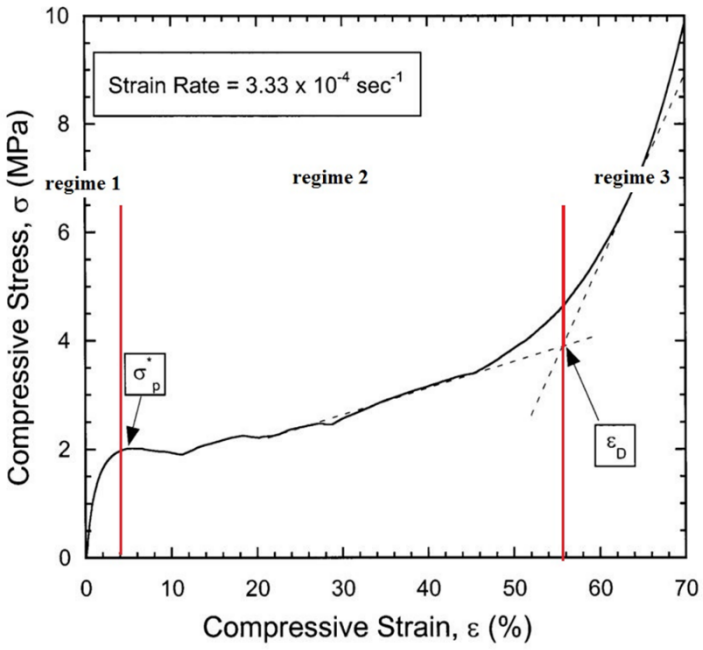

Figure 3-6. Example of stress-strain curve of a typical aluminium foam under quasi-static crushing with three regimes and the illustration of densification strain (25)

The behaviour of all foldcores under quasi-static crushing, as shown in Figure 3-7, are similar to that of the aluminium foam (22, 24, 25). As shown in Figure 3-6, three regimes are present for a typical stress-strain curve of aluminium foam under quasi-static crushing. They are: 1) Linear elastic regime at low stresses; 2) Long plateau regime where localized plastic collapse propagates through foldcore; and 3) Densified regime that structure is fully collapsed with a rapid rise in stress with further strain.

Similar to aluminium foam, the densification strain (ε_D) calculated in this chapter is defined by the intersection of two asymptotic curves of the stress-strain response at plateau and densified regimes, as illustrated in Figure 3-6. The average plateau stress is the internal energy absorption before densification divided by densification strain, and it is calculated as $\sigma_{ave} = \frac{\int_0^{\varepsilon_D} \sigma(\varepsilon) d\varepsilon}{\varepsilon_D}$. Since the initial peak stress of TSP foldcores is much lower than its average stress, σ_{peak} is defined herein by the peak value of stress in plateau regime as marked in Figure 3-7. The uniformity ratio U between peak stress and average stress acts as an indicator of the uniformity of energy absorption.

3.4.1 Stress-strain curve comparison among five foldcores

Stress-strain curves of different foldcores are presented in Figure 3-7. TSP20-OT demonstrates the best performance among these foldcores, with a low initial peak stress, a relatively high plateau stress and a high densification strain. Similar significant reduction of initial peak stress at the end of linear elastic regime can be observed when comparing other three proposed TSP foldcores with cube strip. Although these three TSP foldcores, i.e. TSP10-CT, TSP10-OT and TSP20-CT, have a slightly decrease in plateau stress and densification strain than cube strip foldcore. The occurrence of the overall peak stress is also delayed for all TSP foldcores to strain at about 0.1 to 0.3 at the plateau regime instead of initial linear elastic regime as cube strip foldcore. When comparing the open-top TSP foldcores i.e. TSP20-OT, TSP10-OT to their same-sized TSP foldcores with closed top i.e. TSP20-CT and TSP10-CT, a noticeable rise in plateau stress and slight increase in densification strain can be observed. It is because the closed top TSP folcores have a thinner wall thickness than their same-sized open top foldcores, while the top face provides little resistance against quasi-static flatwise crushing of the foldcore.

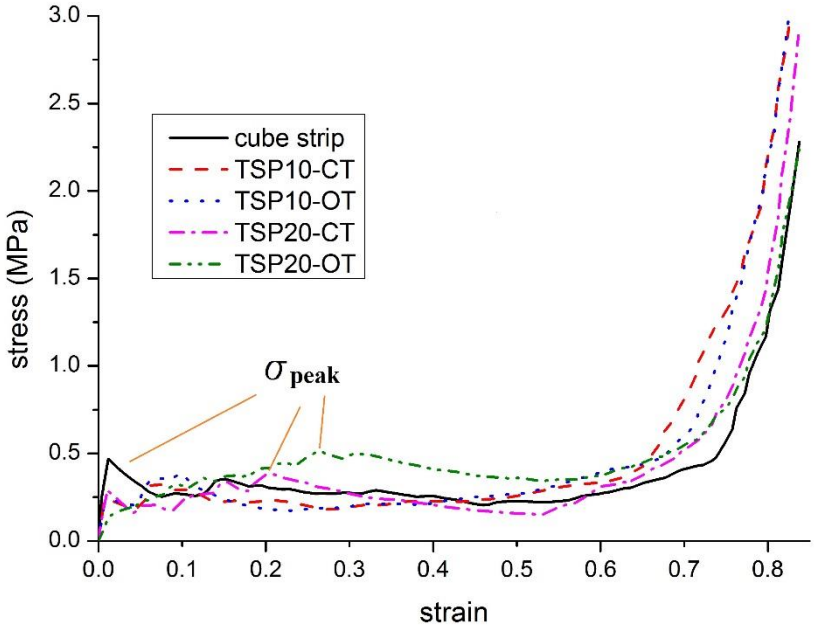

Figure 3-7. Stress-strain curves of five foldcores under quasi-static flatwise crushing

The average stress, peak stress, densification strain and uniformity ratio are listed in Table 3-3. Comparing the plateau stress before densification, cube strip foldcore and three TSP foldcores i.e. TSP10-OT, TSP10-CT and TSP20-CT, have similar value. TSP20-OT holds the highest average plateau stress at 0.389 MPa, around 36% higher than the second highest average plateau stress of the cube strip foldcore of 0.286 MPa. TSP10-OT, TSP10-CT and TSP20-CT have similar peak stress around 0.35 MPa. Densification strains of these foldcores are similar in value, around 0.7 except for TSP10-CT. For an ideal energy absorption material or structure, the following characteristics are expected: low initial peak stress, high plateau stress, less variation in crushing resistance and high densification strain. As can be observed from Table 3-3, TSP20-OT has a low uniformity ratio, high plateau stress and densification strain. It can be concluded that TSP20-OT has the best performance with regards to energy absorption capacity among these five foldcores.

Table 3-3. Average plateau stress, peak stress, densification strain ε_D and uniformity ratio U of five configurations of foldcores under flatwise quasi-static crushing

Parameter	Cube strip	TSP10-CT	TSP10-OT	TSP20-CT	TSP20-OT
σ_{peak} (MPa)	0.469	0.325	0.375	0.384	0.508
σ_{ave} (MPa)	0.286	0.250	0.275	0.264	0.389
ε_D	0.72	0.65	0.69	0.71	0.72
$U= \sigma_{peak} / \sigma_{ave}$	1.64	1.30	1.36	1.46	1.31

As given in Table 3-3, although the average stresses of plateau stage of TSP10-CT, TSP10-OT and TSP20-CT are slightly lower than that of the cube strip, their uniformity ratios are significantly improved. Furthermore, a delay of peak stress can be easily noticed from the stress-strain curves of these three TSP foldcores, which indicates that it is easier to deform at the early stage for the proposed TSP foldcores. TSP20-OT outperforms the other three TSP foldcores and the cube strip in all four key indicators, indicating it is the best design among those considered in the chapter for potential application of kirigami TSP foldcore in terms of energy absorption.

3.4.2 Damage mode of the foldcores

The damage modes of the TSP foldcores are different from the cube strip foldcore. Damage modes are shown in Figure 3-8, with flatwise crushed foldcores at the strains of 0.2, 0.4 and 0.6, respectively. Similar to widely investigated square honeycomb structures (17, 130, 131), cube strip foldcore can be treated as square honeycomb without connections between adjacent rows. The deformation mode for cube strip foldcore is governed by buckling and followed by sequential folding of the core sidewalls. Less constraint between adjacent unit cells of cube strip results in an easier buckling behaviour at initial crushing than square honeycomb structures. The TSP foldcores yield different collapse patterns. At initial stage of the crushing, the side walls of TSP foldcore are prone to bend and roll inwards towards the centre of unit cell. This is because the sidewalls are leaning towards the centre, which is different from the vertical sidewall of the cube strip foldcore or square honeycomb structures. Once the rigid plate is in contact with the foldcore, the inclined sidewalls bend under the vertical load. Due to the inward bending of the top edges of sidewalls, the top surface of the folded truncated pyramid, TSP10-CT, TSP20-CT becomes a dent instead of a flat surface, as can be seen in Figure 3-8.

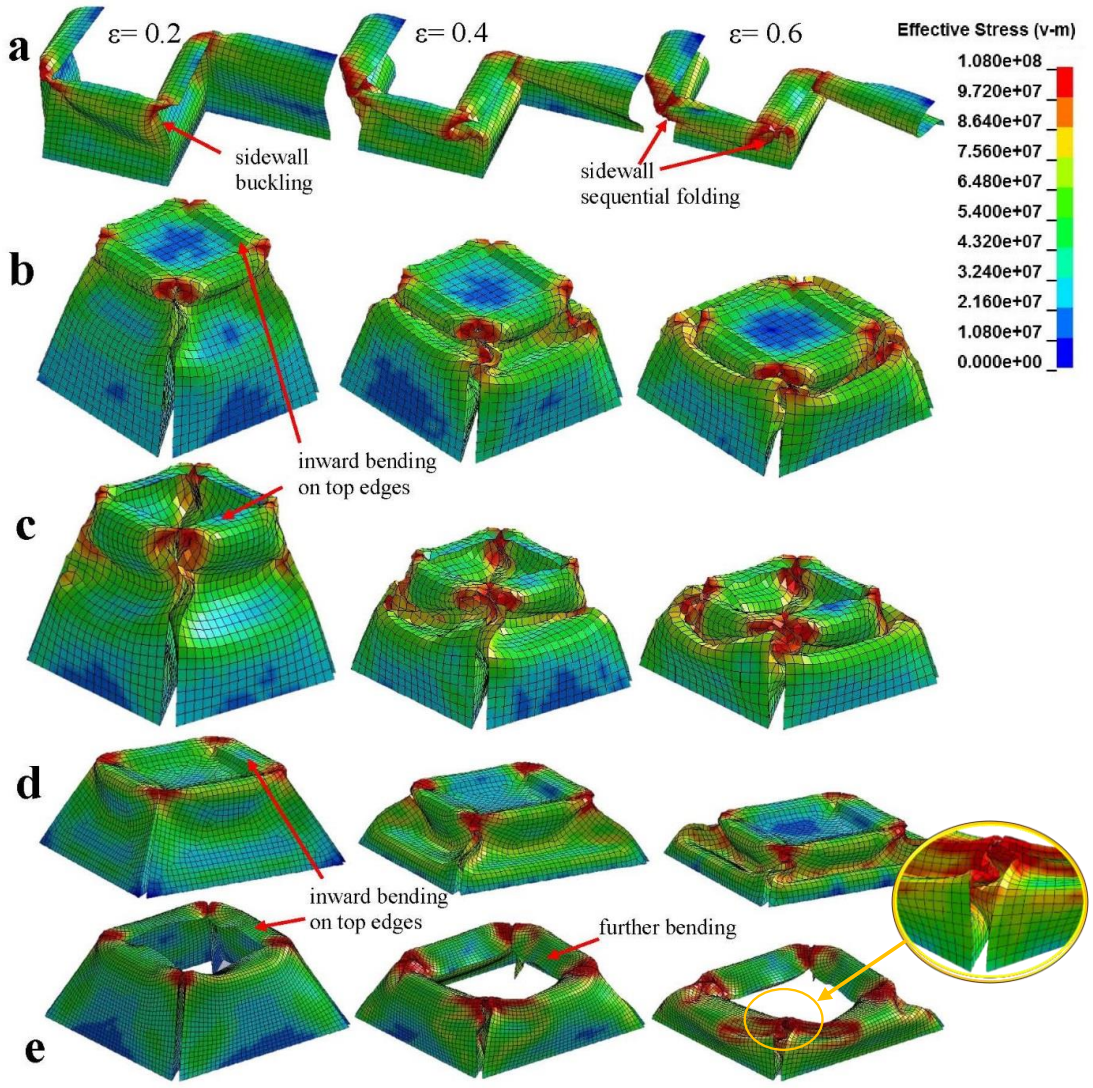

Figure 3-8. Damage modes of five foldcores at the strain of 0.2, 0.4 and 0.6 under quasi-static crushing of 0.05 m/s, a) cube strip; b) TSP10-CT; c) TSP10-OT; d) TSP20-CT; e) TSP20-OT (Note: TSP20-CT and TSP20-OT are scaled down to fit into one graph)

The action of bending and rolling stops with further crushing, as there are two triangular interconnections at each corner for the TSP foldcores, providing increased resistance against bending and rolling. Because of the triangular geometries of the interconnections, with increasing cross-section area from top to bottom, the crushing resistance increases with the crushing deformation. It can be confirmed by comparing damage mode of TSP10-CT with TSP20-CT and comparing TSP10-OT with TSP20-OT as shown in Figure 3-8. Due to the smaller size of triangular interconnections which are determined by the unit cell parameter a, b and H, the bending of the sidewalls towards centre for TSP20-CT is more severe than TSP10-CT at the strain of

0.2. Similarly, more bending deformation at the top edge of the sidewall for TSP20-OT can be observed than TSP10-OT at the same strain. It is because TSP20-OT has a smaller interconnection at each corner of the cell. Another reason is that TSP20-OT has a more inclined sidewall toward centre of each unit cell than TSP10-OT, thus making the sidewalls of TSP20-OT easier to bend and roll inward.

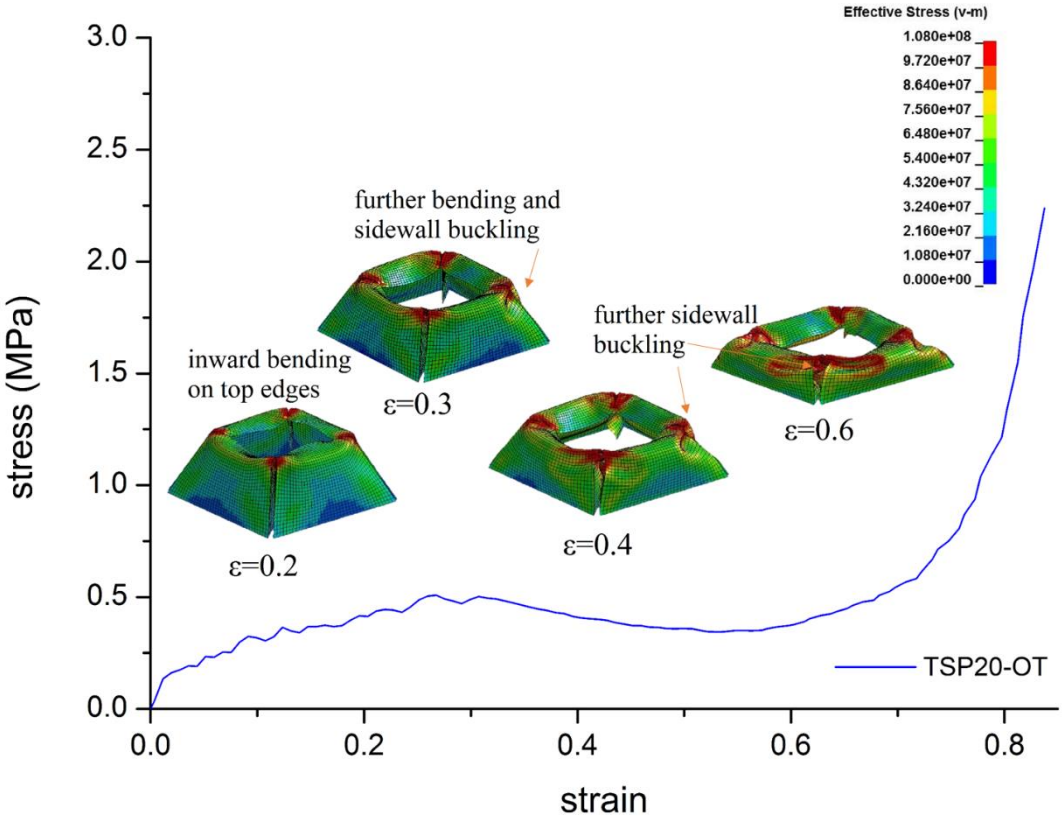

Figure 3-9. Stress-strain curve and damage mode of foldcore TSP20-OT at the strain of 0.2, 0.3, 0.4 and 0.6

The damage of the foldcore can be reflected from the stress-strain curves. The peak stress of the plateau regime represents the end of the top edge sidewall bending deformation towards the centre. As shown in Figure 3-7, peak stress occurs before or around the strain of 0.2 for TSP10-CT, TSP10-OT, TSP20-CT foldcores and TSP20-OT foldcore has peak stress around the strain of 0.3. In Figure 3-8 (b-d), there are no further bending of sidewalls at top edges from the strain of 0.2 to 0.4 for TSP10-CT, TSP10-OT and TSP20-CT. In Figure 3-8 (e), further bending deformation of TSP20-OT can be found when comparing the deformation at the strain of 0.2 and 0.4. As observed in Figure 3-9, crushing stress of TSP20-OT increases from the strain of 0.2 to 0.3 and reaches the peak value at the strain around 0.3, where bending deformation

stops and sidewall buckling initiates. After the strain of 0.3, the damage of foldcore is dominated by the buckling of the sidewall only without any further bending of the top edges.

This correlation between peak stress and buckling initiation indicates the occurrence of peak stress is associated with the bending deformation on sidewall top edges and the resistance of the interconnections. Smaller size of the triangular interconnections leads to lower resistance against bending of top edge of sidewalls and a delayed occurrence of peak stress. Once the bending deformation on top edges of sidewalls stops, typical buckling deformation of the cell walls is then followed along with multi-folding of the interconnections. Buckling of the interconnections are circled and enlarged in Figure 3-8.

3.5 Dynamic flatwise crushing

3.5.1 Stress-strain curves under various crushing velocities

In this section, the foldcores are studied under different constant loading rates of crushing i.e. 0.05 m/s, 0.25 m/s, 0.5 m/s, 2.5m/s, 12.5 m/s and 25 m/s. The quasi-static crushing speed of 0.05 m/s is used as a baseline to evaluate the performance. The same parameters as quasi-static crushing are used in the dynamic crushing scenario analyses. Stress-strain curves of foldcores under various loading rates are shown in Figure 3-10. Average stress, peak stress, densification strain and uniformity ratio are given in Table 3-4.

It is found that loading rate has only slight effect on the densification strain of cube strip foldcore. However, the initial peak stress is greatly affected by the increase of loading rate for cube strip foldcore. The initial peak stress increases by 362% from 0.469 MPa to 2.165 MPa with the loading rate increasing from 0.05 m/s to 25 m/s as shown in Table 3-4 and Figure 3-10 (a), indicating great loading rate sensitivity of the structure. Due to less evident strain rate effect of aluminium material (70, 122), strain rate effect on aluminium material properties are not considered in the present numerical study. Therefore, the observed increase in the initial peak stress is a loading rate effect on the structure, which as shown in Figure 3-10 is structural form dependent. The peak stress of the TSP foldcores is less influenced by the increasing in crushing speed, especially for the foldcores with open top. For the two foldcores with closed

top, i.e. TSP10-CT and TSP20-CT, a significant increase in the initial peak stress due to the top face is also observed. However, the crushing resistance in plateau regime is less affected comparing with cube strip foldcore. For the two TSP foldcores with open top, i.e. TSP10-OT and TSP20-OT, their initial peak stress are barely affected at low crushing speed below 2.5 m/s as shown in Figure 3-10(c), (e). When the crushing velocity is 12.5m/s and 25.0m/s, the initial peak stress of the two TSP foldcores with open top also increases at a smaller rate as compared to the other three foldcores considered in the chapter. The increase of the initial peak stress of the TSP20-OT is insignificant with the crushing velocity, indicating it is insensitive to the loading rate. These observations demonstrate that TSP foldcores with open top outperform the cube strip foldcore and the TSP foldcores with closed top, and due to the less sidewall constraints, smaller inclining angle of sidewalls and smaller interconnections, TSP20-OT has a better performance under dynamic loading conditions than TSP10-OT. Dynamic effects on this proposed structure are discussed in the following section.

Table 3-4. Average stress, peak stress, densification strain ε_D and uniformity ratio U of foldcores under various loading rates.

Type	Crushing speed	σ_{peak} (MPa)	σ_{ave} (MPa)	ε_D	U= σ_{peak} /σ_{ave}
Cube strip	**0.05 m/s**	0.469	0.286	0.72	1.64
	0.25 m/s	0.460	0.326	0.71	1.41
	0.5 m/s	0.690	0.339	0.71	2.04
	2.5 m/s	1.195	0.426	0.69	2.81
	12.5 m/s	1.940	0.627	0.69	3.09
	25 m/s	2.165	0.939	0.62	2.31
TSP10-CT	**0.05 m/s**	0.325	0.250	0.65	1.30
	0.25 m/s	0.338	0.247	0.65	1.37
	0.5 m/s	0.355	0.246	0.66	1.44
	2.5 m/s	0.408	0.273	0.67	1.50
	12.5 m/s	0.666	0.382	0.70	1.74
	25 m/s	1.180	0.485	0.72	2.43
TSP10-OT	**0.05 m/s**	0.375	0.275	0.69	1.36
	0.25 m/s	0.398	0.295	0.68	1.35
	0.5 m/s	0.373	0.276	0.69	1.35
	2.5 m/s	0.493	0.280	0.69	1.76
	12.5 m/s	0.610	0.369	0.69	1.65
	25 m/s	0.730	0.442	0.66	1.65
TSP20-CT	**0.05 m/s**	0.384	0.263	0.71	1.46
	0.25 m/s	0.359	0.256	0.71	1.40
	0.5 m/s	0.346	0.247	0.70	1.40
	2.5 m/s	0.494	0.228	0.69	2.16
	12.5 m/s	0.644	0.293	0.69	2.20
	25 m/s	1.494	0.355	0.71	4.20
	0.05 m/s	0.508	0.389	0.72	1.31

TSP20-OT	**0.25 m/s**	0.504	0.381	0.72	1.32
	0.5 m/s	0.519	0.377	0.72	1.38
	2.5 m/s	0.529	0.381	0.73	1.39
	12.5 m/s	0.559	0.393	0.69	1.40
	25 m/s	0.694	0.413	0.67	1.68

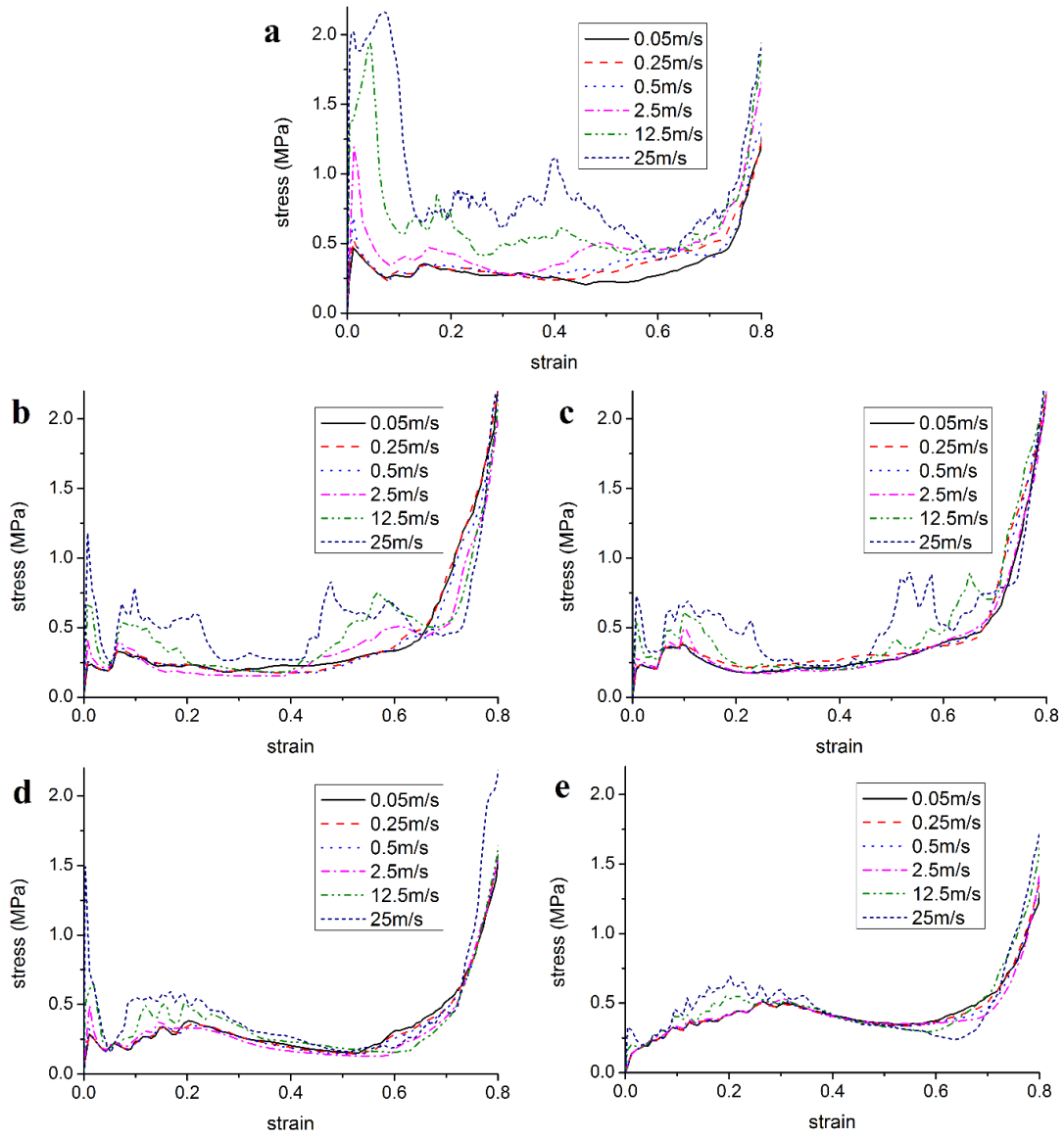

Figure 3-10. Stress-strain curves of five foldcores under different loading rates, a) cube strip; b) TSP10-CT; c) TSP10-OT; d) TSP20-CT; e) TSP20-OT

Although a sharp rise of initial peak stress can be observed for closed top TSP foldcore at high crushing rate, the average plateau stress of both closed and open top TSP foldcores demonstrate superior insensitivity than cube strip foldcore. Insensitivity of uniformity ratio to loading rate is observed for the open-top TSP foldcores. In a previous study (28), it was reported that the plateau stress of aluminium foam was

dependent on the relative density of the core by a power law and it was not sensitive to strain rate under low or medium loading rate. This strain rate insensitivity of plateau stress of TSP foldcore is similar to that of aluminium foam. Therefore, the TSP foldcore can be a potential replacement of aluminium foam core. In addition, foldcore can be cheaper, easier to manufacture and customized to fit different purposes.

3.5.2 Dynamic effects of the foldcores

Three dynamic effects: i.e. inertial resistance, inertial stabilization of cell walls against buckling and material strain-rate dependence were identified by Xue and Hutchinson in their study of square honeycomb sandwich cores (17). As aluminium material shows less strain rate effect (122), the strain rate effect of material is not considered in the numerical material model. The dynamic effects on cube strip and TSP foldcores are only determined by structural forms rather than material itself. As cube strip foldcore has the similar geometry as square honeycomb, except that each row of unit cells is separated along vertical edges. Therefore, beside the inertial resistance of the sidewalls, the perpendicular cell walls delay the onset of wall buckling and maintain the strength of the core under dynamic loading due to the inertial stabilization of the sidewalls, which is similar to dynamic effect of square honeycomb structures. Hence, great rise of reaction force is expected for cube strip foldcore at initial stage with the increase of crushing loading rate, as shown in Figure 3-10 (a). Similar stress-strain response can be found in dynamic response of square honeycomb structure (17).

For the TSP foldcores, the deformation mode is different. At the early stage of the crushing, the vertical wall experiences no buckling and the top edges of sidewalls undergo bending deformation followed by the buckling deformation of the sidewall. For TSP foldcores with closed top, the square top face can act similarly as cell wall of honeycomb structure, to resist the bending deformation of top edges on sidewalls and stabilizing the adjacent sidewalls during dynamic loading. Secondly, as the flat top face is parallel to the crushing plate, impact time is extremely short and inertial resistance increase dramatically with loading rate. Consequently, the closed top foldcores, i.e. TSP10-CT, TSP20-CT are more sensitive to loading rate in terms of initial peak than the open-top TSP foldcores, i.e. TSP10-OT, TSP20-OT. Moreover, as shown in Figure 3-10 after the initial contact between top face and the crushing

plate, the crushing resistance of closed top TSP foldcores are less influenced by the loading rate as compared to the cube strip foldcore.

The inclining angle of sidewalls, size of the unit cell and triangular interconnections affect the crushing resistance of the structure under dynamic loading. With a higher inclining angle, the sidewalls of TSP10-OT are more vertical and it has a higher initial peak stress than the less inclined TSP20-OT especially under high loading rate. Similar results were obtained by comparing honeycomb structure with perfectly vertical cell walls and pre-bend cell walls (17). The initial peak of the foldcore is also related with the aspect ratio of the unit cell which is defined as the height over the size of the cell. Under the same height, smaller cell size leads to a higher constrain factor, therefore, a higher initial peak stress (16). In other word, foldcore with smaller unit cell has more sidewall constraints per unit area, which leads to a stronger stabilization effect under high loading rate. However, under the same relative density, cell thickness is depended on the size of the unit cell as well. Increase in size of unit cell reduces the constraints per unit area but increases the thickness of the cell and may lead to an overall increase in initial peak stress. The larger size of vertical triangular interconnections also increases the initial crushing resistance under high loading rate. To conclude, due to the larger size of the interconnections, TSP10-OT with smaller cell size and higher inclining angle of sidewalls is more sensitive to the loading rate than TSP20-OT, as shown in Figure 3-10 (c) (e).

3.5.3 Energy absorption under dynamic loading

Specific Energy absorptions before densification of five foldcores are shown in Figure 3-11. Energy absorption (*E*) is calculated based on unit mass. Specific Energy absorption (*SEA*) is obtained by using the energy absorbed before densification of one unit cell dividing the mass of each unit cell, expressed with the following equations (94).

$$E = \int_0^{\delta_D} P(\delta)\, d\delta = A_{base} \cdot H\varepsilon_D \cdot \int_0^{\varepsilon_D} \sigma(\varepsilon)\, d\varepsilon = A_{base} H \cdot \sigma_{ave} \cdot \varepsilon_D ;$$

$$SEA = \frac{E}{m} = \frac{E}{\rho \cdot V} = \frac{A_{base} H \cdot \varepsilon_D \cdot \sigma_{ave}}{\rho \cdot \rho_v \cdot A_{base} H} = \frac{\varepsilon_D \cdot \sigma_{ave}}{\rho \cdot \rho_v} ;$$

where P is the crushing force, A_{base} is the base area for each unit cell, H is the height of foldcore, δ is the crushing distance, δ_D is the crushing distance at densification, σ_{ave} is the average stress before densification, $\varepsilon_{D,}$ is the densification strain, V is the volume of the material in the foldcore, ρ is the material density, ρ_v is the volumetric density of the foldcore, m is the mass of each unit cell.

As observed in Figure 3-11, energy absorption of cube strip is the mostly affected foldcore by crushing speed among these five structures. The energy absorption of cube strip increases by 184% from 2.51 to 7.13 J/g with the loading rate rising from 0.05 m/s to 25 m/s. TSP20-OT has the highest energy absorption capacity per unit mass under low speed crushing, around 3.46 J/g comparing with 2.51 J/g of cube strip foldcore. It also demonstrates an insensitive characteristic of energy absorption against different crushing velocities. Similar insensitivity can be found in another foldcore with open top, TSP10-OT. The closed top foldcores, TSP10-CT and TSP20-CT show a good performance under low crushing speed, the increase of crushing resistance under high loading rate leads to large increase in energy absorption.

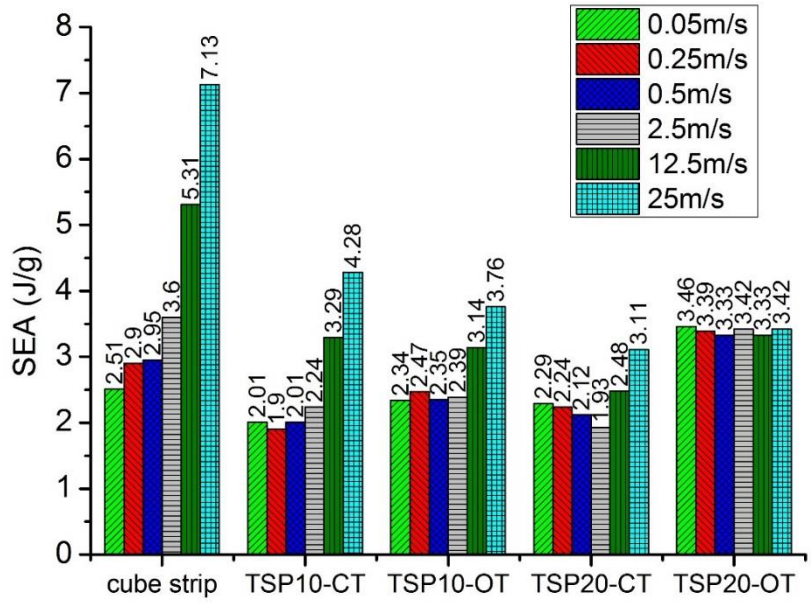

Figure 3-11. Specific energy absorption (SEA) before densification of five foldcores under various crushing speeds.

Increase in energy absorption of cube strip foldcore can be caused by the inertial effect of the structure and inertial stabilization of cell wall against buckling. Both initial peak stress and sequential folding stress rise with increasing in crushing velocity as shown in Figure 3-10 (a). For the TSP foldcores with closed top, i.e. TSP10-CT and TSP20-

CT, their energy absorption capacities are more consistent with varying loading rate comparing with cube strip foldcore, although they are affected greatly only at high crushing speed. Extra constraints are added to the sidewalls for closed top foldcores because of the top face. The top face provides crushing resistance and stabilises the sidewalls under dynamic loading, which explains the sharp increase of initial peak stress. Under high loading rate, the buckling location of the sidewalls is shifted upwards, as shown in Figure 3-12. With the sidewall buckling location closer to the top face where extra inertia and stabilization effect provided by top face, the foldcore becomes stiffer to deform. As mentioned previously, inertial effects increase significantly at high loading rate. Therefore, the closed top TSP foldcore TSP10-CT, TSP20-CT have a relatively consistent energy absorption capacity at low crushing speed, but a significant increase at high crushing speed.

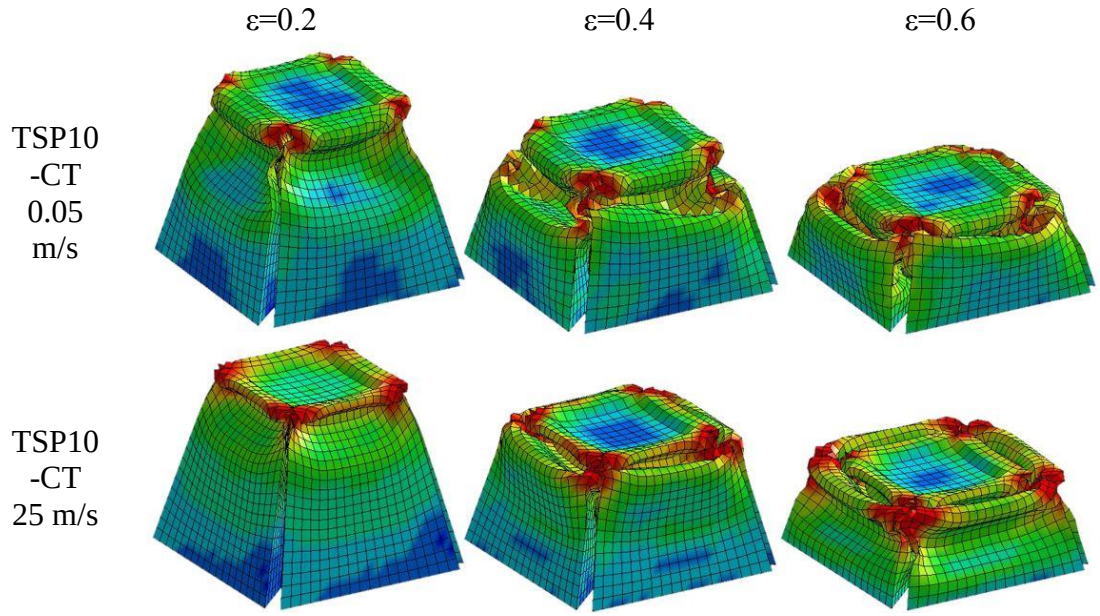

Figure 3-12. Damage modes of TSP10-CT at the strain of 0.2, 0.4 and 0.6 under the loading rates of 0.05 m/s and 25 m/s (Effective stress contour plot)

As for the TSP foldcores with open top, the stabilization effect of top square face no longer exists in dynamic crushing which leads to a more consistent energy absorption behaviour regardless of the loading rate. As explained previously, the top face provides resistance to the bending action of sidewalls at the top edges and it stabilizes sidewalls of unit cell under a higher crushing speed. TSP20-OT with a larger unit cell size and smaller interconnections than TSP10-OT, shows a more consistent energy absorption capacity with varying loading rates. Without the top face and less vertical resistance from interconnections, the damage mode of TSP20-OT at the early stage is

not much affected by the increasing crushing rate from 0.05 m/s to 25 m/s, as shown in Figure 3-13. The damage modes of the foldcore at the strain of 0.2 show little change under different loading rates. The initiating location of buckling moves from corners to the centre of the sidewalls as shown in Figure 3-13 at the strain of 0.4 and 0.6 when the loading rate changes from 0.05 m/s to 25 m/s. The bending on top edge and overall buckling of sidewall, however, shows little difference between the two loading rates. Therefore, the reaction force remains similar in value, and there is little influence in energy absorption capacity for open-top TSP foldcore TSP20-OT under different loading rates.

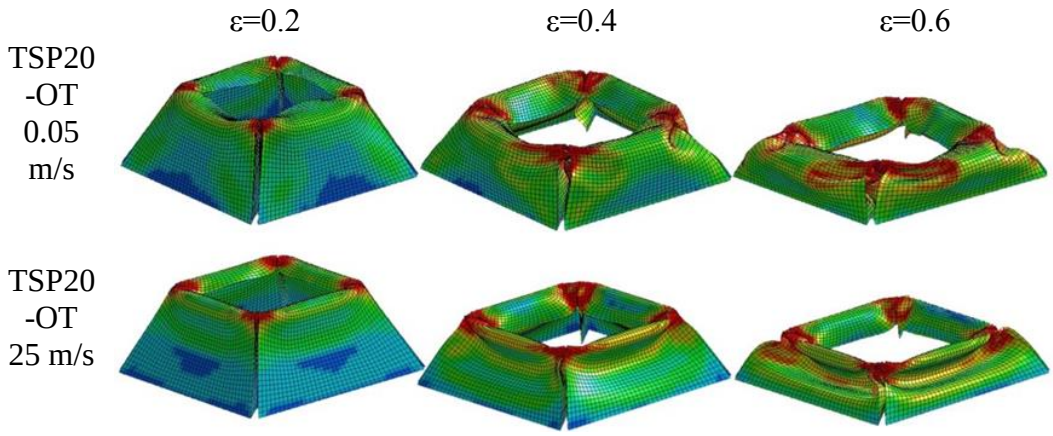

Figure 3-13. Damage modes of TSP20-OT at the strain of 0.2, 0.4 and 0.6 under the loading rates of 0.05 m/s and 25 m/s (Effective stress contour plot)

3.6 Summary

A new form of kirigami foldcore with TSP is proposed in this chapter. Unlike the existing top-performing kirigami foldcores, the proposed foldcore can be manufactured by using one whole patterned sheet instead of strips. Energy absorption capability is examined under both quasi-static and dynamic flatwise crushing. Good uniformity of collapsing of cell wall is demonstrated with low ratio of peak and average stress. The foldcore TSP20-OT outperforms the other three configurations of TSP foldcores and cube strip core by providing lower initial peak stress, higher plateau stress and energy absorption capability. Different crushing speeds are also applied onto these foldcores, and all the proposed TSP foldcores show less sensitivity of strain rate than cube strip core due to their unique geometries. The TSP foldcores experience different damage modes because of the top face, the inclining sidewalls and the triangular interconnections. The TSP foldcore with open top outperforms the closed-

top ones with the initial peak stress and energy absorption capacity less sensitive to strain rate. As the structure is proposed to be folded using one pre-cut sheet, the dimensions of the truncated pyramid are restrained. Given a set of base length and height, the inclining angle and interconnections geometries are restrained in a set of value, unlike the cube strip kirigami foldcore where the height, width, length of unit cell can be any arbitrary number. The geometries such as inclining angle, core height and interconnection dimension can potentially affect the damage modes and energy absorption capacity, especially under dynamic loading conditions.

Chapter 4. Open-top truncated pyramid structures with different base shapes

The related work in this chapter has been published in Thin-Walled Structures.

Li Z, Chen W, Hao H. Numerical study of open-top truncated pyramid folded structures with interconnected side walls against flatwise crushing. Thin-Walled Structures. 2018;132:537-48. DOI: doi.org/10.1016/j.tws.2018.08.023

4.1 Introduction

Given the demonstrated performance of the newly proposed truncated pyramid kirigami (TSP) structures with square base in Chapter 3, open-top TSP foldcores with different base shapes including triangle, square and pentagon are experimentally and numerically studied in this chapter. Three types of samples are named as truncated triangular pyramid (TTP), truncated square pyramid (TSP) and truncated pentagonal pyramid (TPP). Samples of these foldcores are folded by hand and crushed under quasi-static loading condition. The crushing test data is used for the calibration of the numerical model. Dynamic out-of-plane crushing studies are then carried out numerically for these foldcores and compared with standard Miura-type foldcore of the same density and similar dimensions. The effects of TSP geometric parameters such as base shape and interconnection size are investigated and discussed.

4.2 Geometric parameters

Table 4-1. Geometric parameters of three folded structures with base shapes of triangle, square and pentagon

	Truncated triangular pyramid (TTP)	**Truncated square pyramid (TSP)**	**Truncated pentagonal pyramid (TPP)**
c	$\sqrt{\left[\left(\frac{a-b}{2}\right)tan\frac{\pi}{6}\right]^2+H^2}$	$\sqrt{(\frac{a-b}{2})^2+H^2}$	$\sqrt{\left[\left(\frac{a-b}{2}\right)tan\frac{3\pi}{10}\right]^2+H^2}$
l	$\sqrt{\left(\frac{a-b}{2sin\pi/3}\right)^2+H^2}$	$\sqrt{(\frac{a-b}{2})^2+c^2}$	$\sqrt{\left(\frac{a-b}{2sin\pi/5}\right)^2+H^2}$
γ	$\arcsin\left(\frac{c}{l}\right)$	$\arctan\left(\frac{2c}{a-b}\right)$	$\arcsin\left(\frac{c}{l}\right)$

β	$\arcsin\left(\frac{H}{l}\right)$	$arcos\left(\frac{\sqrt{2}a-\sqrt{2}b}{2l}\right)$	$\arcsin\left(\frac{H}{l}\right)$
α	$\gamma-\frac{\pi}{6}$	$\gamma-\frac{\pi}{4}$	$\gamma-\frac{3\pi}{10}$
x	$\frac{sin\beta\cdot l}{sin(\pi-\alpha-\beta)}$	$\frac{sin\beta\cdot l}{sin(\pi-\alpha-\beta)}$	$\frac{sin\beta\cdot l}{sin(\pi-\alpha-\beta)}$
A_{surf}	$3\times\frac{1}{2}c(a+b)+6\times\frac{1}{2}sin\alpha\cdot xl$	$4\times\frac{1}{2}c(a+b)+8\times\frac{1}{2}sin\alpha\cdot xl$	$5\times\frac{1}{2}c(a+b)+10\times\frac{1}{2}sin\alpha\cdot xl$
ρ_v	$\frac{4A_{surf}\cdot t}{a^2 tan\frac{\pi}{3}H}$	$\frac{A_{surf}t}{a^2H}$	$\frac{4A_{surf}\cdot t}{a^2\cdot\tan\frac{2\pi}{5}\cdot(2\cos\frac{2\pi}{5}+1)^2\cdot H}$

Figure 4-1. Sample of a single unit of truncated square pyramid folded from aluminium sheet （hand folded）

As can be observed in Figure 4-1, small folding gaps near the corners of the unit cell may exist, which are considered in the numerical models. Folding configurations of three truncated pyramid kirigami structure are shown in Figure 4-2. Triangular interconnections are placed to connect all adjacent inclined sidewalls along the vertical folding creases for each unit cell. Therefore, the geometry of the folded structure is governed by three parameters only, the length of bottom and top edges, *a*, *b* and the foldcore height *H*. Other geometric parameters (*c, l, α, β, γ, x*) marked out in Figure 4-2 can be expressed by three governing parameters a, b and H as shown in Table 4-1. Note that A_{surf} is the surface area of a single unit cell of the foldcore, ρ_v is the volumetric density of the foldcore, and *T* is the thickness of the cell walls of foldcore. ρ_v is calculated using the volume of sheet material in one unit cell divided by the overall volume.

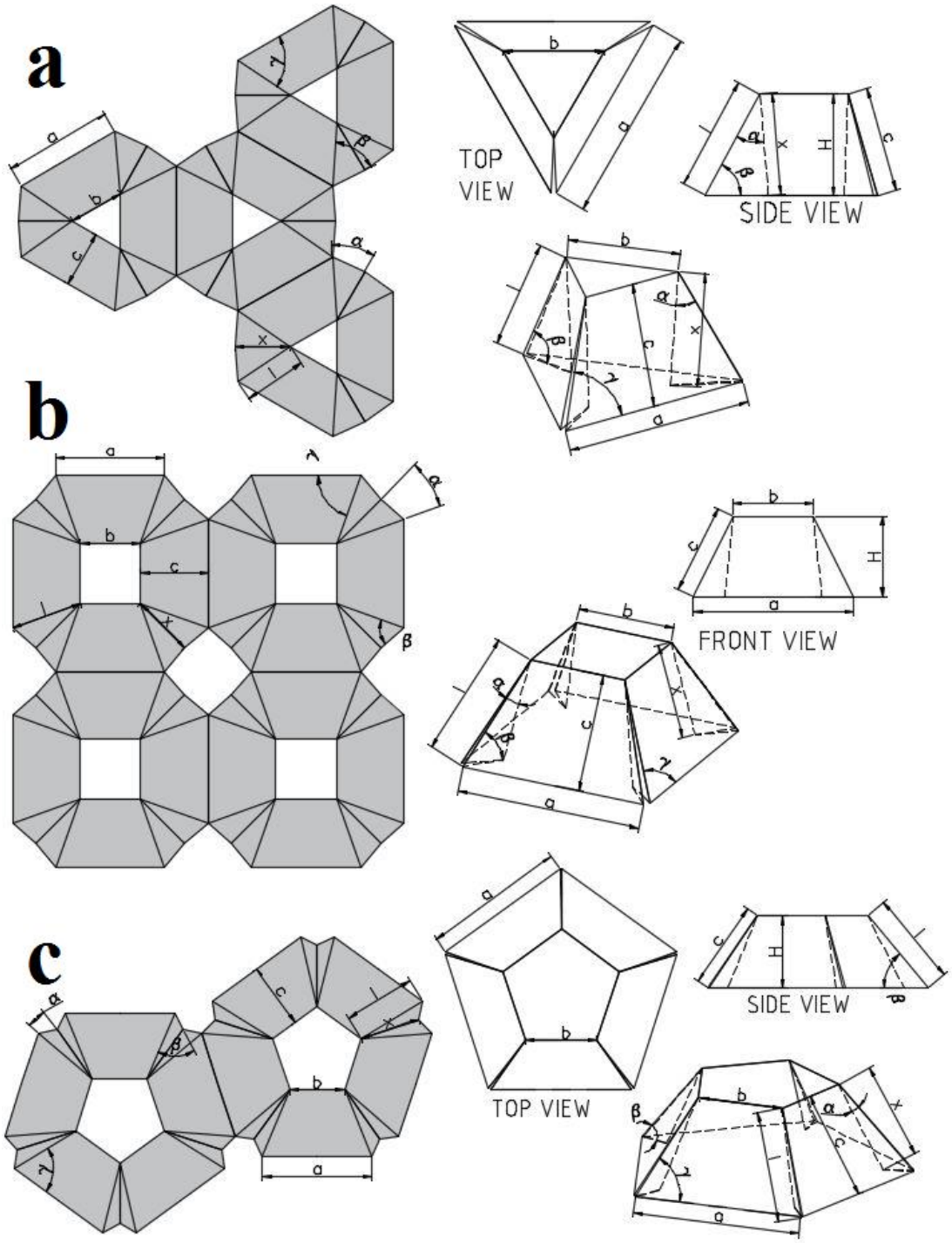

Figure 4-2. Folding creases and folding configurations with geometric parameters marked out for (a) truncated triangle; (b) square and (c) pentagon pyramid folded structures

In order to form a tessellated pattern using these structures, polygons on both top and bottom planes are set to be regular polygons in this chapter. In other words, sides of polygons are in equal length for individual unit cell of triangle, square and pentagon truncated pyramid structures. Tessellated pattern can be easily formed without any gap

for triangle and square truncated pyramid kirigami structures. As for pentagon, there is no possible way to arrange them in a plane in order to form edge-to-edge contact with all adjacent ones. Different arrangements are studied where various patterns are formed with slight gaps between adjacent regular pentagons (132). One of the simplest tessellated pattern for pentagon is used for this chapter as shown in Figure 4-3, where a single unit cell is marked out in dash lines including the pentagon and small gaps on both sides. Note that the base area used in calculation is the unit cell base area including the pentagon and the small gap marked out. This unit cell area selection is important for crushing behaviour of pentagonal truncated pyramid as sidewalls from adjacent units may slide towards and interact with each other. Boundary conditions for quasi-static test and numerical simulation are set accordingly.

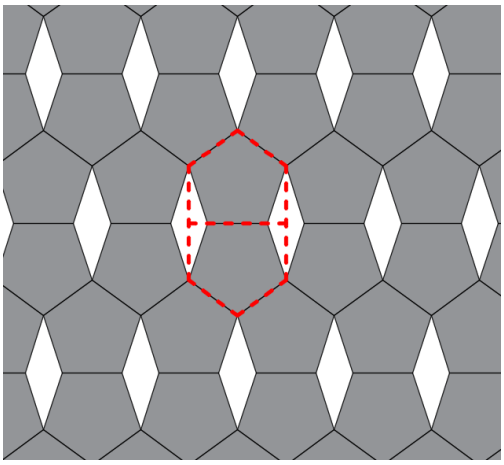

Figure 4-3, Simple tessellated pattern for regular pentagons where single unit cell area is marked out in dash lines

4.3 Numerical model validation

4.3.1 Quasi-static compression test

Hand-fold samples of three structures are crushed under quasi-static compression test with a constant rate of 1 mm/min, as shown in Figure 4-4. The three key governing parameters, bottom and top edge length, *a*, *b* and height *H* are kept same for all the three structures, where *a*=40 mm, *b*=20 mm, *H*=20 mm. Other parameters are shown in Table 4-2.Three samples have the same top and bottom edge length and height. The samples are folded from Aluminium sheet with thickness of 0.15 mm and 0.26 mm, where the volumetric density of the core is calculated accordingly. In later sections,

the thickness of these structure is modified to achieve the same relative density of the foldcore in the validated numerical model.

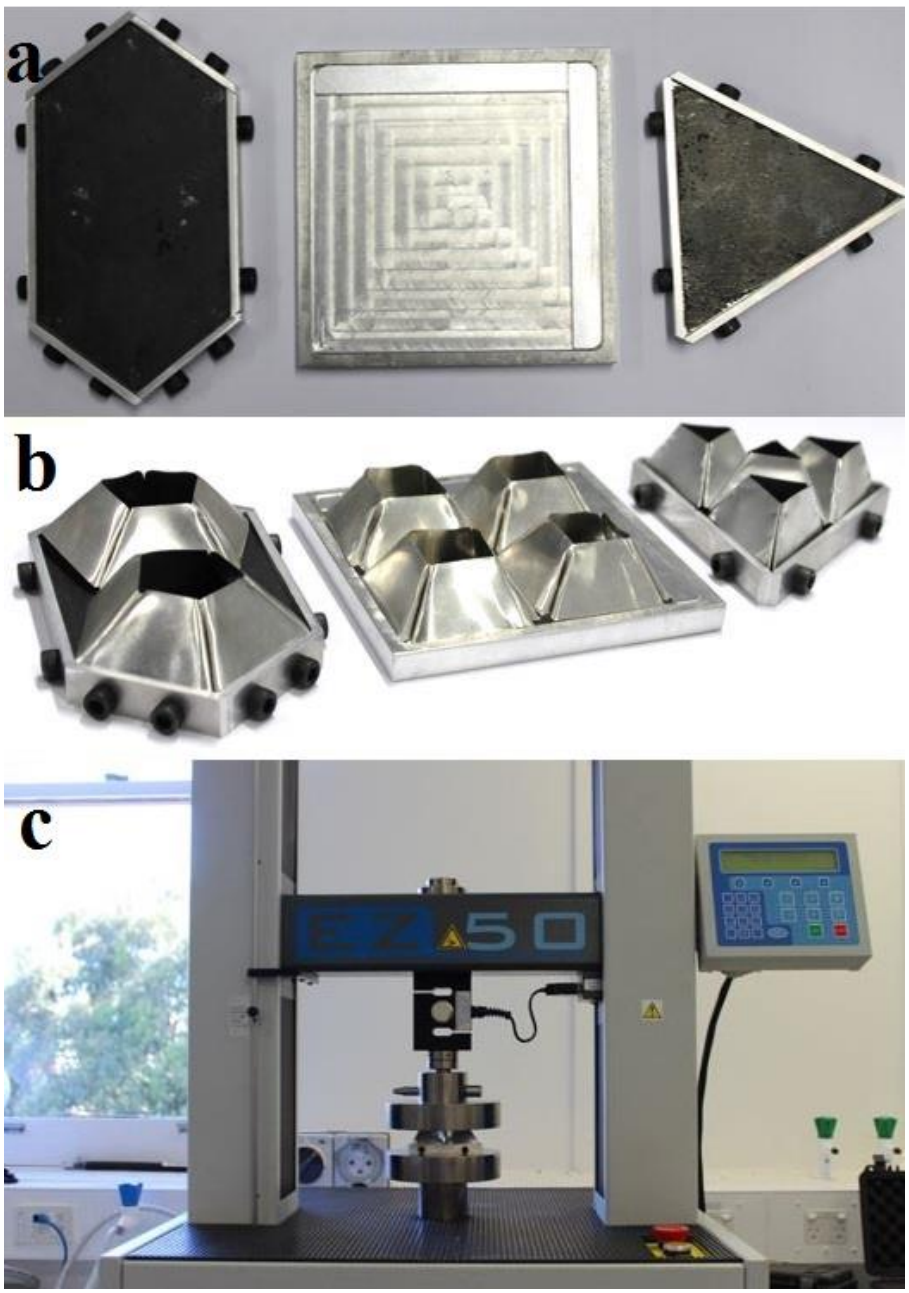

Figure 4-4. (a) Base plates of the foldcores with 2 mm high outer boundary; (b) foldcores set-up with base plates; (c) quasi-static crushing test set-up

Table 4-2. Geometric parameters of hand folded samples

Fold core	a mm	b mm	H mm	c mm	l mm	γ degree	β degree	α degree	x mm	t mm	ρ_v %
TTP	40	20	20	21	23	64	60	34	20	0.15	2.7
TSP	40	20	20	22	24	67	55	22	21	0.26	2.7

TPP	40	20	20	24	26	68	50	14	22	0.26	1.7

As shown in Figure 4-4 (b), some slightly bent sidewalls and minor gaps can be observed near the bottom edges, caused by hand folding process. These hand folding induced imperfections are unlikely to be avoided. Advanced machining such as stamping can be developed in future to reduce the imperfections and enhance folding speed. Samples are simply supported by a steel plate with the boundary of 2 mm high to constrain the sidewall movements along the bottom edges. This is to better investigate the behaviour of a foldcore with an array of unit cells where the interaction between adjacent sidewalls shall be considered. Glue and other types of fixing between foldcore and support plate are not used.

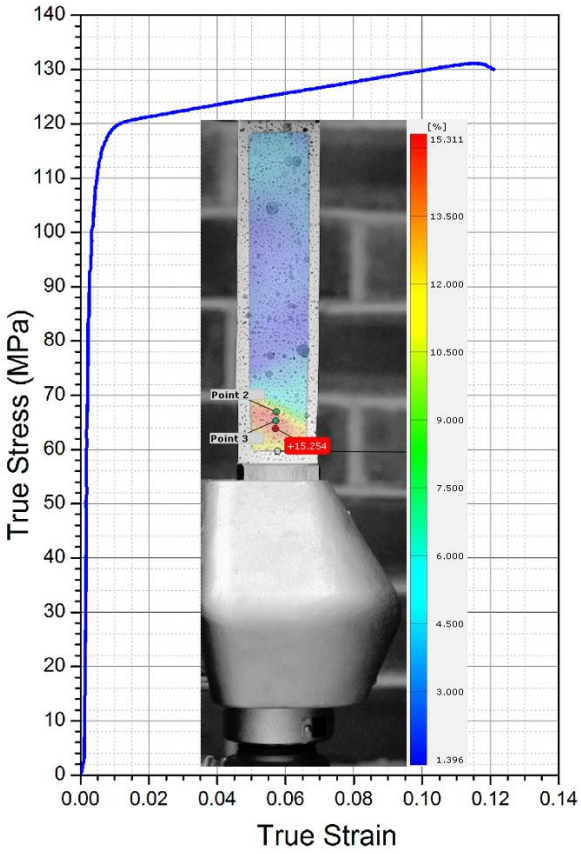

Figure 4-5. DIC image of aluminium strip specimen under direct tensile test at its maximum strain and true stress strain curve of aluminium 1060 strip tested

Tensile test of the aluminium sheet used for sample fabrication is carried out to obtain its stress strain data based on ASTM E8M-04 (133). A constant loading rate of 0.5 mm/min is applied for the aluminium strip specimen with the thickness of 0.26 mm. The full fields of displacement and strain of the specimens are measured using Digital Image Correlation (DIC-2D) techniques. The DIC image of strain field along loading

direction of aluminium strip specimen at maximum strain and the obtained true stress strain curve are shown in Figure 4-5.

4.3.2 Numerical modelling

Finite element software LS-DYNA is used for numerical simulation. The folded structures are constructed using Belytschko-Tsay type shell element and placed between two rigid solid blocks. The bottom solid block is set to be a fixed rigid block, and the top block moves at a constant speed of 0.05 m/s towards the fixed base plate till around 80% crushing strain is reached for the foldcores. The 1 mm/min quasi-static crushing speed used in test is time consuming for the numerical simulation and 0.05 m/s was found sufficient to simulate accurate quasi-static loading in the numerical simulation (87). Similar to the testing set up in Figure 4-4, simple boundary condition is applied for foldcore where the base plate has a 2mm high boundary and no glue or fixing is used in the numerical model as presented in Figure 4-6.

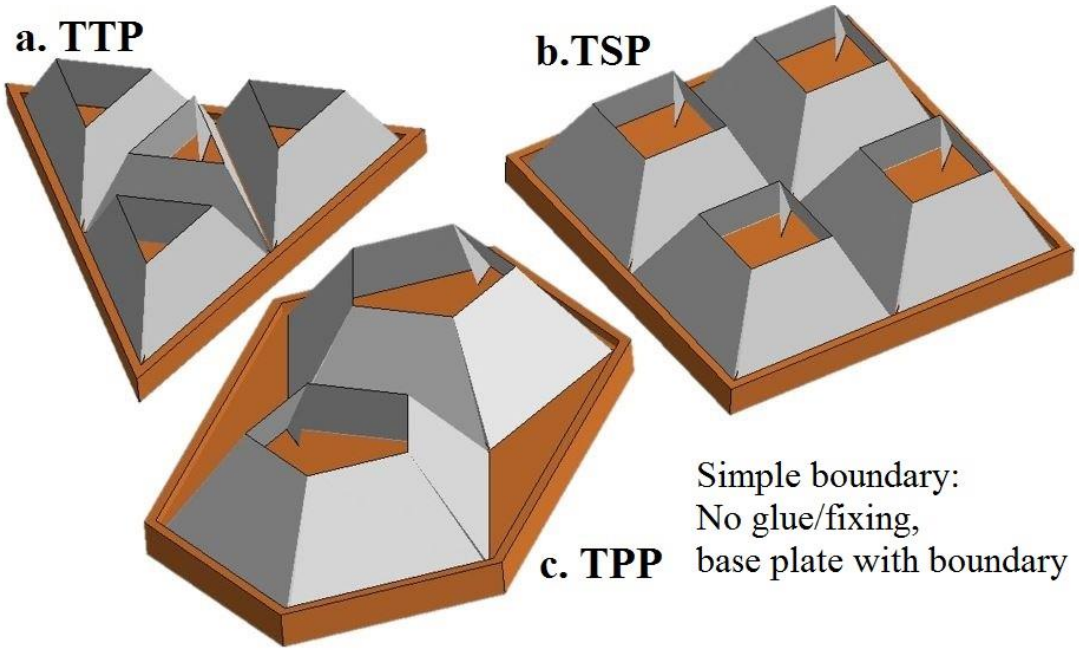

Figure 4-6. Numerical models of TTP, TSP and TPP folded structures with simple boundary

Material model *MAT024 PIECEWISE LINEAR PLASTICITY is used for the foldcore. Measured material properties and true plastic stress-strain data of aluminium 1060 sheet material are listed in Table 4-3 and Table 4-4. The strain rate effect of aluminium is not considered in this chapter, as it is not significant for aluminium (65). Contacts are described using keyword *CONTACT AUTOMATIC SINGLE

SURFACE and *CONTACT AUTOMATIC NODES TO SURFACE for self-contact of the cell walls during the crushing process and the contact between foldcore and the support plate/top crushing plate, respectively. Friction coefficient of 0.25 is considered for both contacts.

Table 4-3. Material properties of Aluminium 1060

Parameter	Young's modulus (GPa)	Poisson's ratio	Yield stress (MPa)	Density (kg/m^3)
Value	69	0.33	66.7	2710

Table 4-4. True plastic stress-strain data of Aluminium 1060

Strain	0	0.002	0.005	0.013	0.063	0.121
Stress (MPa)	0	66.7	112.3	120.1	125.8	130.6

4.3.3 Model validation

The stress-strain curves for the three types of truncated pyramid kirigami structures from both numerical simulation and quasi-static experiment are presented in Figure 4-7. Some discrepancies of initial peak crushing force are shown in all the three types of structures, which is caused by the imperfections of the samples induced by hand folding process. As can been observed from Figure 4-4 (b), the sidewalls are slightly bent and some gaps are shown between the foldcore and the base plate, which leads to uneven loading and easier buckling of some walls in the initial crushing stage. Similar discrepancy has been observed for other folded structures (87). Once initial deformation occurs and the loading plate is in full contact with the core structure, the FE simulation and experimental results match well. The key parameters including initial peak crushing force, P_{peak}, average crushing force, P_{ave}, uniformity ratio, U, and densification strain, ε_D, from both experiment and numerical simulation are compared and given in Table 4-5. The initial peak forces from FE results are larger than those from experiments because of the imperfection of the hand folded cores. However, other key parameters, including plateau stress and densification strain, are in good agreement for all foldcores. These two parameters determine energy absorption capability of the core (87). Therefore, the numerical models of these open-top

truncated pyramid folded structures are considered acceptable for evaluating the foldcore behaviour and energy absorption.

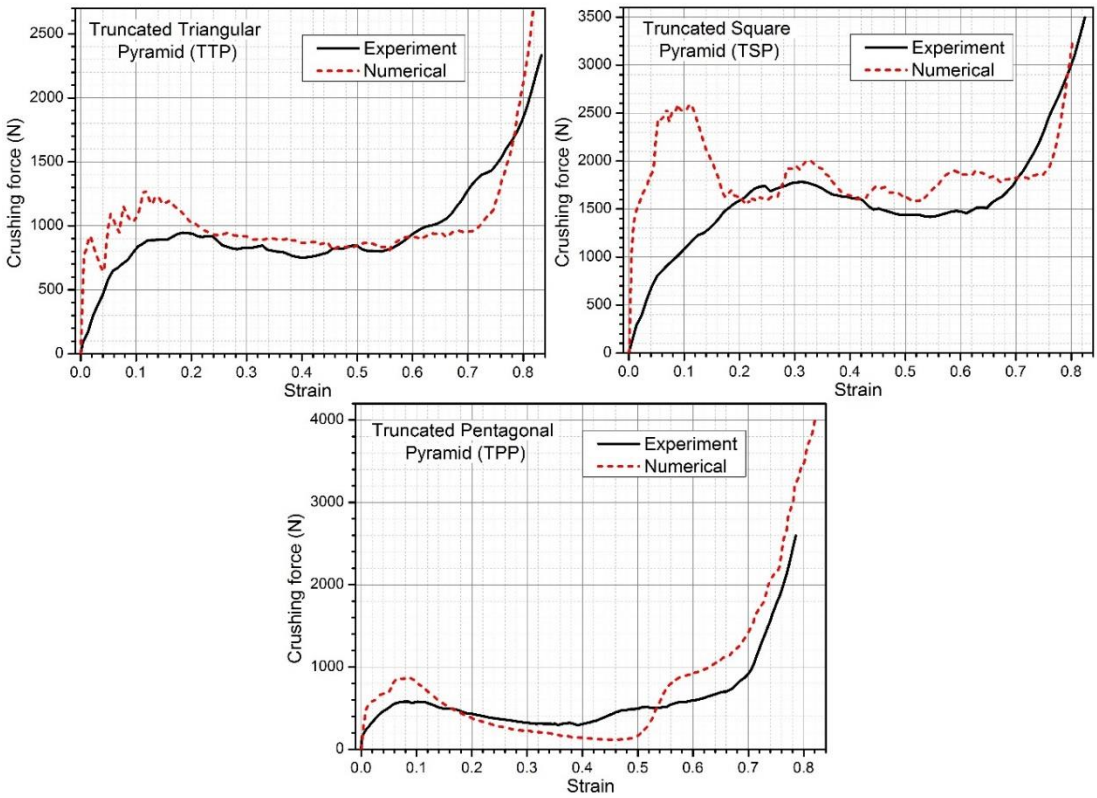

Figure 4-7. Comparison of stress-strain curves of three types of foldcores from numerical simulation and experimental tests

Table 4-5. Key parameters from experiment and numerical simulation

Foldcore		P_{peak} (kN)	P_{ave} (kN)	U= P_{peak} /P_{ave}	ε_D
TTP	Exp	0.95	0.82	1.16	0.67
	FE	1.27	0.94	1.35	0.71
	Difference	33.6%	14.6%	16.4%	6.0%
TSP	Exp	1.78	1.49	1.19	0.70
	FE	2.59	1.83	1.42	0.73
	Difference	45.5%	22.8%	19.3%	4.3%
TPP	Exp	0.58	0.46	1.26	0.68
	FE	0.86	0.46	1.86	0.65
	Difference	48.3%	0	47.6%	-4.4%

Damage modes of the three types of folded structures are shown in Figure 4-8 by comparing both results from experimental test and numerical simulation. Due to the high inclination angle of TTP and TSP, multiple buckling on sidewalls especially along the intersection lines is presented. Deformations of these two types are less symmetrical and more randomly distributed in the experiment as compared to the numerical results. TPP, however, experiences less deformation on the sidewalls and no obvious buckling along intersection lines as the folded joints remain relatively straight. The sidewalls are bent towards centre of each unit cell and the lift-up of the corners can be observed during crushing as shown in Figure 4-8 (g, h). The lift-up of corners is caused by the sliding in this simple boundary condition and the low inclination angle of TPP foldcore. The overall damage modes between experimental and numerical results are in good agreement.

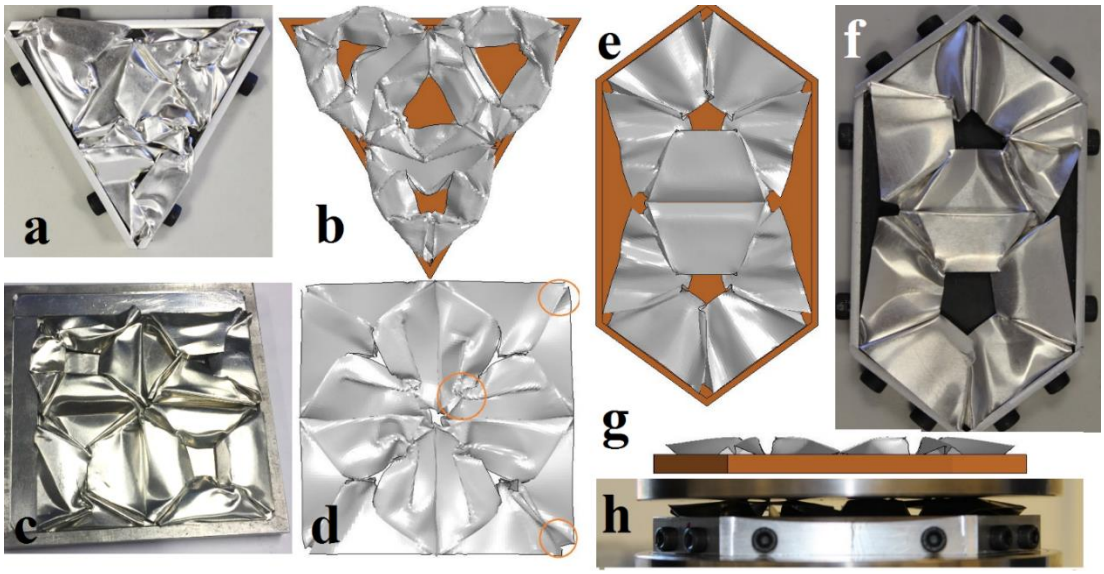

Figure 4-8. Damage modes (a) TTP experimental; (b) TTP numerical; (c) TSP experimental; (d) TSP numerical; (e) TPP numerical; (f) TPP experimental; (g) front view of TPP numerical; (h) front view of TPP experimental

4.4 Quasi-static crushing

Structural responses of three folded structures, i.e. TTP, TSP and TPP are numerically simulated and compared with one of the most common folded structure, i.e. Miura type origami (82). The Miura type foldcore sample has the same overall dimensions as the truncated square pyramid (TSP), with the dimension of 80×80×20 mm and four unit cells. Other geometric parameters are shown in Figure 4-9. Same simple boundary condition is used for the numerical simulation as well as the material and contact

settings. Because of the differences in geometries the tested samples have different relative densities. In numerical simulations, for comparison the relative density of all the considered core structures are made the same, i.e. 2.7%, which is achieved by adjusting the thickness of all foldcores including the Miura type. The corresponding parameters are listed in Table 4-6.The wall thickness is calculated as: $t = \frac{\rho_v \cdot A_{base} \cdot H}{A_{surf}}$

where t is the wall thickness, ρ_v is the volumetric relative density, A_{base} is the base area of the model, H is the height of foldcore and A_{surf} is the outer surface area of the model.

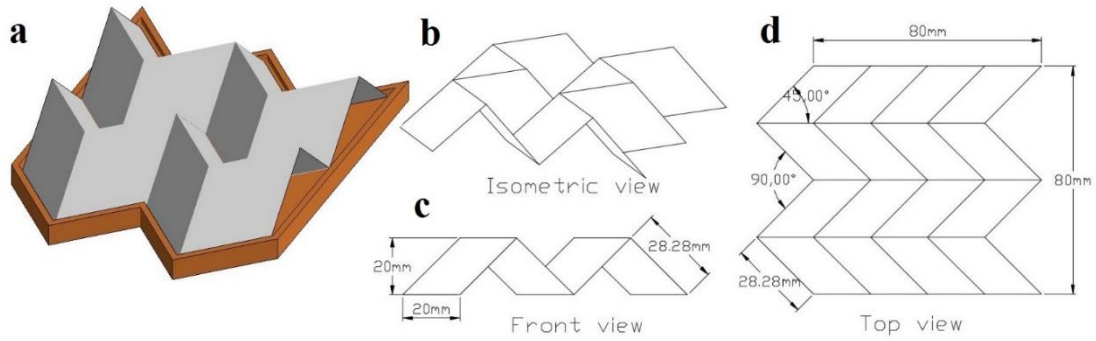

Figure 4-9. Miura-type origami foldcore with four unit cells (a) numerical model and base plate; (b) isometric view; (c) front view; (d) top view

Table 4-6. Parameters of the foldcores

Foldcore with relative density 2.7%	**Miura type foldcore**	**Truncated triangular pyramid (TTP)**	**Truncated square pyramid (TSP)**	**Truncated pentagonal pyramid (TPP)**
Wall thickness (mm)	0.31	0.15	0.26	0.43
Model base area (mm^2)	6400 (4 unit cell)	2771 (4 unit cell)	6400 (4 unit cell)	6449 (2 unit cell)
Model surface area (mm^2)	11081	10207	13337	8539

4.4.1 Stress-strain curve comparison with simple boundary

The stress strain curves of these simply supported foldcores under quasi-static loading are presented in Figure 4-10. Truncated triangular pyramid (TTP) structure demonstrates the best performance among the considered foldcores. It has a lower initial peak stress, a higher average stress and larger densification strain comparing with the other truncated pyramid structures and the Miura-type foldcore. All the three types of truncated pyramid structures have a low initial peak stress resistances of

truncated pyramid structures reach their overall peak at around 0.1 strain in indicating relatively low crushing resistance at early stage as compared to Miura-type foldcore. The crushing the plateau stage of the crushing as compared to the initial elastic stage for Miura-type which reaches its overall peak at around 0.02 strain. The average crushing stress of TTP and TSP exceed the Miura-type foldcore and possess a larger densification strain, which corresponds to a sudden increase of the stress-strain gradient at the end of the plateau stage of the deformation. As for TPP, the average crushing resistance is slightly lower than the other types and it has a similar densification strain as Miura-type, even though it has the lowest overall peak stress among these foldcores.

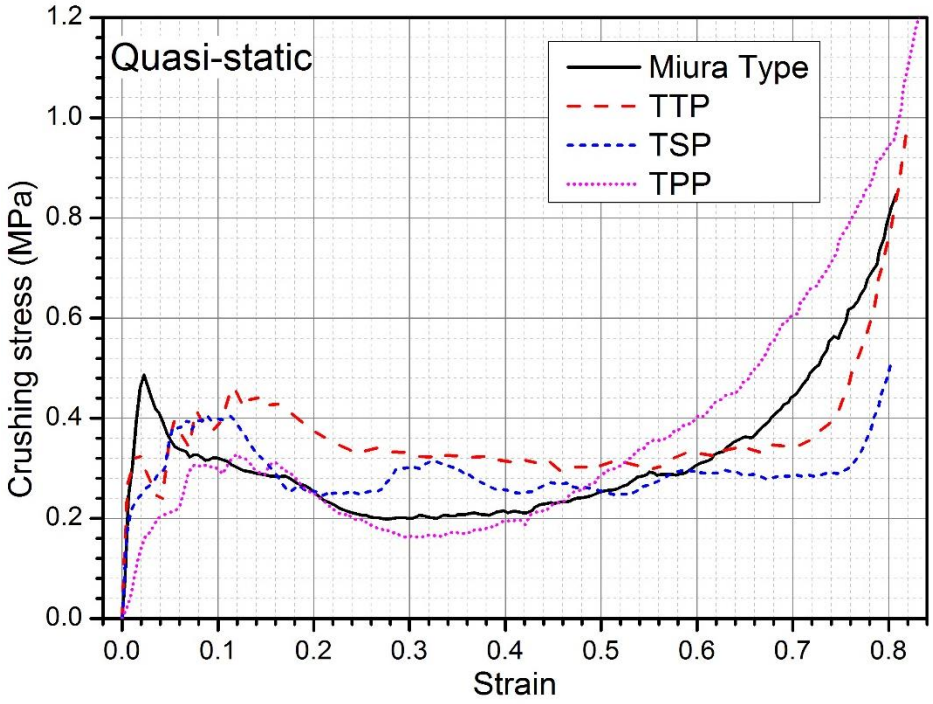

Figure 4-10. Stress strain curves of four types of foldcores under flatwise quasi-static crushing with simple boundary

Table 4-7. Peak and average stress, uniformity ratio (U) and densification strain (ε_D) of four foldcores under flatwise quasi-static crushing

Foldcore	σ_{peak} (MPa)	σ_{ave} (MPa)	U= σ_{peak} /σ_{ave}	ε_D
Miura	0.486	0.268	1.81	0.66
TTP	0.458	0.340	1.35	0.74
TSP	0.405	0.286	1.42	0.76
TPP	0.326	0.262	1.24	0.66

As listed in Table 4-7, the criteria used to evaluate crushing performance of the foldcores include peak and average stress, uniformity ratio which is the ratio between the peak and average stress, and densification strain. Both TTP and TSP have superior performance comparing to Miura-type foldcore in all four criteria, with higher average crushing resistance, lower initial peak stress, lower uniformity ratio and larger densification strain. Out of these four configurations of folded structures, TTP folded structure has the highest average crushing stress at 0.34MPa, around 27% higher than the standard Miura-type foldcore and 12% higher densification strain as well. This suggests an enhanced performance in terms of energy absorption capability. As concluded in a previous study (134), more corners could lead to higher crushing resistance and energy absorption capability. In the current study, the decreasing trend of plateau stress from TTP to TSP to TPP under this loading condition may be also attributed to the decreasing number of folds per unit area, since TTP (12 folds/2770mm^2) has more folds per unit area than TSP (16 folds/6400mm^2) and TPP (10 folds/6449mm^2).

Furthermore, all truncated pyramid folded structures have a delayed peak stress at around 0.1 strain comparing with 0.02 strain for Miura-type as shown in Figure 4-10. Delayed peak stress with lower value indicates that the deformation is more consistent and easier to initiate at early stage for the proposed foldcores, which is another advantage of energy absorber.

4.4.2 Damage mode of foldcores with simple boundary

Damage modes of the foldcores at different strains under quasi-static crushing are shown in Figure 4-11. Different damage modes can be observed for the foldcores. For the widely studied Miura-type, the faces start to buckle along horizontal directions around the middle of the foldcore faces, which is followed by the sequential folding of faces along the buckling line at middle of the faces under further crushing. As shown in Figure 4-11 (a), sequential folding of the foldcore faces along the buckling creases can be observed with the increasing strain. This initial sheet buckling failure mode leads to a sharp increase in the crushing resistance followed by the sudden drop of the resistance. This failure mode is in good agreement with the previous studies of Miura-type foldcore (82, 135).

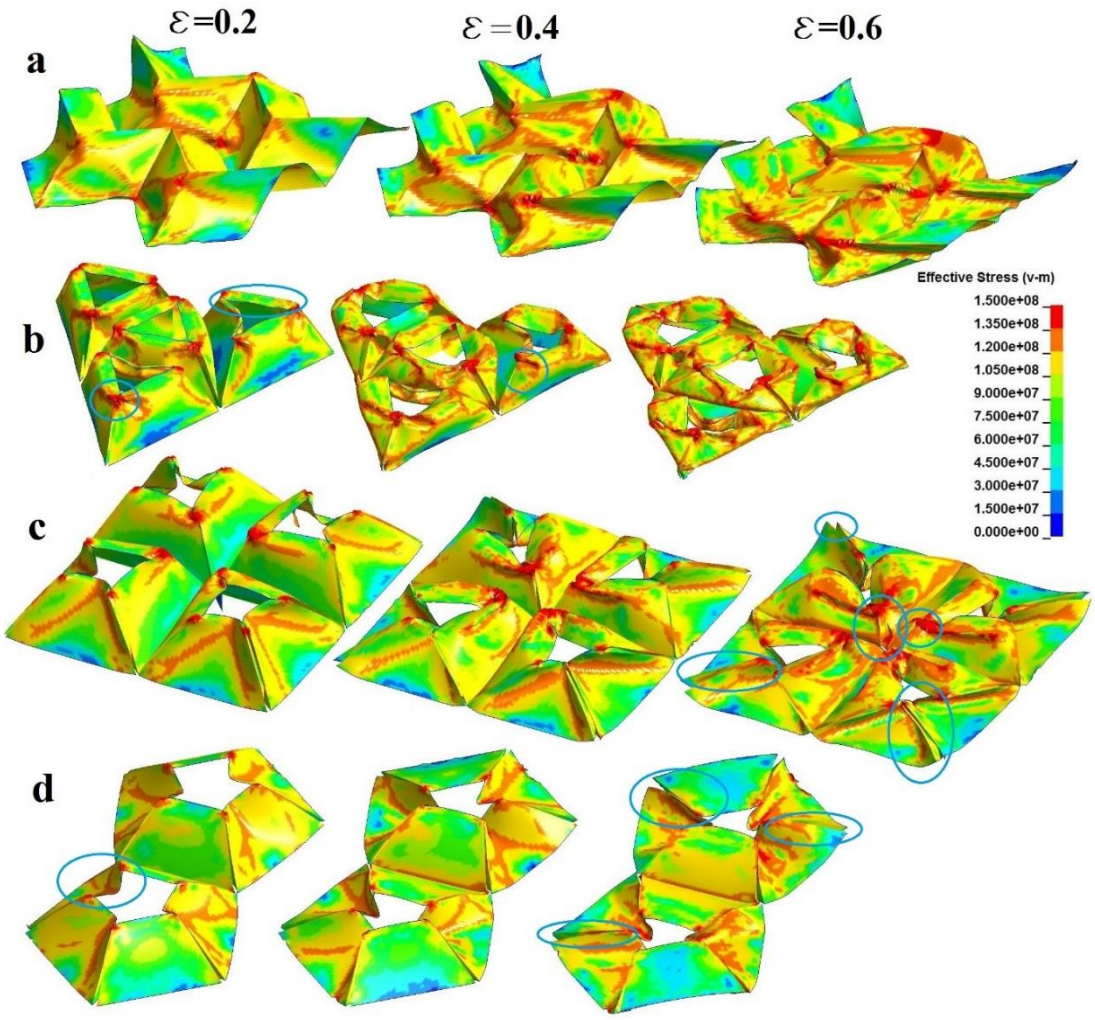

Figure 4-11. Damage modes of the foldcores with simple boundary at the strain of 0.2, 0.4 and 0.6; (a) Miura-type; (b) Truncated Triangular Pyramid; (c) Truncated Square Pyramid; (d) Truncated Pentagonal Pyramid

For the three types of truncated pyramid structures, the damage modes vary as well, because of the differences in inclination angle, the interconnection size and shape. For the TTP structure, bending of the top edges of sidewalls towards the unit cell centre can be observed at the strain of 0.2. Local buckling can be observed near the top corners at the interconnections, which is different from the Miura-type foldcore where buckling occurs horizontally at the middle of foldcore face. For the TSP foldcore, some faces have similar deformation modes as the TTP with the top edge sidewalls bending inward and occurrence of local buckling along the corners. Other faces, however, have no local buckling along the interconnections, because of the reduction in inclination angle of the sidewall compared to the TTP. As can be observed from those circled in Figure 4-11 (c), some intersection lines at corners are straight and

some are buckled at 0.6 strain. Lift-up of the outer corners can also be observed. The predicted deformation of the TSP is also symmetrical whereas in experiment is more randomly distributed. As for the TPP, no buckling along the corner of unit cell can be observed, only sidewall faces vertically bend toward centre. As shown in circles, almost all corner edges of the TPP foldcore still remain straight at the strain of 0.6.

As investigated in the previous study (136), the top edge inward bending at initial stage leads to low initial crushing resistance of the truncated square pyramid foldcore. The deformation of the sidewall buckling corresponds to the peak stress under crushing. Since the inward bending on top edges occurs prior to sidewall buckling for the proposed truncated structures, their initial peak stress are much lower than Miura foldcore. For the TPP without experiencing any sidewall buckling near the unit cell corners, the average crushing resistance is much lower than the other two types (TTP and TSP foldcores). This is due to the lower inclination angle of sidewalls on TPP which leads to sidewall sliding and corner lift-ups under lateral crushing. Furthermore, the triangular interconnection size decreases with the increasing number of the sides, i.e., the size of vertical triangular interconnections which provide extra crushing resistance reduces from TTP to TSP to TPP. This is consistent with the stress-strain curves of the foldcores as well.

4.4.3 Fixed boundary condition

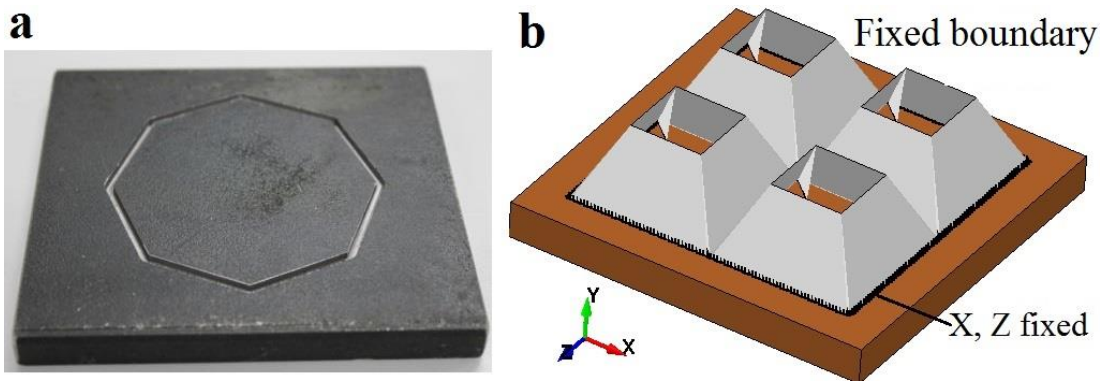

Figure 4-12. (a) Grooved base plate for origami-tube crushing test (137); (b) Fixed boundary with outer edges of foldcore fully fixed along the in-plane directions

Corner lift-up can be observed for TPP foldcore due to the non-ideal simple boundary condition, which leads to different damage modes and lower crushing resistance comparing to TTP foldcore. Different boundary conditions are, therefore, studied to examine its effect on structural behaviour. The bottom outer edges of the foldcore unit

area are fixed in both the in-plane directions, while other parameters such as contact, friction and loading rates are kept the same. In other words, instead of modelling the base plate with 2 mm boundary (Figure 4-6), where sliding of the sidewalls might occur, the foldcore outer bottom edges are now fixed with no displacement allowed. This is to simulate one of the most common connection of sandwich core to its skin where glue or fully fixed connection is often used. For the folded structure, this fixed boundary condition may be also achievable by using grooved base plate as shown in Figure 4-12 (a), which was used as the testing base plate for an origami-tube (137). Deformation and crushing resistance of the foldcores are investigated under the fixed boundary condition.

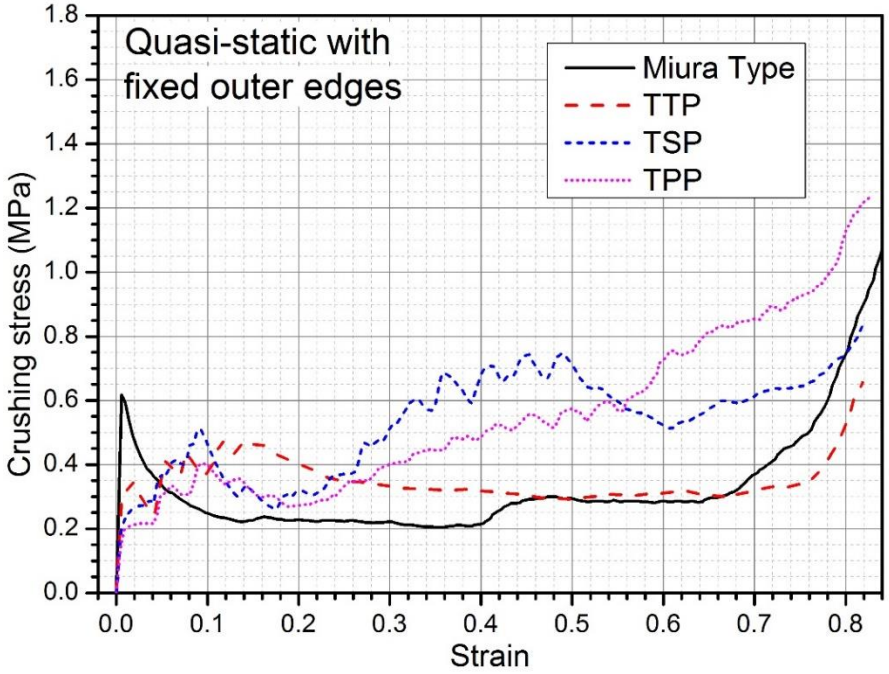

Figure 4-13. Stress strain curves of four types of foldcores with fixed outer edges under flatwise quasi-static crushing with fixed boundary condition

The numerical results of engineering stress-strain curves for these foldcores with fixed boundary under quasi-static loading are shown in Figure 4-13. Similar crushing behaviours are shown for Miura-type and TPP foldcore as those obtained from simple boundary condition as shown in Figure 4-10. Miura-type foldcore experiences higher initial peak stress with a slightly shorter elastic stage, where the peak stress occurred earlier than the case with simple boundary condition. Other than this, the stress-strain response including the average stress and densification strain remains similar for the cases with the two different boundary conditions. For the other two types of truncated

pyramid foldcores, i.e., TSP and TPP, distinct discrepancy of structural response can be observed from the strain of 0.2 onwards, as compared to the case with simple boundary condition. Although the structural response seems similar at the early stage of the crushing for the both boundary conditions, both foldcores of TSP and TPP show significant increase in the average crushing resistance during the plateau stage of crushing when the boundary of the foldcores is fixed.

This increased resistance is caused by the change of deformation mode of these two types of foldcores (TSP and TPP) under fixed boundary. The damage modes of foldcore under this boundary condition at the strain of 0.4 are shown in Figure 4-14. Consistent with the stress-strain curves, the damage modes of the Miura-type and TTP foldcore under fixed boundary are similar to the case with simple boundary condition as shown in Figure 4-11 (a, b). The Miura-type foldcore has similar buckling failure occurred at the middle of the faces on foldcore along the horizontal direction for two boundary conditions. Similar damage mode for TTP foldcore with the two boundary conditions is also observed. Top edges of the foldcore bend slightly toward centre of each unit cell and obvious buckling can be observed along the interconnection lines of the sidewalls.

Significant differences in the deformation mode of TSP and TPP foldcores are shown for two boundary conditions. As shown in Figure 4-11 (c) with simple boundary, some sidewalls of TSP foldcore are bent vertically towards centre. No deformation is presented along the outer intersection lines, other faces and interconnections are buckled near the intersection lines. For TPP foldcore with simple boundary condition shown in Figure 4-11 (d), only vertical bending of sidewalls towards centre is presented. All the intersection lines between faces of foldcore remain straight and un-deformed. Under fixed boundary condition, however, as shown in Figure 4-14, TSP and TPP foldcores deform similarly, with rolling of the top edges towards centre, and buckling along top of the intersection lines. No lift-up or deformation of foldcore corners at bottom is observed. The change of deformation mode is correlated to the change of crushing resistance under the two boundary conditions for TSP and TPP folded structures. The vertical bending of sidewalls towards the centre, shown in simply supported scenario, requires less force. With simple boundary, faces are free to slide causing corners to lift-up. The foldcore with lower inclination angle is easier to initiate the sliding of sidewalls due to the larger force in horizontal direction.

Therefore, the foldcore with low inclination angle such as TSP and TTP is prone to experience the sliding and corner lift-up as shown in Figure 4-8 (g,h) and Figure 4-11 (c,d). With fixed boundary, sliding of the sidewalls and the corner lift-ups are minimized, and the buckling deformation occurs along the triangular interconnections between sidewalls rather than vertical bending of sidewalls. Therefore, with fixed boundary, the crushing resistance capacity is enhanced for TSP and TPP foldcores which have lower sidewall inclination angle.

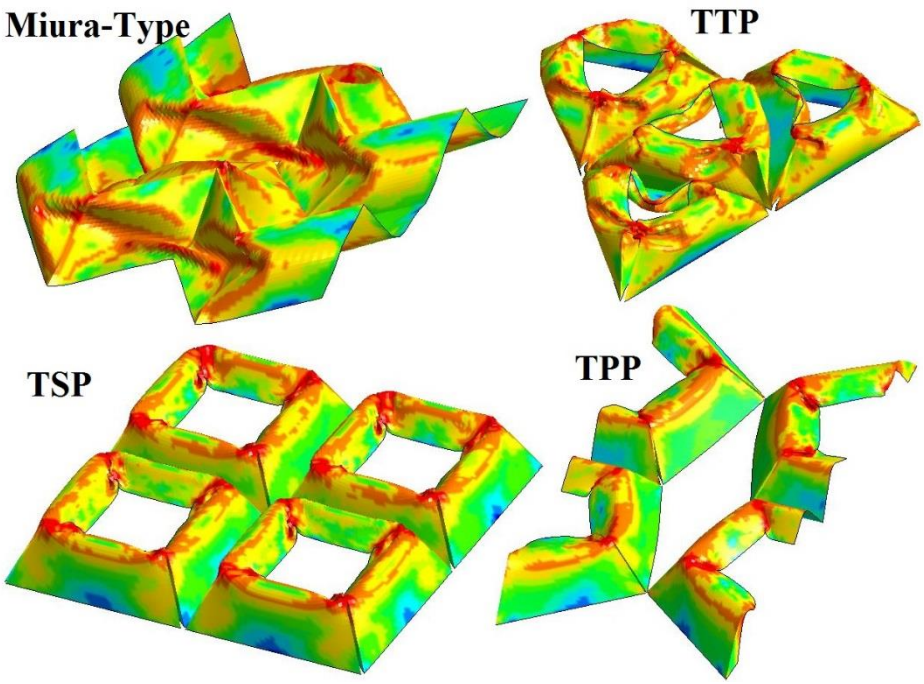

Figure 4-14. Damage modes of the foldcores at the strain of 0.4 with fixed boundary; Note: symmetric model used for TPP to simulate the interaction of adjacent unit cell at the gap

4.5 Simple boundary dynamic crushing

4.5.1 Stress-strain curve comparison under dynamic loading

In this section, structural behaviours of the foldcores are studied under different crushing velocities. The foldcores have the same unit number with simple boundary condition as in quasi-static testing where foldcore are simply supported by the same base plate with a 2 mm high outer boundary. Stress-strain curves of these foldcores under dynamic crushing speeds of 0.05, 0.5, 5, 10 and 20 m/s are presented in Figure 4-15. Key criteria of these foldcore are listed in Table 4-8.

The initial peak stress of Miura-type foldcore is greatly affected by crushing speed. It increases almost three times from 0.486 to 1.906 MPa with crushing rate increasing from 0.05 to 20 m/s as shown in Figure 4-15. Similar drastic increase can be found for its uniformity ratio as well from 1.81 to 4.25, while the densification strain of Miura-type foldcore is only slightly affected by the crushing velocity. The Miura-type folded structure shows great loading rate sensitivity on its initial peak stress.

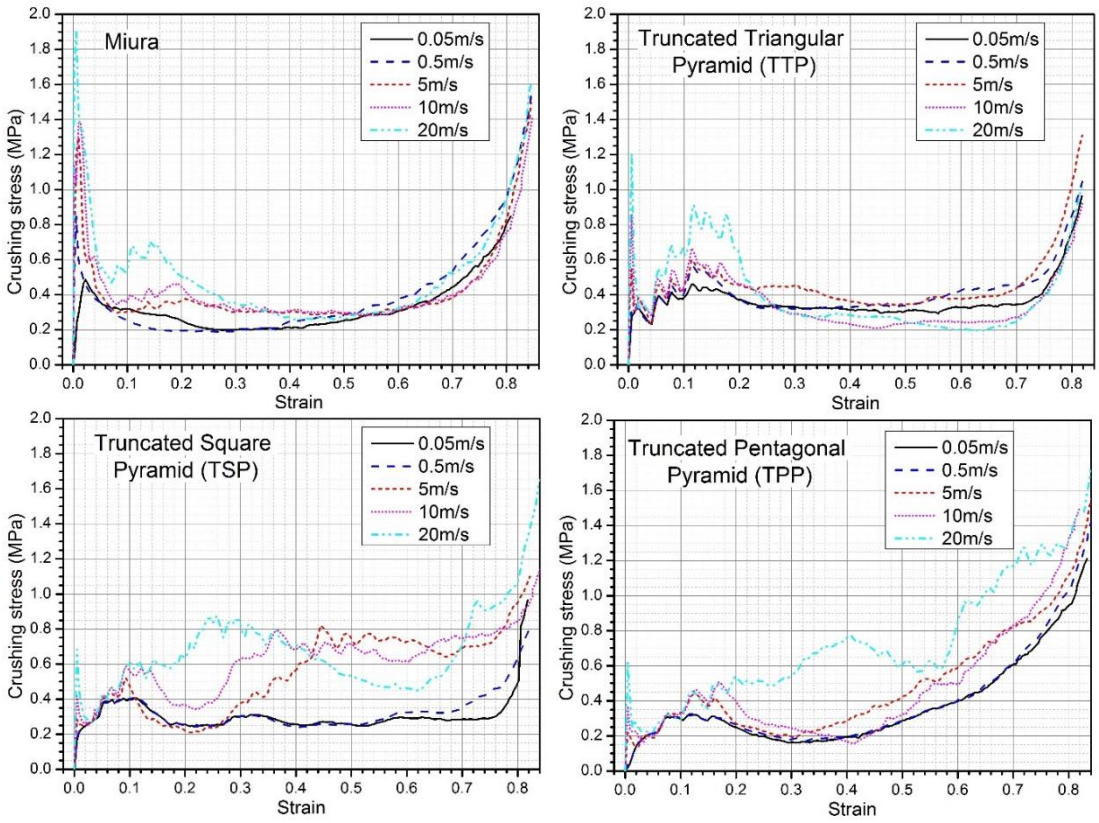

Figure 4-15. Stress-strain curves of foldcores under flatwise dynamic crushing with simple boundary

For the truncated pyramid folded structure, loading rate effect is dependent on the base shape and the geometry of the foldcore. Different dynamic behaviours with increasing crushing speed are observed for TTP, TSP and TPP as shown in Figure 4-15. For TTP folded structure, the increase in initial peak stress is obvious, from less than 0.4 MPa to 1.2 MPa, even though the increase is not as drastic as Miura-type foldcore. The average crushing stress of TTP structure, however, remain similar in value irrespective of the crushing velocity. For TSP folded structure, crushing behaviour remains almost unchanged under low speed crushing (0.5m/s). The initial peak stress has a smaller increase under the crushing speed of 20 m/s comparing with Miura-type and TTP folded structure. The crushing behaviour, on the other hand, is greatly changed under

higher crushing speeds (e.g. 5, 10 and 20 m/s). Significant increase in average crushing resistance and some reductions in densification strain can be observed in Figure 4-15. Similar trend of change in structural behaviour is shown for TPP folded structure with the increasing crushing speed as well. These crushing behaviours corresponding to the high crushing speed are somewhat similar to the quasi-static crushing case of the foldcores with the fixed boundary as shown in Figure 4-13. This is because the change of the crushing behaviour related to strain rate is caused by the change in damage modes, similar to the case associated with changing boundary conditions. More detailed discussions are given in Chapter 4.5.2.

Table 4-8. Peak and average stress, uniformity ratio and densification strain of four foldcores under flatwise dynamic crushing

Foldcore type	Crushing speed (m/s)	σ_{peak} (MPa)	σ_{ave} (MPa)	$U = \sigma_{peak}/\sigma_{ave}$	ε_D
Miura	**0.05**	0.486	0.268	1.81	0.66
	0.5	0.847	0.283	2.99	0.67
	5	1.300	0.348	3.74	0.70
	10	1.384	0.382	3.62	0.70
	20	1.906	0.448	4.25	0.66
TTP	**0.05**	0.458	0.340	1.35	0.74
	0.5	0.559	0.380	1.47	0.75
	5	0.599	0.410	1.46	0.72
	10	0.859	0.331	2.60	0.73
	20	1.205	0.377	3.20	0.73
TSP	**0.05**	0.405	0.286	1.42	0.76
	0.5	0.409	0.297	1.38	0.72
	5	0.819	0.521	1.57	0.76
	10	0.792	0.604	1.31	0.80
	20	0.877	0.599	1.46	0.67
TPP	**0.05**	0.326	0.262	1.24	0.66
	0.5	0.324	0.271	1.20	0.66
	5	0.436	0.357	1.22	0.66
	10	0.462	0.338	1.37	0.66
	20	0.775	0.532	1.46	0.58

Overall, strong strain rate sensitivity is demonstrated for Miura-type foldcore with huge increase in the initial peak stress, which is non-ideal for some sandwich panel applications such as cladding or impact attenuator. The truncated structures are much less strain rate dependent owing to their geometries. The TTP folded structure with high inclination angle also shows a dependent crushing behaviour with strain rate, as the initial peak stress increases with the crushing speed, but at a less level as compared

to that of Miura-type foldcore. For TSP and TPP folded structures, the initial peak stress is not significantly affected by the strain rate. The average crushing stress or plateau stress, however, increases with crushing speed due to the change of deformation mode. Their dynamic crush behaviour with the simple boundary condition is similar to the case with fixed boundary condition under quasi-static crushing. The increase of plateau stress under higher crushing speed could lead to a superior energy absorption capability, since with the same crushing distance the foldcore would absorb more energy without inducing a significant increase in initial peak stress.

4.5.2 Damage mode comparisons

The effective stress contour plot of Miura-type foldcore under 20m/s crushing is shown in Figure 4-16, the same legend is used as in Figure 4-11. Distinct deformation mode of the foldcore with simple boundary condition under dynamic loading is observed as compared to the case with simple boundary condition under quasi-static crushing shown in Figure 4-11. The plate buckling location shifts up to near the top of the foldcore instead of at around the middle of foldcore faces when crushing at a higher speed. Deformation along the bottom edges of the Miura-foldcore is less significant than quasi-static scenario, less rising of corners can also be observed under dynamic scenario. Similar dynamic behaviour of Miura-type foldcore has been identified in the previous studies as well (78, 82).The buckling location shifted closer to impact end and initial peak stress increased dramatically, which was explained by the inertia force developed inside the core under dynamic crushing (78). The sharp rise of initial peak stress might be related to the constraints provided by the faces of adjacent rows as well. At a lower crushing speed, the buckling location is around the middle faces of the foldcore, at some distance to the intersection of faces from adjacent row. Therefore, with the buckling location shifting up, closer to the intersection line of adjacent row, larger inertia stabilization is provided by the adjacent faces, causing significant increase in initial crushing resistance. This inertia stabilization effect is similar to the perpendicular webs of square honeycomb where sharp rises of initial crushing resistance are also observed under higher loading rate (11, 17).

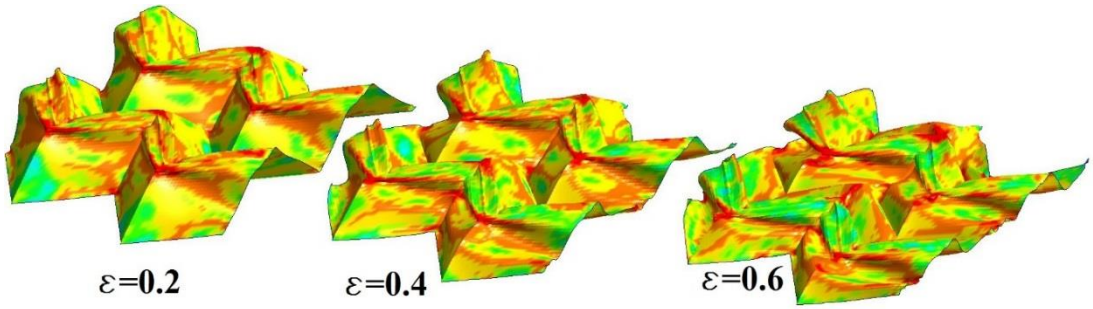

Figure 4-16. Damage modes of Miura-type foldcore at the strain of 0.2, 0.4 and 0.6 under 20m/s crushing with simple boundary

As shown in Figure 4-17, the damage mode of TTP folded structure with simple boundary under dynamic crushing is similar to that with simple boundary under quasi-static crushing as shown in Figure 4-11 (b). The top edge rolling towards unit cell centre and the buckling along the interconnections of sidewalls are observed. The sidewall buckling direction, however, shifts from bending towards outsides to inwards buckling. This is caused by the slight shifting up of the top edge bending location and the changed deformation modes. The high inclination angle of the sidewall of TTP unit cell leads to the increasing resistance to initial rolling on the top edge. Furthermore, due to the larger size of the vertical triangular interconnections as shown in Figure 4-2, the initial inertia effect is stronger for TTP than TSP and TPP which have smaller interconnections. Therefore, a sharp increase of initial peak stress occurs for TTP under dynamic loading as compared with the other two types of truncated pyramid structures. As previously studied (136), similar sharp rise in initial peak stress with the increasing crushing speed is observed for TSP foldcore with different geometric parameters (e.g. higher inclination angle and larger interconnection size) than the TSP with the geometry used in this chapter.

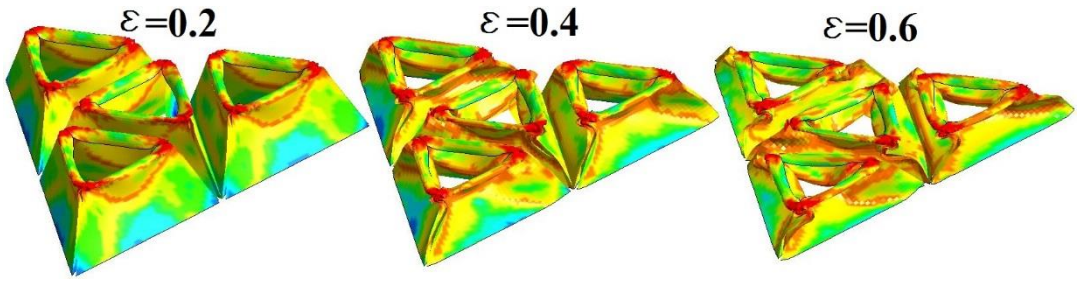

Figure 4-17. Damage modes of TTP folded structure with simple boundary at the strain of 0.2, 0.4 and 0.6 under 20m/s crushing

The deformation of the TSP folded structure is similar to the TTP foldcore under dynamic loading, as shown in Figure 4-18. Structural behaviour of TSP folded structure with simple boundary, however, shows distinct change under dynamic crushing as compared to the case under quasi-static loading. The deformation of vertical sidewall bending, which occurs on some faces of TSP foldcore unit cell under quasi-static loading, is not observed, instead top edge inwards rolling in the early stage and then sidewall horizontal buckling towards centre of each unit cell are observed under 20 m/s crushing speed. This damage mode of TSP foldcore with simple boundary under dynamic loading is quite similar to the foldcore with fixed boundary under quasi-static loading as shown in Figure 4-14. Correlated to similarity of deformation mode, the stress-strain responses under the two scenarios (i.e. 20 m/s crushing on the foldcore with simple boundary condition and quasi-static loading on the foldcore with fixed boundary condition) are also similar, with an increasing crushing resistance during plateau stage, as seen in Figure 4-13 and Figure 4-15.

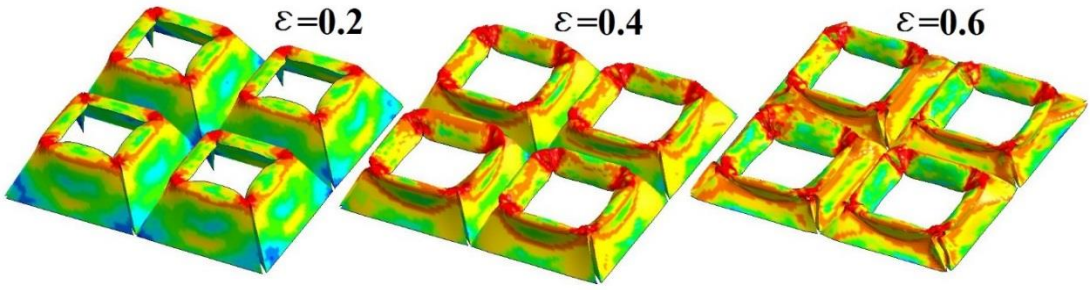

Figure 4-18. Damage modes of TSP folded structure with simple boundary at the strain of 0.2, 0.4 and 0.6 under 20m/s crushing

Deformation mode of TPP foldcore under 20 m/s crushing is similar to TSP under the same loading rate. The top edge of the sidewalls bends towards centre of each unit cell and further bending occurs along with further crushing of the foldcore. No sidewall buckling can be observed other than the deformation of top edges. As circled in Figure 4-19, slight corner open-up can be observed between two foldcores, where constraint is not provided due to the gap between tessellations of the pentagon shape. No lift-up of corner is seen for this simple boundary TPP under dynamic loading as opposed to foldcore under quasi-static crushing. Similar damage mode of the structure with simple boundary under dynamic crushing is observed as the case with fixed boundary condition under quasi-static crushing (Figure 4-14).

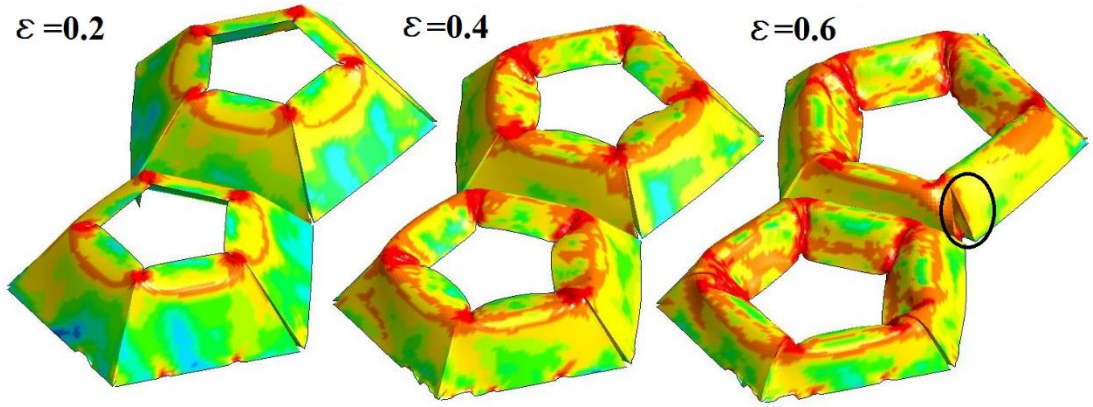

Figure 4-19. Damage modes of TPP folded structure with simple boundary at the strain of 0.2, 0.4 and 0.6 under 20m/s crushing

4.6 Summary

Three types of truncated pyramid folded structures (i.e. TTP, TSP and TPP) are proposed in this chapter with different base shapes (i.e. triangle, square and pentagon). Quasi-static crushing experiments of the hand-folded samples with simple boundary are carried out. Numerical models of these structures are calibrated with quasi-static crushing test data and good agreement is achieved. Numerical simulations are then conducted for quasi-static and dynamic crushing of various loading rates under simple and fixed boundary conditions. The crushing behaviours of proposed foldcores are also compared with Miura-type foldcore. The findings in this chapter are summarized below.

- Under quasi-static crushing of the foldcores with simple boundary condition, superior performances of TTP and TSP are demonstrated over Miura-type foldcore with higher average crushing stress, lower initial peak and longer densification strain. TPP shows less ideal performance than TTP and TSP, because of lower inclination angle and smaller interconnection size of TPP foldcore.
- Under quasi-static crushing of foldcores with fixed boundary condition, superior performances in terms of the key indicators, i.e., high average stress, low initial peak resistance and low uniformity ratio, are shown for all three types of truncated folded structures as compared to Miura-type foldcore. Significant change in deformation mode and increase in crushing resistance are observed for TSP and TPP foldcores as compared to the case with simple boundary condition.

- Under dynamic loading of the foldcores with simple boundary condition, TTP foldcore shows strain rate sensitivity with rise in initial peak stress due to the high inclination angle of sidewall. For TSP and TPP foldcores, the crushing resistances are significantly enhanced while the initial peak stress is not significantly increased. This is caused by the change of damage mode due to inertia effect that reduces the sidewall sliding and corner lifting-up of TSP and TPP foldcores. TSP foldcore outperforms the other three types under higher loading rate, demonstrating great application potentials for energy absorption.

Chapter 5. Blast mitigation performance of sacrificial cladding with TSP folded structure as core

The related work in this chapter has been published in International Journal of Mechanical Sciences.

Li Z, Chen W, Hao H. Blast mitigation performance of cladding using Square Dome-shape Kirigami folded structure as core. International Journal of Mechanical Sciences. 2018;145:83-95.
DOI: doi.org/10.1016/j.ijmecsci.2018.06.035

5.1 Introduction

As demonstrated in Chapter 3 and 4, TSP foldcores show good performance with uniform deformation and low initial peak crushing resistance. In this chapter, the performance of cladding with truncated square pyramid (TSP) foldcore subjected to blast loading is investigated through intensive numerical simulations. For comparison, the responses of square honeycomb and aluminium foam of the same density subjected to the same loading conditions are also simulated. The numerical model is firstly calibrated using the quasi-static crushing testing data of TSP foldcore. The model is then used to simulate structural response of claddings under blast loading. Different blast intensities are considered. Criteria including energy absorption by cladding core and the peak load transmitted to the protected structure are used to evaluate the performance among these claddings. In addition, Single Degree of Freedom (SDOF) analysis is applied to develop a simplified design procedure and guideline for estimating the required height of TSP foldcore sacrificial cladding under specific blast loading scenarios.

5.2 Model validation

For sample geometric parameters, dimensions, and fabrication please refer to Chapter 4.3. For material testing, crushing test set-up, experiment procedures please refer to Chapter 4.3.1. For numerical modelling including model keyword, boundary condition, material properties please refer to Chapter 4.3.2. For the quasi-static crushing result, numerical result, crushing response comparison and discussion please refer to Chapter 4.3.3.

5.3 Performance under various blast loads

5.3.1 Sacrificial cladding set up

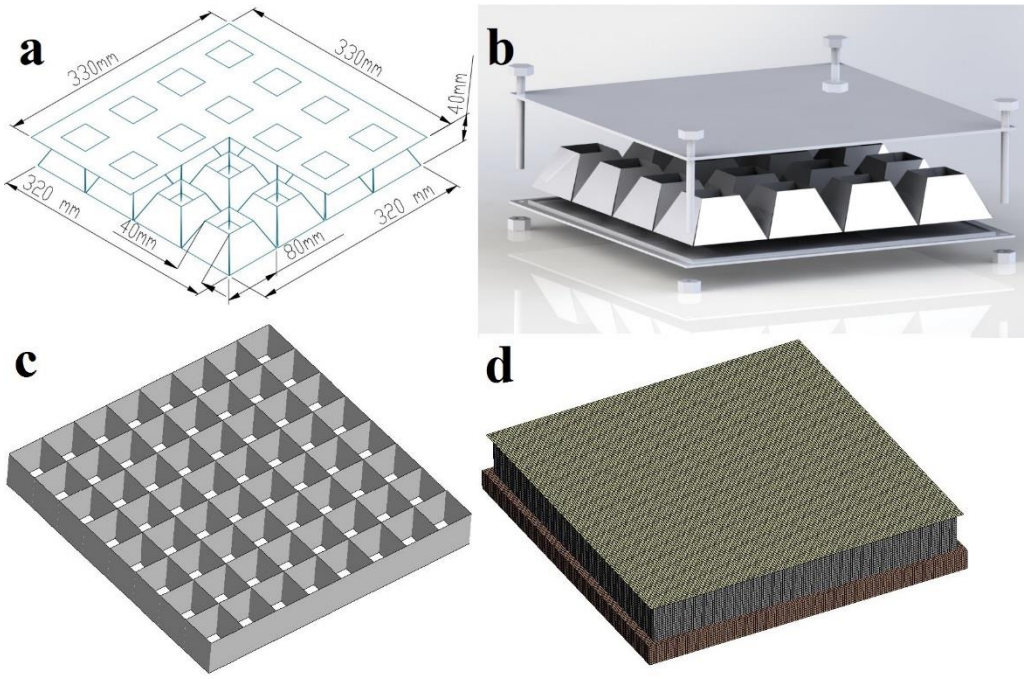

Figure 5-1. (a) Numerical model of cladding with TSP foldcore as core; (b) proposed assembling of TSP foldcore sandwich structure as sacrificial cladding; (c) square honeycomb core; (d) cladding with aluminium foam core

The performance of sacrificial cladding with TSP foldcore as core is evaluated and compared with square honeycomb and aluminium foam in this chapter. The dimension of unit cell of TSP foldcore, as shown in Figure 5-1 (a), is scaled up twice compared to the tested specimen to have a more reasonable configuration with a 40 mm-thick sacrificial cladding core. The resultant unit cell size of TSP foldcore increases from 40×40×20 mm used in compression test to 80×80×40 mm for the cladding setup. The unit cell of square honeycomb is 40×40×40 mm, so it has the same top-opening dimension as TSP foldcore. The same cladding core height of 40 mm is set for aluminium foam. The 330×330×5 mm aluminium plate is used for all three sacrificial claddings as top layer, where the core spaces of these claddings are kept the same as 320×320×40 mm.

In this chapter, blast mitigation performances of the sacrificial claddings with different cores are compared using the energy absorption by the core and the peak load transmitted to the protected structure as criteria. Therefore, the back skin of the

cladding is neglected and the core is placed directly on top of the rigid block as illustrated in Figure 5-1 (d). The rigid block is set with density of 2400 kg/m^3 and Young's modulus of 200 GPa (116), modelled by *MAT020 RIGID in LS-DYNA. Similar boundary conditions as in many current cladding studies (35, 116, 138) are applied in the model where sacrificial cladding is simply placed on the surface of structure. For the cladding with aluminium foam core and square honeycomb, the core and top plate are simply supported. The rigid block is fixed in all degree of freedom. The top plate is set to be fixed along the in-plane directions at corners and free to move vertically as shown in Figure 5-1 (b). No glue or other fixing is applied for all three claddings. For cladding with TSP foldcore, similar to the crushing experiment and numerical model calibration, outer boundary is constructed in the model to constrain the horizontal movements of foldcore outer edges. It should be noted that the interaction between cladding core and the protected structure is neglected in this chapter to save computational effort. This assumption is believed having insignificant influence on the numerical results because the stiffness of sacrificial cladding is usually substantially smaller than that of the protected structure.

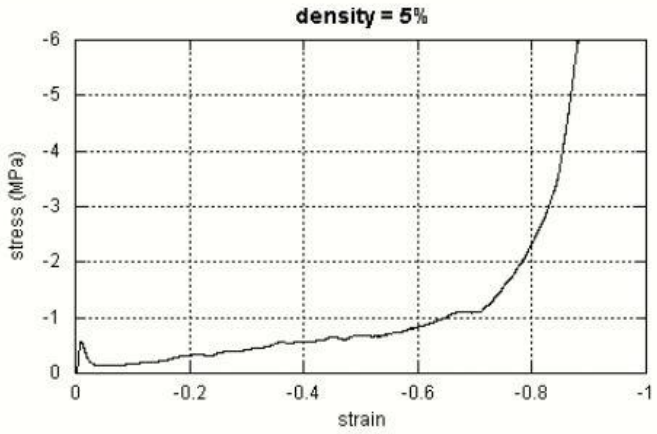

Figure 5-2. Stress-strain curve of CYMAT closed cell aluminium foam with 5% relative density crushed in out-of-plane direction (139)

Due to the limitation of aluminium foam fabrication technology, the lowest relative density for aluminium foam is 5% from CYMAT^{TM} (139). Therefore, the wall thickness for TSP foldcore and square honeycomb is calculated to be 0.94 mm and 0.87 mm respectively to make the relative density of the core the same as 5% aluminium foam for comparison. It is worth noting that the wall thickness of 0.94 mm is only used to match the light aluminium foam with 5% relative density. It is likely

to be too thick for the folding process and also leads to the increase of strain rate dependency for cladding structure, which might be a drawback for the application such as sacrificial cladding due to the thickening of vertical triangular interconnections.

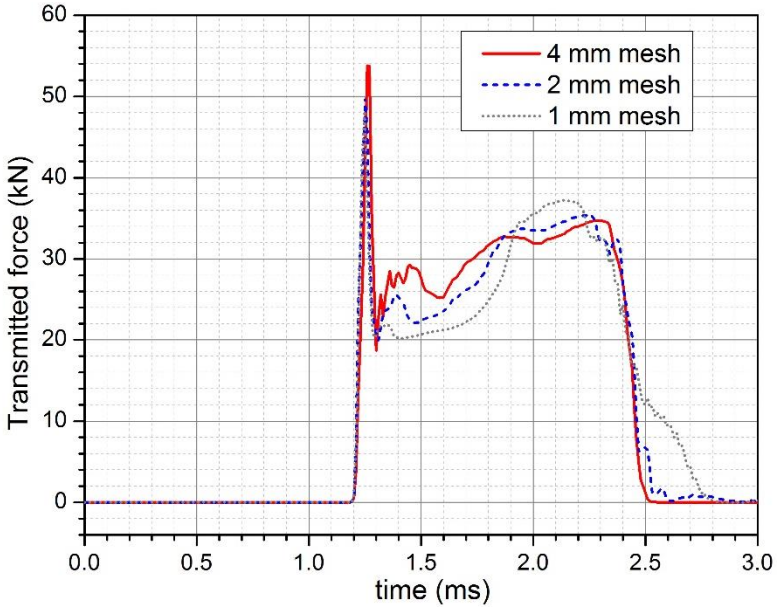

Figure 5-3. Mesh convergence test for numerical model under 1 kg TNT explosion with stand-off distance 1.5 m

The same material model and parameters obtained from quasi-static tests are used for TSP foldcore and square honeycomb in numerical simulation. Aluminium foam is modelled by *MAT063 CRUSHABLE FOAM, with stress-strain data found in CYMAT manual as shown in Figure 5-2 (139), where the strain rate effect for the plateau stress of aluminium foam is not obvious (27) and not included in this numerical study. The Belytschko-Tsay type shell element with material properties given in Chapter 4.3.2 is used for TSP foldcore, square honeycomb and their flat top plates. The same contacts as in the numerical model calibration are used with friction taken into consideration. As shown in Figure 5-3, mesh convergence test is carried out for aluminium foam cladding model under 1 kg of TNT explosion with 1.5 m stand-off distance. Good agreement can be observed for mesh size of 1 and 2 mm in terms of peak transmitted force and average transmitted force exerted on the protected structure. Therefore 2 mm mesh, which leads to more than half a million elements for the aluminium foam cladding core, is sufficient for the following numerical studies. Mesh size of 2 mm is used for all three models.

5.3.2 Structural response comparison

Different blast intensities are simulated with 1, 2, 4 and 6 kg of TNT placed at 1500 mm above the center of the front plate of claddings, in accordance with some previous experiments on the claddings with the stand-off distance of 1 to 2 m (115, 116). The keyword * LOAD BLAST ENHANCED is used in LS-DYNA. The structure without cladding is also simulated to obtain the force time history for comparison. The stand-off distance for this unprotected structure is 1540 mm, since the cladding has a height of 40 mm.

Table 5-1. Peak transmitted load, duration, crushed distance at cladding center and energy absorption by core of different cladding configurations under various TNT blast loads

Cladding types		P_{peak} (kN)	$P_{average}$ (kN)	Duration (ms)	Peak crushed distance at centre δ (mm)	Energy absorption by core (J)
1 kg TNT 1.5 m/kg$^{1/3}$	**Without cladding**	146	-	0.78	-	-
	Square honeycomb	281	44.7	0.78	0.1	2
	Aluminium foam	50	27.9	1.30	9.6	278
	TSP foldcore	120	45.4	0.78	0.6	43
2 kg TNT 1.19 m/kg$^{1/3}$	**Without cladding**	285	-	0.79	-	-
	Square honeycomb	456	74.1	0.78	0.3	15
	Aluminium foam	75	49.4	1.28	19.9	965
	TSP foldcore	160	83.1	0.75	2.7	318
4 kg TNT 0.95 m/kg$^{1/3}$	**Without cladding**	562	-	0.80	-	-
	Square honeycomb	652	130	0.78	0.4	167
	Aluminium foam	414	121	0.95	33.3	3070
	TSP foldcore	236	131	0.82	10.9	1910
6 kg TNT 0.83 m/kg$^{1/3}$	**Without cladding**	831	-	0.79	-	-
	Square honeycomb	676	191	0.74	10.2	1260
	Aluminium foam	1750	247	0.70	36.7	5530
	TSP foldcore	272	170	0.88	17.9	3860

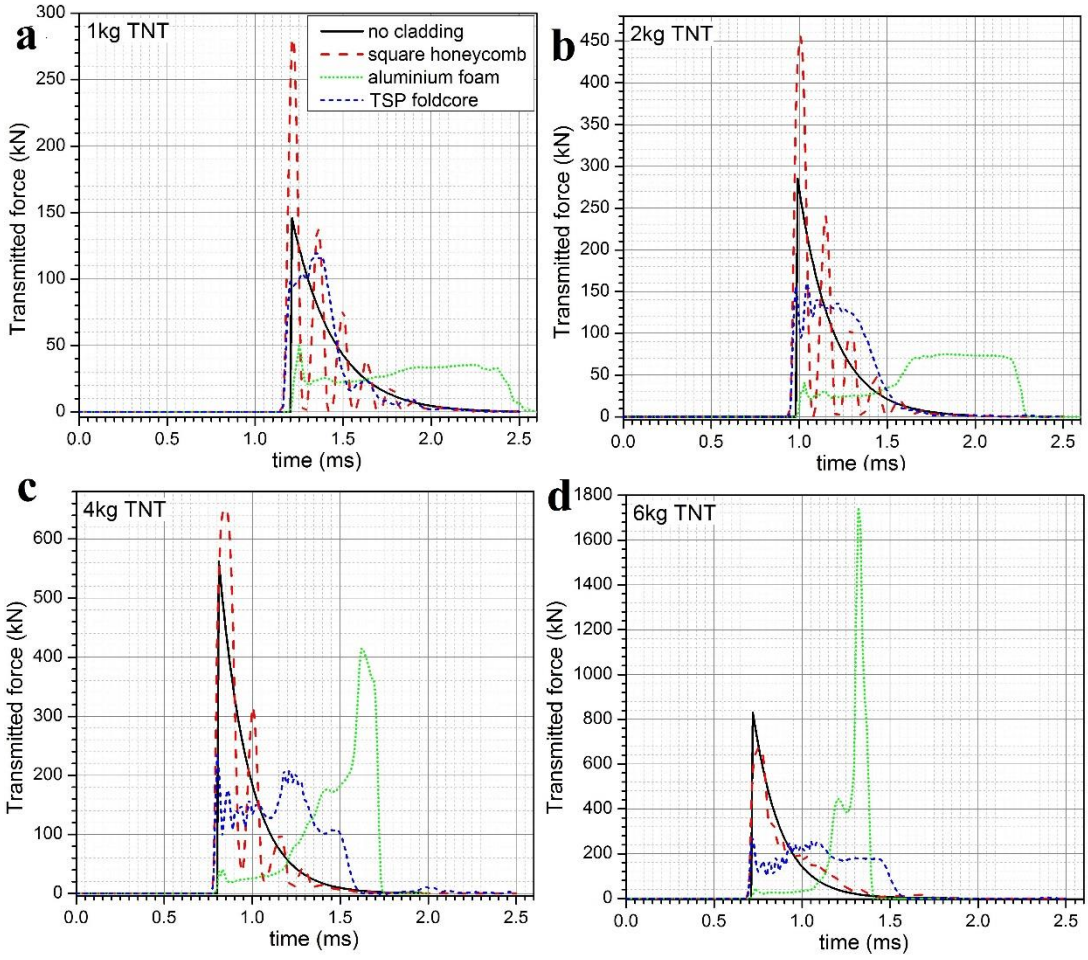

Figure 5-4. Comparison of transmitted force-time history curves under different blast loads; (a) 1kg TNT; (b) 2kg TNT; (c) 4kg TNT; (d) 6kg TNT; note y-scales are different for each graph

The time history curves of transmitted force to the protected structure with different claddings under various blast loads are shown in Figure 5-4. The forces are measured as the transmitting force to the supporting structure behind the cladding systems. When subjected to the blast load of 1 kg TNT, the peak force exerted on structure is around 146 kN for the case without cladding. Force reduction is observed for the aluminium foam and TSP foldcore claddings, whereas the square honeycomb cladding configuration experiences higher peak transmitted load than the case without any protective cladding. Force reduction for cladding with TSP foldcore is not as significant as that with the aluminium foam core for this loading scenario. Similar observations for the case with the blast load of 2 kg TNT can be drawn, i.e., the aluminium foam core results in the largest force reduction, followed by the TSP

foldcore claddings, while the protected structure experiences a larger peak load if the square honeycomb cladding is used than unprotected structure. For the scenarios with blast loads of 4 kg and 6 kg, large reduction in transmitted peak force is observed for TSP foldcore. The peak transmitted force to the protected structure with aluminium foam cladding becomes higher than the other two cladding configurations and even higher than the structure without cladding under 6 kg of TNT explosion. It should be noted that only crushing deformation is considered in this numerical simulation, fractures of the cladding core as previously investigated by Langdon et al (114) is not considered.

The observations indicate that the aluminium foam cladding and the square honeycomb cladding have mixed performances, while the performance of TSP foldcore is consistent, i.e., it always leads to a reduction on the peak transmitted force to the protected structure in the blast loading range considered in the chapter. The mixed performance of the aluminium foam cladding and the square honeycomb cladding is related to their stiffness and strength. The deformation of the cladding includes three states i.e. (1) elastic state, (2) plastic state and (3) fully densified state and all of which are demonstrated in Figure 5-4. For the structure with TSP foldcore under 1 kg and square honeycomb cladding under 1 kg, 2 kg and 4 kg blast loading, transmitted forces fluctuate multiple times, representing elastic state of the deformation as shown in Figure 5-4 (a-c). This is because the applied load is relatively small and no significant buckling damage and plastic deformation of the core occur. The core is still primarily in elastic state. This is confirmed by the very small centre panel crushed deflections of these two cores as listed in Table 5-1. Because the core structure remains primarily in elastic stage, it acts like a conduit to transmit the blast load instead of reducing blast load. On the other hand, the aluminium foam cladding is relatively weak and experienced significant crushing failure, which absorbs significant amount of blast energy. Therefore the transmitted load to the protected structure is largely reduced. The second state is the plastic deformation where the impulse from blast wave is fully absorbed by the deformation of the cladding core before it reaches densification, as shown in Figure 5-5 (a-c). This phenomenon can be observed for the square honeycomb cladding under 6 kg TNT blast loading, the Aluminium foam cladding under 1 and 2 kg TNT explosion and the TSP foldcore cladding under 2, 4 and 6 kg TNT explosions. The third state of core deformation is

the full densification of cladding before the end of blast loading, as shown in Figure 5-5 (d). Full densifications are presented for the aluminium foam cladding under 4 and 6 kg TNT blast loading. Once a cellular core reaches its densification, the stress required for further deformation increases drastically. In some cases, the transmitted load can exceed the blast loading due to the impact of the accelerated fully compacted material onto the protected structure. Similar analysis has been carried out in the study (35) and deteriorating effect of protective cladding has been observed in the experiment (18) as well.

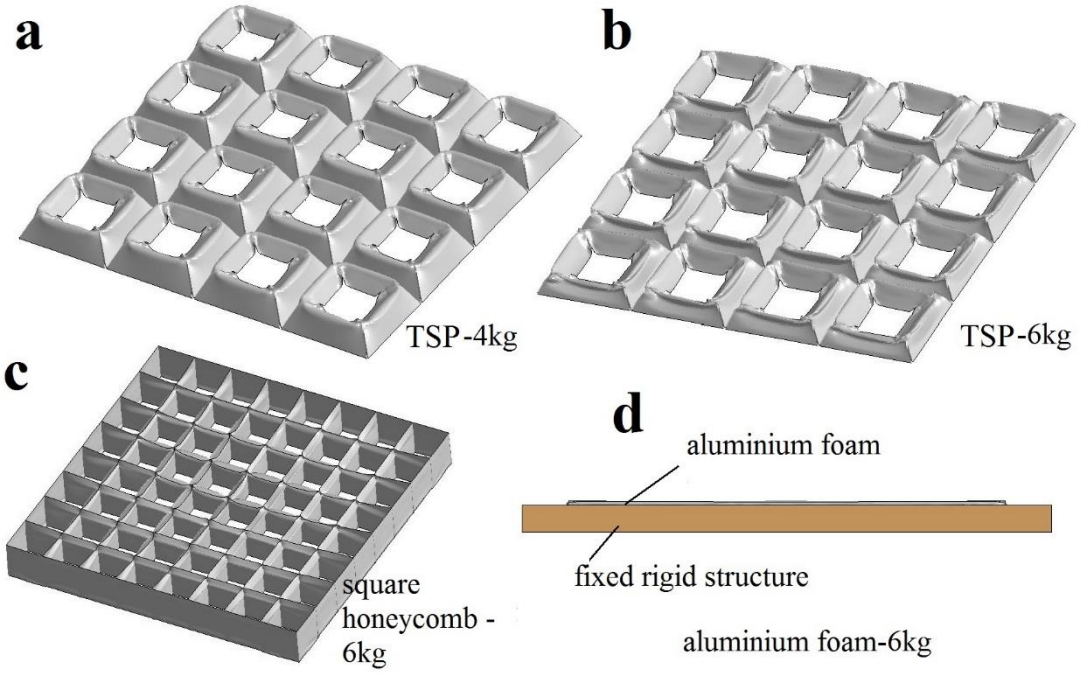

Figure 5-5. Damage modes of cladding core of (a) TSP foldcore under 4kg TNT blast load; (b) TSP foldcore under 6 kg TNT blast load; (c) square honeycomb under 6 kg TNT blast load; (d) side view of aluminium foam cladding under 6 kg TNT blast load

The second state i.e. plastic state is the most effective in energy absorption for the cladding, where the cladding core undergoes plastic deformation and not yet fully compacted during an event of blast. Large amount of energy is dissipated through core deformation and significantly reduces force to be transmitted to the protected structure. Other two states (i.e., elastic state and fully densified state) are caused by too strong or too weak of the cladding core comparing to the reflected blast pressure. The core with lower plateau stress leads to a lower average transmitted load to the protected structure before densification, but it is easier to reach the fully densified state and possibly causes more damage to the protected structure as shown for cladding with

aluminium foam under 6 kg TNT blast loading in Figure 5-4 (c, d) and Figure 5-5 (d). For the other case (elastic state), it is caused by high crushing resistance of the cladding core or the low value of blast peak pressure, and both of these two causes lead to less effectiveness of the cladding. This can be observed for the cladding with square honeycomb core under 1, 2 and 4 kg TNT blast loading, as shown in Figure 5-4 (a-c).

Overall, the TSP foldcore outperforms the other two cladding configurations by producing a consistent and moderate plateau stress during the whole process of deformation. As shown in Figure 5-4, TSP foldcore yields much more consistent transmitted load than square honeycomb cladding and a higher plateau stress than the most commonly used cladding material i.e. aluminium foam with the same relative density, which leads to a wider range of applicability of the cladding. However, it is worth noting that the initial peak force of TSP foldcore is greater than that of aluminium foam with the same density due to the vertical triangular interconnections of TSP foldcore. It was previously studied that the initial peak force of square honeycomb is in a power relationship with cell wall thickness and it was strain rate dependent due to inertia effect and inertia stabilization effect of the vertical cell walls (13, 16, 17). As mentioned previously, the thickness of TSP cell wall used in this chapter might be too thick for the folding process and it is only used to match the aluminium foam with the lowest density of 5% available on the market. Therefore, the initial peak stress of TSP foldcore can be greatly reduced by reducing the cell thickness as demonstrated in the previous work where 2.7% relative density of TSP foldcore was studied (8, 140), and providing similar plateau stress to 5% aluminium foam (Figure 5-2).

Comparisons of energy absorption by the core of the claddings are shown in Figure 5-6. Energy absorption of each cladding configuration increases with the rising blast load. The low value of square honeycomb foldcore under 1 and 2 kg TNT explosion indicates the elastic state of the core. The aluminium foam cladding has the highest energy absorption capability by the core among these three. With a higher crushing resistance, the TSP foldcore absorb less energy than aluminium foam under the same level of blast load. However, as discussed previously, the TSP foldcore has a higher plateau force and a wider range of applicability of the cladding against different blast loadings comparing with aluminium foam of the same density. It also has a much

lower initial peak stress and a more uniform collapsing resistance than the square honeycomb cladding, which demonstrates the superiority of TSP foldcore.

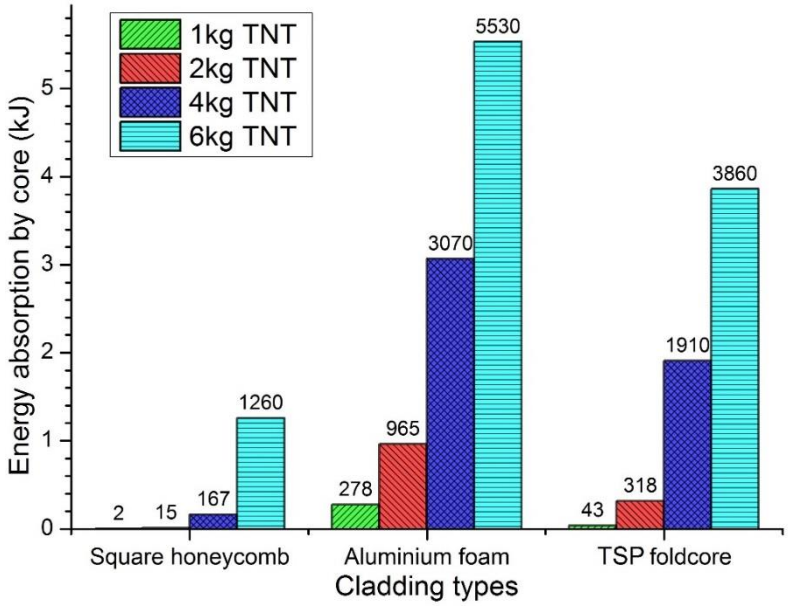

Figure 5-6. Energy absorption by the core with different cladding configurations and blast loads

5.4 Single Degree of Freedom (SDOF) model

5.4.1 Analytical model

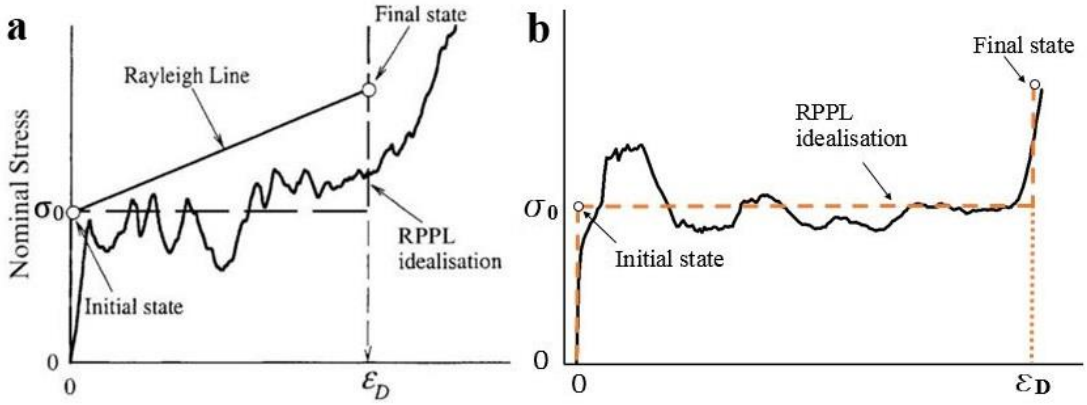

Figure 5-7. Idealized Rigid-Perfectly Plastic-Locking model for (a) aluminium foam material (29); (b)FE results of TSP foldcore under quasi-static loading

The SDOF analysis of aluminium foam cladding and the protected main structure was carried out based on shock wave propagation theory in the previous studies (7, 35, 138, 141). Blast load is simplified as a triangular pulse which follows the form:

$$P(t)=\begin{cases} P_r\left(1-\dfrac{t}{t_0}\right); t \le t_0 \\ 0; t > t_0 \end{cases} \qquad (5\text{-}1)$$

where *P(t)* is the blast pressure at time *t*, P_r is the initial reflected peak pressure of the blast load and t_0 is the duration of the blast load. As shown in Figure 5-7 (a), idealized rigid-perfectly-plastic-locking (RPPL) material with a plateau stress of σ_0 (29) is used for aluminium foam cladding in SDOF analysis. Stress-strain curve and idealized RPPL model for TSP foldcore are presented in Figure 5-7 (b) for comparison. Non-dimensional parameters of foam cladding were then introduced based on cladding properties and blast parameters to evaluate the effectiveness of the foam cladding (35). It was suggested that the foam cladding should be selected carefully. It is only effective when the impulse from blast load is fully absorbed prior to or at the full densification of the foam cladding. Regions of the effectiveness of foam cladding are divided based on cladding system mechanical parameters and blast loads (35). In some cases, the foam-protected structure may experience an even larger transmitted load, if the foam is fully densified before the end of the blast impulse. This phenomenon has been recorded in blast test using lightweight polymeric foam as sacrificial claddings (18).

Free body diagrams of the foam cladding system at *t* and *t+dt* are shown in Figure 5-8, based on the deformation modes observed in the previous experimental study (7). It is assumed that the foam behind shock front is fully compacted with the same density as base material ρ_{f0}. The compacted zone x and the front-panel displacement u have the following relationship based on the conservation of mass, where both sides of equation equal to the original length of compacted zone before deforming.

$$\frac{u}{\varepsilon_D}=\frac{x}{1-\varepsilon_D} \qquad (5\text{-}2)$$

where ε_D is the densification strain of the foam material ranging between 0 and 1.

The following equation can be obtained by the conservation of momentum of the small compacted foam dx at time *t+dt* as shown in Figure 5-8:

$$\rho_{f0}\cdot A dx\left(\dot{u}+d\dot{u}\right)=\left(\sigma_D-\sigma_0\right)A dt \qquad (5\text{-}3)$$

where ρ_{f0} is the density of foam base material; A is the cross-section area of the cladding, σ_D and σ_0 are the foam stress immediately behind shock front and foam plateau stress respectively. Similarly, based on the force balance of the front plate and compacted region of foam on the left of element *dx*:

$$\left[M_1 + \frac{\rho_f A}{1-\varepsilon_D} x\right]\ddot{u} + \left(\sigma_D - P(t)\right)A = 0; \qquad (5\text{-}4)$$

where M_1 is the mass of front plate; ρ_f is the foam density; $P(t)$ is the blast pressure.

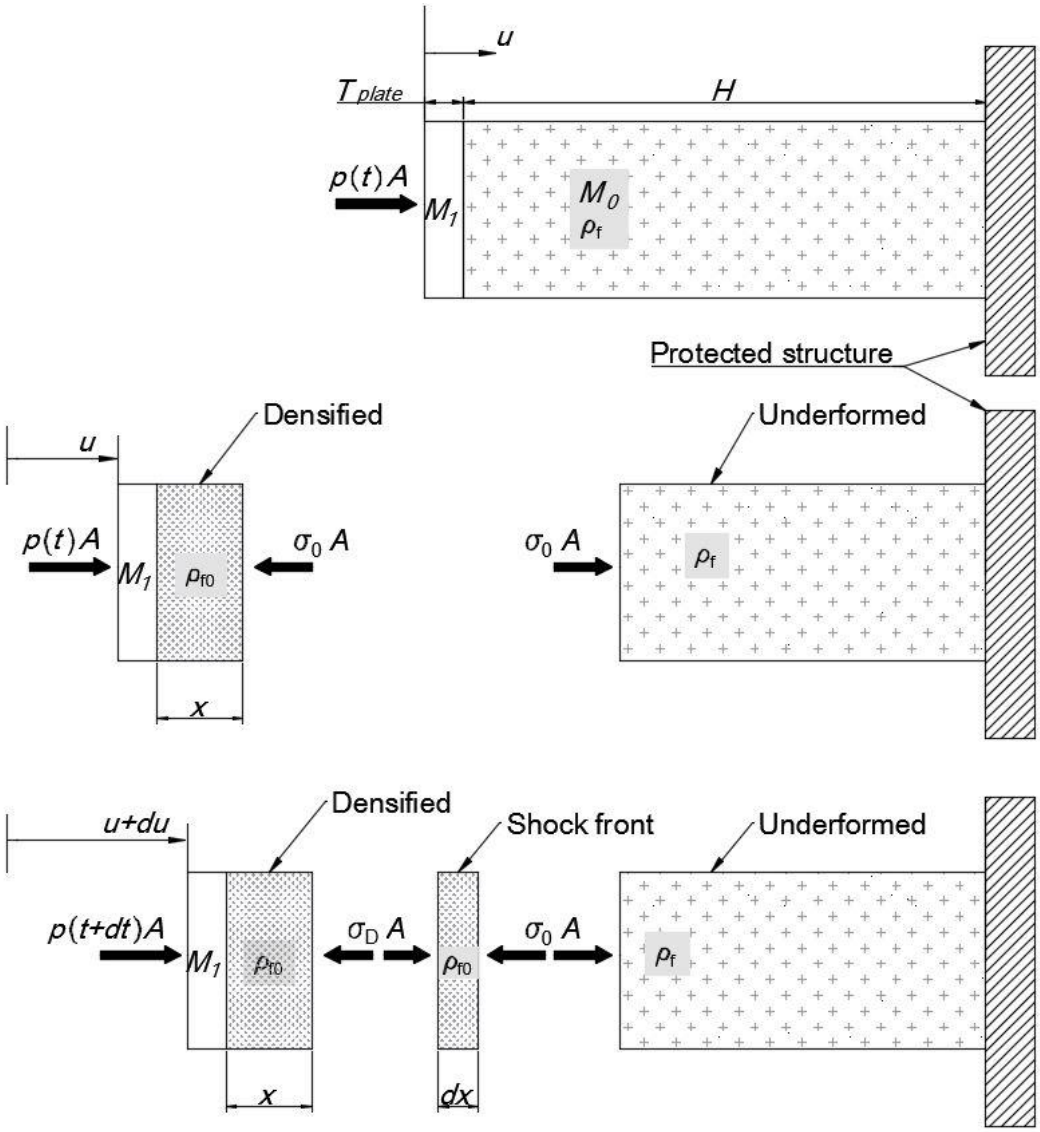

Figure 5-8. Free body diagrams of aluminium foam cladding system under uniform blast loading at the beginning, time t and t+dt (7)

Complete solution can be solved from the above equations and a minimum height H required to fully absorb blast loading is given as

$$H \geq \frac{I^2}{\left(M_0 + 2M_1\right) P_r A \varepsilon_D} \left[\frac{P_r}{\sigma_0} - \frac{4}{3} \right]; \frac{P_r}{\sigma_0} > 2 \qquad (5\text{-}5)$$

where I is the total blast impulse and M_0 is the mass of foam cladding.

The crushed distance of the cladding can be expressed as

$$\delta = \frac{I^2}{\left(M_0 + 2M_1\right) P_r A} \left[\frac{P_r}{\sigma_0} - \frac{4}{3} \right]; \frac{P_r}{\sigma_0} > 2 \qquad (5\text{-}6)$$

5.4.2 Displacement comparison with numerical results

Table 5-2. Comparison of centre displacements of numerical (δ_1) and analytical (δ_2) results

	P_r (MPa)	I (Ns)	Aluminium foam				TSP foldcore			
			σ_0 (MPa)	δ_1 (mm)	δ_2 (mm)	Difference	σ_0 (MPa)	δ_1 (mm)	δ_2 (mm)	Difference
1 kg TNT	1.34	34.7	0.256	9.6	9.1	-5%	-	-	-	-
2 kg TNT	2.62	57.4	0.457	19.9	14.7	-26%	0.763	2.7	6.5	141%
4 kg TNT	5.16	98.3	-	-	-	-	1.203	10.9	14.0	28%
6 kg TNT	7.63	131.7	-	-	-	-	1.561	17.9	21.2	18%

Since the TSP foldcore has a similar crushing resistance as aluminium foam, the RPPL material can be assumed for the TSP foldcore as shown in Figure 5-7, then the SDOF analysis can be applied for simplified calculation of core displacement. The cladding crushed distances are calculated based on the equation (5-6) and given in Table 5-2. Since the assumption of the material model in SDOF of cladding system analysis is RPPL, only the responses with aluminium foam and TSP foldcore are calculated due to the relatively low initial peak stress. Furthermore, the equation is derived under the condition that the fully densified state of cladding core is not reached. Aluminium foam becomes fully densified under 4 and 6 kg TNT explosion. Therefore, these two cases are not included in the analysis. The blast parameters P_r and I are taken from numerical simulations of the scenarios without cladding. Other parameters used in

equation (5-6) are calculated by using the dimensions of the foam, plate and their densities.

The results of numerical ($\boldsymbol{\delta_1}$) and analytical ($\boldsymbol{\delta_2}$) predictions are matched well, indicating that the SDOF analysis can be used as a simplified tool to quickly design the cladding configuration. The only large discrepancy (141%) in centre deformation observed between numerical and analytical predictions appear in the cladding with TSP foldcore under 2 kg TNT explosion. This overestimation of the deformation in analytical prediction is caused by the idealized RPPL model, where initial peak of the crushing is not considered and only plastic stage is modelled, as shown in Figure 5-7. Therefore, under low blast intensities when the deformation of cladding core just reaches the plastic stage, the analytical prediction obtained using SDOF analysis based on perfect plastic deformation assumptions could be overestimated. Furthermore, the deformation and energy absorption of front plate of the cladding system is not considered in this SDOF approach. Thin layer of front plate or cladding with unevenly supported core structure could lead to slight overestimation in this SDOF approach as well. Overall the central displacements analytically predicted by using the above derived formula are in good agreement with the numerical results, indicating the derived formula can be used as a simplified tool to estimate the thickness required for cladding subjected to certain blast loading.

5.5 Simplified design charts for folded TSP core

As per the equation (5-5) derived by Hanssen et al (7), the minimum core height H, of foam sacrificial cladding is defined by the blast peak reflected pressure P_r, blast impulse I, plateau stress of foam σ_0, densification strain ε_D, mass of the front plate M_1 and mass of the foam (cladding core) M_0. However, the mass of the core M_0 is not an independent parameter of the height of the core, H. Therefore, Equation (5-5) for the required core thickness (H), previously derived by Hanssen et al (7) is not the complete solution for the designing of the sacrificial cladding. Mass of the core, M_0, and front plate, M_1, are further defined by the density and the size of the core, as given below:

$$M_0 = \rho_f \cdot HA \qquad (5\text{-}7)$$

$$M_1 = n \cdot \rho_f T_{plate} A \qquad (5\text{-}8)$$

where n is the ratio between plate density and foam (cladding core) density ρ_f, and T_{plate} is the thickness of the front plate. Substitute equation (5-7) & (5-8) into equation (5-5), it has

$$H \geq \frac{I^2}{\left(\rho_f \cdot HA + 2n \cdot \rho_f T_{plate} A\right) P_r A \varepsilon_D} \left[\frac{P_r}{\sigma_0} - \frac{4}{3}\right]; \frac{P_r}{\sigma_0} > 2 \qquad (5\text{-}9)$$

Since all parameters are positive numbers,

$$H^2 + 2n \cdot T_{plate} H \geq \frac{I^2}{\rho_f \cdot P_r A^2 \varepsilon_D} \left[\frac{P_r}{\sigma_0} - \frac{4}{3}\right]; \frac{P_r}{\sigma_0} > 2 \qquad (5\text{-}10)$$

$$H \geq \sqrt{\frac{I^2}{\rho_f \cdot P_r A^2 \varepsilon_D} \left(\frac{P_r}{\sigma_0} - \frac{4}{3}\right) + n^2 \cdot T_{plate}{}^2} - n \cdot T_{plate}; \frac{P_r}{\sigma_0} > 2 \qquad (5\text{-}11)$$

where blast impulse I and blast peak reflected pressure P_r can be obtained from UFC (31). These two curves are fitted using Matlab as shown in Figure 5-9. Z is the scaled distance, R is the stand-off distance and W is the equivalent TNT mass in imperial units and to be converted to metric units before submitted into equation (5-11). Alternatively, fitted curves of reflected pressure (P_r) and impulse (I) in metric units can be found in (142), with the scaled distance ranged from 0.2 to 50 m/kg$^{1/3}$.

The fitted equation of the peak reflected blast pressure P_r is given as:

$$P_r = exp\left\{\begin{matrix} -0.0084\left[\ln(Z)\right]^5 + 0.0482\left[\ln(Z)\right]^4 + 0.0743\left[\ln(Z)\right]^3 \\ -0.5382\left[\ln(Z)\right]^2 - 2.1322\ln(Z) + 8.8924 \end{matrix}\right\}; unit: psi \qquad (5\text{-}12)$$

The fitted equation of reflected blast impulse I (i.e. I_r in Figure 5-9) is given as:

$$\frac{I}{W^{\frac{1}{3}}} = \exp\left\{\begin{matrix} -0.00011\left[\ln(Z)\right]^4 - 0.01126\left[\ln(Z)\right]^3 + \\ 0.129\left[\ln(Z)\right]^2 - 1.51731\ln(Z) + 5.4197 \end{matrix}\right\}; unit: psi - ms/lb^{1/3} \qquad (5\text{-}13)$$

These fitted curves have the value of R^2=0.9999 and 1.0000. Good fitting can also be seen from Figure 5-9. It is noted that all parameters in Figure 5-9 are in imperial units. The minimum required height of cladding core can then be predicted by equation (5-11) with any given blast load parameters. These blast loading parameters will be obtained from fitted curves (equations (5-12) & (5-13)) in imperial units and converted to metric

units for required cladding height calculation. Other parameters of the cladding, such as material, relative density, plateau stress and unit cell size of the TSP folded core are set the same as used in the previous sections.

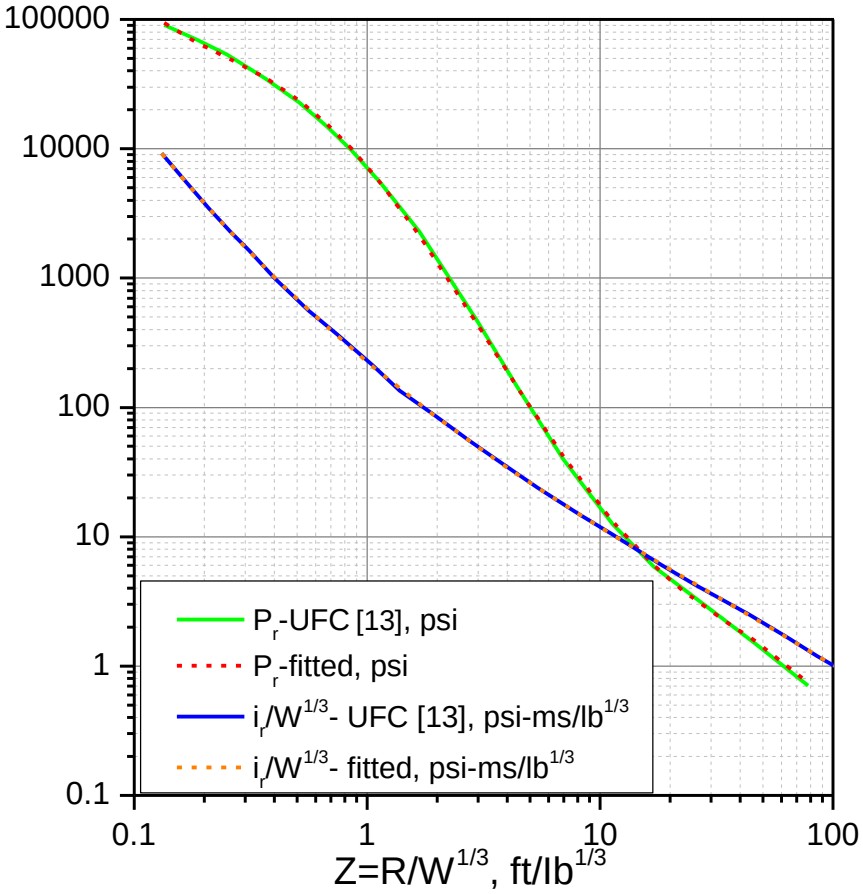

Figure 5-9. Peak reflected pressure and reflected impulse for a spherical TNT explosion in free air (31) and fitted curves; note: values are read in imperial unit from graph and converted to metric units

A total of around 1,000 calculations of required thickness with different stand-off distances and explosive weights are shown in Figure 5-10. The front plate thickness is set to be 5 mm made of aluminium with the density of 2700 kg/m^3, cladding core is set to be 5% density of TSP foldcore with a densification strain of 0.7 and a plateau stress of 1.2 MPa which is calculated from average force of TSP foldcore under 2 kg TNT explosion in Chapter 5.3.2. Such cladding with similar plateau stress has been used for blast protection for RC slab and demonstrated the effectiveness of its blast mitigation capacity (116). The scaled distance of these blast loading cases, Z, is ranged between 0.5 and 3.7 ft/lb$^{1/3}$ (0.2 to 1.46 m/kg$^{1/3}$), the stand-off distance, R, varied from 0.1 m to 30 m, and the equivalent TNT charge weight, W, is calculated accordingly. Since this proposed TSP foldcore is a layered structure, the foldcores can be stacked

by layers to achieve a larger height. The two blast parameters are manually selected so that the required height of cladding core is within practical range, varying from 10 to 200 mm (equivalent to up to five layers of this TSP foldcore) as shown in the legend in Figure 5-10. As previously investigated (8), the multi-layered TSP foldcore performs similarly or superior than single layered TSP foldcore under the same blast loading condition, if the interlayer is thick enough and harder to deform than the core.

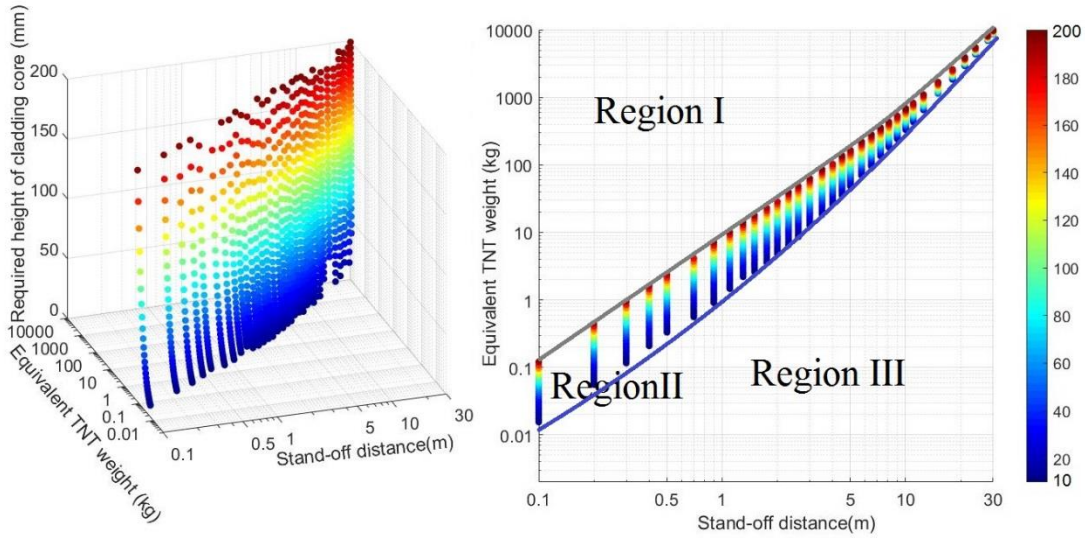

Figure 5-10. Minimum height of cladding core required at various stand-off distances and blast loads; (L) 3D plot; (R) 2D plot with regions marked out based on performance

As expected, the higher blast load or the smaller stand-off distance is, the thicker cladding core is required. The height of cladding core is determined by both blast impulse and peak blast pressure. It is worth noting that the two lines marked out Region II in Figure 5-10 (R) is roughly the boundary where this type of TSP foldcore would be effective and the region III marked in Figure 5-10 represents the area of unnecessity of the cladding with this type of TSP foldcore. In other words, under any explosion scenario with the equivalent TNT weight and stand-off distance falls in between the marked two lines (Region II), the structure behind the cladding can be effectively protected by using less than five layers of TSP foldcore. Under such scenario, the pressure transmitted to the protected structure will be greatly reduced to around the plateau stress of the cladding core as compare to the reflected peak blast pressure. For the blast scenario falling in Region III in Figure 5-10 (R), this cladding will have slight or even no deformation at all, due to the low blast pressure or low impulse. However, this current cladding configuration will not be effective and may

cause more damage to the structure behind the cladding for the explosion scenario falling in the region I shown in Figure 5-10 (R).

This chapter is based on the proposed geometries of the TSP foldcore with the relative density of 5%. Various geometries, relative densities and material configurations including foam infill can be further investigated and their mechanical properties such as plateau stress and densification strain can be obtained. These material and mechanical parameters will affect the performance and the effectiveness of the cladding. They can be used as inputs in this SDOF approach for estimating the required height of core based on the maximum allowable force transmission to the protected structure and the blast load rating during the design phase.

5.6 Summary

Blast mitigation performance of sacrificial cladding with TSP foldcore as core is evaluated and compared with square honeycomb and aluminium foam of the same density in this chapter. The TSP foldcore demonstrates a rather uniform crushing resistance and a lower initial peak crushing force under blast loading compared with square honeycomb. This results in an easier initiating of the core deformation and a more efficient blast mitigation capability. Comparing with the aluminium foam, the TSP foldcore of the same mass has a higher average crushing force and a similar consistent collapsing resistance, therefore applicable to wider range of blast intensities. It is worth noting that the thickness of TSP foldcore cell wall can be reduced in order to reduce the initial peak stress during crushing and make it more feasible to fold while maintaining similar plateau stress as aluminium foam of higher density. The cladding performance in general is strongly blast load dependent, sacrificial cladding configurations are required to be selected based on blast loading parameters. Minimum required height of sacrificial cladding core is calculated by using the SDOF analysis of the sacrificial cladding system and the parameters of free air blast from UFC (31). The height of sacrificial cladding core can be estimated based on the basic cladding material and blast parameters, which could be useful for sacrificial cladding design.

Chapter 6. Numerical study of blast mitigation performance of foam filled TSP folded structure

The related work in this chapter has been published in Structures.

Li Z, Chen W, Hao H. Numerical study of blast mitigation performance of folded structure with foam infill. Structures. 2019;20:581-93.
DOI: doi.org/10.1016/j.istruc.2019.06.012

6.1 Introduction

TSP foldcore is demonstrated effective in mitigating blast loading in Chapter 5. However, the wall thickness of TSP foldcore is limited due to the folding process, which limits further increase in density and compressive strength of the folded structure. Therefore, in this chapter, foam fillers are inserted into the TSP foldcores and their blast mitigation performances are investigated. Two shapes of filled foam, i.e. cubic and shaped rigid Polyurethane (PU) foam are considered. The foam infills provide constraints to the inclined sidewalls of TSP folded structure during the collapsing of the structure, therefore achieving the "1+1>2" effect. In other words, the foam filled TSP foldcore would have higher crushing resistance than the summation of stand-alone TSP foldcore and stand-alone foam block. Quasi-static crushing tests of foam filled TSP foldcore are carried out and the test results are used to calibrate the numerical model. Structural response of the proposed foam filled structure under different blast intensities is then simulated to evaluate its blast mitigation capacities. The responses of foam filled TSP foldcores are compared with non-foam filled TSP foldcore of the same density. Criteria such as peak load transmitted to protected structure, energy absorption and cladding centre displacement are used to evaluate the performance of the claddings with different configurations.

6.2 Quasi-static crushing tests

6.2.1 Materials

Rigid PU foam has been widely used as insulation layer or shock absorbing material for transportation packages. Performance of PU foam has been also investigated as cladding for blast loading (18), or infill of sandwich panel against impact loading (105).

PU foam has similar crushing behaviour to aluminium foam which can be divided into three regimes: elastic, plastic and densification (18, 29).

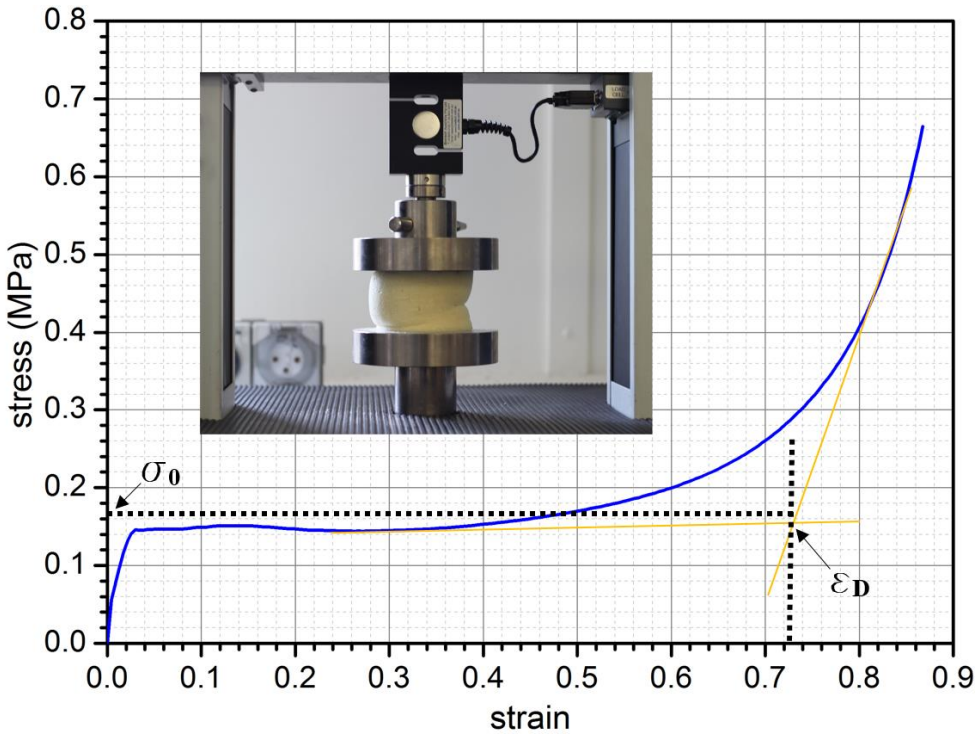

Figure 6-1. Engineering stress-strain curve of PU35, two yellow lines are the asymptotic lines which determine the densification strain ε_D at their intersection

PU foam used in this chapter has a density of 35 kg/m^3, named as PU35. Its mechanical properties are measured under quasi-static loading condition (2 mm/min, $\dot{\varepsilon}$=0.00033 s^{-1}) using Lloyd-Ametek EZ50 material testing machine. Cylindrical specimens with diameter of 100 mm and height of 100 mm are prepared for the material compression tests. The stress-strain curve is shown in Figure 6-1, where both the plateau stress σ_0 and densification strain ε_D are marked. For material properties of aluminium 1060 sheet, please refer to Chapter 4.3.1.

6.2.2 Test setup

A total of five cases are tested in this chapter including: 1) shaped foam; 2) cubic foam; 3) TSP foldcore; 4) shaped foam filled TSP foldcore; 5) cubic foam filled TSP. The dimensions of single unit cell of shaped and cubic foam are shown in Figure 6-2 (a, b), respectively. Because the sidewalls are connected via triangle interconnections, as

shown in Figure 6-2 (c), the geometry of TSP foldcore is determined by three parameters only, please refer to Chapter 4.3.

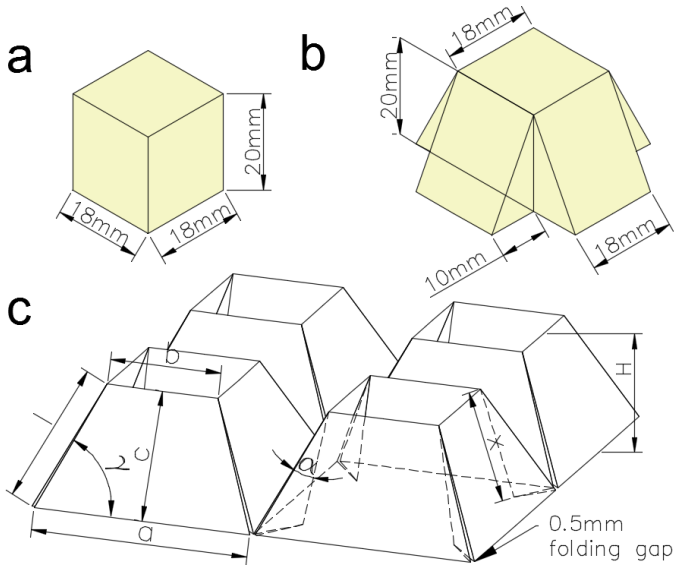

Figure 6-2. (a) dimension of cubic foam infill; (b) dimension of shaped foam infill; (c) TSP foldcore with four unit cells

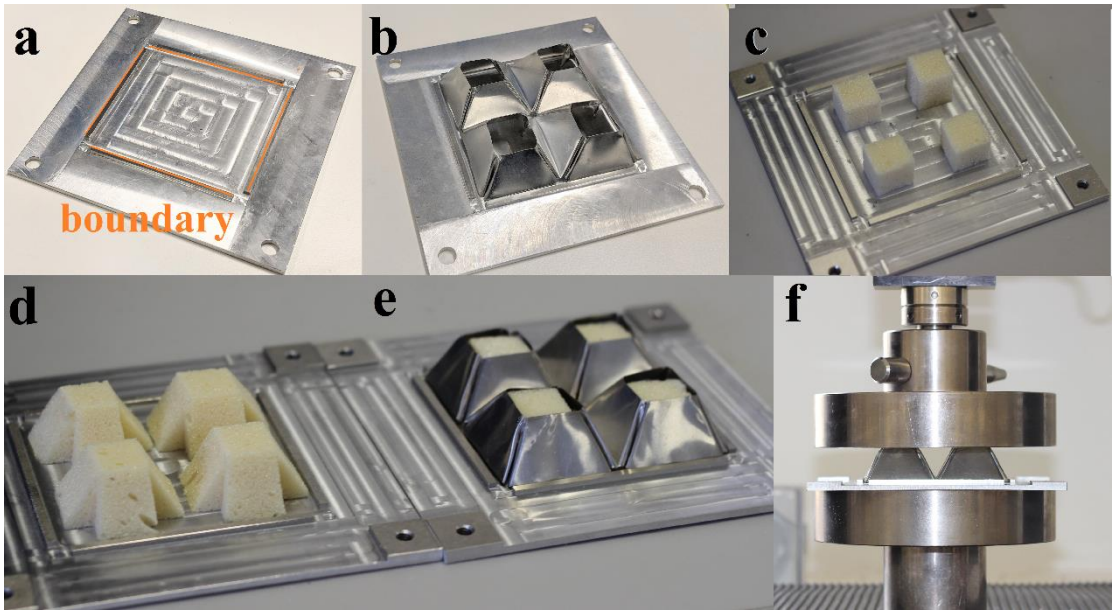

Figure 6-3. (a) steel base plate with 2 mm high boundary strip; (b) TSP foldcore without foam infill; (c) cubic foam units; (d) shaped foam units; (e) shaped foam filled TSP foldcore; (f) crushing of foldcore specimen

All specimens are crushed under quasi-static loading condition with a constant loading rate of 1mm/min ($\dot{\varepsilon}$=0.00083 s^{-1}) using Lloyd-Ametek EZ50 material testing machine. All specimens have four unit cells and the same height *H* of 20 mm. Imperfections are

inevitable at this stage as all specimens are manually folded. The designed base size of TSP foldcore is 80×80 mm whereas the actual base size of manually folded specimen is around 82×82mm, slightly larger than the designed size. To justify this handcrafting variations, three tests are carried out for each case, and the curve closest to the average is picked for analysis. It is worth noting that the variations between the specimens are between 10 to 15%, in terms of average crushing resistance. The foam and foldcore specimens are placed on a steel plate which has 2 mm high boundary strip to constrain the movement of outer bottom edges of the folded structure under lateral crushing. Neither fixing nor glue is applied between the supporting plate and the specimens. Specimens and base plate are shown in Figure 6-3.

6.2.3 Crushing tests results

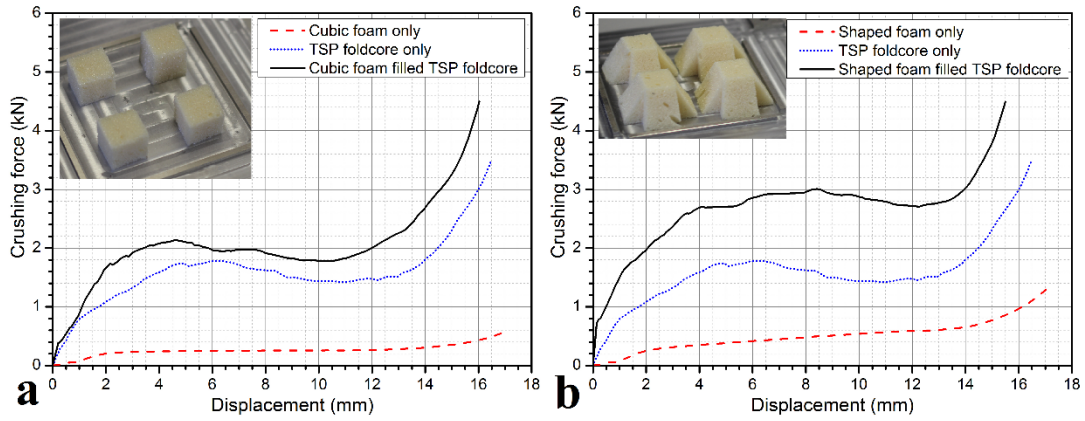

Figure 6-4. Quasi-static crushing load-displacement curves of (a) cubic foam cases; (b) shaped foam cases

The load-displacement curves of the five cases under quasi-static crushing are shown in Figure 6-4. The results are divided into two graphs as shown in Figure 6-4. One includes the cases of cubic foam, TSP foldcore and cubic foam filled foldcore. The other graph includes the cases with shaped foam, TSP foldcore and shaped foam filled foldcore. As shown in Figure 6-4 (a), the increment of crushing resistance from blue to black lines is slightly larger than the red dash line. In other words, the increase in crushing resistance TSP foldcore with cubic foam infill is larger than the crushing resistance of cubic foam itself. This is more obvious for the case with shaped foam, as shown in Figure 6-4 (b). The crushing resistance of shaped foam filled foldcore almost doubles that without foam fill, which is consistent with previous studies of foam filled tapered tubes (143, 144).

The significant enhancement in crushing resistance with foam fillers can be observed from Table 6-1 as well. The average crushing force is calculated from the zero strain to the densification strain, as given in Equation (1). Similar to Figure 6-1, the densification strain is estimated through the sudden rise in the load-displacement curve. For both cases of foam infills, the enhancements of average crushing resistance are obvious, where the cubic foam filled foldcore has an average crushing force of 1.85 kN slightly greater than 1.49 kN+0.24 kN. Shaped foam filled foldcore has an average crushing force of 2.55 kN, which is 71% higher than TSP foldcore without infill and 33% higher than the sum of the crushing resistance of the two components (1.49 kN+0.43 kN), indicating a "1+1>2" effect.

Table 6-1. Average crushing forces (P_{ave}) of five specimens

	TSP foldcore	**Cubic foam**	**Shaped foam**	**Cubic foam infilled foldcore**	**Shaped foam infilled foldcore**
P_{ave} (kN)	1.49	0.24	0.43	1.85	2.55

The significant increase in crushing resistance of light weight PU foam filled TSP foldcore is caused by the constraint effect to the foldcore sidewalls provided by the foam infill. Similar study of foam or honeycomb filled column had been conducted (98, 100, 145). It was suggested that the cause of increase in crushing resistance of foam filled single column can be divided into two parts, the direct compressive resistance of the foam infill and the constraint or interaction between foam and the column. For a single square column, the interaction between foam and column accounts for 80% of the direct compressive resistance of foam. This factor is strongly related to the geometry of the column. As given in Table 6-1, the increment of crushing resistance of cubic foam infill to TSP foldcore is 0.36 kN (1.85-1.49 kN) which is around 1.5 times the compressive resistance of cubic foam (0.24 kN). This means the interaction between cubic foam and foldcore sidewalls accounts for around 50% of the compressive resistance of the cubic foam. The effect of foam-wall interaction is more obvious for the shaped foam filled TSP foldcore. The increment of crushing resistance is 1.06 kN, around 2.47 times of the compressive resistance of shaped foam (0.43 kN), suggesting that the interaction between the shaped foam and sidewalls accounts for 147% of the compressive resistance of the shaped foam. This is because the shaped

foam has the same inclined slope as the sidewalls of TSP foldcore. As discussed in the previous study (136), for the TSP foldcore without infill under compressive loading, the top edges of each unit cell tend to bend towards the centre opening, followed by the buckling of the sidewalls,. With the shaped foam infill, the bending of the top edges and buckling of the sidewall become much harder, as the foam infill provides support to the sidewalls from inside each unit cell. Therefore, this foam greatly increases the crushing resistance of TSP foldcore without adding too much weight or alter the crushing behaviour of the TSP foldcore itself. The foam filled TSP foldcores (cubic and shaped) have ideal crushing behaviour to be used as energy absorber with uniform collapsing, low ratio of initial peak to average stress and large densification strain.

6.3 Numerical simulation for quasi-static loading

6.3.1 Numerical modelling

For the modelling of the folded structure and the base plate, please refer to Chapter 4.3.2. The numerical models of two shapes of foam infilled TSP foldcore are shown in Figure 6-5.

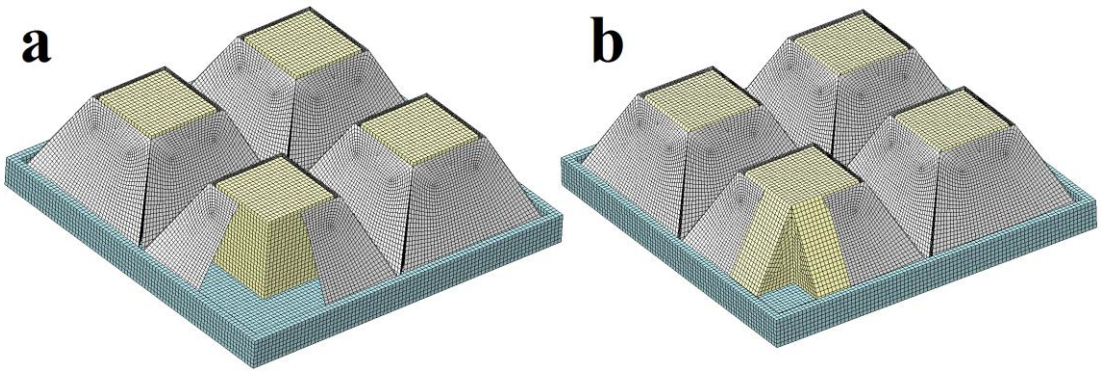

Figure 6-5. Numerical models of (a) cubic foam filled TSP foldcore; (b) shaped foam filled TSP foldcore, and the rigid base plate with outer boundary. Note a quarter of unit cell has been removed to illustrate the foam infill

The material of PU foam sheet is modelled by *MAT063 CRUSHABLE FOAM. The material parameters and mechanical properties of PU foam are given in Figure 6-1 in chapter 6.2.1. The keyword *CONTACT INTERIOR is used for PU foam to eliminate the issue of negative volume for soft material under large deformation. Mesh convergence test of foam and TSP foldcore had been conducted in previous studies (9,

136), the same element size of 0.5 mm is used for the model in this chapter. The total number of elements is around 155,000. It takes about 23 hours of CPU time for each case of the quasi-static simulation and around 3 hours for each blast loading simulation. The computer used has the configuration of 8-core Intel Xeon CPU and 32 GB of RAM.

6.3.2 Model validation

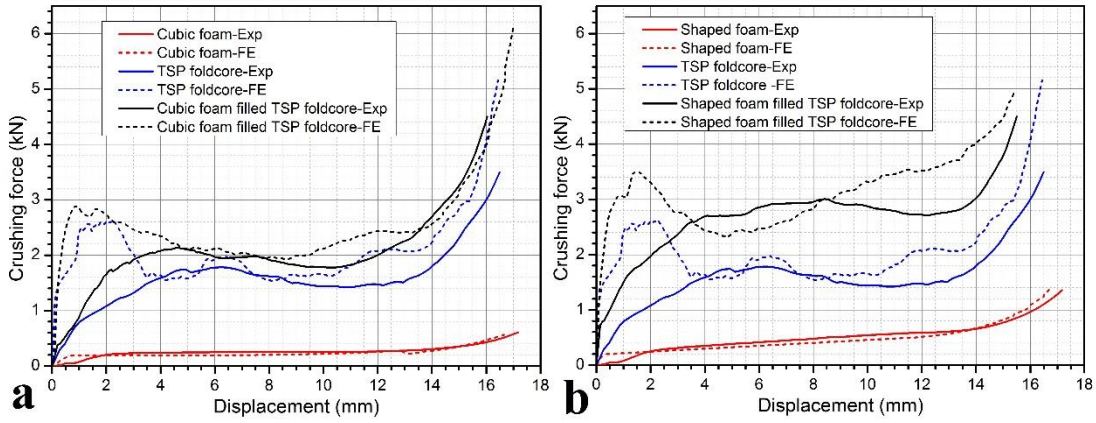

Figure 6-6. Load-displacement curves of TSP foldcore specimens with (a) cubic foam infill; (b) shaped foam infill, from both experiments (Exp) and FE simulations (FE)

Structural responses of all cases obtained from quasi-static crushing tests and finite element analysis are compared in Figure 6-6. The experimental and numerical results including initial peak crushing force, P_{peak}, average crushing force P_{ave}, uniformity ratio, U, and densification strain, $\boldsymbol{\varepsilon_D}$ are listed in Table 6-2. The densification strain is estimated using the displacement where sudden increase in crushing resistance occurs, dived by the overall height of the core. The numerical results including average crushing force and densification strain of all foldcore specimens are in good agreement with the experimental data. However, large discrepancies of initial peak force ($\boldsymbol{P_{peak}}$) between numerical simulation and tests are observed. This initial differences of crushing resistance are caused by the inevitable imperfection, as all the foldcore specimens were prepared manually. As shown in Figure 6-3, slight gaps and uneven level of the TSP foldcore unit cell exist. The top surface may not be perfectly at the same level. During the test, the top surface of foam or top edges of TSP foldcore are not perfectly in contact with the top loading plate at the same time. The higher part of the foldcore is in contact with the crushing plate and deforms firstly which led to a smaller initial stiffness of the foldcore and smaller crushing force than FE results. The

numerical results matches well with the testing results after the entire core is in contact with the top crushing plate. Similar discrepancy in initial crushing stress between FE and test results has been reported in the hand-folded structure owing to the same reason (87). A machine pressed Miura-type foldcore using forming dies also showed a lower initial peak stress than FE result (81) owing to imperfect manufacturing.

Table 6-2. Key parameters from experiments (Exp) and FE simulations (FE)

Specimens		P_{peak} (kN)	P_{ave} (kN)	$U= P_{peak} / P_{ave}$	ε_D
TSP foldcore	Exp	1.78	1.49	1.19	0.70
	FE	2.59	1.83	1.42	0.71
Cubic foam	Exp	0.20	0.24	0.83	0.75
	FE	0.20	0.21	0.95	0.72
Shaped foam	Exp	0.26	0.43	0.60	0.73
	FE	0.25	0.39	0.64	0.72
Cubic foam filled TSP foldcore	Exp	2.14	1.85	1.16	0.70
	FE	2.89	2.27	1.27	0.71
Shaped foam filled TSP foldcore	Exp	3.01	2.55	1.18	0.71
	FE	3.50	3.04	1.15	0.72

Damage mode of the shaped foam filled TSP foldcore from numerical simulation and test is shown in Figure 6-7. Similar damage mode can be observed. The sidewalls bend towards the centre of unit cell. The sidewalls on the outer edges of the specimen buckle toward outside of the plate (marked as 1), where some face buckling along the interconnections between sidewalls are presented (marked as 2). The inner faces that connected to other unit cells also buckle toward the centre of unit cell as circled (marked as 3). However, comparing to the numerical results, the damage mode of the crushed specimen from testing is less symmetric and the damage is more randomly distributed.

Overall, the numerical results are in good agreement with the test results as similar values for average crushing force and densification strain are obtained for all cases. The objective of this chapter is to investigate the effect of foam infill on the blast resistant performance of the TSP foldcore as sacrificial cladding. Due to the perfect geometry of the foldcore in the numerical model, numerical results overestimate the initial stiffness of the structure and thereby overestimate the initial peak stress

comparing to the test results. The higher value of initial peak force leads to a larger peak load transmitted to the protected structure when used as sacrificial cladding under blast loading. Therefore, the numerical model provides a slightly conservative prediction for the foldcore as sacrificial cladding.

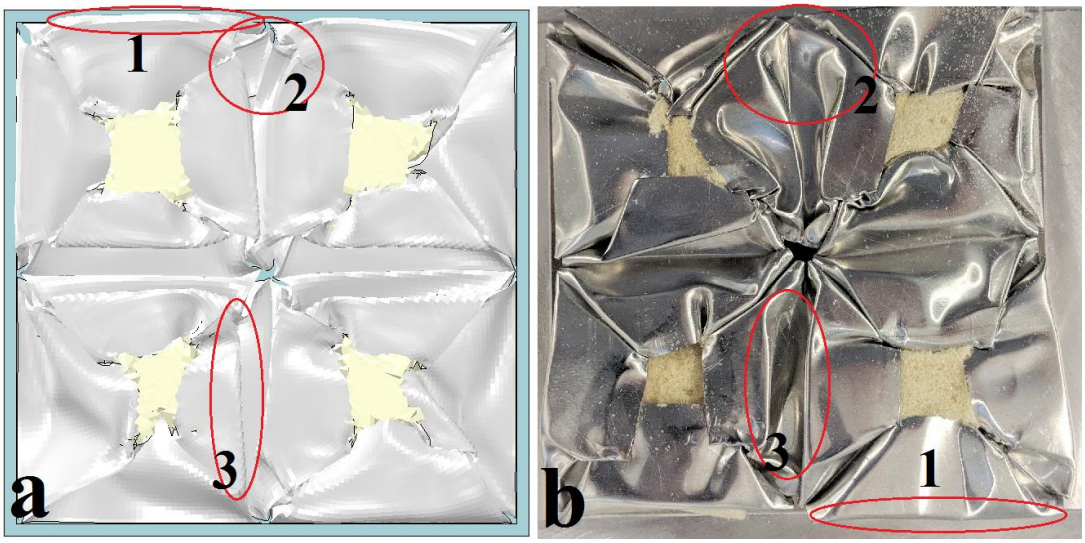

Figure 6-7. Damage mode of shaped foam filled TSP foldcore (a) FE; (b) experiment

6.3.3 Damage mode comparison

As shown in the chapter 6.3.2, the foam filled TSP foldcores demonstrate higher average crushing resistance than the sum of the crushing resistance of two components. The damage modes of three specimens are compared and discussed in this section to explain this observation. Damage modes of three different TSP foldcores at crushed distance of 10 mm (i.e. 0.5 strain) are shown in Figure 6-8 (a-c) respectively. For the TSP foldcore without foam infill as shown in Figure 6-8 (a), the sidewalls around outer boundary bend vertically towards unit cell centre (as circled and marked as 1), other deformations such as corner lift-up and buckling along the intersection of faces can also be observed. For cubic foam filled foldcore, shown in Figure 6-8 (b), the damage mode of the foldcore is similar to that without foam. Due to the presence of the foam, the sidewalls experience higher resistance on inward bending, resulting in a slight increase in the lateral crushing resistance of the cubic foam infilled foldcore.

With the shaped foam infill, the damage mode is quite different from the other two cases. In the numerical results as shown in Figure 6-8 (c), some sidewalls on the outer edges are no longer bending vertically towards centre. For instance, the right side of

the sidewalls in Figure 6-8 (c) bends horizontally near the middle plane towards the outer boundary, while the top edge of these sidewalls rolls towards centre of each unit cell (as circled and marked as 2). This is because the sidewalls of the foldcore and the shaped foam have the same inclined angle. Under lateral crushing, the inward vertical bending (marked as 1) of TSP foldcore sidewalls is much harder to occur due to resistance from the shaped foam. With the bottom edges of foldcore sidewalls constrained by strips on base plate, the sidewalls bend horizontally at middle height. The insertion of shaped foam greatly increases the crushing resistance of the TSP foldcore. It provides extra support to the sidewalls of TSP foldcore under lateral crushing which greatly increases the force required for the sidewalls to deform towards centre of unit cell. In the quasi-static crushing tests, similar change of deformation mode can be observed from inward vertical bending (marked as 1) for foldcore without foam to horizontal bending (marked as 2) for shaped foam filled foldcore, as shown in Figure 6-8 (d) & (e).

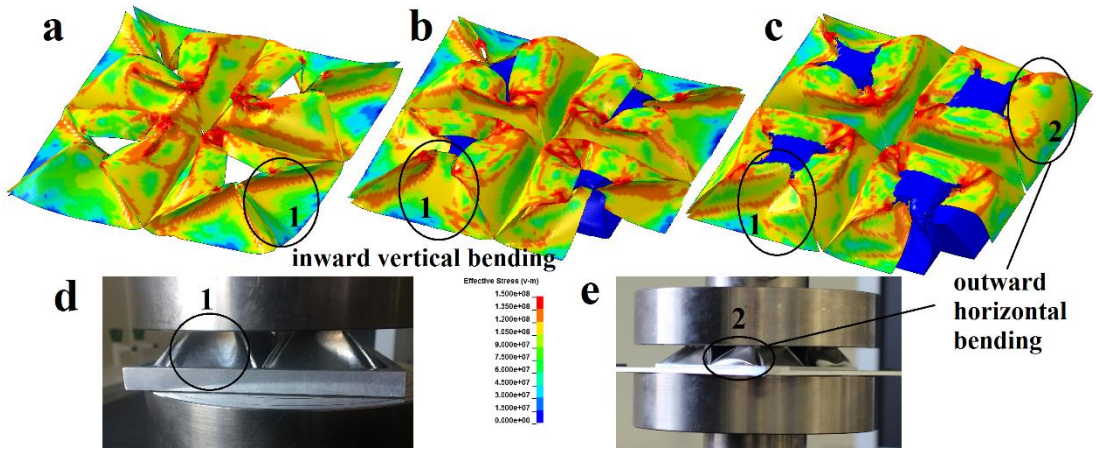

Figure 6-8. Damage modes of specimens at 10 mm crushed distance (i.e. strain of 0.5) (a) FE results of TSP foldcore; (b) FE results of cubic foam filled foldcore; (c) FE results of shaped foam filled foldcore (d) crushing test of TSP foldcore without foam infill; (e) crushing test of shaped foam filled TSP foldcore; Note: d and e are not at the same crushed distance

6.4 Blast mitigation capability of foam infilled TSP foldcore

6.4.1 Sacrificial cladding set up

As previously studied, sacrificial cladding with TSP foldcore as core outperforms conventional honeycomb, Miura-type foldcore and aluminium foam of similar density

in terms of blast mitigation capability (9, 10). This finite element analysis study is aimed to evaluate blast mitigation capability of foam filled TSP foldcore are considered. Four cladding configurations: no cladding, TSP foldcore without foam infill, cubic foam filled TSP foldcore and shaped foam filled TSP foldcore. The dimensions of unit cell of the TSP foldcore including the foam infill are doubled with respect to the quasi-static case to have a more practical height of 40 mm as sacrificial cladding. The dimension of TSP foldcore unit cell is scaled from 40×40×20 mm to 80×80×40 mm for the blast cladding simulation. The same boundary conditions are applied for the cladding simulation. No glue nor fixing is applied between the front plate, core and the base plate. The base plate is set as rigid plate with a 2 mm-high boundary around the outer edges of the base plate to constrain the in-plane movement of the foldcore sidewalls.

Table 6-3. Mass distribution of four cladding core configurations with average core density of 100 kg/m^3

Parameter	TSP foldcore	Cubic foam filled TSP foldcore	Shaped foam filled TSP foldcore
Wall thickness (mm)	0.708	0.658	0.604
Mass of foam (g)	-	7.3	15.1
Mass of foldcore (g)	102.4	95.1	87.3
Average core density (kg/m^3)	100	100	100

In the numerical model, mechanical properties for both PU foam and aluminium remain unchanged. The densities and overall masses of three foldcore configurations are kept the same by varying the wall thickness of TSP foldcore. Masses of these cladding cores are listed in Table 6-3, where the average core density of the core is kept constant as 100 kg/m^3. This density is approximately equal to 3.7% relative density of aluminium foam, which is a common material used as core of sacrificial cladding (7, 35, 116). However, this density of 3.7% used in the chapter is lower than that of aluminium foam which has the minimum relative density of 5% available on the market (139). The top skin of the cladding made of aluminium 1060 is set as 160×160×5 mm for all four cladding configurations. The front plate is constructed with solid element in LS-DYNA. It is worth noting that Aluminium has an insignificant strain rate effect (65), and the PU foam also has low strain-rate sensitivity

especially under higher strain rate (e.g. 2000 s^{-1}) (20). Therefore, the strain rate effect is not considered in the numerical analysis.

The keyword *LOAD BLAST ENHANCED is used to generate blast loading in LS-DYNA. Different blast intensities are considered by varying the explosive weight. The stand-off distance is set at 1500 mm above the centre of the cladding front plate which is in accordance with the previous field-testing for sacrificial claddings (115, 116). For the structure without sacrificial cladding, the stand-off distance is 1545 mm, as the cladding has a height of 40 mm plus the 5 mm-thick front plate.

6.4.2 Structural response

6.4.2.1 Transmitted force

Table 6-4. Peak transmitted force, peak crushed distance at centre and energy absorption by parts of different cladding configurations under various blast intensities

Cladding types		P_{peak} (kN)	Peak crushed distance at centre δ (mm)	Energy absorption (J)	
				by TSP foldcore	by foam
1 kg TNT 1.5 m/kg$^{1/3}$	**No cladding**	34.3	-	-	-
	TSP foldcore	33.9	1.6	37	-
	Cubic foam filled	25.7	2.3	35	2
	Shaped foam filled	32.3	2.7	40	3
2 kg TNT 1.19 m/kg$^{1/3}$	**No cladding**	67.1	-	-	-
	TSP foldcore	38.5	9.1	147	-
	Cubic foam filled	35.0	9.2	141	8
	Shaped foam filled	37.7	10.0	148	15
4 kg TNT 0.95 m/kg$^{1/3}$	**No cladding**	132.1	-	-	-
	TSP foldcore	39.2	22.2	567	-
	Cubic foam filled	36.0	24.5	555	25
	Shaped foam filled	31.4	27.8	540	65

The blast intensities from the detonation of 1, 2 and 4 kg of TNT explosion are considered. The time history curves of transmitted force to the base structure with different cladding configurations are shown in Figure 6-9 to Figure 6-12. Other parameters are given in Table 6-4. The transmitted load-time history curves are obtained from FE result by plotting the reaction forces exerted on base plate of

structure. The purpose of using sacrificial cladding is to mitigate blast pressure and reduce the force transmitted to the protected structure. Under blast loading, the front plate moves toward the protected structure and crushes the core of sacrificial cladding. The crushing strength of cladding core is usually much lower than the peak blast pressure, thus reduces the force transmitted during the deformation of the core. Hence, these time-history curves of transmitted force to base structure are used to evaluate the performances and the peak transmitted load to protected structure is selected as the main criterion for the evaluation.

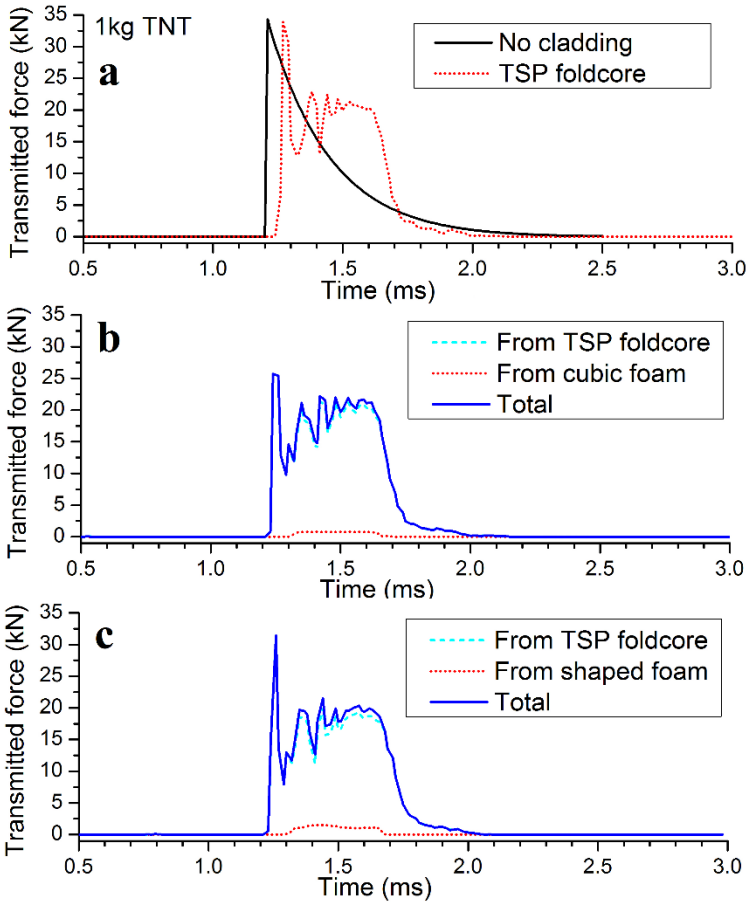

Figure 6-9. Computed time-history of transmitted forces to protected structure under 1kg TNT explosion at 1.5 m stand-off distance of four cladding configurations (a) no cladding and TSP foldcore without foam infill; (b) cubic foam filled TSP foldcore; (c) shaped foam filled TSP foldcore

As can be observed in Figure 6-9, the peak value of force transmitted to the base structure from TSP foldcore is similar to the case without cladding under 1 kg TNT explosion weight. By using two types of foam filled TSP foldcores as cladding, the peak transmitted force slightly reduces, while the peak crushed distance at panel center

increases slightly. Similar responses can be observed for these three cladding configurations (TSP foldcore, cubic and shaped foam filled TSP foldcores). The transmitted force history curves start with an initial peak and sudden reduction, followed by a more consistent plateau stage and gradual reduction to zero.

The results shown in Figure 6-9 indicate that the three types of TSP foldcores have insignificant mitigation capability on the protected structure under this blast intensity, which is too low for cladding to effectively mitigate shock waves. As previously studied (9, 35), each cladding system is only effective under certain blast scenarios. For the case of 1 kg TNT explosion at 1.5 m stand-off distance considered here, these cladding cores have very little deformation due to the low blast pressure comparing to the collapsing stress of the cladding core. Limited energy is absorbed in this process, thus resulting in a less effective blast mitigation performance of these claddings.

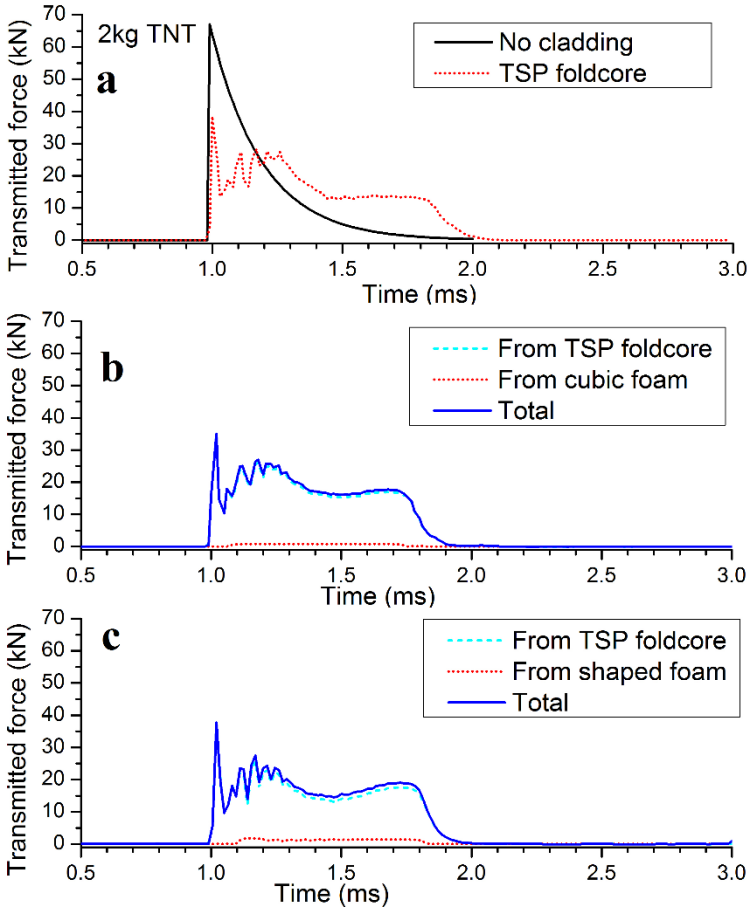

Figure 6-10. Computed time-history of transmitted forces to protected structure under 2kg TNT explosion at 1.5m stand-off distance of four cladding configurations (a) no cladding and TSP foldcore without foam infill; (b) cubic foam filled TSP foldcore; (c) shaped foam filled TSP foldcore

The time-history curves of the transmitted force under 2 kg TNT explosion are shown in Figure 6-10. Comparing to the unprotected structure, the peak transmitted force is reduced by 42.6%, 47.8% and 45.8% for TSP foldcore without foam infill, cubic and shaped foam filled TSP foldcores, respectively. Similar to the 1kg TNT explosion, the peak transmitted force of TSP foldcore is slightly higher than that of the shaped foam filled TSP, followed by the cubic foam filled TSP. However, during the later stage of crushing, slight rise in transmitted force can be observed for the shaped foam filled TSP foldcore between 1.5 and 2 ms (Figure 6-10 c), which indicates the increase of crushing resistance due to the compacting of the foam at the later stage of deformation. Very little increase can be observed from the cubic foam filled cladding (Figure 6-10 b) and the cladding without foam infill (Figure 6-10 a) from 1.5 to 2 ms.

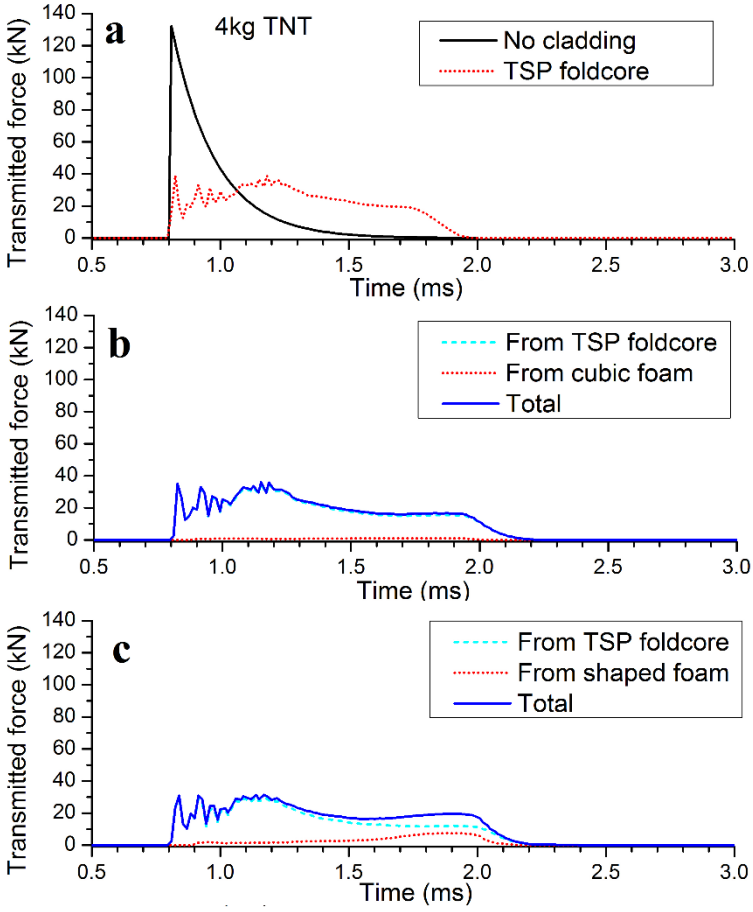

Figure 6-11. Computed time-history of transmitted forces to protected structure under 4kg TNT explosion at 1.5m stand-off distance of four cladding configurations (a) no cladding and TSP foldcore without foam infill; (b) cubic foam filled TSP foldcore; (c) shaped foam filled TSP foldcore

The results from the scenario of 4kg TNT explosion is shown in Figure 6-11. Compared to the case of unprotected structure, the peak transmitted force is reduced by 70.3%, 72.7% and 74.8% using TSP foldcore cladding without foam infill, cubic and shaped foam filled TSP foldcores as cladding, respectively. Good blast mitigation capabilities are demonstrated for all the three cladding configurations. The peak transmitted force to protected structure remains similar in value with the increasing blast intensities (1, 2 and 4kg TNT) as shown in Figure 6-9 to Figure 6-11. Low uniformity ratio, which is the ratio between peak force and average force, is also shown for all three cladding configurations. It is worth noting that loading duration under 4 kg TNT explosion is not the same for these three claddings. The foam filled TSP foldcore shows longer loading duration starting from 0.8 ms to 2.1 ms (Figure 6-11 b&c). For the foldcore without foam infill, the loading finishes at around 1.9 ms, which leads to slightly less energy absorption.

As previously studied, TSP foldcore without foam infill demonstrated superior blast mitigation capability over conventional square honeycomb and aluminium foam of the same weight (9). The performances of foam filled TSP foldcore, however, show no significant difference with the non-foam filled case. The foam filled TSP foldcores including cubic and shaped foams have a lower peak transmitted force but a slightly larger peak crushed distance compared to the TSP foldcore without foam infill of the same mass. This indicates that under blast loading, the cubic and shaped foam infilled TSP foldcores are slightly easier to deform as compared with the TSP foldcore without infill which has slightly thicker walls (i.e. 0.708 mm). This slightly lower value of initial peak transmitted force of foam filled TSP foldcore is caused by the difference in wall thickness, as given in Table 6-3. The initial peak force of TSP foldcore is strongly correlated to the thickness of the vertical triangular interconnections between sidewalls. It was found that the initial peak crushing force of honeycomb structure had a power relationship with the wall thickness (13). Slight increase in wall thickness may lead to a significant increase in initial peak force for these cellular structures with vertical faces, such as this TSP foldcore.

It can be concluded that the shaped and cubic foam infilled foldcores have slightly better performance in mitigating the peak blast loading transmitted to protected structure than the foldcore without any foam infill when the blast intensities are sufficiently large. The foam filled TSP foldcore can further reduce the peak force

transmitted to the protected structure, and the peak centre crushed distance is larger as compared to the case without foam infill, implying more energy dissipation. However, when the blast intensities are small, the blast mitigation performance of three foldcores (TSP foldcore, cubic and shaped foam filled TSP foldcores) are similar in terms of peak transmitted force to the protected structure. As mentioned previously, this is because of limited plastic deformation of the cladding core under low intensity of explosion. It is also worth mentioning that due to the conservation of momentum, the duration of the loading transferring to protected structure is proportional to the reduction in peak stress level, and the impulse transmitted is not necessarily reduced. The global response of the structure may not be affected with this added sacrificial cladding. The sacrificial cladding act as a local protective structure to mitigate local damage caused by the high peak pressure. Similar results have been observed in the previous studies of aluminium foam and PU foam as sacrificial cladding for structure (7, 18).

6.4.2.2 Damage mode

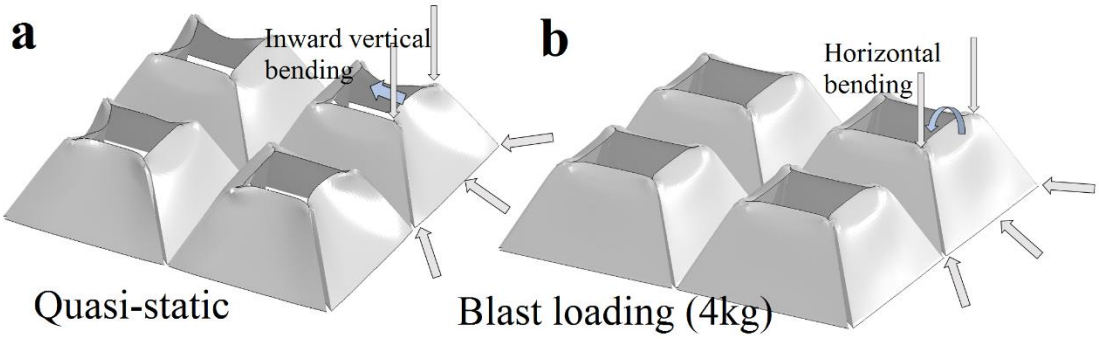

Figure 6-12. Comparison of computed damage mode of TSP foldcore without foam under (a) Quasi-static crushing; (b) Blast loading of 4 kg TNT explosion

The damage modes of these TSP foldcores with three foam configurations are very different from those under quasi-static loading. The comparison of computed deformation of TSP foldcore without foam under two different loading conditions is shown in Figure 6-12. The inward vertical bending of the sidewall under quasi-static loading changes to the top edge horizontal bending of the sidewalls under dynamic loading. This change in deformation mode is caused by the inertia effect and the inertial stabilization effect of the lower part of the sidewall under higher crushing speed, as explained in the previous study (146). As shown in Chapter 6.3.3, under

quasi-static loading, the damage modes are different for all three configurations of the foldcores, resulting in different crushing resistances among the three foldcores. However, under blast loading with 1, 2 and 4 kg TNT blast scenarios, the performances of these claddings including peak transmitted force and energy absorption are similar owing to the similar damage mode under dynamic loading.

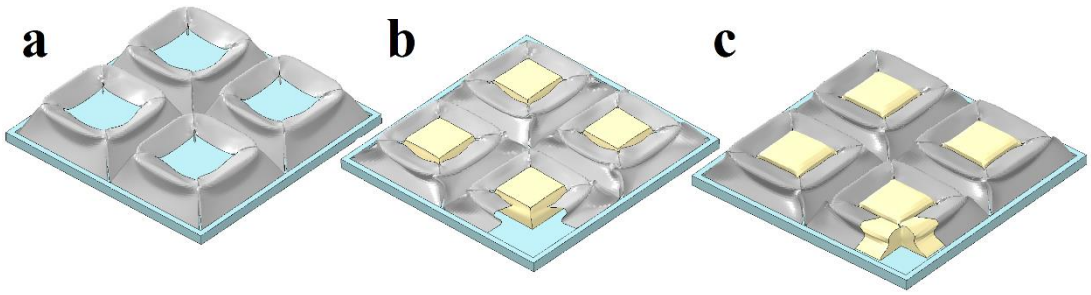

Figure 6-13. Cladding core computed deformation of (a) TSP foldcore; (b) cubic foam filled; (c) shaped foam filled, at the maximum displacement under 4 kg TNT explosion at 1.5m stand-off distance; Note the front plate is removed for illustration

The computed damage modes of three cladding configurations, i.e., TSP foldcore, cubic foam filled and shaped foam filled TSP foldcore are shown in Figure 6-13. The vertical mid-plane cross-section views at early and later stages during deformation under both loading conditions are shown in Figure 6-14. Similar change of deformation mode of TSP foldcore without foam infill was observed as in the previous study (146) under different loading rates. As shown in Figure 6-14, the deformation modes under blast loading are almost identical for the three foldcore configurations despite different foam geometries. The top edges of the TSP foldcore bend towards centre opening, and the sidewalls buckle along the horizontal middle line of each sidewall face which is different from the quasi-static damage mode shown in Figure 6-8 and Figure 6-14 (a, c). The cubic foam is not in contact with sidewall and provides no support to the foldcore at the early stage of deformation, as can be seen in Figure 6-14 (b). Under quasi-static loading, the shaped foam is in full contact with the sidewalls of TSP foldcore and provides support to the sidewalls since the starting of the deformation as shown in Figure 6-14 (c, e). This is caused by the inward vertical bending of the sidewalls. However, under dynamic loading, the deformation is more locally distributed along the top edges of the sidewalls therefore resulting in only partial contact to the foam, as in Figure 6-14 (d, f). Due to the change of deformation

mode of the sidewalls under dynamic loading, shaped foam only provides support to sidewalls at the later stage of the deformation when sidewalls buckle and are in full contact with the foam infill, as shown in Figure 6-14 (c, d). Similarly, under lower blast intensities where the deformation is small and the sidewalls are not in full contact with the foam, the foam infill provides little support to the sidewalls and thus leads to less effectiveness of the foam infill.

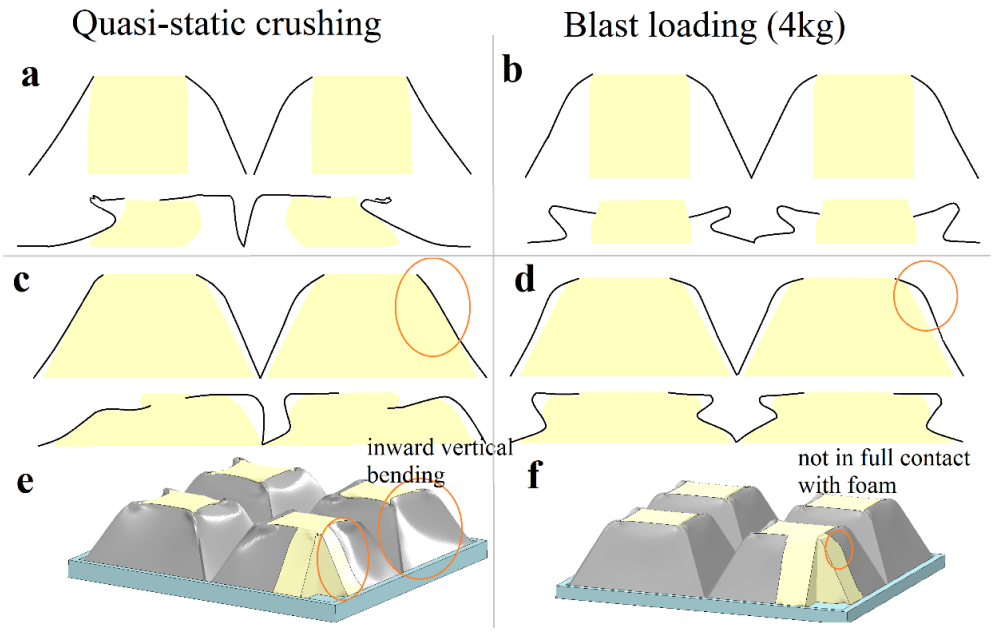

Figure 6-14. Mid plane cross-section view of the TSP foldcores with (a, b) cubic and (c, d) shaped foam infill at the early and later stages of computed deformation under two loading conditions; (e, f) damage modes of shaped foam filled TSP foldcore at the early stage under two loading conditions

The effect of the foam-wall interaction at later stage can also be confirmed in the transmitted force time-history curves as shown in Figure 6-10 and Figure 6-11, where the shaped foam infilled TSP foldcore shows higher transmitted force than the other two configurations at the later stage of the loading, i.e. from 1.5 to 2.0 ms. At later stage of the deformation, the foldcore sidewalls buckled and come in full contact with the shaped foam which provides extra support. Therefore, the noticeable difference in initial peak force is mostly caused by the wall thickness of the TSP foldcores rather than by the foam infills.

6.4.2.3 Energy absorption

Specific energy absorption (SEA) of the components including the TSP foldcore and the foam infills are shown in Figure 6-15 for three cladding configurations and blast intensities. Significant increase of SEA along with the increasing blast load can be observed for all components of three cladding cases. It can be found that the TSP foldcore has a higher SEA than the foam infill under any blast intensity. This is due to the material difference between PU foam and aluminium.

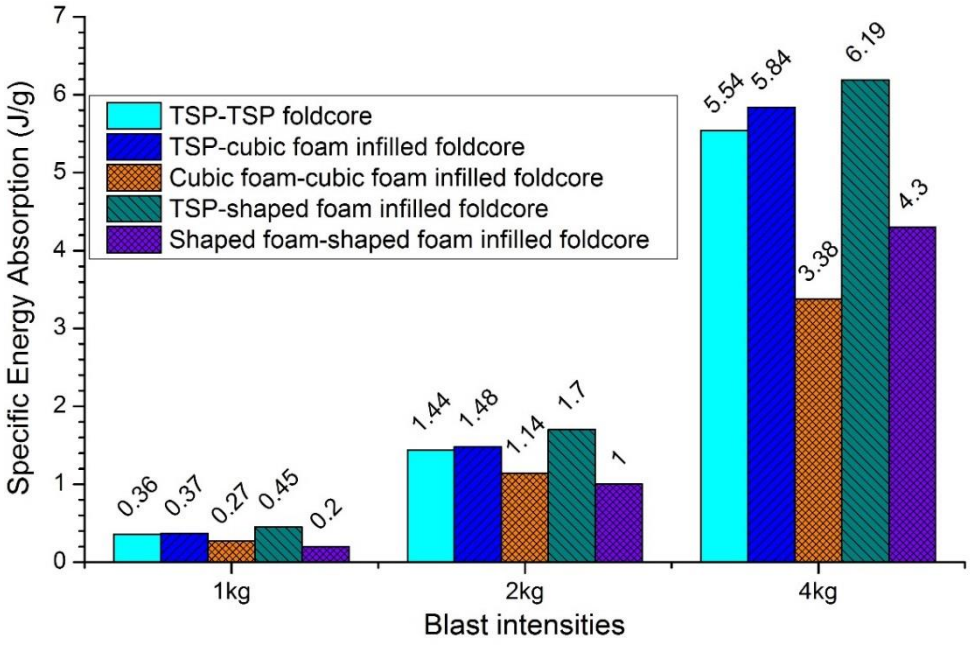

Figure 6-15. Specific energy absorption (SEA) of different parts of three cladding configurations under different blast intensities

The SEA of shaped foam is lower than that of cubic foam under 1, 2 kg TNT explosion, and higher than that of cubic foam under 4 kg TNT explosion. This can be explained by the geometry of the foam infill. Under lower blast intensity, only the top part of shaped foam deforms during the process and the sidewalls are not in full contact with the foam, therefore foam provides little support to the sidewalls as shown in Chapter 6.4.2.2. With higher blast intensity, the larger portion of the shaped foam is deformed. Because of its increasing cross-section area from top to bottom, higher crushing resistance of shaped foam at the later stage of the deformation can be observed as shown in Figure 6-11. Furthermore, the SEA of TSP foldcore increases when the shaped foam is inserted. Due to the buckling of the sidewalls at the later stage of the deformation, extra support is provided to the foldcore sidewalls by the shaped foam,

which increases the crushing resistance of the TSP foldcore at the later stage. Therefore, SEA of shaped foam filled foldcore is higher than that of the other two cases under intensive blast load, where larger deformation occurs.

6.4.3 Influence of density

Table 6-5. Mass distribution of three cladding core configurations with average core density of 150 kg/m^3

Configuration	TSP foldcore	Cubic foam infilled TSP foldcore	Shaped foam infilled TSP foldcore
Wall thickness (mm)	1.062	1.011	0.958
Mass of foam (g)	-	7.3	15.1
Mass of foldcore (g)	153.6	146.3	138.5
Density of core (kg/m^3)	150	150	150

In this section, claddings with average core density of 150 kg/m^3 are simulated under 7kg TNT explosion at 1.5m stand-off distance. This is to match the minimum density of one of the most common cladding core materials, i.e. 150 kg/m^3 aluminium foam with 5% relative density (139). Furthermore, the initial peak crushing force is in power relationship with wall thickness for cellular structures. The effect of wall thickness of the TSP foldcore on the initial peak force is greatly reduced with higher average core density of the core, and the effect of foam infill is more obvious. Given the overall core density of 100 kg/m^3 same as the previous section, the wall thickness of TSP foldcore has a difference of 17.2% between the cladding without foam and the cladding with shaped foam infill. This difference reduces to 8.9% for the core density of 150 kg/m^3. Only overall core density and the blast loading are changed in this section, other parameters and boundary conditions are kept the same as in the previous sections. The configurations of three cladding cores are given in Table 6-5.

Structural responses of the three claddings and the case with no cladding are listed in Table 6-6 and the transmitted force time-history curves are shown in Figure 6-16. The peak value of the transmitted force to the protected structure is very different for three configurations of claddings. The peak force is reduced by 50.8% for the cladding with TSP foldcore as compared to the unprotected case. For the two cases with foam infill, the peak transmitted force is reduced by 69.6% and 71.1% for the cubic and shaped foam filled foldcores, respectively. This difference in initial peak force is mainly caused by the variation of sidewall thickness. The cellular structure with thicker wall

greatly increases the peak crushing force and greatly affects their crushing behaviours under dynamic loading due to the increasing inertia effect and the stabilization effect provided by the adjacent connecting faces (17).

Table 6-6. Peak transmitted force, peak crushed distance at centre and energy absorption by parts of different cladding configurations under 7 kg TNT explosion at 1.5 m stand-off distance

Cladding types	P_{peak} (kN)	Peak crushed distance at centre δ (mm)	Energy absorption (J)	
			by TSP foldcore	by foam
Without cladding	213.5	-	-	-
TSP foldcore	105.0	25.3	1328	-
Cubic foam filled	64.9	27.3	1253	32
Shaped foam filled	61.6	29.6	1241	98

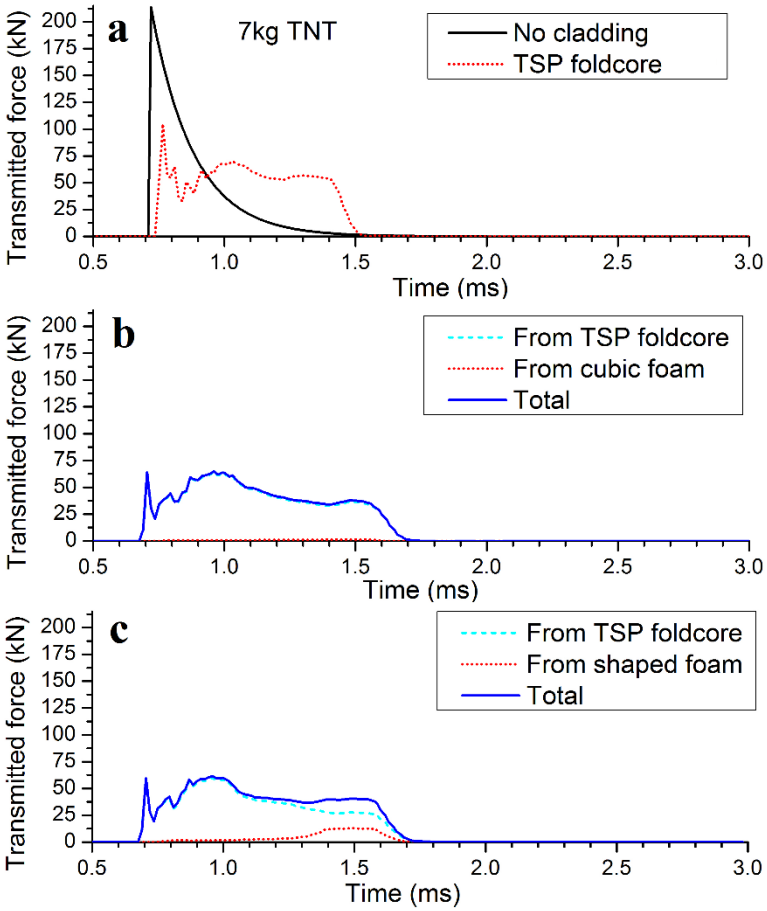

Figure 6-16. Computed time-history of transmitted forces to protected structure under 4kg TNT explosion at 1.5 m stand-off distance of four cladding configurations (a) no cladding and TSP foldcore without foam infill; (b) cubic foam filled TSP foldcore; (c) shaped foam filled TSP foldcore

Furthermore, a prolonged force-transmitting phase can be observed for the foam filled TSP foldcore as cladding. The force transmitting to the protected structure stops at around 1.5 ms for the cladding with TSP foldcore and 1.7 ms for the claddings with cubic and shaped foam filled TSP foldcore. The time-history curves of cubic foam and shaped foam infilled TSP foldcores are almost identical at the early stage of the loading (less than 1 ms). As explained previously, the deformation mode of the TSP foldcore under blast loading is different from that crushed under quasi-static loading. The top edges of the foldcore sidewalls bend towards unit cell centre under high loading rate, followed by the middle face buckling of the sidewalls. Therefore, the shaped foam infill provides little support to the sidewall at the early stage of the deformation under dynamic loading. However, slight crushing resistance increase is shown in the later stage of deformation (after 1.3 ms) for the shaped foam infilled TSP foldcore. This is caused by the support provided by the shaped foam to the buckled sidewalls, which is similar to the scenario shown in Figure 6-13 and Figure 6-14.

A great reduction in transmitted force is demonstrated for foam filled foldcores in this section (i.e. 7 kg TNT blast scenario). A further 41% reduction for shaped foam filled TSP foldcore is achieved comparing to the foldcore with foam infill. However, in the previous section (i.e. 1, 2, 4 kg TNT blast scenarios), the peak force reduction with three cladding configurations are similar. As higher overall core density is required for mitigation of higher blast loading (7 kg TNT blast), wall thickness increases for the case without foam infill which lead to increase in initial peak crushing resistance. This indicates that the foam infill is more effective than simply increasing the wall thickness of the foldcores to mitigate blast loading of higher intensity. In other words, to increase the blast mitigation capacity, the crushing resistance of cladding shall be increased which can be achieved by either thickening sidewall of foldcore or inserting lightweight foam. Foam insertion shows superior peak transmitted force reduction than using thicker wall of foldcore when experiencing higher intensity of blast loading.

6.5 Summary

The crushing behaviour under quasi-static loading condition and the blast mitigation capacity of foam filled TSP foldcore are examined in this chapter. Under quasi-static crushing, significant increase in crushing resistance of shaped foam filled TSP foldcore is observed, due to extra support provided by the foam to the foldcore

sidewalls. Experimental results show that under quasi-static loading, the crushing resistance of shaped foam filled TSP foldcore is higher than the summation of two stand-alone components, indicating an effect of "1+1>2". A numerical model is developed and verified against the quasi-static test. The calibrated numerical model is then used for the simulation of sacrificial cladding under various blast intensities. Significant reductions in peak transmitted force are observed for all claddings. The global damage may not be greatly reduced due to the mechanism of the sacrificial cladding (7, 35), as the total impulse transmitted on the protected structure is not greatly affected by the cladding configurations. The added cladding acts as a protective structure to reduce the local damage on the structure, which is often caused by the high peak pressure in the event of blast.

Unlike quasi-static crushing test, both foam infilled (cubic and shaped) TSP foldcores show similar blast mitigation capability as the TSP foldcore without foam infill under lower blast intensities (i.e. 1, 2, 4 kg TNT). This is because of the change of the deformation mode under blast loading as compared to quasi-static crushing. The shaped foam provides little support to the sidewalls during the early bending of the top edges of foldcore towards the center under blast loading. The crushing resistance has a slight rise at the later stage of the crushing due to compacting of the foam and the buckling at middle of sidewalls. It is also worth noting that under dynamic loading, shaped foam infill is more effective at the later stage of the foldcore deformation. The constraint provided to the TSP foldcore sidewalls by the shaped foam infill becomes active only when they are in contact with the foldcore at the later stage of deformation. Furthermore, the foldcore of higher density is studied under higher blast intensity (i.e. 7 kg TNT blast). It shows that both foam filled foldcores have much lower initial peak force transmitted to the protected structure as compared to the foldcore without foam infill, and the foam filled TSP foldcore experiences slightly larger peak centre displacement. Therefore, to withstand blast load of higher intensity, PU foam can be inserted inside the foldcore and it is more effective than simply increasing the wall thickness by yielding a much greater reduction in peak transmitted force to protected structure.

Chapter 7. Experimental study of multi-layer folded truncated structures under dynamic crushing

The related work in this chapter has been published in International Journal of Impact Engineering.

Li Z, Chen W, Hao H, Cui J, Shi Y. Experimental study of multi-layer folded truncated structures under dynamic crushing. International Journal of Impact Engineering. 2019;131:111-22. DOI: doi.org/10.1016/j.ijimpeng.2019.05.010

7.1 Introduction

In Chapter 3 to 6, Open-top Truncated Square Pyramid (TSP) folded kirigami structure with interconnected sidewalls is proposed and investigated. Its crushing behaviours under quasi-static and dynamic crushing are numerically studied and compared with the existing cube-strip kirigami foldcore. Due to its unique geometry, superior performance of TSP foldcore is demonstrated (136, 146). It has a high average crushing resistance, low initial peak force and low loading rate sensitivity. Blast mitigation capability of sacrificial cladding with TSP folded structure as core is investigated in (9), the effect of foam fillers is investigated in (147). It should be noted that the above studies are based primarily on numerical simulations and single-layer set-up. Experimental tests were conducted only under quasi-static loading conditions. As for composite structures, crushing behaviours of structures could significantly be affected by loading rates and layer configurations (43, 148). Therefore, the performance of the proposed foldcores under dynamic loading conditions need be experimentally verified. The concept of reusable multi-layer set-up for proposed foldcore shall be tested as well.

In this chapter, multi-layer truncated square pyramid and truncated triangular pyramid folded structures are investigated experimentally under various crushing speeds. The results and observations are used to further confirm the conclusions obtained in the previous numerical studies (9, 136, 146, 149) based on single-layer truncated pyramid foldcore. Unlike conventional energy absorbing sandwich panels, such as honeycomb and foam panels where the core and skins are often permanently bonded, this multi-

layer design does not require any fixed bonding between foldcore and skin plates as shown in Figure 7-1. This allows the replacement of the deformed core after each loading and the interlayer plates can be reused. Furthermore, with this multi-layer design, the height of sandwich panel can be easily adjusted on site by simply adding or removing layers in order to suit the specific loading scenarios. In this chapter, single-layer TSP foldcore is firstly compared with multi-layer TSP under quasi-static loading condition. The effects of crushing speed, foldcore wall thickness and base shape are then experimentally investigated for the multi-layer folded sandwich panels. Reusability of the multi-layer set up is also examined, only one set of plates and rods is used for all the tested specimens by simply replacing the foldcores after each loading.

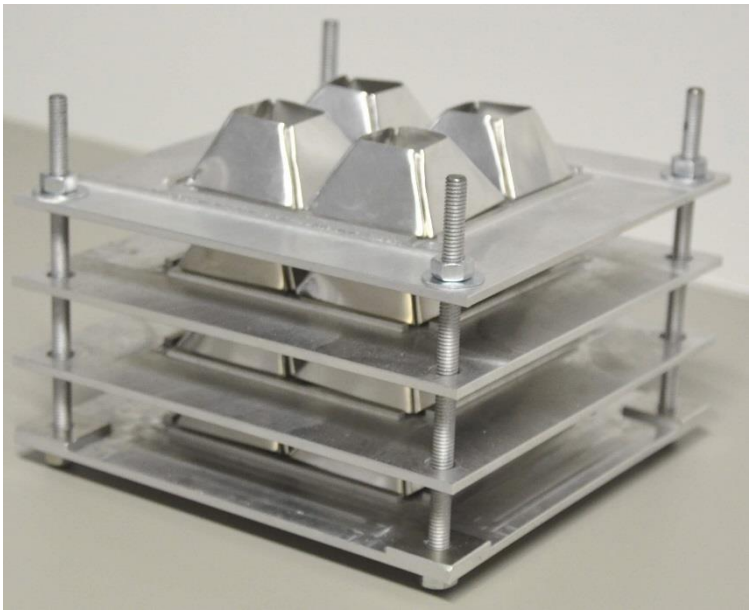

Figure 7-1. Multi-layer set up of Truncated Square Pyramid (TSP) folded sandwich structure

7.2 Geometric parameters and specimen folding

Pre-cut patterns, folding configurations and folding creases of truncated triangular pyramid (TTP) and truncated square pyramid (TSP) foldcore used in this chapter are shown in Figure 7-2 with geometric parameters marked out. For the geometric parameters and their relationships of the TTP and TSP single unit cell, please refer to Chapter 4.2.

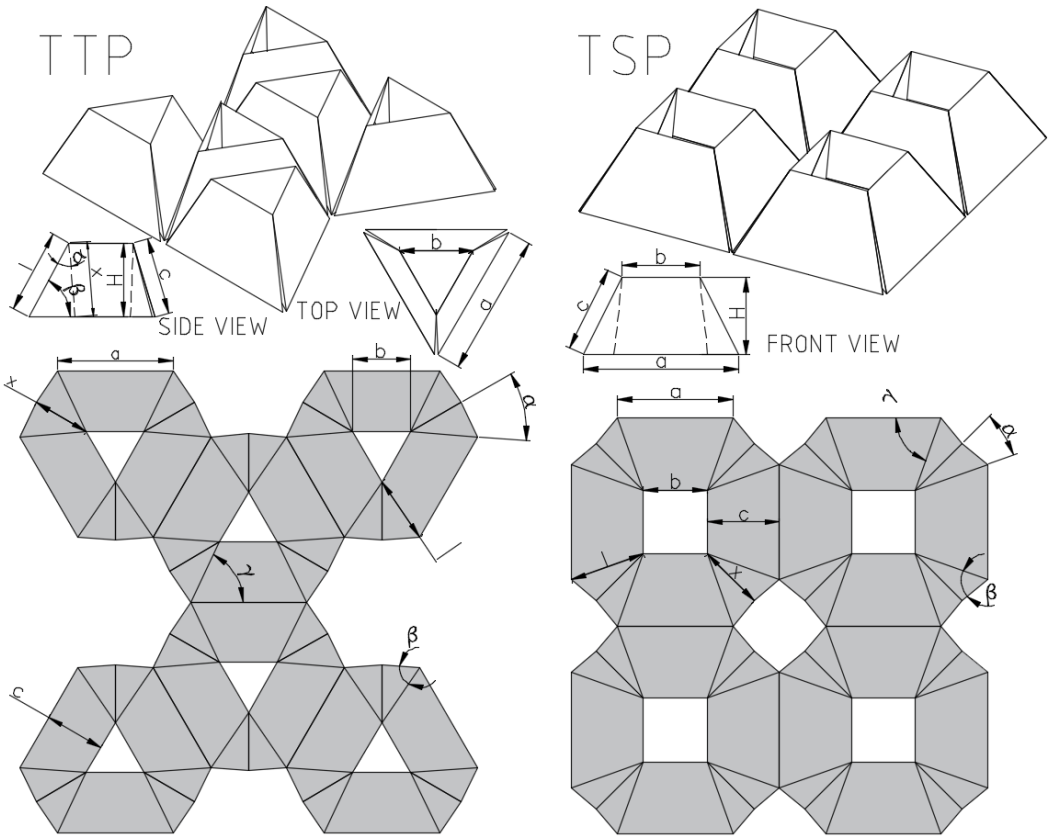

Figure 7-2. Folding configurations and pre-cut patterns for TTP and TSP foldcores

Table 7-1. Designed geometric parameters of manually folded specimens

Fold core	a mm	b mm	H mm	c mm	l mm	γ degree	β degree	α degree	x mm	t mm	ρ_v %
TTP	40	20	20	21	23	64	60	34	20	0.15	2.7
TSP	40	20	20	22	24	67	55	22	21	0.26	2.7

The specimens were prepared using Aluminium 1060 with thickness of 0.15 mm (for TTP foldcore) and 0.26 mm (for TSP foldcore), which give a volumetric density around 2.7% for both foldcores. The designed geometries of the different foldcores are listed in Table 7-1. Material properties of Aluminium 1060, which has a minimum aluminium content of 99.6% (150) are listed in Table 7-2. The measured true stress-strain curve of aluminium 1060 is shown in Chapter 4.3.1 (9). Multiple thin sheets were firstly stacked together and clamped using thicker plates. The clamped stacked sheets were then cut into designed pattern shown in Figure 7-2, using water jet cutting machine. Multiple patterned sheets can be cut in one go. These patterned sheets are then manually folded into the designed TTP and TSP structures. To better suit the crushing head which is later used for quasi-static and dynamic crushing, the foldcores

are designed as connected multiple units. Four units are connected for each TSP foldcore specimen and six unit cells for each TSP foldcore specimen as shown in Figure 7-2.

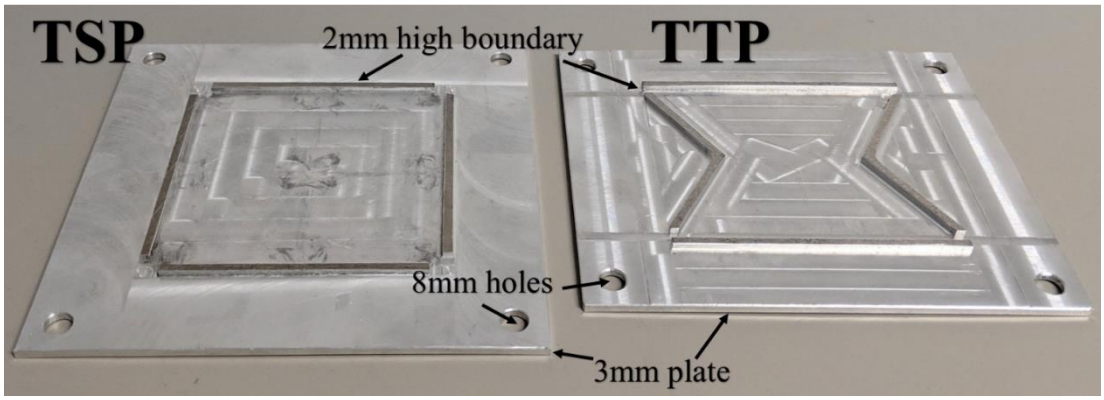

Figure 7-3. Inter-plate of TTP and TSP foldcores with 2 mm high boundary (after test)

The after-test base plate and interlayer plates are also fabricated for the multi-layer set up for both TSP and TTP foldcores as shown in Figure 7-3. The material used for base plate and inter-plates is Aluminium alloy 5083, with material properties provided in Table 7-2 (151). Stress-strain response of Al 5083 is not measured, as it is only used as interlayer plates. Yield stress of Al 5083 is more than 3 times of Al 1060 and the plate has a thickness of 3 mm (151), which is much thicker than that of the foldcores (0.26 mm or 0.15 mm). As observed from the tests, the significantly thicker and stronger plates have nearly no deformation throughout the repetitive tests as shown in Figure 7-3. The plate had a 2 mm high boundary around the foldcores to constrain the movement of the bottom edges of foldcore sidewall along in-plane directions. There are no bonding between plates and foldcores. Four holes with diameter of 8 mm are drilled near four corners of the inter plates. Four M6 threaded rods were fastened onto the base plate and used as a movement guide of the plates under out-of-plane crushing. This same set up was used throughout the quasi-static and dynamic crushing.

Table 7-2. Material properties of aluminium 1060 sheet and aluminium 5083 plate

Parameter	Young's modulus (GPa)	Poisson's ratio	Yield stress (MPa)	Density (kg/m^3)
Aluminium 1060	69	0.33	66.7	2710
Aluminium 5083	71	0.33	215	2660

One of the hand folded TTP foldcore specimen with surface flatness analysis is shown in Figure 7-4. 3D Direct Image Correlation (DIC) technique is used for analysing the imperfection on the sidewalls of the foldcore. Relatively good flatness of sidewall is shown, with the variation around 1.2 mm (varying from -0.79 mm to 0.49 mm as shown in the scale of Figure 7-4) from the designed plane of the sidewall, which has a base length of 40 mm. However, there are still some imperfections presented along the folding creases and the unit cells of foldcore are not exactly at the same level. This results in the multi-layer foldcore panel specimen slightly higher than the designed height of 20 mm for each layer. New tools and folding techniques need be implemented to reduce the folding imperfections associated with manual folding in the future. As proposed in (152), pressing tool with multiple moveable prisms along both in-plane directions can be used for folding patterns with multiple major bending axes.

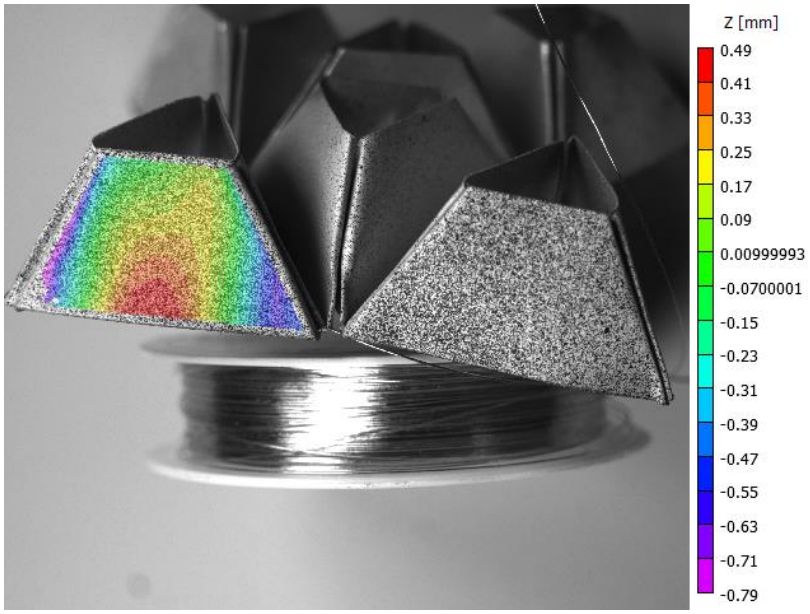

Figure 7-4. Surface flatness analysis of sidewall of TTP foldcore using 3D Direct Image Correlation (DIC)

7.3 Quasi-static crushing

7.3.1 Quasi-static crushing test set up

Both single-layer and multi-layer TSP foldcores are tested under quasi-static loading condition. The specimens are crushed under constant speed of 2 mm/min using Lloyd-Ametek EZ50 material testing machine. As shown in Figure 7-5, the cylindrical

crushing head has a diameter of 150 mm, which is smaller than the diagonal distance between threaded rods. This allows the crush head to move vertically downwards without interaction with the rods. The interlayer plates are not moving downwards parallel with each other throughout the whole crushing process as shown in Figure 7-5 (c). However, the foldcore is eventually crushed to horizontal position at the later stage when the plates are more or less parallel with each other. This might be caused by the uneven strength of unit cells of the foldcore specimen due to folding process. Since the holes for threaded rod are larger than the rod diameter, there is almost no interaction between rods and plates. The plates and rods remain un-deformed after crushing, which therefore can be reused in subsequent specimens. The same setup is used for the dynamic crushing tests.

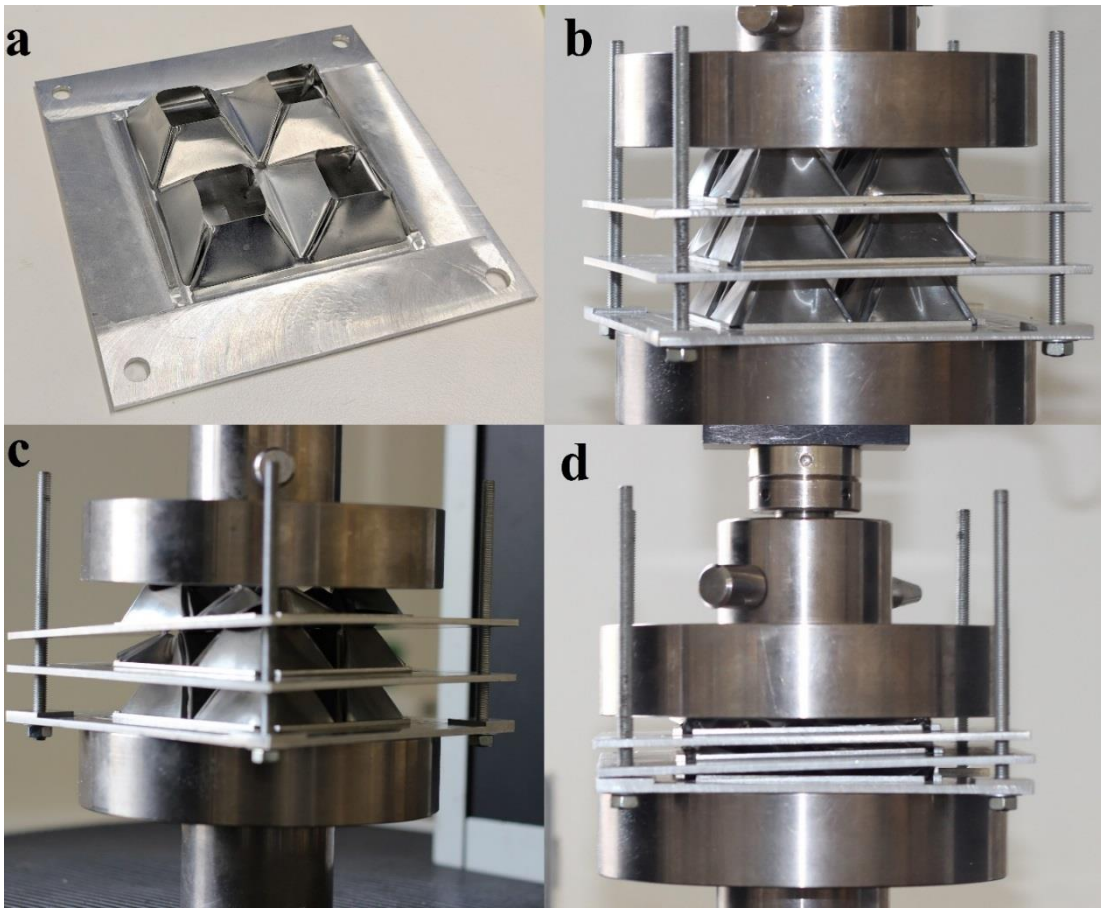

Figure 7-5. (a) Single-layer TSP foldcore; (b) multi-layer TSP foldcore under flatwise crushing (c) middle stage of the crushing; (d) final stage of the crushing

Normalized stress-strain curves of the single-layer and three-layer TSP foldcores under quasi-static crushing are shown in Figure 7-6, where stress and strain are normalized by base area and designed height respectively. It is noted that the thickness

of the base and inter plates are not included in the estimation of strain, as these plates are much stiffer than the foldcore and do not deform during the crushing process. The base area is taken as 80x80 mm and the designed height of the panel is 20 mm for each layer. Other parameters such as initial peak and average stress, densification strain and uniformity ratio are listed in Table 7-3. Densification strain, ε_D is the strain where sudden rise of compressive stress occurs due to the compacting of cellular structure. Initial peak force is the peak crushing force at early stage of the deformation, even though crushing force near densification may be higher. This is because that the initial peak force is more critical for the structure to be used as energy absorber. Average or plateau stress σ_{ave} is the average crushing stress before densification, and can be defined by the following equation:

$$\sigma_{ave} = \frac{\int_0^{\varepsilon_D} \sigma(\varepsilon) \cdot d\varepsilon}{\varepsilon_D} \qquad (7\text{-}1)$$

where σ is the crushing stress, ε is strain.

7.3.2 Test results

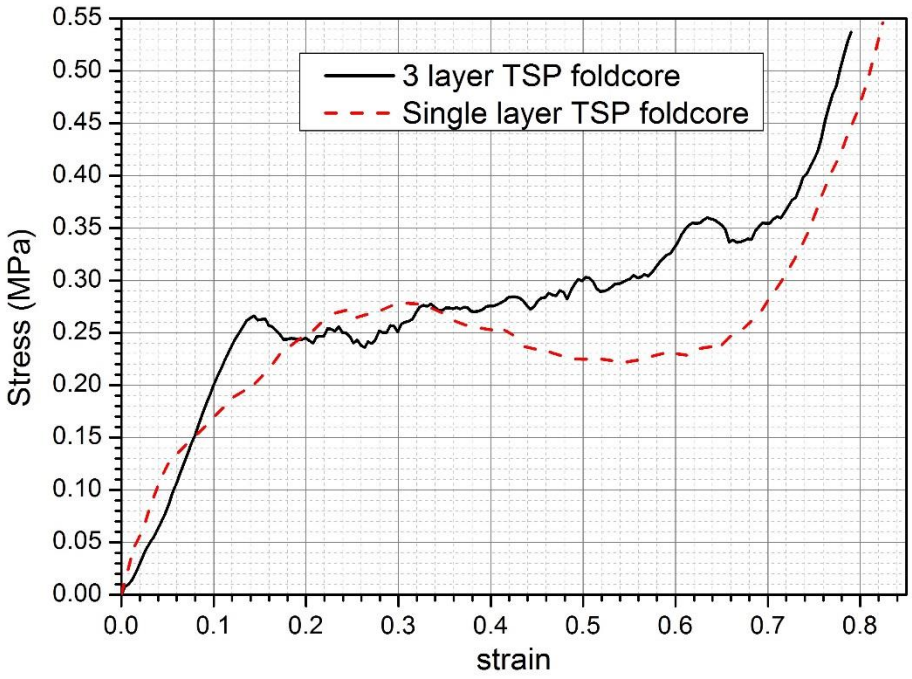

Figure 7-6. Normalized stress-strain curves of two cases under quasi-static loading condition

As shown in Figure 7-6, three-layer TSP foldcore has a slightly lower crushing resistance at early stage and a higher resistance at later stage comparing to single-layer TSP foldcore under quasi-static loading condition. All three layers of foldcore deform simultaneously along with the crushing process at early stage, rather than one layer getting fully crushed followed by other layers. Therefore, at early stage of the crushing, the weaker part of the foldcore deforms more, as shown in Figure 7-5 (c). This leads to uneven deformation and tilting inter-plate, which is different from single-layer foldcore crushing. At later stage of the deformation, the tilted plates of three-layer TSP foldcore get back to horizontal again, as the most deformed parts provide higher crushing resistance due to the compaction of the sheet material.

Table 7-3. Peak and average stress, densification strain and uniformity ratio of two configurations of TSP foldcore under quasi-static loading condition

Foldcore		σ_{peak} (MPa)	σ_{ave} (MPa)	U= σ_{peak} / σ_{ave}	ε_D
TSP	Single-layer	0.279	0.226	1.232	0.70
	Three-layer	0.266	0.259	1.027	0.71

The key parameters of single-layer and three-layer TSP foldcore under quasi-static crushing are given in Table 7-3. Due to simultaneous deformation across all layers, the multi-layer set-up improves the crushing behaviour as compared to single-layer TSP foldcore by yielding a more uniform deformation. Three-layer TSP foldcore has a slightly lower initial peak stress and higher average stress than single-layer TSP foldcore while the densification strains are similar. Both foldcores have a low uniformity ratio between 1.0 and 1.2. It is worth noting that the conventional honeycomb structure usually has a peak to average crushing force ratio varying between 2 to 3 under quasi-static loading (95). Many of the existing kirigami and origami have a uniformity ratio between 1.3 to 2.0 (84). This low uniformity ratio of multi-layer TSP foldcore indicates that this configuration is ideal for the application of energy absorption. The deformation is uniform with low fluctuation in resistance and it is easy to initiate due to low value of initial peak stress. Overall, single-layer and three-layer TSP foldcores have similar crushing behaviour, although tilting of the interlayer plates may occur during the crushing process.

7.4 Dynamic crushing

7.4.1 Dynamic crushing test set-up

Dynamic crushing tests of the multi-layer truncated folded pyramid structures were carried out using high speed testing machine INSTRON VHS 160/100-20. This test machine uses servo-hydraulic and control technologies to provide constant crushing velocity for dynamic crushing with a crushing speed ranging from 0.1 to 25 m/s. The crushing head and base support were both circular shapes with diameter of 100 mm. The load cell is located at the base of the testing machine with a capacity of 100 kN. In the test, INSTRON VHS software was used for data acquisition. High speed camera Fastcam APX RS with one light was used to capture the crushing process. The frame rate of the camera was set to 2,000 to 5,000 fps depending on the crushing speed. The testing setup is shown in Figure 7-7.

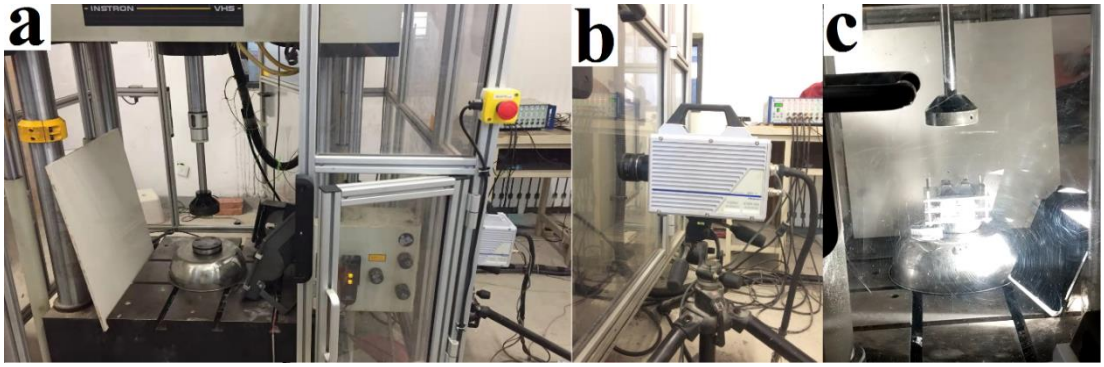

Figure 7-7. Photograph of (a) Instron VHS testing machine; (b) high speed camera; (c) lighting and setup of foldcores

Three types of foldcores were tested under dynamic crushing, including truncated square/triangular pyramid (TSP/TTP) foldcores with volumetric density of 2.7% and TSP foldcore with volumetric density of 1.6%. Testing scheme is listed in Table 7-4. At least three specimens were folded and tested for each case. A total of 24 dynamic tests were carried out and more than 72 foldcores were prepared for dynamic crushing tests. The label 3TSP-15-02 stands for the second sample of three-layer TSP foldcore crushed at 15 m/s. The designed height of the setup was 69 mm, which included three layers of foldcores with height of 20 mm and three interlayer plates each with a thickness of 3 mm. However, the actual heights of the specimens varied between 71 to 74 mm due to the gap between the foldcore and plates. As highlighted in red circle

in Figure 7-8, unit cells were not at the same level owing to imperfections of hand folding in preparing the specimens, resulting in small gaps between plate and foldcore bottom edges. This error associated with hand folding process of specimens could be reduced by advanced machine folding process as mentioned in the previous sections.

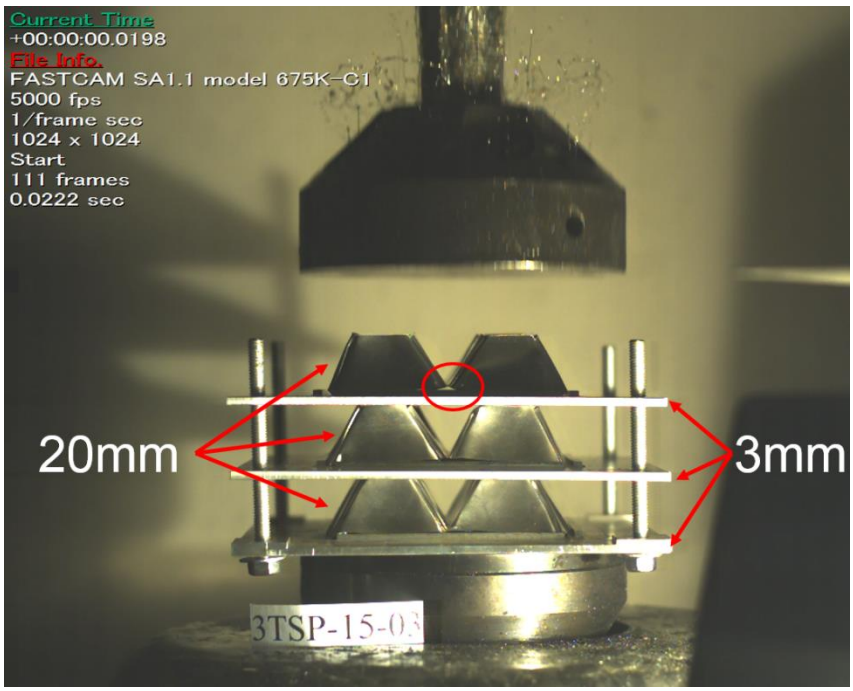

Figure 7-8. Crushing test of multi-layer TSP foldcore under 15 m/s crushing

Table 7-4. Testing scheme of multi-layer truncated folded sandwich structures

Test specimen	Foldcore type	Crushing speed (m/s)	Wall thickness (mm)	Volumetric density of the core
3TSP-1	TSP	1	0.26	2.7%
3TSP-10	TSP	10	0.26	2.7%
3TSP-15	TSP	15	0.26	2.7%
3TTP-1	TTP	1	0.15	2.7%
3TTP-10	TTP	10	0.15	2.7%
3TTP-15	TTP	15	0.15	2.7%
3TSP-0.15-10	TSP	10	0.15	1.6%
3TSP-0.15-15	TSP	15	0.15	1.6%

7.4.2 Dynamic crushing speed

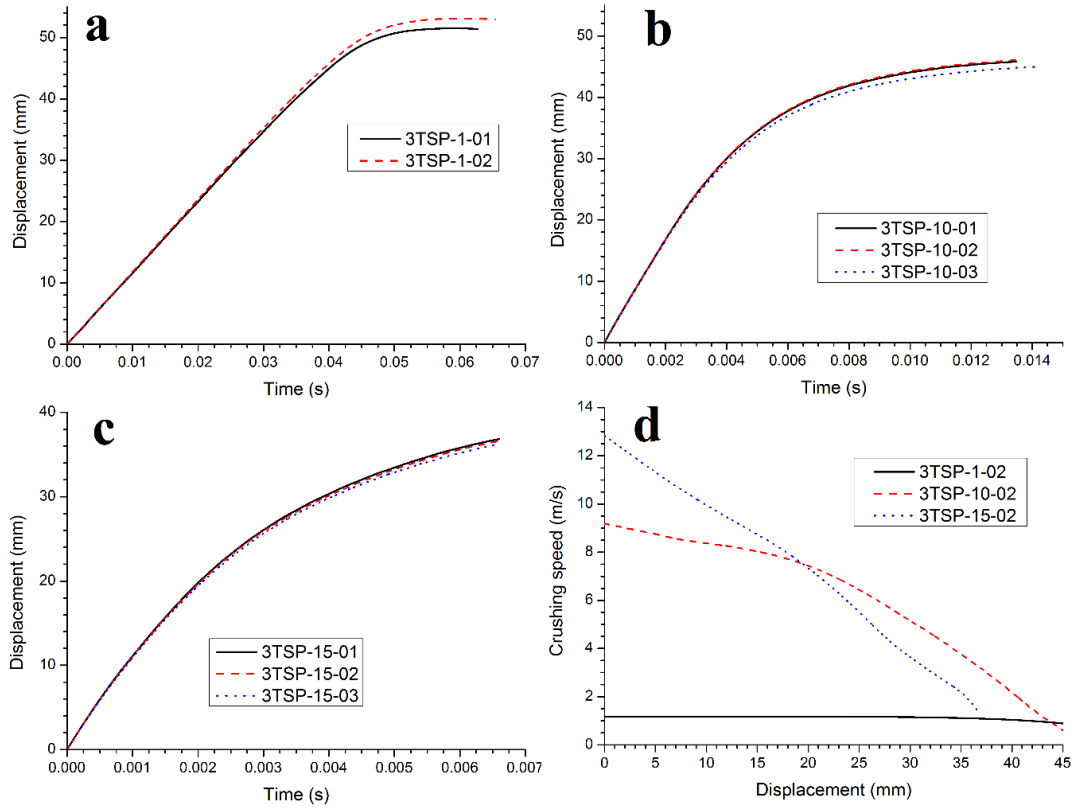

Figure 7-9. Smoothed displacement time history curves for TSP foldcore under (a) 1 m/s; (b) 10 m/s; (c) 15 m/s crushing; (d) actual crushing head speed versus displacement

The testing machine INSTRON VHS 160/100-20 is designed to maintain a relatively constant speed throughout the crushing process. However, the crushing speeds of crushing tests are not necessarily constant especially toward the later stage of the crushing or under higher crushing speed. This is caused by the distance required for the crushing head to decelerate from the designated testing speed. In dynamic crushing test, crushing head starts at certain distance above the specimen and accelerates to the desired speed followed by the deceleration to zero speed. The displacement-time histories of multi-layer TSP foldcore under various speeds measured by the testing machine are shown in Figure 7-9 (a-c). The linear portion of the curve represents the constant crushing speed of the crushing process, whereas the gradient of the curves decreases at later stage of the crushing, indicating the crushing speed is reduced. This is especially obvious with the higher crushing speed. As for the case with higher speed of the crushing head, a longer distance for deceleration is needed for the crushing head

to fully stop. Therefore, as shown in Figure 7-9 (d), a constant crushing speed is maintained only when the designated crushing speed is low, i.e., 1 m/s. When the desired crushing speed is high, the crushing speed in the test is actually decreasing with specimen deformation. The crushing speed is slightly smaller than the designated impact speed even before the specimen deforms. Hence the crushing speed here only refers to the designated impact speed for the test, instead of the actual crushing speed, which is not a constant and decreases with the specimen deformation.

7.5 Results and discussions

7.5.1 Multi-layer TSP foldcore

7.5.1.1 Crushing behaviour of multi-layer TSP foldcore

Load-displacement curves of the multi-layer TSP foldcores under different loading speeds are shown in Figure 7-10. For each loading scenario, one curve was selected from three tests. The general trends of the load-displacement curves are similar for the tests under same loading scenario especially for lower crushing speed (1m/s). Both the average crushing force and energy absorption are similar among the tests, while some discrepancies exist among the peak crushing forces and some fluctuations of the curve. The response of multi-layer TSP foldcore under quasi-static is also included for comparison. As represented by the initial gradient of the curves, the initial stiffness of the foldcores increases with the crushing speed, indicating loading rate sensitivity. This is caused by the inertial effect and the change of damage mode of the foldcores under higher crushing speed. For the test specimen 3TSP-10-02, the initial stiffness from 0 to 2 mm displacement has different trend as compared to other loading speeds. This may be caused by the initial gap between foldcore and plates or the uneven edges of foldcores, which results in different stiffness before and after the full contact of the foldcore and plates at around 2mm displacement. It is also worth noting that the final displacements of different loading rates are not the same. The specimens crushed under higher velocities have a smaller recorded final displacement. This is because that the crushing head requires longer distances for deceleration and a larger residual height is required for test with higher crushing speed as shown in Figure 7-9 (d).

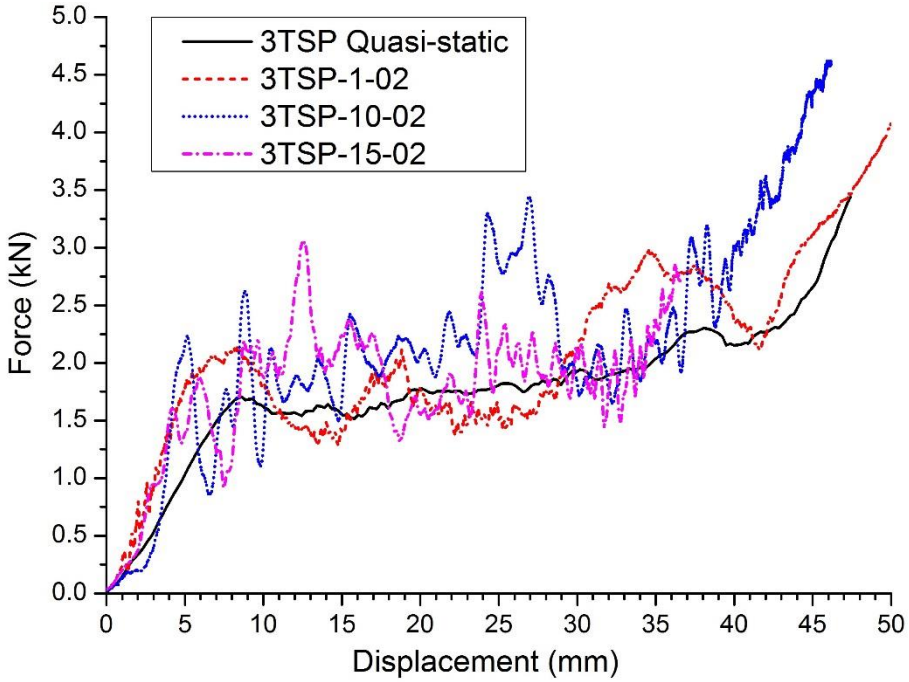

Figure 7-10. Load-displacement curves of multi-layer TSP foldcores under various loading speeds

The key parameters measured from the load-displacement curves including peak and average crushing resistance, uniformity ratio and energy absorption are listed in Table 7-5. The average crushing force is defined as the average force from beginning to densification of the core, which is shown in equation (7-1) in Chapter 7.3.2. Typically, the energy absorption of a structure is defined as the area under stress-stain curve obtained prior to the onset of densification (25). However, since the final displacements are not the same for these foldcores and the smallest displacement is 36.5 mm for 3TSP-15-02, as shown in Figure 7-10. This is due to the self-protection mechanism of the Instron testing machine. Crushing distance is reduced for the higher crushing speeds. In this section, to make a fair comparison of the performance among the different loading cases, the average crushing force and energy absorption are calculated using the smallest final displacement i.e. 36.5 mm. It should be noted that at this crushed distance of 36.5 mm, the densification stage is not yet reached for some loading scenarios as shown in Figure 7-10. Therefore, the average crushing force and energy absorption capacity are slightly underestimated for some loading scenarios of the foldcores. The peak crushing force is taken as the initial peak force which is more critical for energy absorption capability. For many conventional cellular structures other than foam, such as honeycomb (95), lattice (53) and Miura-type foldcore (82),

the initial peak force is often the overall peak force throughout crushing before densification and it is also very sensitive to loading rate. In this chapter, however, the initial peak force is not necessarily the overall peak force throughout crushing.

As found in the previous studies, the initial peak force of honeycomb (17) and Miura-type foldcores (82, 146) can increase several times under dynamic crushing than quasi-static loading. As shown in Table 7-5, the increment in peak crushing force of TSP foldcore is around 78% from quasi-static loading to 15 m/s crushing. The average crushing force increases from 1.549 kN under quasi-static loading to 1.783 kN for 15 m/s crushing speed. The uniformity ratio, U, increases from 1.1 to 1.71 with the crushing speed, which is much less than that of conventional cellular structures and other foldcores. For instance, uniformity ratio of multi-layer corrugated aluminium structure is about 4.5 (at the strain rate of $40s^{-1}$) (43). The uniformity ratio of Miura-type and cube strip foldcore are 3 to 4.4 under dynamic crushing (80, 136, 146) . Energy absorption is calculated by integrating the load-displacement curve for each case, and it has the same trend as the average crushing force. Overall, this multi-layer TSP foldcore shows better characteristics for energy absorption comparing to other folded structures and conventional cellular structures including honeycomb. It has a lower initial peak crushing resistance, uniform deformation and good energy absorption under dynamic loading.

Table 7-5. Initial peak, average crushing force, uniformity ratio and energy absorption of multi-layer TSP foldcore under different loading conditions, note: energy absorption and average crushing force are calculated till 36.5 mm displacement

Test specimen	Initial peak crushing force (kN)	Average crushing force (kN)	$U=P_{peak}/P_{ave}$	Energy absorption (J)
3TSP quasi-static	1.705	1.549	1.10	56.82
3TSP-1	2.135	1.748	1.22	63.82
3TSP-10	2.623	1.894	1.38	69.12
3TSP-15	3.046	1.783	1.71	65.19

It is noted that the average crushing force under 15 m/s decrease slightly compared with crushing under 10 m/s. This is because that the actual crushing speed of 15 m/s

at later stage is lower than that of 10 m/s, as deceleration distance is larger for the crushing head under higher speed as shown in Figure 7-9 (d). As also can be observed from Figure 7-10, before 20 mm of displacement, the TSP foldcore crushed under 15 m/s has a slightly larger crushing force than 10 m/s, while after 20 mm of displacement, the crushing resistance under 10 m/s loading rate is higher than that of 15 m/s. These results are therefore caused by the limitation of the testing equipment, i.e., the crushing speed could not be maintained at a constant value. Nonetheless, the results shown in Figure 7-10 and the crushing speed shown in Figure 7-9 (d) indicate that crushing force is positively related with the crushing speed, increasing crushing speed leads to an increase in crushing force. Therefore the performance of the foldcore is loading rate sensitive.

7.5.1.2 Damage mode comparison

Damage modes of TSP foldcores under different loading speeds, i.e., 1 m/s and 15 m/s are shown in Figure 7-11. Under 1 m/s crushing, only one damage mode is present on the outer sidewalls. The sidewalls bend inwards along vertical axis on all three layers, as marked out in red circles in Figure 7-11 (a, c, e). Under higher crushing speed of 15 m/s, however, the damage mode on top layer of the foldcore is different from other layers, as marked out in yellow circles in Figure 7-11 (d). Each sidewall of the top layer bends outwards along horizontal axis. This difference in damage mode is consistent with numerical result of single-layer TSP foldcore in the previous chapter, which is shown in Figure 7-11 (g, h). Under lower crushing speed, each outer sidewall of TSP foldcore bends inward vertically as four corners are strengthened by the triangular interconnections. As marked out in Figure 7-11 (c), these interconnections are not deformed during the inward vertical bending of the sidewall, which requires less force. With the increasing crushing speed, the deformation of the outer sidewalls is more localized along top edges and the sidewalls bend horizontally. The interconnections at corners also buckle during crushing, therefore this damage mode provides higher crushing resistance. It is noticeable that three layers have different damage modes under 15 m/s, this is caused by different crushing speeds at each layers. Under high speed impact, deformation initiates on top layer while bottom layers remain un-deformed due to the inertia effect, as shown in Figure 7-11 (b). It is then followed by the deformation of middle and bottom layers as shown in Figure 7-11 (d,

f). The top and middle/bottom layers therefore have different damage modes due to the reduced crushing speed of each individual layer.

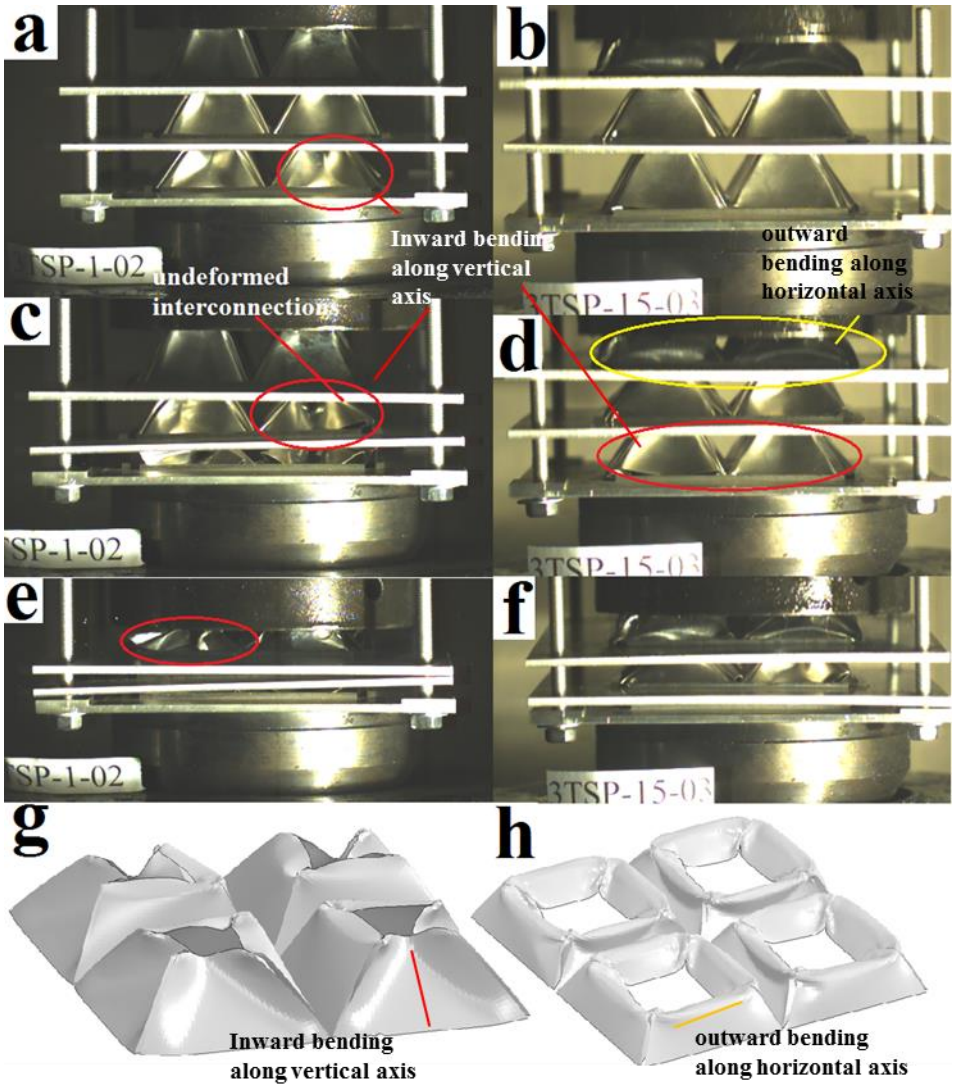

Figure 7-11. Damage modes of multi-layer TSP foldcore, (a, c, e) under 1 m/s crushing speed; (b, d, f) under 15 m/s crushing speed; Damage modes of single-layer TSP foldcore from numerical simulation under (g) 0.05 m/s crushing; (h) 15 m/s crushing

Damage modes of multi-layer TSP foldcore under 1 m/s and 15 m/s are shown in Figure 7-12. Two damage modes can be observed under two loading speeds. Under 1 m/s crushing, many sidewalls bend inwards where the four corners of interconnections of unit cell remain un-deformed and sidewall walls bend toward centre. Since the sidewalls bend vertically towards centre (circled in red), the square shape of the openings is no longer presented after crushing. Under 15 m/s crushing, the square opening of the top layer remains its square shape (marked out in orange). This is

because the damage mode under 15 m/s impact changes to local buckling of the sidewalls on the top layer of foldcore, as more clearly illustrated in Figure 7-11, instead of the bending of the entire sidewall. Therefore, the square opening can be observed on top layer of TSP foldcore after crushing under 15 m/s, which is marked out in yellow colour in Figure 7-12. Furthermore, more buckling of the four corners on top layer can be observed for this loading rate. The damage modes of the middle and bottom layer are similar to those under 1 m/s impact because the crushing speeds of these two layers are reduced from the 15 m/s as discussed above.

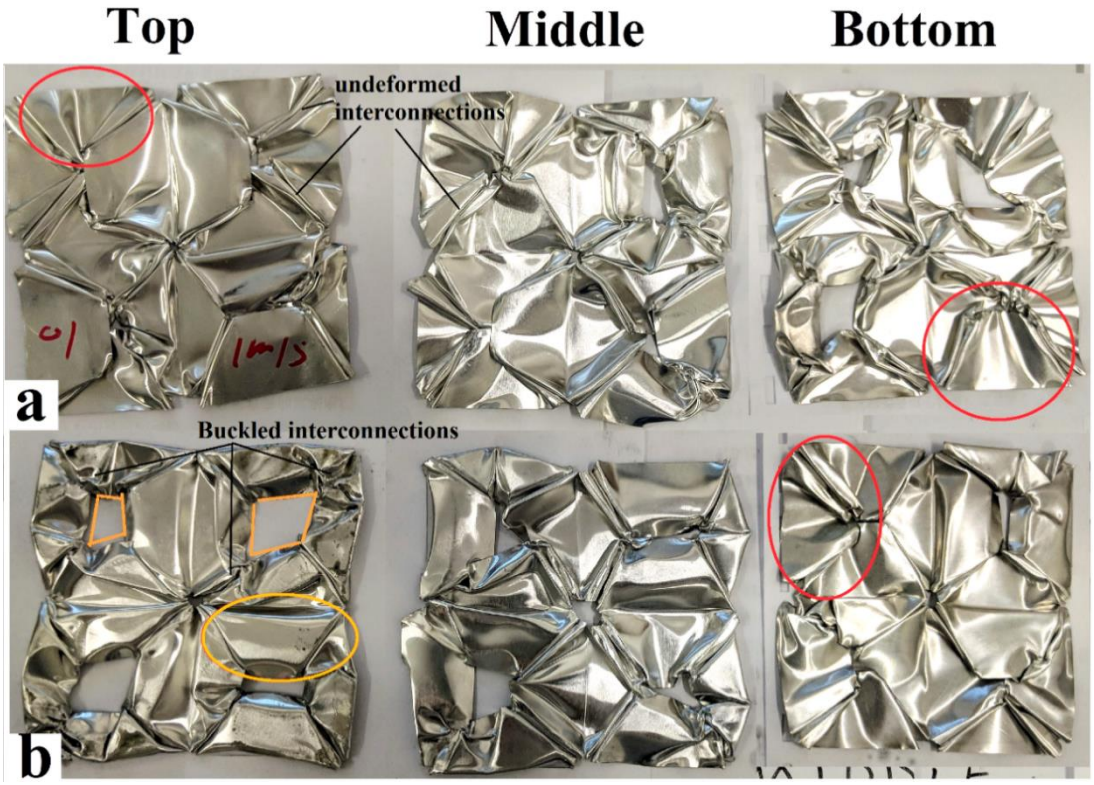

Figure 7-12. Damage modes of top, middle and bottom layer of TSP foldcore under (a) 1 m/s crushing; (b) 15 m/s crushing

This change in deformation modes for multi-layer TSP folded structures especially on top layer under two different crushing velocities can be explained by the geometry of the foldcore and the inertia effect. Under quasi-static crushing and low speed dynamic crushing, the top layer of TSP foldcore experiences global deformation where sidewalls vertically bend towards centre. This is because that the sidewalls are indirectly connected via triangular interconnections to the adjacent sidewalls. These triangular interconnections located at four corners of each unit cell strengthen the out-of-plane crushing resistance of the structure. Therefore, under low crushing speed the

interconnections rotate about the base rather than buckle. Under high crushing speed, the initiation of the deformation on top layer is localized on top part. When the crush head is firstly in contact with the foldcore, the top edge of the sidewalls roll towards centre of the unit cell, where the lower part of the unit cell remains undeformed. There is no sufficient time for the foldcore sidewalls and interconnections to undergo global deformation. Therefore, both sidewalls and interconnections buckle together throughout the crushing.

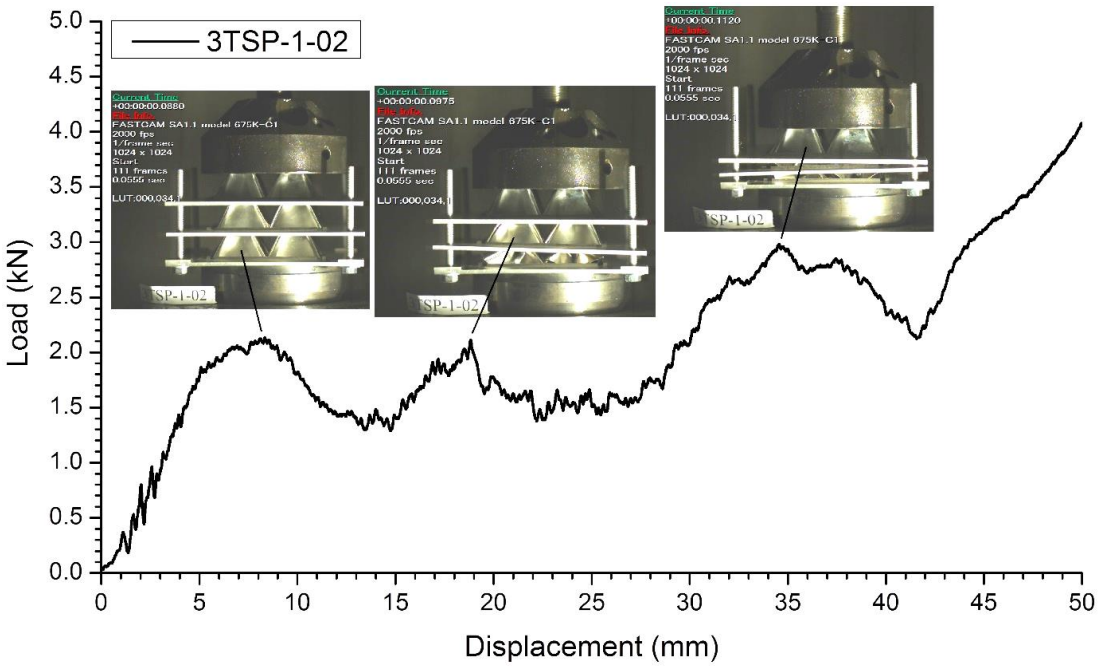

Figure 7-13. Correlation between layer deformation and load-displacement response of three-layer TSP folded structure under 1 m/s crushing

Deformation of three layers of TSP folded structure crushed under 1m/s are correlated with the load-displacement curve as shown in Figure 7-13. Three distinct peaks can be observed on the load-displacement curve. The three peaks correspond to the initiation of the sidewall buckling of the bottom, middle and top layer, respectively. As previously mentioned, the gaps between foldcores and plates exist due to imperfections induced from manual preparation of the specimen. At initial stage, these gaps will firstly be closed up when the multi-layer folded structure is subjected to out-of-plane crushing. This portion of crushing response is similar to the deformation mode of multi-layer folded structure under quasi-static loading as discussed in Chapter 7.3. After the complete closure of the gaps, deformation initiated slightly on all three layers, then followed by layer-by-layer collapsing. Each peak corresponds to the

initiation of the buckling of the foldcore sidewall of each individual layer as shown in Figure 7-13. The order of layer collapsing is also related to the crushing speed. For instance, two different orders of layer collapsing are shown in Figure 7-11 under two crushing speeds. Under dynamic crushing, collapsing starts from bottom layer, as shown in Figure 7-13. This layer-by-layer deformation is completely different from the response of this structure under quasi-static loading. Under quasi-static crushing, all three layers deform simultaneously and result in a smoother load-displacement response than that under dynamic loading.

7.5.2 Multi-layer TTP foldcore

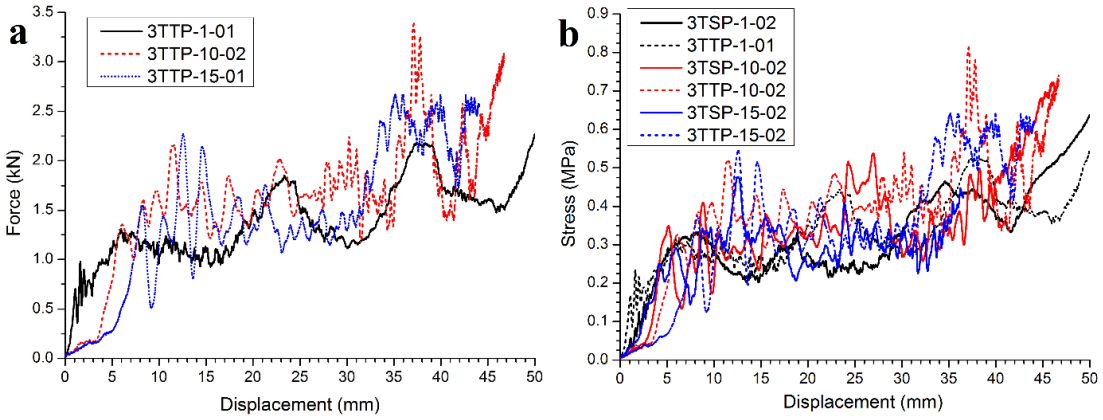

Figure 7-14. (a) Load-displacement curves of multi-layer TTP crushed under different speeds; (b) Stress-displacement curves of multi-layer TTP and TSP foldcores crushed under different speeds.

The force-displacement curves of multi-layer TTP foldcores are shown in Figure 7-14 (a). The crushing stress-displacement curves of TTP foldcores are also compared with TSP foldcore in Figure 7-14 (b), where crushing stress is calculated via dividing the force by the base area of the foldcore. Initial peak force, average force, uniformity ratio and energy absorption of multi-layer TTP foldcore under different crushing speeds are given in Table 7-6. Multi-layer TTP foldcore shows a slightly less uniform deformation and larger fluctuation of the crushing resistance as compared to TSP foldcore, especially under high crushing speed, as shown in Figure 7-14 (b). The increase in initial peak force of multi-layer TTP foldcore is 64.8% and 73.4%, respectively when crushing speed is increased from 1 m/s to 10 m/s and then to 15 m/s, while the corresponding increase in initial peak force of multi-layer TSP foldcore is 22.8% and 42.7%. This indicates the multi-layer TSP foldcore is less sensitive to

loading rate than TTP foldcore, as smaller percentage rise in initial peak force is observed with the increase in crushing speed for TSP foldcore. As explained in the previous study (146), TTP foldcore has a larger size of triangular interconnection, a higher inclination angle and corner/area ratio, resulting in a higher inertia effect and stabilization effect of the interconnection than TSP foldcore under dynamic crushing. However, comparing to the conventional folded structure, TTP foldcore still demonstrates a good performance under dynamic loading. As given in Table 7-6, TTP foldcore has a uniformity ratio of around 1.5 under both 10 and 15 m/s crushing, which is lower than many conventional folded structures. Slight reduction in average crushing force is observed, when crushing speed increases from 10 to 15 m/s, for multi-layer TTP foldcore specimen. Three distinct peaks are shown for multi-layer TTP folded structures under 1m/s crushing similar to TSP folded structure, and can be explained by the layer-by-layer deformation of the foldcores.

Table 7-6. Initial peak, average crushing force, uniformity ratio and energy absorption of multi-layer TTP foldcore under different loading conditions

Test specimen	**Initial peak Crushing force (kN)**	**Average crushing force (kN)**	**$U=P_{peak}/P_{ave}$**	**Energy absorption (j)**
3TTP-1	1.308	1.223	1.07	44.96
3TTP-10	2.156	1.426	1.51	52.14
3TTP-15	2.269	1.264	1.80	46.21

Damage mode of multi-layer TTP foldcore under 15 m/s is shown in Figure 7-15. The dynamic damage mode of multi-layer TTP foldcore is similar to that of TSP foldcore shown in Figure 7-12, where the top edges bend inward horizontally. The similar damage mode of the TTP foldcore can be identified by observing the remaining shape of top openings (as marked out in orange). The top openings at the middle and bottom layers deform completely. However, the middle and bottom layers of TTP foldcore show different damage modes as compared to the middle and bottom layers of TSP foldcore. The lower layers of TTP foldcore show random damage where inner cells buckle and outer cells show a combination of horizontal outward bending and vertical buckling. No corner lift-up occurs in any layer of this TTP folded structure, because the inclination angle of TTP foldcore is larger than that of TSP foldcore. In other words, the cell sidewalls of TTP foldcore is closer to vertical than TSP foldcore. With larger

angle of the sidewalls, vertical buckling of sidewalls is more likely to occur than vertical bending inwards for TSP foldcores as shown in Figure 7-11 (g). Furthermore, two inner cells are completely surrounded by other unit cells. These constraints from the adjacent unit cells prevent the corners of the inner cells from lifting up. Therefore, multi-layer TTP foldcore has different damage mode from the TSP foldcore.

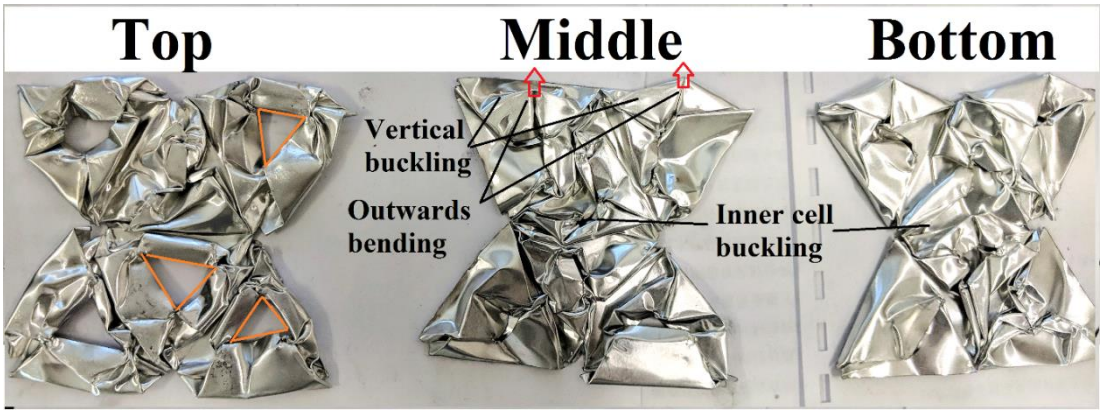

Figure 7-15. Damage modes of top, middle and bottom layer (left to right) of multi-layer TTP foldcore after 15 m/s crushing

7.5.3 Multi-layer TSP foldcore with lower density

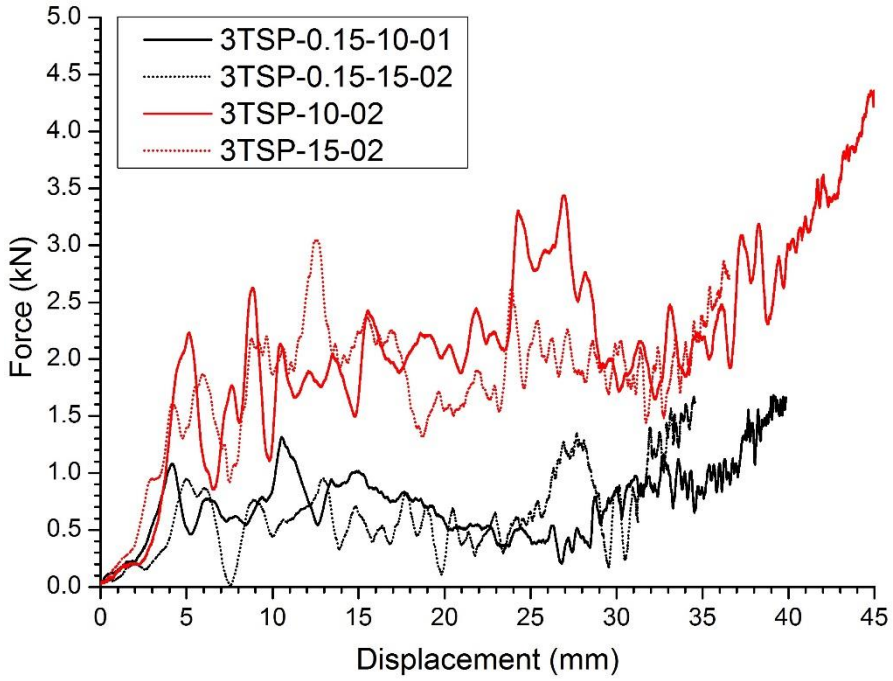

Figure 7-16. Load-displacement curves of multi-layer foldcores of TSP with two wall thicknesses under various loading rates.

In this section, multi-layer TSP foldcore with thinner walls is investigated under dynamic crushing. This is to investigate the relationship between density and crushing resistance, which has been reported in a power relationship for many cellular structures. Their crushing resistances increase much quicker than the increase of the density of the core (24, 50). TSP foldcore with wall thickness of 0.15 mm and volumetric density of 1.6% is compared to TSP foldcore with wall thickness of 0.26 mm and volumetric density of 2.7%. The representative force-displacement curves of multi-layer TSP foldcores with two densities are observed in Figure 7-16, and other parameters are listed in Table 7-7. Thicker foldcore has higher crushing resistance, as expected. Under 10 m/s crushing speed, the average crushing force increases from 0.667 kN (TSP-0.15-10) to 1.894 kN (TSP-0.26-10) with the increasing wall thickness. The increase in average crushing resistance is 184% while the density only increases by 73% from TSP-0.15 to TSP-0.26 mm. Similarly, under 15 m/s crushing speed, the increase in average crushing resistance is 182% with 73% increase in density.

Table 7-7. Initial peak, average crushing force, uniformity ratio and energy absorption of multi-layer TTP foldcore under different loading conditions

Test specimen	Initial peak crushing force (kN)	Average crushing force (kN)	$U=P_{peak}/P_{ave}$	Energy absorption (J)
3TSP-0.15-10	1.078	0.667	1.97	23.06
3TSP-0.15-15	0.955	0.632	1.51	21.84

As given in Table 7-7, it is interesting to observe that the average crushing force decreases slightly under higher crushing speed, as well as the peak crushing force. The reductions in average crushing force and energy absorption are mainly caused by sliding out of boundary of the foldcore bottom edges. Similarly, the sliding out of the bottom edges may cause the reduction of crushing resistance at around 7 mm displacement for the case of 15 m/s crushing, resulting a slightly lower initial peak force than the foldcore crushed under 10 m/s. As presented in Figure 7-17, many edges in different layers have slid out of the 2 mm high boundary of base plate. The approximate position of plate boundaries are marked out in black square in Figure 7-17. This lack of constraint reduces the crushing force resistance as well as energy absorption of the foldcore. When the wall thickness is thinner (0.15mm), it is easier

for the bottom corner to be lift-up and to slide out of the boundary under high impacting speed. However, this phenomenon is less likely for foldcore TSP-0.26 mm due to its thicker sidewalls, which make the failure mode different from that of TSP foldcores with 0.15 mm wall thickness. TTP folded structures tested in this chapter has the same thickness (0.15mm), but no sliding out or corner lift-up are observed due to the higher angle of the sidewall slope. A slightly higher boundary constraint needs be used in the future experimental tests.

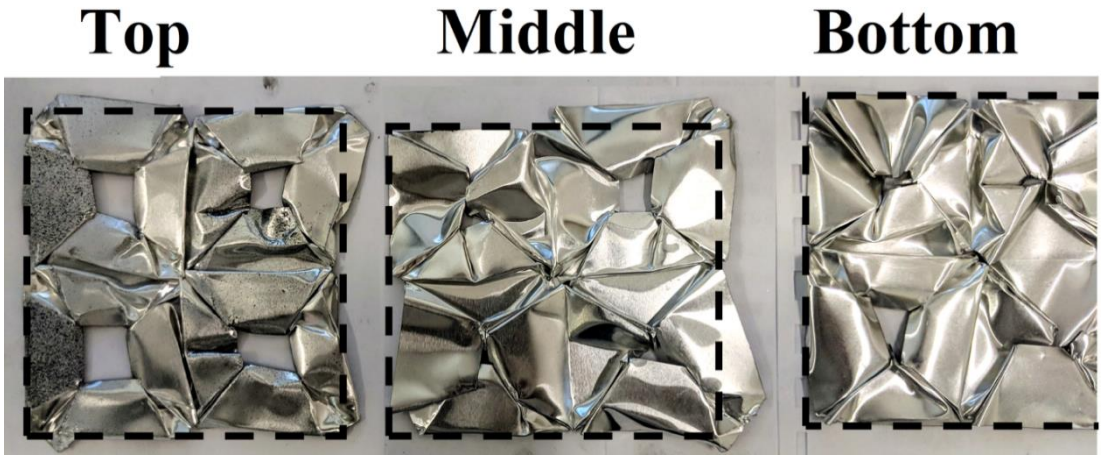

Figure 7-17. Damage mode of TSP-0.15 mm foldcore under 15 m/s crushing, note: black line are the position of the boundary

7.5.4 Specific energy absorption of multi-layer foldcores

The specific energy absorptions (SEA) of the multi-layer foldcores are calculated and shown in Figure 7-18. Multi-layer TTP foldcores show slightly higher specific energy absorption than multi-layer TSP foldcore, despite the fact that crushing process of TTP fluctuates more than that of TSP foldcores. It is also noted that the specific energy absorption increases for all multi-layer foldcores with the crushing speed increased from 1 to 10 m/s. The increase is caused by the change of damage mode under dynamic loading. As for the crushing speed increasing from 10 to 15 m/s, the specific energy absorption slightly reduces which is mainly attributed to the reduced stroke length or compressed distance of the machine crush head under higher speed. In addition, the actual traveling speed of crushing head under 15 m/s speed is less than that under 10 m/s speed in the late stage of crushing, as presented in Figure 7-9 (d). This leads to a slight increase in initial peak force but a slight decrease in average crushing resistance and the specific energy absorption of the multi-layer structures.

Error bar of specific energy absorption (SEA) is also included in Figure 7-18. In general, SEA for each loading case from all tests agree with each other quite well, especially for the case with low crushing speed of 1 m/s. Maximum difference in SEA among all testing scenarios is about 20.4% for TTP multi-layer structure crushed under 10 m/s.

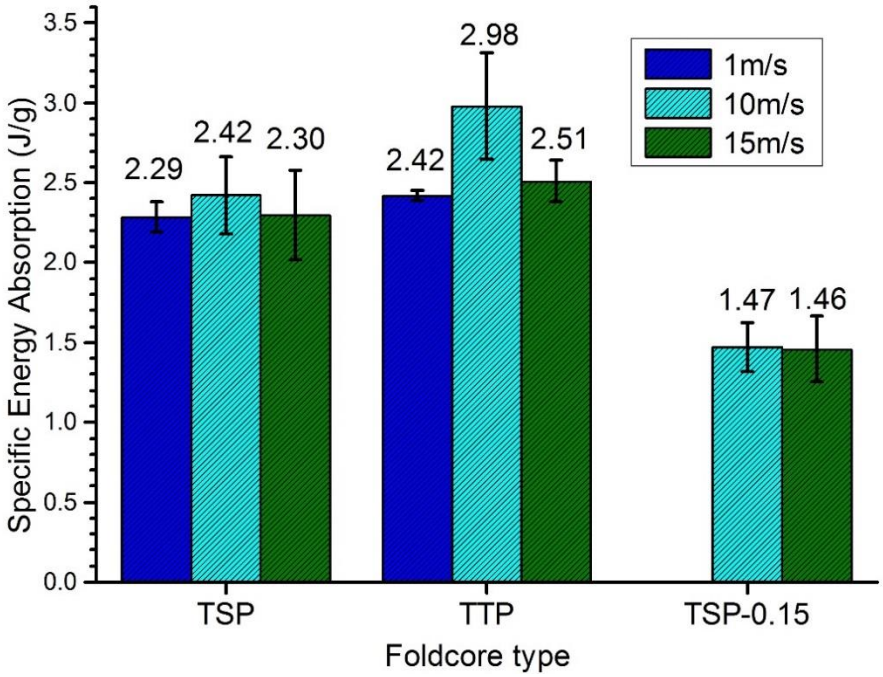

Figure 7-18. Specific energy absorption (SEA) of multi-layer folded structures under various loading speeds.

The specific energy absorptions of multi-layer TSP and TTP foldcore are much higher than that of conventional energy absorbers. For instance, under quasi-static loading, eggbox made from aluminium sheet with a volumetric density of 2.8% has a SEA around 1 J/g, and Cymat aluminium foam with volumetric density of 3.1% has a SEA between 0.5-0.8 J/g (46). The aluminium material used for eggbox is Al 1050 H111 (46), which is in the same series of commercially pure aluminium as the Al 1060 sheet used in this study (150). Both Al 1050 and Al 1060 have a minimum 99% aluminium composition and have similar mechanical properties, while the yield strength of Al 1050 H111 is about 45 MPa (46). Cymat closed cell aluminium foams are made of aluminium alloy with Young's modulus of 93 GPa and compressive yield strength of 310 MPa (28), which is much higher than Al 1060 used in this study. The SEA of the proposed multi-layer TSP and TTP foldcores folded from aluminium sheet are all above 2.2 J/g, which greatly exceeds that of conventional structures by more than

twice while maintaining a uniform deformation and low initial peak crushing resistance. Although both TSP and TTP foldcore have a slightly smaller volumetric density of 2.7 % than the studied eggbox and aluminium foam (46). Even for TSP-0.15 foldcore which has a volumetric density of 1.6%, its SEA (1.3-1.4 J/g) also exceeds two common energy absorbers listed above. It is also worth noting that the SEA calculated in this chapter are conservative, as the energy absorption is only calculated to 36.5 mm for fair comparison as explained in Chapter 7.5.1.1 and densification is not yet reached at this crushed distance for many cases. To sum up, the foldcores especially multi-layer TSP foldcores show consistent crushing resistance and superior energy absorption under different loading rates, comparing with other folded structures and conventional cellular structures.

7.6 Summary

In this chapter, three types of multi-layer truncated pyramid folded sandwich structures, i.e. TSP, TTP and TSP-0.15 are manufactured and tested under impact loading condition. The multi-layer truncated pyramid structures show improved structural behaviors as energy absorber under dynamic loading condition, comparing with conventional cellular structures and other folded structures. Out of these two types, multi-layer TSP folded structure slightly outperforms TTP foldcore. It has a more uniform crushing behavior with less fluctuation and lower initial peak force than multi-layer TTP foldcore. The change in damage mode of the foldcore is observed with crushing speed which is consistent with the previous numerical study. The average crushing resistance of foldcore is also found increasing with the density of the foldcore. Overall these truncated pyramid panels show good performance under dynamic loading with uniform deformation and low initial peak crushing resistance. In addition, the multi-layer unit proves replaceable after crushing as no bonding between core and skins is required for the unit. This replaceable concept of multi-layer protective structure could be very promising, as conventional protective sandwich structure requires glue or fixed bonding between core and skin of the sandwich panel. It takes much longer time to manufacture and the properties of the panel are also related to the bonding strength (65, 153). Another advantage of this unit is that the foldcore layer can be easily stacked or removed to better suit different loading scenarios.

Chapter 8. Experimental and numerical study of foam filled multi-layer folded TSP folded structures under dynamic crushing

The related work in this chapter has been published in International Journal of Impact Engineering.

Li Z, Chen W, Hao H. Dynamic crushing and energy absorption of foam filled multi-layer folded structures: Experimental and numerical study. International Journal of Impact Engineering. 2019;133:103341.
DOI: 10.1016/j.ijimpeng.2019.103341

8.1 Introduction

In Chapter 7, multi-layer TSP foldcores without foam filler have been tested under dynamic loading and show good performance with uniform deformation and low initial peak crushing resistance. In this chapter, the dynamic crushing behaviour of foam-filled multi-layer TSP foldcore with different types of foams, material densities and foam filler shapes are investigated experimentally and numerically. As lightweight material has the ability to undergo large deformation at almost constant stress (2, 27), foam materials including metallic and polymeric foams have been used as fillers in composite structures to improve their crushing resistance and energy absorption (100, 144). It was suggested that the increase in crushing strength and energy absorption of foam filled structures was much higher than that of foam filler itself (98, 108, 154), due to the interaction between the foam filler and cellular structure cell walls. The blast mitigation capacity of single-layer PU filled TSP foldcore cladding has been numerically investigated in Chapter 6 as well, with promising performance demonstrated.

In this chapter, five foam filler configurations are considered: cubic expanded polystyrene (EPS) foam of three densities (13.5, 19, 28 kg/m^3), rigid polyurethane (PU) foam (35 kg/m^3) of two shapes. Quasi-static crushing tests of single layer foam-filled TSP foldcores are carried out, followed by dynamic crushing tests of multi-layer foam filled TSP foldcores. Numerical analysis of dynamic crushing of these foam filled multi-layer TSP foldcores is also conducted. Key parameters including average

crushing force, initial peak crushing force and specific energy absorption are selected as criteria to evaluate the crushing responses of these foam filled multi-layer TSP foldcores and compare with the samples without foam filler.

8.2 Geometric parameters, multi-layer setup and material properties

8.2.1 Truncated square pyramid foldcore and multi-layer set-up

For geometries of the truncated square pyramid (TSP) foldcore specimen, please refer to Chapter 4.2. For the multi-layer set-up, please refer to Chapter 7.2.

8.2.2 Foam filler types

Two types of foam materials i.e. expended polystyrene (EPS) and rigid polyurethane (PU) foam are considered as foam filler. In total five foam filler configurations of foldcore are considered in this chapter: TSP foldcore; TSP foldcore with cubic SL density grade (density of 13.5 kg/m^3) EPS foam; TSP foldcore with cubic M density grade (density of 19 kg/m^3) EPS foam; TSP foldcore with cubic VH density grade (density of 28 kg/m^3) EPS foam; TSP foldcore with cubic PU foam (density of 35 kg/m^3); TSP foldcore with shaped PU foam (density of 35 kg/m^3). The notation of the foam filler configuration includes foam type, foam density and foam shape. For instance, TSP-EPS13.5C stands for TSP foldcore infilled with cubic EPS foam with density of 13.5 kg/m^3. Other notations and mass of each layer are listed in Table 8-1. For the dimensions of cubic and shaped foam infill, please refer to Chapter 6.2.2.

Table 8-1. Foam configurations and mass of each layer (four unit cells)

Foam filler configurations	Foam density (kg/m^3)	Foam shape	Foldcore mass (g)	Foam mass (g)	Increment in mass
TSP	-	-	9.3	-	-
TSP-EPS13.5C	13.5	Cubic	9.3	0.3	3.2%
TSP-EPS19C	19	Cubic	9.3	0.5	5.4%
TSP-EPS28C	28	Cubic	9.3	0.7	7.5%
TSP-PU35C	35	Cubic	9.3	0.9	9.7%
TSP-PU35S	35	Shaped	9.3	1.9	20.4%

8.2.3 Material properties

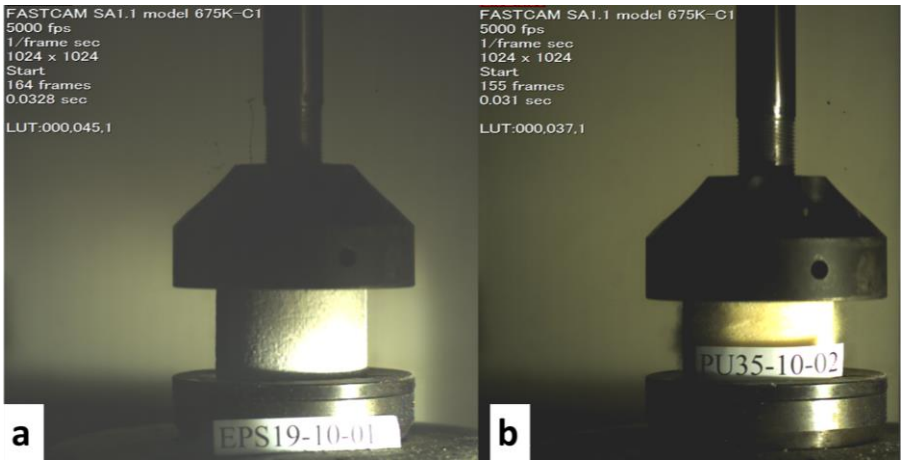

Figure 8-1. Dynamic compression test under 10m/s speed (a) EPS19; (a) PU35 foam

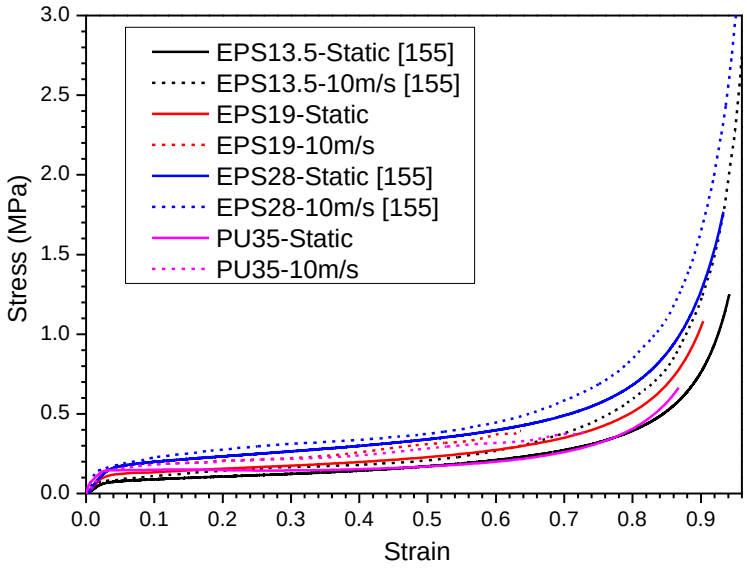

Figure 8-2. Engineering stress-strain curves of EPS13.5 (155), EPS19, EPS 28 (155) and PU35 under 1 m/s and 10 m/s crushing speed

Uniaxial compression tests of EPS19 and PU35 foams were carried out in this chapter under both quasi-static and dynamic loading conditions. Properties of the other two types of foam material, EPS13.5 and EPS28 are obtained from the previous study using the same setting and testing machines (155). The foam specimen with the diameter of 75 mm was used and three specimens are tested for each case. Lloyd-Ametek EZ50 material testing machine was used for quasi-static compression test applied with a constant loading rate of 1 mm/min. The dynamic compressive tests of foam samples were carried out using INSTRON VHS 160/100-20 high speed testing

machine, which is designed to provide constant crushing velocity between 0.1 to 25 m/s. Crushing speed of 10 m/s was tested for both foam and foam filled multi-layer TSP foldcores in the later sections. It is worth noting that the actual crushing speed is not constant throughout dynamic crushing. More details of the dynamic test set-up and actual crushing speed are provided in Chapter 3.2. Photographs of dynamic crushing test on foams are shown in Figure 8-1. Their engineering stress-strain curves under quasi-static and dynamic crushing conditions are shown in Figure 8-2. For material properties of Al 1060 (used for foldcore) and 5083 (used for interlayer plates), please refer to Chapter 7.2.

8.3 Experimental analysis

8.3.1 Quasi-static crushing test

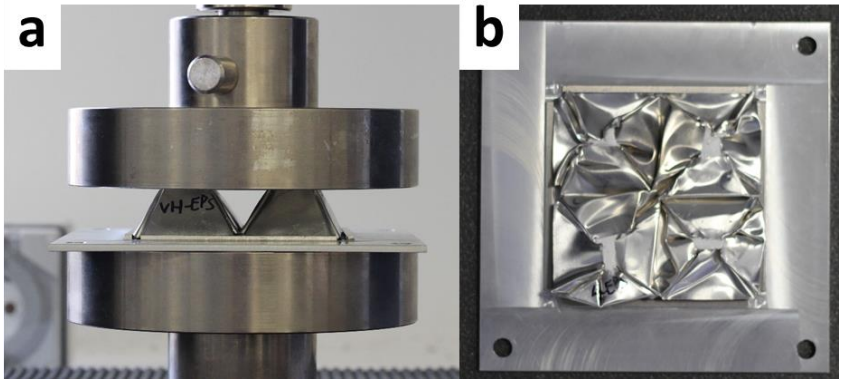

Figure 8-3. Single-layer cubic EPS28 foam filled TSP foldcore (a) during quasi-static crushing; (b) after crushing

Single-layer crushing tests were conducted first for these five foam filler configurations. As found in the previous study (110), under quasi-static loading condition, the single-layer TSP foldcore shows similar overall crushing behaviour as the three-layer TSP foldcore. The average crushing force and the initial peak crushing force are similar for both cases, although the initial stiffness of multi-layer TSP foldcore is slightly lower than that of single-layer foldcore which is caused by the accumulated gaps between core and plates in each layer. The same base plate is used with a 2 mm boundary to constrain the in-plane movement during lateral crushing of the foldcore as shown in Figure 8-3. There is no bonding between the foldcore and the base plate. The loading speed is set as 1 mm/min and the specimens are crushed till around 80% of the total height. The design height of the foldcore is 20 mm for each

layer and 3 mm for the base plate, slight gap between the base plate and the foldcore exists due to the imperfect preparation. This leads to a slightly higher overall height and a lower initial stiffness during crushing.

The representative load-displacement curves of these foldcores under quasi-static crushing are shown in Figure 8-4. Uniform and smooth crushing responses are demonstrated for all foam configurations. Conventional cellular structures such as Miura-type foldcore (82), honeycomb (16) and lattice structure (53) often have non-uniform crushing responses under quasi-static and dynamic crushing, where a relatively large initial peak stress is followed by a sudden decrease in crushing resistance and fluctuation of crushing load throughout deformation. As shown, single-layer foam filled TSP foldcore has no obvious initial peak and the crushing resistance is rather uniform throughout the deformation till crushed distance reaching densification stage at around 60% to 70% of the overall height. This crushing behaviour is very similar to foam materials and is ideal to be used as core sandwich structure for energy absorption purposes (2). With foam filler, the crushing resistance increases without inducing an initial peak force. For the EPS foam filled foldcore, the heavier foam yields a higher enhancement in crushing resistance of foldcores and this enhancement is much greater than the crushing resistance of the foam itself. For instance, the average crushing resistance of foam fillers alone is estimated ranging between 180 N and 410 N, from the measured foam compressive strength and the cross-section area of foam fillers. As given in Table 8-2, the average crushing resistance of TSP foldcore increases from 1.43 kN to 2.55 kN by adding the foam filler. The increase of 1120 N is much higher than the average crushing resistance of foam fillers alone, indicating the interaction between TSP foldcore and the infilled foam further enhances the impact resistance. Similar foam-wall interactions have been investigated and sometimes the contribution from the interaction is greater than the compressive strength of the added foam itself (98). The foam-wall interaction effect also explains the significant increase in crushing resistance of PU shaped foam filled foldcore, as the shaped foam filler has the similar geometry as the TSP foldcore. The shaped foam provides higher constraint to the entire sidewalls throughout crushing than cubic foam filler which has gaps between sidewalls and foam surfaces.

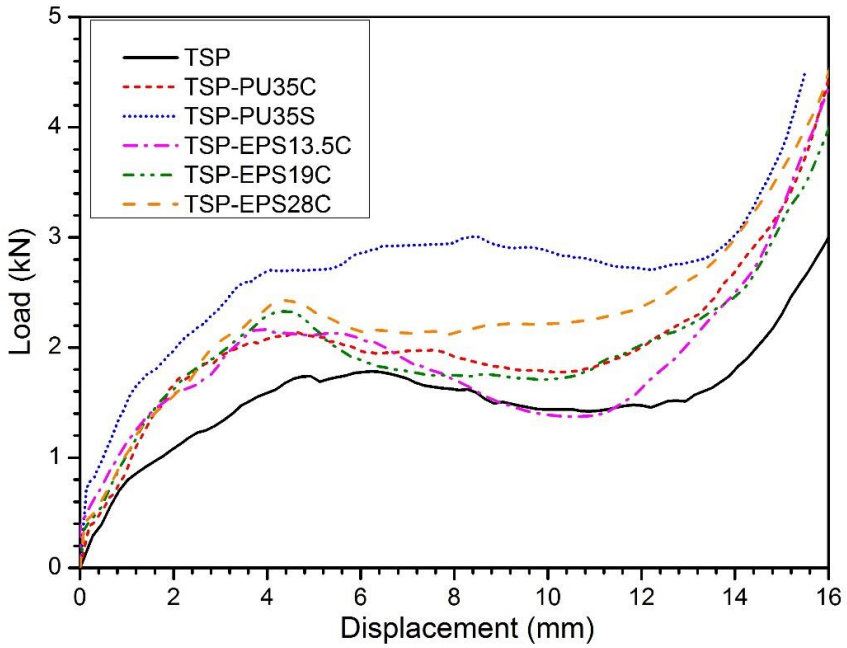

Figure 8-4. Representative load-displacement curves of TSP foldcore with different foam filler configurations under quasi-static crushing

The results including peak and average crushing force, P_{peak} , P_{ave} , increment in P_{ave}, uniformity ratio, U, densification strain ε_D , and specific energy absorption, SEA are listed in Table 8-2. In this chapter, the peak force is taken as the peak value before crushed distance reaches 50% of total core height, the crushing force before densification is generally higher due to the very uniform crushing response of the foldcores. As for many cellular structures, the peak force often occurs at the initial stage of the crushing. Densification crushed distance is defined by the sudden increase of crushing force at the later stage due to compaction of material and is estimated by the starting point of a consistent high slope over a certain distance in the load-displacement curve. Other parameters are calculated as follows

$$P_{ave} = \frac{\int_0^{h_D} P(\mathrm{h}) \cdot dh}{h_D} \tag{8-1}$$

$$SEA = \frac{\int_0^{h_D} P(\mathrm{h}) \cdot dh}{m_{TSP} + m_{foam}} \tag{8-2}$$

$$\varepsilon_D = \frac{h_D}{H} \tag{8-3}$$

where P is the crushing force, h is the crushed distance, h_D is the crushed distance at densification, m_{TSP} and m_{foam} are the mass of TSP foldcore and foam filler, respectively, ε_D is the densification strain, H is the overall height of the foldcore.

Table 8-2. Summary of crushing response of single-layer foam filled foldcores under quasi-static crushing

Foam filler configurations	P_{peak} (kN)	P_{ave} (kN)	Increment in P_{ave}	U= P_{peak} /P_{ave}	ε_D	SEA (J/g)
TSP	1.78	1.43	-	1.245	0.70	2.16
TSP-EPS13.5C	2.17	1.65	15.4%	1.312	0.61	2.11
TSP-EPS19C	2.33	1.82	28.0%	1.280	0.71	2.64
TSP-EPS28C	2.43	2.06	44.1%	1.180	0.68	2.79
TSP-PU35C	2.14	1.81	26.6%	1.182	0.68	2.40
TSP-PU35S	3.01	2.55	78.3%	1.180	0.69	3.14

An increase in average crushing force of foam filled TSP foldcore is observed. Up to 78.3% increase is observed for PU shaped foam filled foldcore than TSP foldcore without foam while the uniformity ratio remains similar. The significant increase in average crushing force is due to the inclined geometry of TSP foldcore sidewalls which are connected via triangular interconnections. The unique tapered geometry reduces the initial stiffness of the structure as compared to straight tubes, honeycombs and Miura-type foldcores. The interaction effect between foam and foldcore walls remains, resulting in a higher average crushing force. Likewise, the specific energy absorption of the foam filled foldcore is higher than that of TSP without foam filler, except TSP-EPS13.5C which has a lower densification strain. A 45% increase in SEA is shown for shaped PU foam filled foldcore, from 2.16 to 3.14 J/g while the mass and density increment is 20.4% over the case without foam filler. For comparison, these foam filled foldcores have much higher SEA than many conventional energy absorbing aluminium structures with similar relative densities (2.7% for TSP foldcore without foam filler), e.g. SEA of CYMAT aluminium foam ranges between 0.5-0.8 J/g (3.1% relative density), aluminium eggbox with constrained boundary is around 1 J/g (2.8% relative density) and aluminium eggbox (3.5% relative density) with bonded boundary is about 2 J/g (46). The Al 1050 H111 alloy was used for the eggbox preparation in the above-mentioned study, which has similar mechanical properties

and chemical composition (minimum 99% aluminium by weight (150)) as Al 1060 alloy used in this study.

8.3.2 Dynamic crushing test

For dynamic testing machine and test set-up please refer to Chapter 7.4.1. Core densities of foam filled three-layered TSP foldcore are listed in Table 8-3, which are calculated using the volume of 80×80×20 mm. It is similar to the volume used in the relative density calculation of TSP foldcore without foam infill. Three specimens are tested for each configuration. The representative curve from three test results is selected for result analysis.

Table 8-3. Core densities of three-layered foam filled TSP foldcores for dynamic crushing test

Foldcores	**3TSP**	**3TSP-EPS13.5C**	**3TSP-EPS19C**	**3TSP-EPS28C**	**3TSP-PU35C**	**3TSP-PU35S**
Core density (kg/m^3)	73	75	77	78	80	88

8.3.2.1 Dynamic crushing speed

For the information about crushing speeds, please refer to Chapter 7.4.2. The crushing speed is set as 10 m/s for all tests. It is worth noting that the actual impact speed is slightly smaller than the desired moving speed of 10 m/s when the crushing head is in contact with the sample. As the actual crushing speed is not a constant value, the crushing speed in this study only refers to the designated speed of the test, instead of the actual crushing speed. The maximum strain rate demonstrated in this study is calculated around 150 s^{-1}, which is a typical intermediate strain rate (156).

8.3.2.2 Results comparison

The load-displacement curves of multi-layer foldcore samples under 10 m/s dynamic crushing are shown in Figure 8-5. The results of these six different foam filler configurations are shown separately in two charts for clarity. Fluctuations are observed in all the curves under dynamic crushing compared to quasi-static loading conditions. Distinct enhancements in crushing resistance are observed for TSP foldcore with foam filler. As expected, heavier foam provides higher enhancement of crushing resistance

to the multi-layer foldcore, as higher density leads to higher plateau stress for the same type of foam material. Furthermore, the structure with shaped PU foam filler has a much higher crushing resistance than the structure with cubic PU foam filler, as shaped foam has a larger mass and provides better support to the tapered sidewalls of TSP foldcores than cubic foam filler. It is also noted that the initial stiffness of the structures is relatively low at the very beginning of the deformation around 0-3 mm displacement, as a result of the incomplete contact of the foldcores and plates. Due to the fabrication induced imperfections, slight gaps exist between foldcore and plate at each layer, which lowers the initial stiffness at the early stage of the loading.

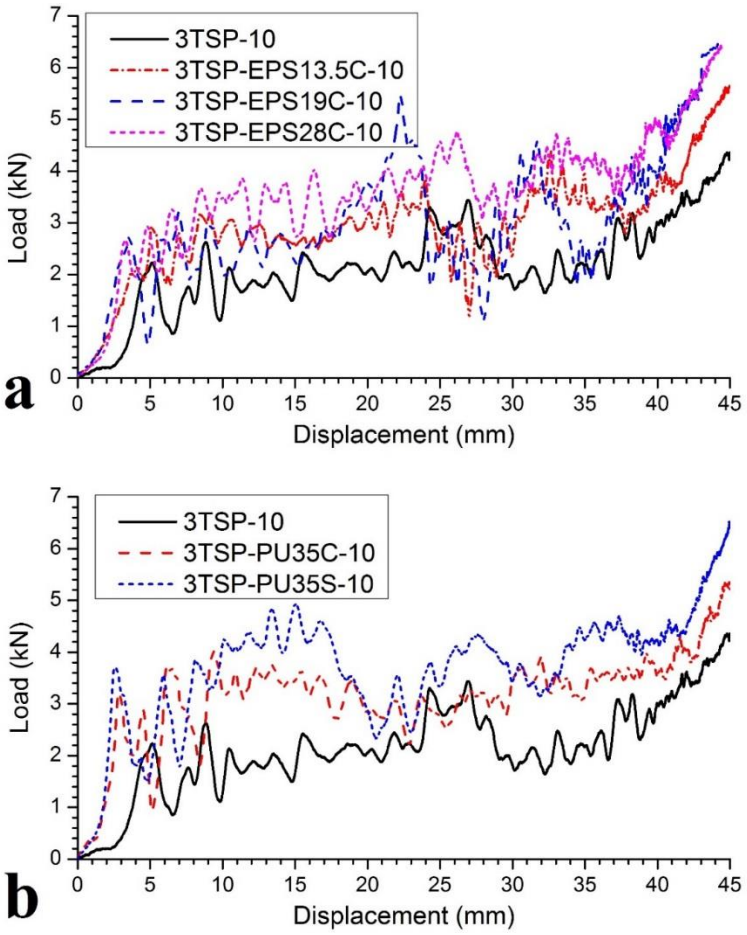

Figure 8-5. Load-displacement curves of (a) EPS foam filled multi-layer TSP foldcores; (b) PU foam filled multi-layer TSP foldcores; under 10 m/s crushing

Other data of structural response are listed in Table 8-4. Similar to the Chapter 8.3.1, the densification strain, ε_D is estimated by the crushed distance where the sudden increase of crushing force occurs, dividing the overall height of the foldcore. The average crushing force is averaged from the beginning till the densification of the core.

The densification strains of these foam filled foldcore under 10 m/s crushing are similar to single-layer foldcores crushed under quasi-static loading condition. The uniformity ratio, which is the ratio between peak and average crushing force, remains between the values of 1.32 to 2.05, which is slightly higher than the quasi-static crushing of the single-layer foldcore. The increase is caused by the dynamic effect of the foldcore structures and the interaction with the foam material. The increase may be also caused by the fluctuation in recording data under 10 m/s loading rate. However, the slight increase in uniformity ratio with increasing crushing speed is minimal comparing to many conventional structures, such as honeycomb, cube strip and Miura-type foldcore, where their peak crushing force as well as uniformity ratio can increase several times under dynamic loading (17, 78, 82, 146) as compared to the quasi-static loading condition.

Table 8-4. Summary of crushing response of multi-layer foam filled foldcores under 10m/s crushing

Foam filler configurations	**P_{peak} (kN)**	**P_{ave} (kN)**	**Increment in P_{ave}**	**U= P_{peak} /P_{ave}**	**ε_D**	**SEA (J/g)**
3TSP-10	3.44	1.94	-	1.773	0.65	2.70
3TSP-EPS13.5C-10	4.38	2.69	38.7%	1.628	0.63	3.53
3TSP-EPS19C-10	5.44	2.65	36.6%	2.053	0.59	3.20
3TSP-EPS28C-10	4.76	3.40	75.3%	1.400	0.68	4.62
3TSP-PU35C-10	4.01	3.04	56.7%	1.319	0.71	4.25
3TSP-PU35S-10	4.92	3.53	82.0%	1.394	0.70	4.41

Significant improvement in both the average crushing force and specific energy absorption can be observed for all foam filled structures. The increases in average crushing force and specific energy absorption for foam filled structure range from 36.6% to 82% and from 18.5% to 71.1%, respectively. Among the five foam filler configurations, shaped PU foam filled TSP foldcore has the highest average crushing resistance, i.e., 82% higher than that without foam filler. EPS28 cubic foam filled TSP foldcore, however, has the highest specific energy absorption among these foam configurations. As shown in Figure 8-2, the EPS28 foam material has higher crushing resistance than PU35 material especially at the later stage of the crushing.

8.3.3 Damage modes

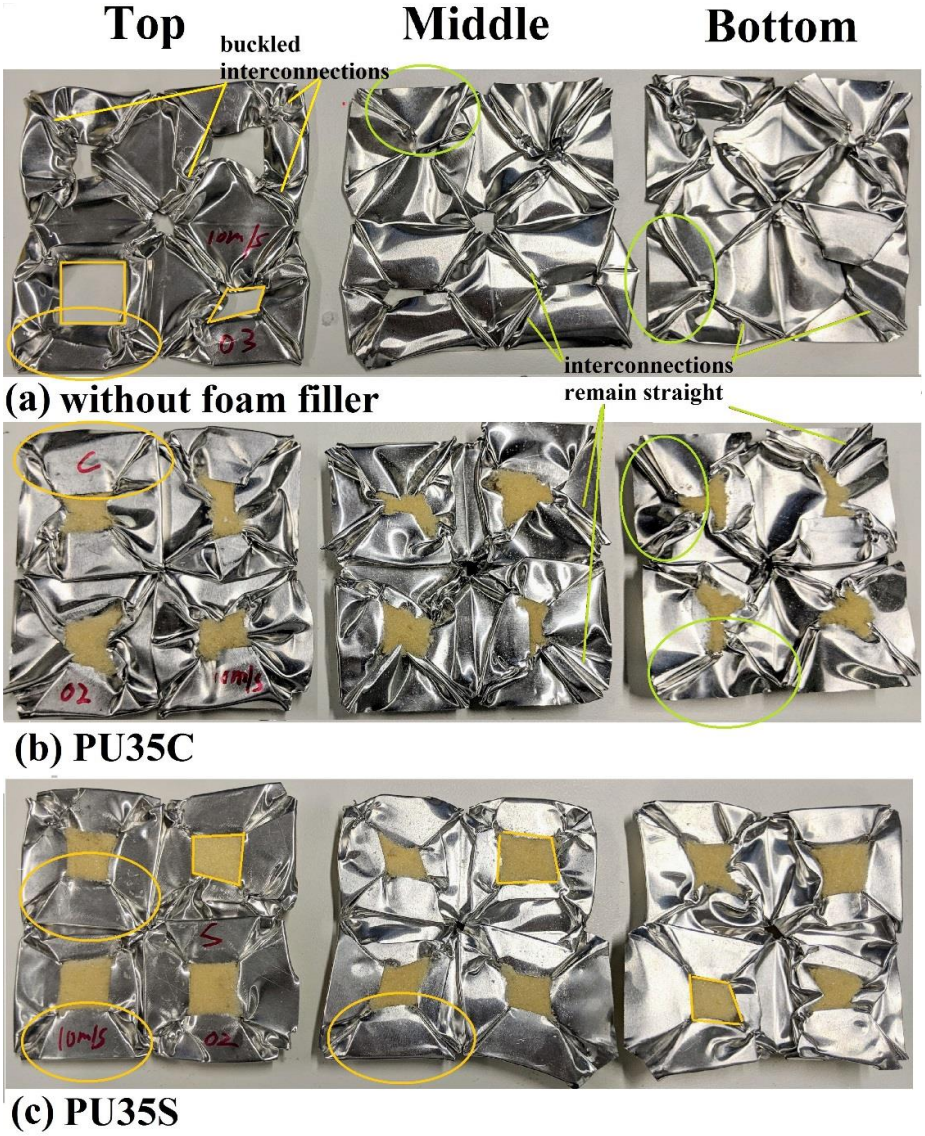

Figure 8-6. Damage modes of individual layers of (a) TSP foldcore without foam, (b) with cubic PU foam and (c) with shaped PU foam after crushing, two damage modes are marked out in yellow and green

Damage modes of these foam filled multi-layer foldcores are shown in Figure 8-6 and Figure 8-7. For TSP foldcore without foam filler, two distinct damage modes are observed on different layers. On the top layer, the sidewalls bend towards outside horizontally, the top edges around the square opening remains its shape as marked out in yellow colour in Figure 8-6. The interconnections which connect the adjacent sidewalls are buckled and twisted on the top layer. No corner lift-up is observed for this damage mode on the top layer. For the middle and bottom layers of TSP foldcore

without foam filler, the damage mode of the structure is quite different. Sidewalls bend inwards along their vertical middle line of the trapezoid sidewalls as circled in green colour. The top edges of sidewalls are also deformed, resulting the closing of the top square shaped openings on the middle and bottom layers after crush test. The interconnections are less deformed in this damage mode and remain straight as marked out. Furthermore, corner lift-up can be also observed in this damage mode. A computed damage modes comparison between the top and middle layer of TSP foldcore without foam filler is shown in Chapter 8.4.3 for illustrating the difference of these two damage modes. The change in damage mode is caused by the increase of loading rate and the inertia effect of the top layer under dynamic impact. As previously studied (146), the damage mode of TSP foldcore changes from the vertical inward bending of sidewalls (marked in green) to outwards horizontal bending (marked in yellow) with the increasing loading rate. For these tests, the crushing speed is different at each layer. The top layer experiences the highest crushing force once the crushing head and foldcore are in contact and the crushing speed is continuously reduced to zero once it reaches 45 mm of stroke.

For the cubic PU foam filled TSP foldcore under dynamic crushing, the corresponding damage mode of each layer is similar to those without infilled foam. The square openings remain their shapes after crushing and sidewalls bend towards outside with almost no corner lift-up observed on the top layer. Other damage mode is observed on the middle and bottom layers. The square openings of the middle and bottom layers are not fully closed in this case as compared to TSP foldcore without foam infill. The remained openings are due to the extra resistance at each unit cell centre provided by the added foam material. The shaped PU foam filled TSP folded structure has a quite different damage mode as comparing with the cases of no foam filler and with cubic PU foam filler. Only one damage mode is presented on all three layers for the shaped PU foam filled structure. No inward vertical bending of the sidewalls occurs on the middle and bottom layers which are presented in both the previous two cases (no foam filler and cubic PU foam filler). The corner lift-up does not occur for all three layers either. Due to the presence of shaped PU foam, the damage mode associated with sidewalls inwards vertical bending is much harder to occur. Shaped foam provides much more support to the sidewalls as they both have similar geometries. Therefore, it is easier for sidewalls of foldcore to bend outwards horizontally as in the first

damage mode. It is also worth noting that some part of foldcore expends outside the boundary after crushing as shown in Figure 8-6 (c). This might be caused by the compression of the shaped foam around the outer edges.

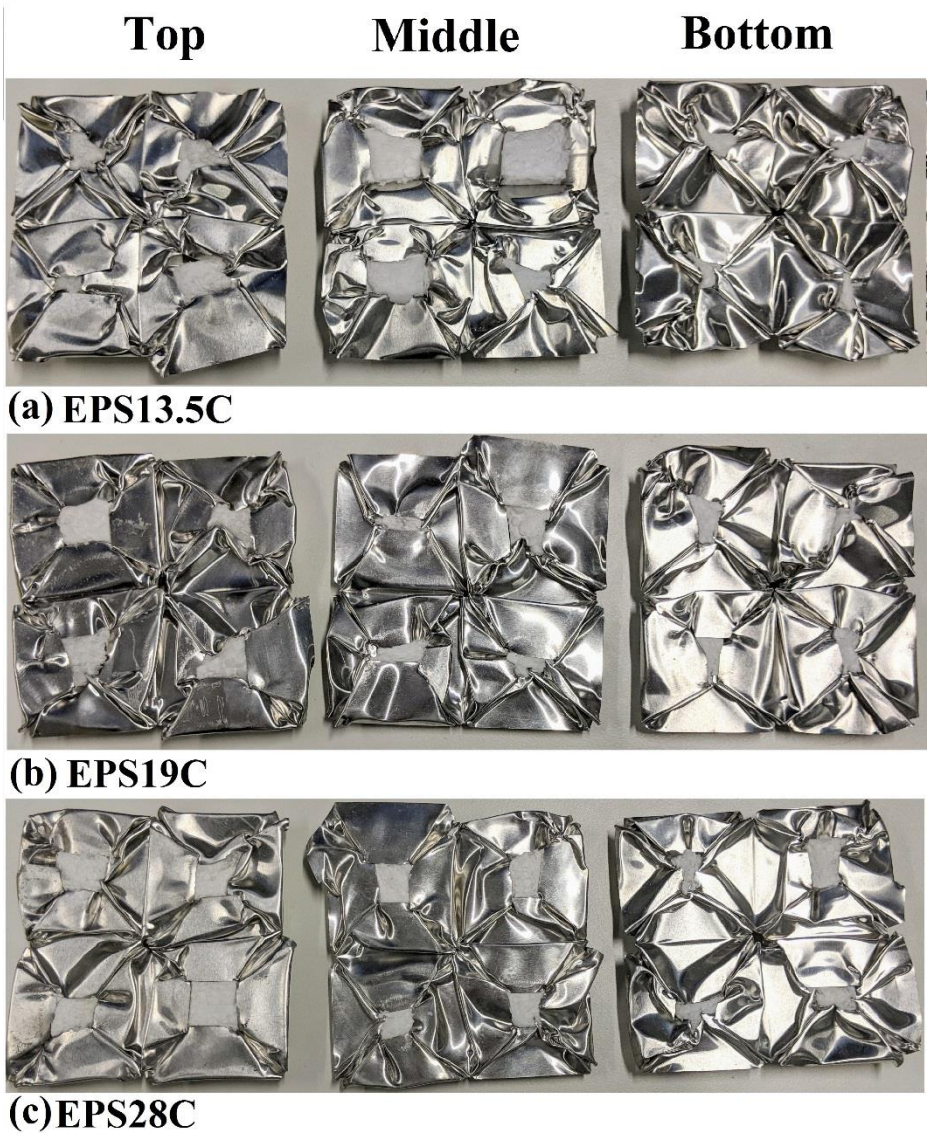

Figure 8-7. Damage modes of individual layers of different EPS cubic foam filled foldcores under crushing

As shown in Figure 8-7, EPS foam filled multi-layer TSP foldcore shows similar damage modes with the corresponding layers of TSP foldcore and cubic PU foam filled foldcore. Both damage modes are presented in all three cubic EPS foam configurations. The square openings at the centre of each unit cell better remain their square shapes with the heavier foam filler added, as can be seen from EPS13.5C to EPS19C to EPS28C. The heavier foam filler has a higher compressive strength which

provides more support to the top edges of the sidewalls. Therefore, with the heavier foam, it is harder for foldcore sidewalls to undergo vertical inwards bending and the top square opening can better remain their shape.

8.4 Finite element analysis

8.4.1 Finite element model

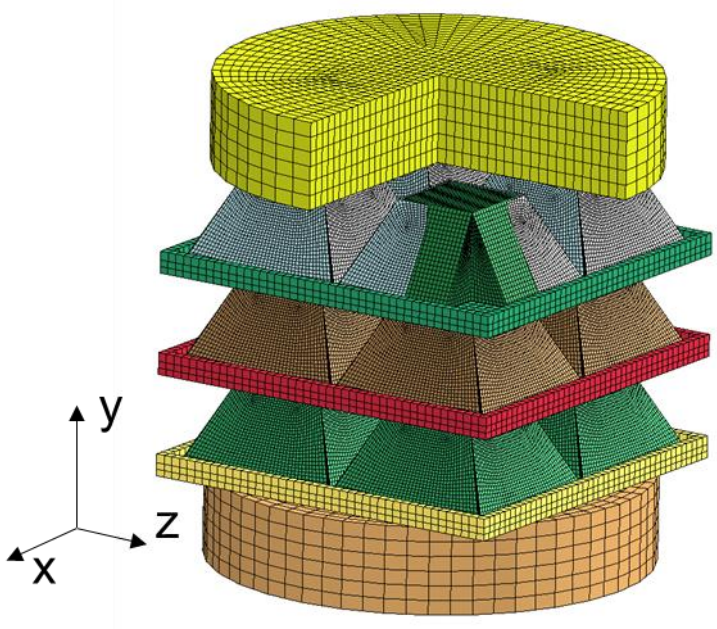

Figure 8-8. Numerical model of crushing setup for shaped foam filled three-layered TSP foldcore; note: portion of crushing disk and top layer TSP foldcore is removed for illustration

Finite element analysis of the foam filled multi-layer TSP foldcores is carried out. Finite element software LS-DYNA is used for the simulations. The TSP foldcores are modelled using shell element and the foam material, plates and crushing disk are modelled using solid element. 2 mm high boundary of the plates are modelled as well as shown in Figure 8-8. The cylindrical crushing disk and base have the diameter of 100 mm. As observed in the crushing test, the deformation of the interlayer plates between foldcore layers is minimal and therefore ignored in the numerical simulation. Interlayer plates, base support and top crushing disk are all modelled as rigid block. Base support was fixed in all six degrees of freedom and crushing disk is fixed in five degrees of freedom with lateral movement in the y direction allowed. No constraint is applied on the interlayer plates.

To minimize the uncertainties, the actual crushing speed of the crushing disk derived from the dynamic crushing test shown in Figure 7-9 (b) is applied on the crushing disk in the numerical models to simulate the changing crushing speed. Material parameters used for EPS, PU foam, 1060 aluminium sheet and aluminium 5083 alloy are listed in Chapter 8.2. Neither glue nor other fixing is considered in the numerical models, same as in the experiment. A friction coefficient of 0.25 is considered for all interfaces (87). Mesh convergence tests of both TSP foldcore and foam material have been carried out in the previous study (136).

8.4.2 Comparison with experimental results

The load-displacement curves of the multi-layer TSP foldcores with different foam filler configurations under 10 m/s crushing are shown in Figure 8-9. The average crushing forces and peak crushing forces from both the FE simulation and tests are marked out for all the cases. Overall, the FE results match well with the test data. The initial peak force at around 5 to 10 mm displacement match well between the two curves for all cases. The first initial peak force corresponds to the initiation of the sidewall buckling of the TSP foldcore. The average crushing forces are in good agreement as well, while some large fluctuations in the later stage are observed in the numerical results. Displacement fluctuations of 3TSP-10 (20-30mm), 3TSP-EPS19C-10 (28-35 mm) and 3TSP-PU35S-10 (27-37 mm) are captured in numerical simulations and well match the experimental data. These fluctuations correspond to the collapsing of the layers. However, the initial stiffness of the structures in all cases from finite element results is higher than the test data. The gradient of all FE curves at initial stage (0 to 2 mm displacement) is higher than the test data, due to the imperfections induced during the sample preparation. Minor bending of the sidewalls, slight gaps between foldcore and plates can lead to the lower initial stiffness. The focus of this chapter is to observe the crushing behaviour and examine the energy absorption of the proposed foam filled folded structures, therefore these minor variations between the FE and test results can be neglected. The overall crushing behaviour and energy absorption from both the numerical simulations and tests match well under the large deformation of the structures.

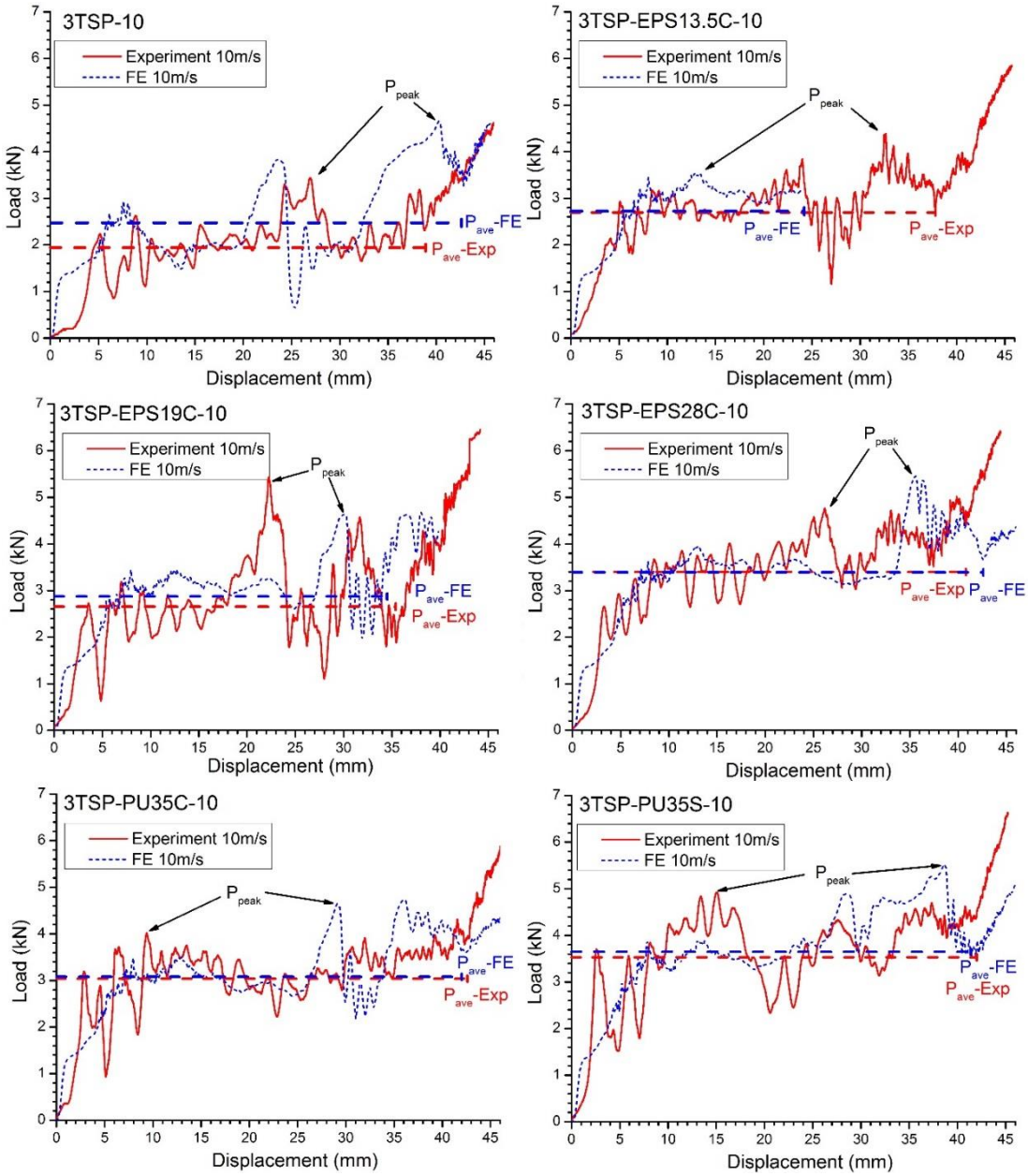

Figure 8-9. Load-displacement curves of multi-layer TSP foldcores with five foam configurations under 10 m/s crushing

Parameters including peak and average crushing force, densification strain and specific energy absorption from both FE and experimental data of these foldcores are listed in Table 8-5. Similar to the load-displacement curves, the average crushing forces are in good agreement for the foam filled foldcores, while discrepancies exist between FE and test results for TSP foldcore without foam filler. Relatively smaller discrepancies of the cases with foam filler indicate that the added foam may help mitigate some of the effect caused by imperfection during specimen preparation. For the case without foam filler, imperfections on sidewalls may locally change the

deformation mode of foldcore. With cubic or shaped foam material added in the centre of each unit cell of the foldcore, extra support provided to foldcore sidewalls makes vertical inwards bending more difficult to initiate and reduces the influence of local imperfections. Higher density of foam filler tends to increase the crushing resistance and the specific energy absorption of the structure. Structure with shaped PU35 foam has the highest average crushing resistance, while cubic EPS28 foam filled structure possess the highest SEA due to the stronger yet lighter EPS foam material as shown in Figure 8-2.

Table 8-5. Comparisons between FE and experimental data of multi-layer foldcores with different foam filler configurations Note: Due to large deformation of the foam material and the significant difference of elastic modulus between aluminium 1060 sheet and EPS13.5, the numerical simulation of 3TSP-EPS13.5C-10 terminates half way and the numerical results are not presented herein.

Foam filler configurations	**P_{peak} (kN)**			**P_{ave} (kN)**			**ε_D**		**SEA (J/g)**	
	Exp	**FE**	**Diff**	**Exp**	**FE**	**Diff**	**Exp**	**FE**	**Exp**	**FE**
3TSP-10	3.44	4.65	35.2%	1.94	2.47	27.3%	0.65	0.71	2.70	3.79
3TSP-EPS13.5C-10	4.38	-	-	2.69	2.72	1.1%	0.63	-	3.53	-
3TSP-EPS19C-10	5.44	4.65	-14.5%	2.65	2.87	8.3%	0.59	0.58	3.20	3.38
3TSP-EPS28C-10	4.76	5.46	14.7%	3.40	3.39	-0.3%	0.68	0.71	4.62	4.71
3TSP-PU35C-10	4.01	4.64	15.7%	3.04	3.08	1.3%	0.71	0.70	4.25	4.24
3TSP-PU35S-10	4.92	5.52	12.2%	3.53	3.65	3.4%	0.70	0.69	4.41	4.52

8.4.3 Comparison of damage modes

The comparison of multi-layer TSP foldcore without foam filler at around 15 mm of crushed distance is shown in Figure 8-10. The damage mode from numerical simulation agrees well with that observed in the test. Comparison of the damage modes on the top and middle layers of TSP foldcore without foam filler obtained from numerical simulation is shown in Figure 8-11. For the top layer of the multi-layer foldcore, the sidewall bends out horizontally. For the middle and bottom layers,

however, the sidewalls bend vertically towards centre of the unit cell. This damage mode leads to lift-up of the corners and the joint lines connecting the adjacent sidewalls remain straight in the middle and bottom layers. As shown in Figure 8-6 (a), the interconnections are buckled and twisted under the first damage mode of the top layer.

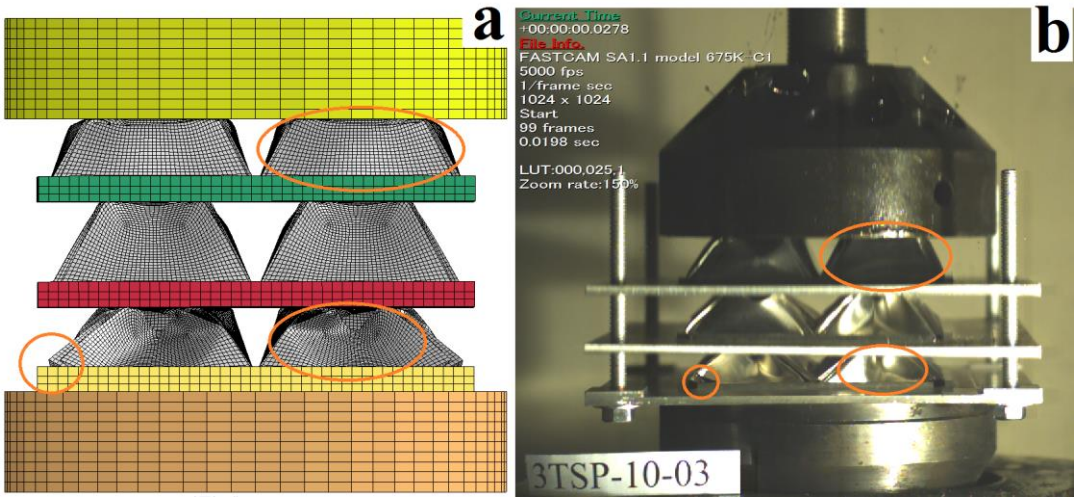

Figure 8-10. Damage modes of TSP foldcore without foam fillers in (a) FE simulation and (b) crushing test at approximately 15 mm displacement

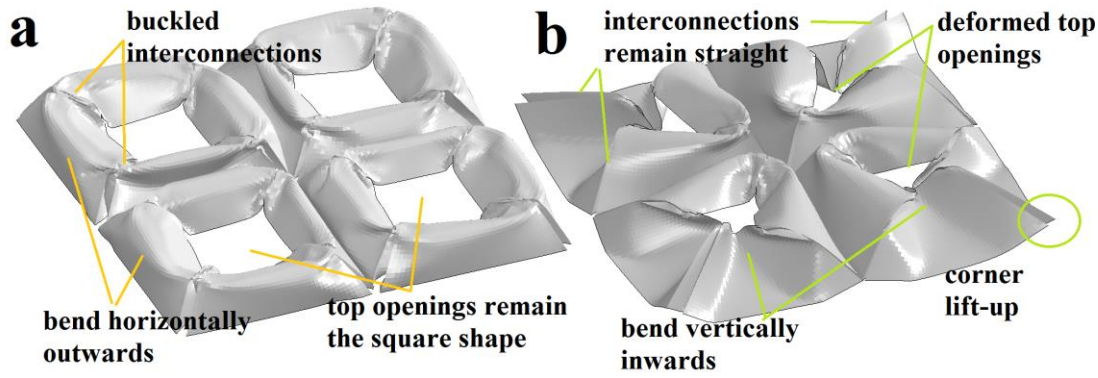

Figure 8-11. Computed damage modes of TSP foldcore without foam filler under 10m/s crushing on (a) top layer; (b) middle layer, note: these images are not captured at the same time as two layers are not deformed simultaneously

The computed damage modes of three typical foam filled multi-layer TSP folded structures are shown in Figure 8-12. Three sets of damage modes are presented on three structures and the similarity in damage mode of each set is demonstrated with crushing tests. For TSP folded structure without foam filler, the top layer shows different damage mode from the middle and bottom layers. The sidewalls bend

horizontally outwards, resulting in the top square opening of each unit cell remains their shape and no corner lift-up is observed. As for the middle and bottom layers, the outer sidewalls bend vertically towards the centre of each unit cell, therefore resulting in the deformation of the top square opening and leading to corner lift-up, which can be also observed on the bottom layer shown in Figure 8-10.

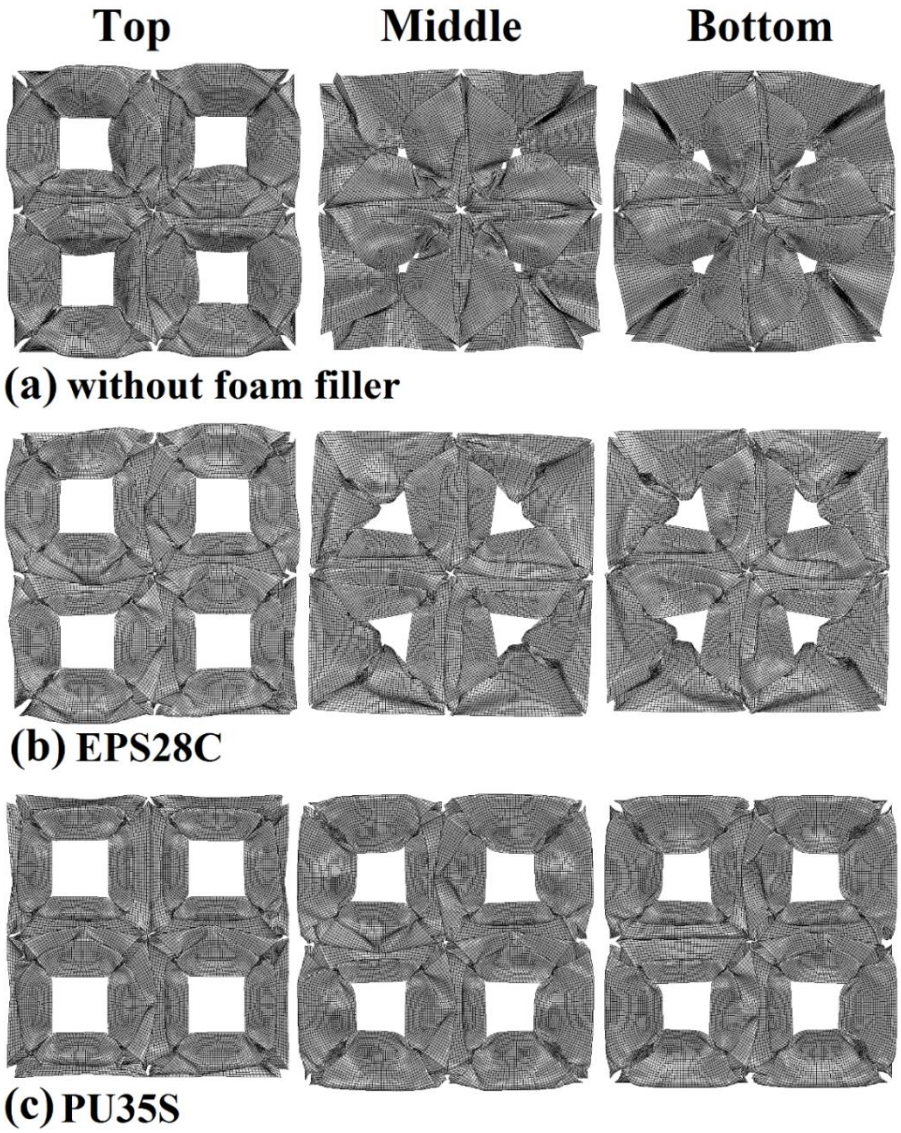

Figure 8-12. Damage modes of three layers of TSP foldcores without foam, with cubic EPS28 foam and with shaped PU35 foam after crushing

For the folded structure with cubic EPS28 foam filler, the damage modes are similar to the case without foam filler. The square openings are clearly demonstrated on the top layer, while these are more or less deformed on the middle and bottom layers. Due to the resistance provided by the filled cubic foam, these openings are less deformed

after crush, while the openings are almost fully closed due to the deformation for the case without foam filler. Less corner lift-up on the middle and bottom layers of the EPS foam filled structure is displayed for the same reason. Only one type of damage mode is shown in three layers of shaped PU foam filled TSP folded structure. Only horizontal bending and buckling of the sidewalls are presented, the top edges of the sidewalls remain straight and the square openings are not deformed after being crushed. The shaped foam has the almost identical slope as the inclined walls of the TSP folded structure, which provides resistance and interacts with the cell walls during the deformation. The added foam filler leads to the change of damage mode for the middle and bottom layers and the improvement in crushing resistance under dynamic crushing as well.

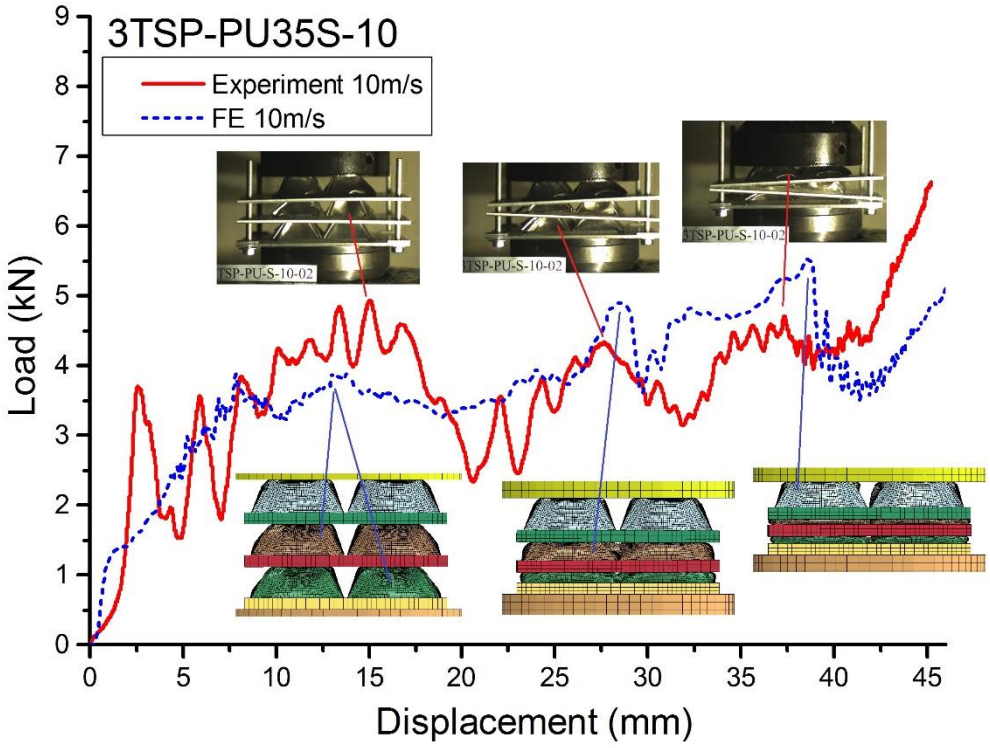

Figure 8-13. Correlation between layer deformation and load-displacement response of three layer shaped PU foam filled TSP folded structure under 10m/s crushing

The correlated deformation modes of three layers of the shaped PU foam filled TSP folded structure are shown in Figure 8-13. The side views of the folded structure from both high speed camera images and FE simulation are compared. For load-displacement curve of test result, three peak values can be identified, and correlate to the buckling of the middle, bottom and top layer, respectively. Slight tilting of the

interlayer plates and uneven deformation of same-layer unit cells are also observed, resulting the slight fluctuation of the load-displacement curve as compared to FE results. For FE simulation of the shaped PU foam infill configuration, the middle and bottom layer deform at same time, while bottom layer reach fully compacted state earlier than middle layer at about 27 mm of displacement. After the densification of bottom and middle layer, the half-crushed top layer further buckles which results a peak load at about the 37 mm marked. This layer crushing order is similar for both FE and test results.

Overall, the damage modes of both computed results and crush tests are in very good agreement. However, the deformation in FE results is more symmetric and uniform, whereas the deformation in crush tests is not necessarily symmetric and uniform. Furthermore, some bottom edges bend over the 2 mm high boundary of the inter-layer plates. All the foldcores stay well inside the boundary after the crushing. These discrepancies might be caused by the imperfections of the samples and slight tilting of the interlayer plates during the crushing. As the slight gaps exist between foldcore and plates, sidewalls slightly bend during folding process and the unit cells of foldcore are not necessarily at the same height level. These leads to a slight reduction in initial stiffness of the structure, as well as the crushing resistance and energy absorption. More precise manufacturing process and better design of the multi-layer set-up could be applied in the future to minimize these imperfections.

8.5 Summary

In this chapter, structural responses of foam filled multi-layer truncated square pyramid (TSP) kirigami structures under dynamic loading are investigated in experimental and FE analysis. Five different foam filler configurations are considered and compared with the case without foam filler. For these five cases: cubic EPS13.5, cubic EPS19, cubic EPS28, cubic PU35, shaped PU35 foam filler, the increase in crushing resistance and the improvement in specific energy absorption are demonstrated. Due to the interaction between the folded structure and the foam material, up to 82% increase in average crushing resistance is shown with only 3% to 20% increment in weight. Among these foam filler configurations, cubic EPS28 infill results in the highest increase in specific energy absorption (SEA), and shaped PU35 foam infill leads to the highest increase in average crushing force under dynamic

loading, which is due to the higher compressive strength of EPS28 foam than PU35 foam. However, shaped foam shows a greater improvement in crushing resistance due to better interaction between foam and cell walls. The uniform crushing responses can be observed for all foam fillers with a uniformity ratio less than 2.0 under both quasi-static and 10 m/s crushing, whereas the uniformity ratio can reach 4.0 for some existing sandwich structures under dynamic crushing (146). As discussed in Chapter 8.3.1, the specific energy absorption of the proposed structure (2.16-3.14 J/g under quasi-static loading) is much higher than conventional cellular structure such as aluminium foam (0.5-0.8 J/g) and aluminium eggbox (1-2 J/g) of the similar density and similar material. This indicates great potential of the proposed foam filled multi-layer TSP kirigami structure for energy absorption applications.

Chapter 9. Experimental study of functionally graded multi-layer folded TSP folded structure with foam filler under dynamic crushing

The related work in this chapter has been published in Composites Part B: Engineering.

Li Z, Chen W, Hao H. Functionally graded truncated square pyramid folded structures with foam filler under dynamic crushing, Composites Part B. 2019:177:107410. DOI:10.1016/j.compositesb.2019.107410

9.1 Introduction

As demonstrated in Chapter 8 and 9, multi-layer TSP foldcores with/without foam fillers have good energy absorption performance under dynamic loads. In this chapter, three-layer TSP folded structure with different foam fillers is designed to achieve a layer-by-layer functionally graded sandwich structure (i.e. negatively and positively graded). Functionally graded materials (FGM), where the material properties vary layer-by-layer or gradually within the material, are used as cores for sandwich structures. The varying material properties can be achieved by changing cell size, wall thickness and density. Many stepwise and continuously graded structures including corrugated (68), honeycomb (157, 158), foams (19), stacked Miura-type foldcore (159) and lattice (160, 161) were investigated. Improved energy absorption and crushing behaviour are shown for functionally graded structures than their uniform counterpart under impact or blast loading. It is worth noting that many existing graded structures are permanently bonded between layers and some complex graded structures such as lattice structures can only be manufactured by additive manufacturing (160, 161), which limits the size of the structure and can be costly.

In this chapter, two sets of foam fillers are used. For the first set, three different densities of cubic expanded polystyrene (EPS) foam fillers are inserted into three layers of foldcore. For the second set, shaped and cubic rigid polyurethane (PU) foam fillers are inserted into two layers with no foam filler added in the third layer. Two different foam filling orders including positively and negatively graded are considered for both sets of EPS and PU foam. These foam filled graded multi-layer TSP structures

along with the uniform TSP structure without filler are tested under different impacting speeds. Crushing response and energy absorption are compared for the different set-ups.

9.2 Layer geometry

9.2.1 Folding geometry of foldcore

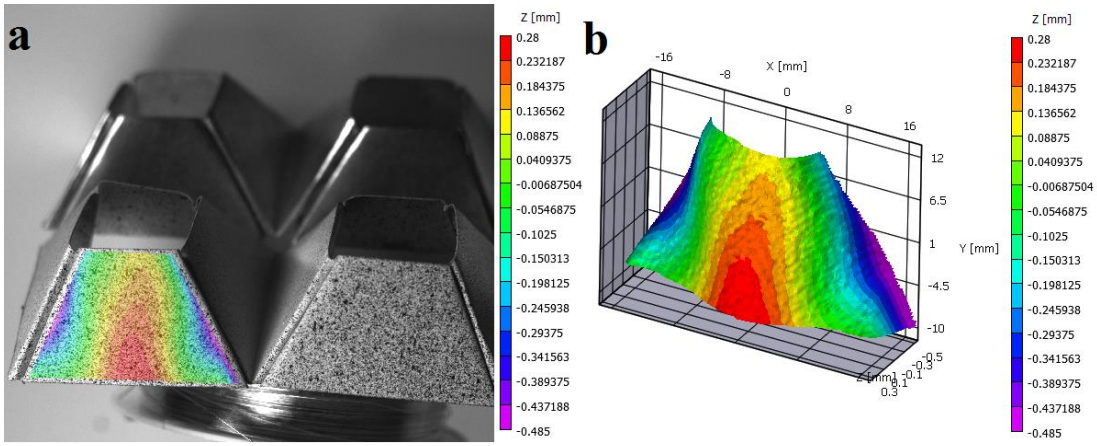

Figure 9-1. (a) Surface flatness analysis of one sidewall of TSP foldcore using 3D direct image correlation (DIC); (b) sidewall model reconstruction

For geometries of the truncated square pyramid (TSP) foldcore specimen, please refer to Chapter 4.2. All testing specimens are prepared by hand folding the patterned aluminium sheets. Imperfections cannot be avoided in this process on the bent sidewalls with uneven levelling for unit cells on the same layer which results in the gaps between foldcore and supporting plate, as well as uneven initial contact of top edges of foldcore to crushing head. The measured height of foldcore specimens varies between 21 to 23 mm, slightly larger than the designed height of 20 mm. These imperfections could lead to reduction in initial stiffness of the proposed TSP foldcore while the overall crushing response and energy absorption are barely affected. As shown in Figure 9-1, 3D Direct Image Correlation (3D DIC) analysis is carried out to evaluate the surface flatness of the sidewalls of folded specimens. The maximum difference on the sidewall is about 0.765 mm (-0.485 mm to 0.28 mm) over the length of 40 mm of the bottom edge, as shown in the scale legend in Figure 9-1. Some imperfections such as bending or torsion may still exist on triangular interconnections between sidewalls and around the crease lines. Overall, the finishing of the TSP foldcore specimens is acceptable. It should be noted this manufacturing error is also

observed even in some of machine pressed Miura-type foldcores in previous studies by other researchers (81), and cannot be completely eliminated. Such errors can be reduced by more advanced machine folding.

9.2.2 Foam filler configurations and multi-layer set-up

Five different graded configurations are listed in Table 9-1. These include a uniform multi-layer folded structure without filler, two sets of negatively and positively graded multi-layer folded structures achieved by varying foam filler densities and shapes. A total of five different types of foam fillers are inserted into the foldcores: cubic expanded polystyrene (EPS) with densities of 13.5, 19 and 28 kg/m^3, cubic and shaped rigid polyurethane (PU) foam with density of 35 kg/m^3. The densities of foam filled TSP core range between 75 and 88 kg/m^3, where a TSP foldcore without foam filler has a density of 73 kg/m^3 (2.7% relative density). Based on previous investigation of multi-layer folded structure with uniform foam fillers, the crushing resistance of the foam filled structure is proportional to the foam strength and the support provided from foam to the foldcore (111). The positively graded structure is defined as increasing density and crushing strength from top to bottom layer, and the negatively graded is defined as opposite. The notations of these structures are listed in Table 9-1. For instance, 3TSP-EPS-C-NG represents three-layer truncated square pyramid structure filled with negatively graded cubic EPS foam fillers from the top to the bottom layer.

Table 9-1. Five graded configurations and total weight of the foldcore

Notation	**Graded order**	**Foam filler (kg/m^3)**			**Total mass (g)**
		Top layer	Middle layer	Bottom layer	
3TSP	Uniform	-	-	-	28.1
3TSP-EPS-C-PG	Positively graded (PG)	Cubic EPS13.5	Cubic EPS19	Cubic EPS28	29.6
3TSP-EPS-C-NG	Negatively graded (NG)	Cubic EPS28	Cubic EPS19	Cubic EPS13.5	29.6
3TSP-PU-PG	Positively graded (PG)	-	Cubic PU35	Shaped PU35	30.9
3TSP-PU-NG	Negatively graded (NG)	Shaped PU35	Cubic PU35	-	30.9

The geometry of the two shapes of foam filler and the graded multi-layer set-up are shown in Figure 9-2. Four units of foam filler are inserted into each layer of foldcore, achieving graded effect on different layers. Each layer of foldcore and foam filler is separated by interlayer plate made of Al 5083 with thickness of 3 mm. To constrain the in-plane movements of foldcore sidewalls, 2 mm high boundary curbs are also included on the interlayer plates along the four sides. Thread rods are bolted onto base plate and function as guide for interlayer plates to move in the vertical direction. The holes located at four corners of the plates have diameter of 8 mm, sufficiently larger than the M6 threaded rods of 6 mm diameter. Unlike the common sandwich structure designs, where the skins and core are often permanently bonded (43, 82), each layer of the proposed graded folded sandwich structure is simply supported. After impact, each layer of deformed core can be easily removed and replaced by a new core structure. Only one set of plates are used for all different graded configurations throughout the impact tests in this study. No noticeable plastic deformation is observed on any plate after dozens of impact tests.

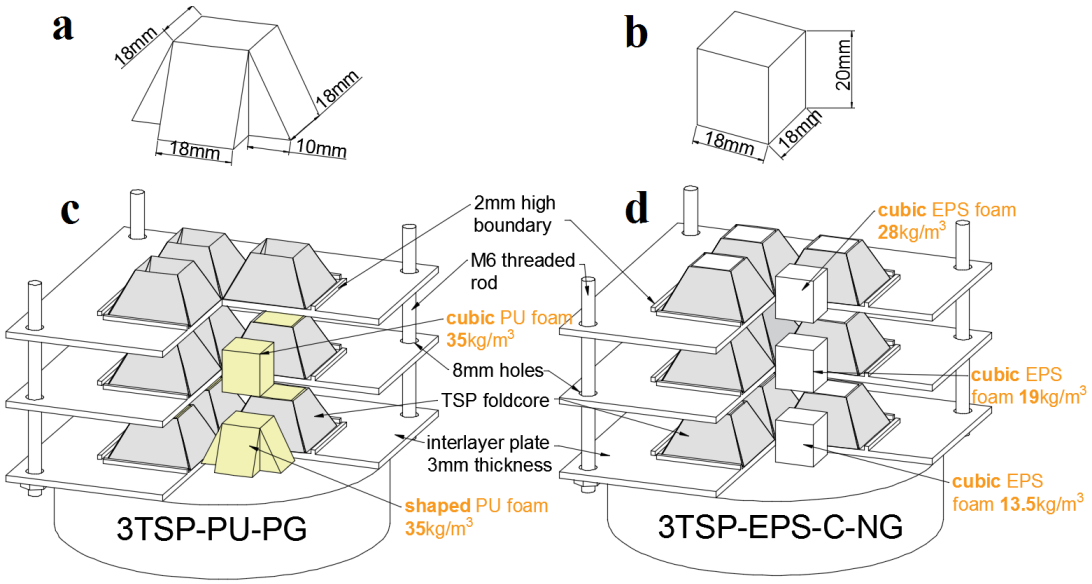

Figure 9-2. (a) Dimension of shaped foam filler; (b) dimension of cubic foam filler; (c) multi-layer set-up of PU foam filled positively graded folded structure; (d) cubic EPS foam filled negatively graded folded structure; Note: quarter of the plates and foldcores are cut out to illustrate the added foam fillers

9.2.3 Material properties

For material properties of Al 1060 and 5083, please refer to Chapter 7.2. Uniaxial compressive tests are carried out for EPS19 and PU35 foam material under the same

crushing rate (1 and 10 m/s). Stress-strain data for EPS13.5 and 28 are obtained from the previous study (155). Engineering stress-strain curves of these foam materials under two loading rates are shown in Figure 9-3. The foam specimens have a diameter of 75 mm and height of 50 mm. Multiple tests are carried out for each loading scenario. Same testing equipment is used to test the graded structures. Two crushing speeds on the foam materials are used for the proposed graded structures. The labelled crushing speed is not necessarily the actual moving speed of the impact head throughout the crushing, due to the deceleration at later stage.

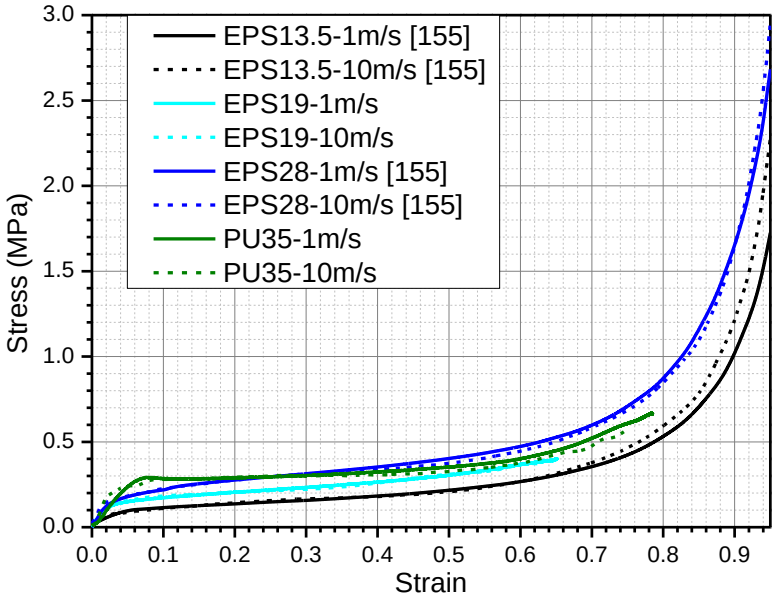

Figure 9-3. Engineering stress-strain curves of EPS13.5 (155), EPS19, EPS 28 (155) and PU35 under 1 m/s and 10 m/s crushing speed

9.3 Test set-up

For the test set-up, please refer to Chapter 7.4.1. For the information about crushing speeds, please refer to Chapter 7.4.2.

9.4 Results and discussions

9.4.1 Low-speed impact (1m/s)

9.4.1.1 Damage mode comparison (quasi-static and 1 m/s crushing)

Deformations of the crushing of three-layer TSP folded structure without foam fillers (three cores and three plates) are shown in Figure 9-4 for quasi-static and 1 m/s crushing cases. The loading rate of 2 mm/min is applied for the structure under quasi-

static crushing. Difference in deformation can be observed between these two loading cases. Simultaneous deformations across all three layers are shown for the quasi-static crushing case. This simultaneous deformation results in a smoother load-displacement response of the structure which is shown in Chapter 9.4.1.2 (Figure 9-8). Furthermore, the interlayer plates are tilted in quasi-static condition as a result of the difference in crushing strength of the unit cells on the same layer. Due to the very low loading rate (2 mm/min), even slight difference in crushing strength of unit cells can cause plate tilting and uneven loading to the next layer. Under crushing speed of 1 m/s, the interlayer plates are less tilted and the layer-by-layer deformation is shown in Figure 9-4 (b, d). The foldcore has less time to deform along the weaker portion of the unit cells as compared to quasi-static crushing, especially during the initial impacting stage. Therefore, foldcore within a same layer is more evenly crushed among unit cells, resulting in less tilting interlayer plates.

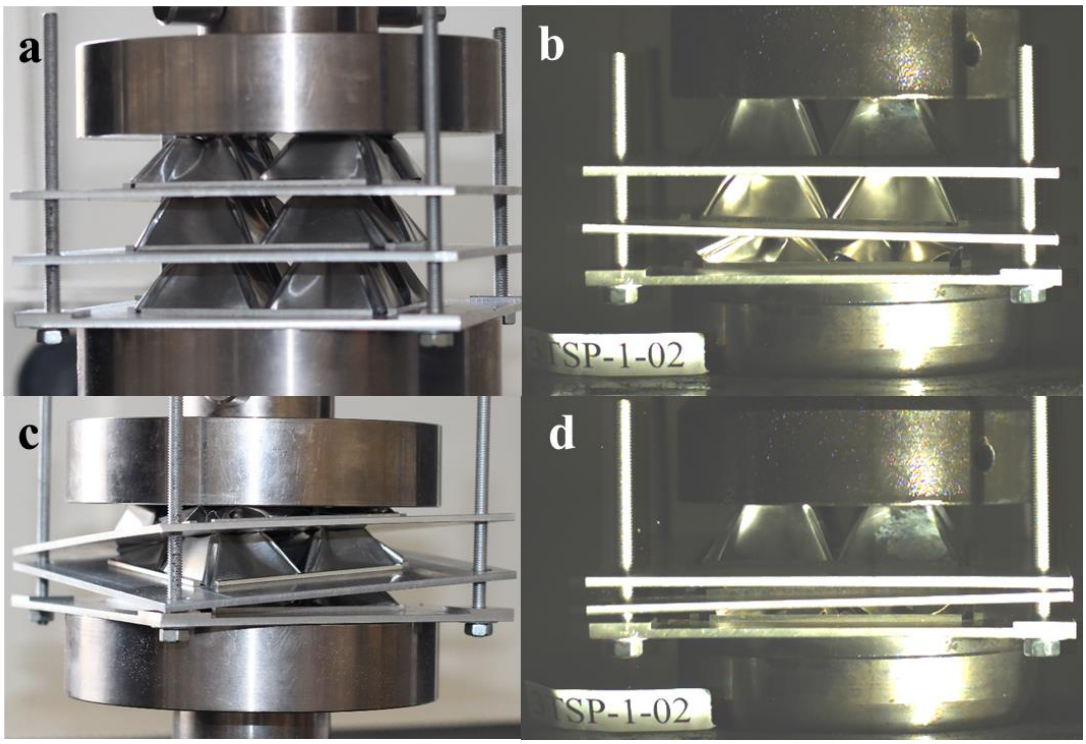

Figure 9-4. Deformation of three-layer TSP folded structure without foam fillers (a) early stage of quasi-static (2 mm/min) crushing; (b) early stage of 1 m/s crushing; (c) later stage of quasi-static crushing; (d) later stage of 1 m/s crushing

In addition, it is observed that only the bottom layer undergoes large deformation while the other two layers almost remain their original shapes at the early stage for all three tests under the same loading condition. The deformation then propagates to the

middle and finally to the top layer. The initiation of the layer-by-layer crushing from the bottom layer is caused by stress wave interferences under impact condition (162, 163). Under the impact of 1 m/s, the stress at top layer is not high enough to cause layer deformation at the moment of impact, thus the stress wave propagates downwards. When the reflected wave from the stationary base meets with the propagating stress wave from the impact end, the superimposed stress exceeds the layer buckling stress and thus the damage occurs near the base end. Under higher speed impact, the stress at the impact end might exceed the buckling stress of the structure, the damage occurs at the impact end rather than the base end. As reported in the previous study, the damage initiates from the top layer under 15 m/s impact.

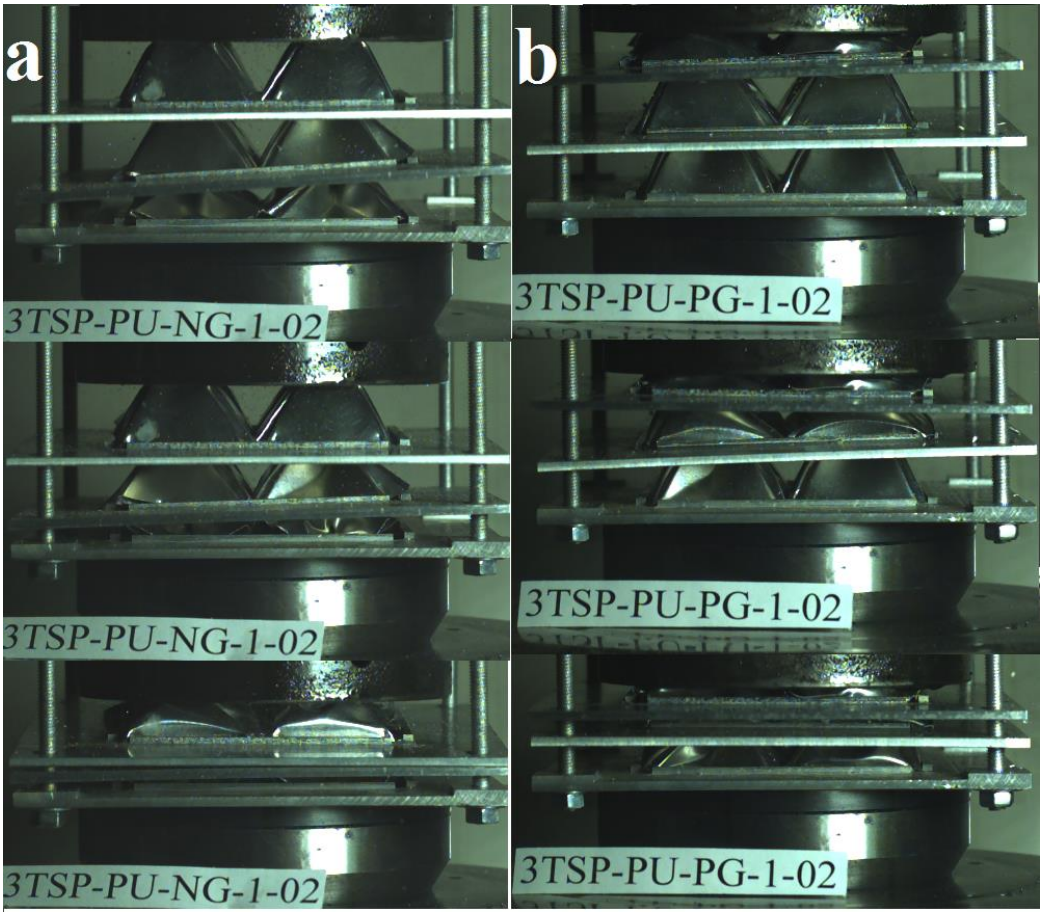

Figure 9-5. Deformation of (a) negatively; (b) positively graded structures with PU foam filler under 1 m/s crushing

Crushing process of the NG and PG folded structure with PU foam fillers under crushing rate of 1 m/s is shown in Figure 9-5. The last two digit in the label is the specimen number. For instance, 3TSP-PU-NG-1-02 stands for the second test of 3-

layer TSP folded structure with negatively graded PU foam fillers from top to bottom. A layer-by-layer crushing of the graded structures can be observed, similar to the uniform TSP folded structure without foam fillers. However, unlike the structure with uniform foldcores that crushing initiates at the bottom layer as shown in Figure 9-4 (b), the crushing initiates at the weaker layer of the graded structure, which is the bottom layer for NG structure and the top layer for PG structure as expected. The initiation of the buckling of each layer corresponds to three peaks as shown in Chapter 9.4.1.2 (Figure 9-8). The differences in load-displacement curves can be found among structures with different graded configurations. Comparing to the uniform TSP folded structure without foam fillers, graded structures have higher local peaks. The foam filler provides not only direct compressive strength to the structure but also the support and interaction to the sidewalls. As previously reported (98), the interactions become more apparent when sidewalls deform. Since more portions of sidewalls are in contact with the foam fillers to resist sidewall buckling, the crushing resistance of the structure significantly increases.

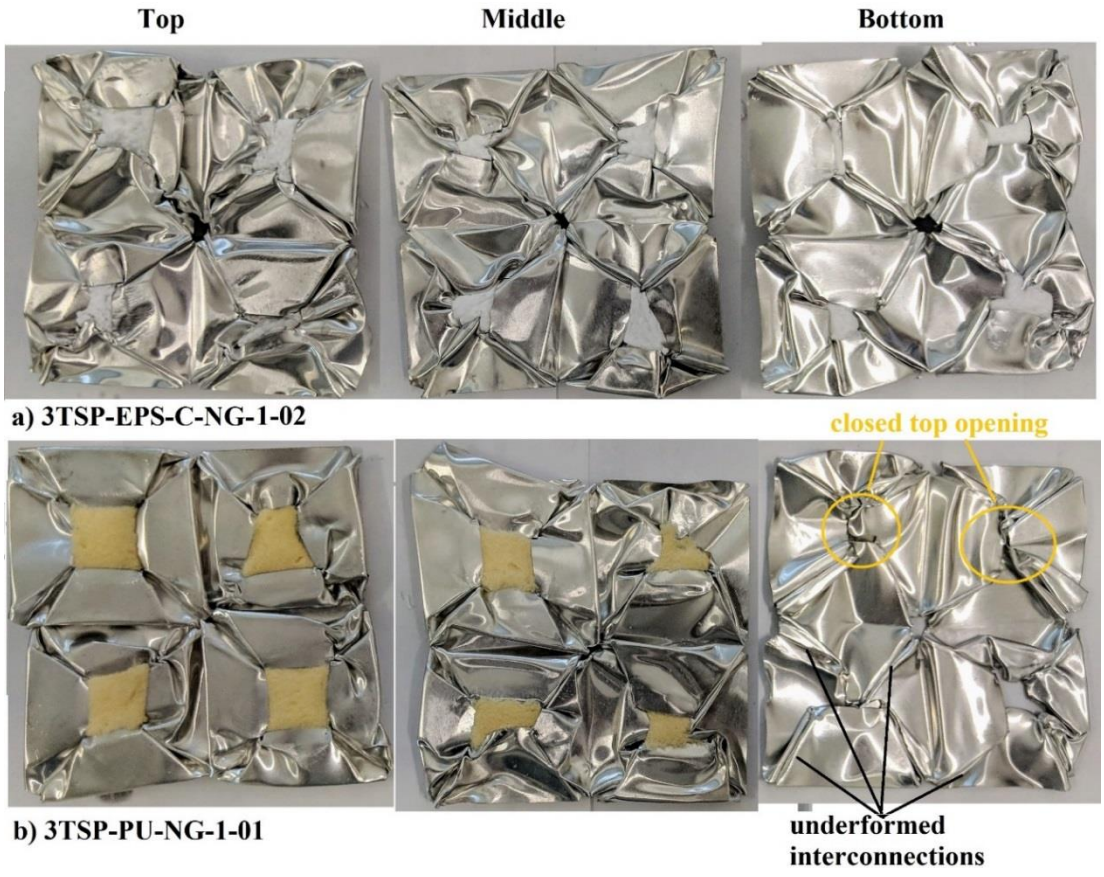

Figure 9-6. Damage modes of negatively graded structure with (a) cubic EPS foam fillers;(b) PU foam fillers, under 1 m/s crushing

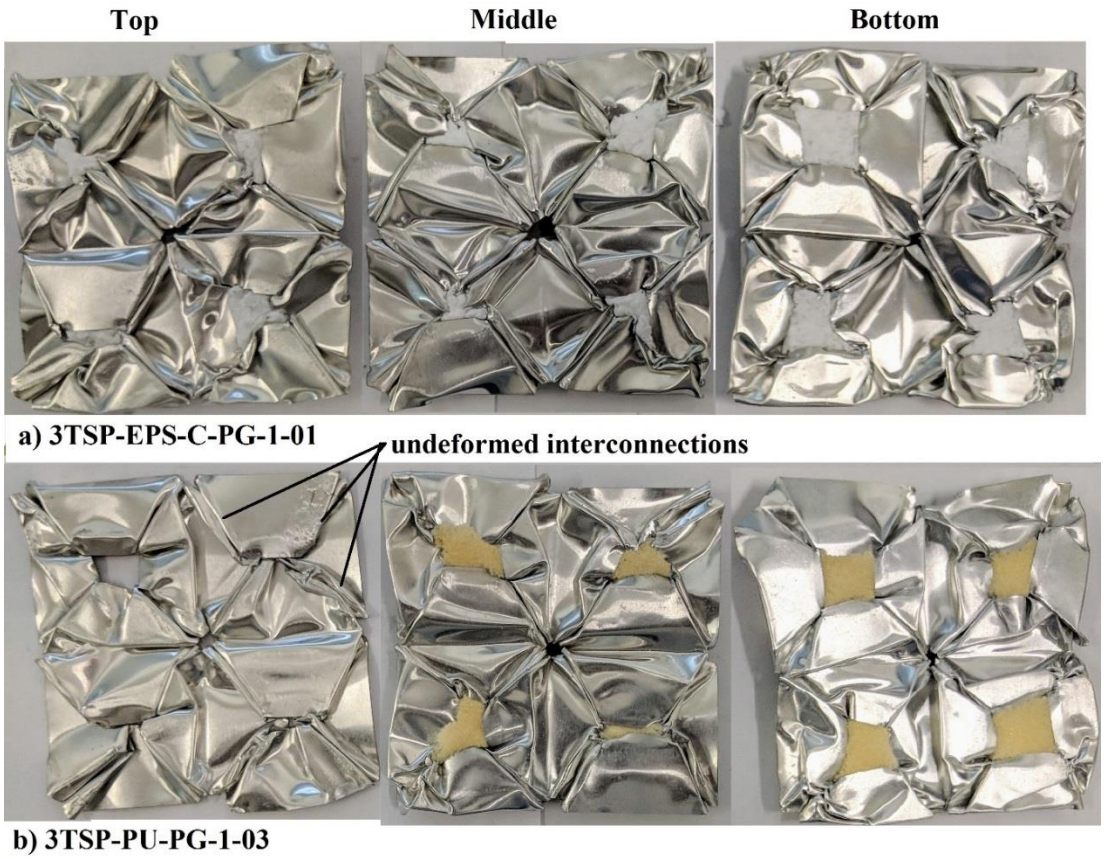

Figure 9-7. Damage modes of positively graded structure with (a) cubic EPS foam fillers;(b) PU foam fillers, under 1 m/s crushing

The NG and PG folded structures with EPS foam fillers show similar behaviour to the PU foam filled graded structures. However, the layers of NG and PG structures show opposite crushing order since the crushing of the structure always starts from the weakest layer under low impacting speed. Due to the difference in material properties between EPS and PU foams, the three peak in the load-displacement curves are not the same as shown in Chapter 9.4.1.2 . The layer with shaped PU foam filler has the highest peak, as the designed shape (Figure 9-2 a) better fits the slope of the sidewalls and enhances the interaction between the foam filler and sidewalls. The added shaped foam filler also results in a change of damage mode as compared to the bottom layer where no foam filler is added, as presented in Figure 9-6 (b). The added shaped foam on the top layer of 3TSP-PU-NG-1-01 provides extra support to the sidewalls during deformation. Therefore, the faces of sidewalls bend outwards horizontally, and the top openings remain their original square shape. For the layer without foam filler or with cubic foam filler (bottom and middle layers), the sidewalls bend inwards, resulting in more deformation on the top openings before deformation. The damage modes on

three layers of positively graded PU filled structures are shown in Figure 9-7 (b). This change of damage mode leads to the highest peak force out of the three peaks in load-displacement curves when the shaped foam filled layer undergoes deformation.

9.4.1.2 Structural response and energy absorption (1 m/s crushing tests)

Structural response and energy absorption are compared in this section. Peak crushing load, P_{peak}, average crushing load, P_{ave}, uniformity ratio, U, densification strain, ε_D, and specific energy absorption (SEA) are selected for evaluation of the crushing response and energy absorption capacities of these different graded structures. The densification strain, ε_D, is calculated by the displacement at the onset of densification divided by the total height of the foldcores. Densification is the stage where crushing resistance rises suddenly due to the compaction of structure. The total height of foldcore in this chapter is 60 mm which consists of 3 layers of 20 mm high foldcore. Total height does not include the thickness of interlayer plates, as deformation of the plates are not observed throughout the tests. The average crushing force, Pave, is the average crushing resistance of the structure before it reaches densification, and is defined as follows:

$$P_{ave} = \frac{\int_0^{\varepsilon_D} P(\varepsilon) \cdot d\varepsilon}{\varepsilon_D} \qquad (9\text{-}1)$$

where P is the crushing force and ε is the strain, which is calculated by crushed distance over total height of foldcores. The peak crushing force (P_{peak}) is defined as the overall peak force before densification in this chapter. Uniformity ratio is the ratio between peak and average crushing forces as:

$$U = \frac{P_{peak}}{p_{ave}} \qquad (9\text{-}2)$$

It is worth noting that the peak crushing force is often defined as the initial peak force in many studies (100, 164). As for conventional sandwich structures such as honeycomb (164), lattice (53) and Miura-type foldcore (82), sudden rise and fall in crushing resistance occurs at initial stage which can be several times larger than its average crushing force. However, for the folded structures considered in the present

study, this initial peak force is not necessarily the overall peak force before densification of the whole multi-layer structure. Therefore in this chapter the uniformity ratio is defined by using the overall peak force instead of the initial peak force. The specific energy absorption is defined as

$$SEA = \frac{P_{ave} \cdot \varepsilon_D \cdot H}{m_{TSP} + m_{foam}} \tag{9-3}$$

where H is the overall height of the foldcores, m_{TSP} and m_{foam} are the overall mass of the TSP foldcore and overall mass of the foam filler, respectively.

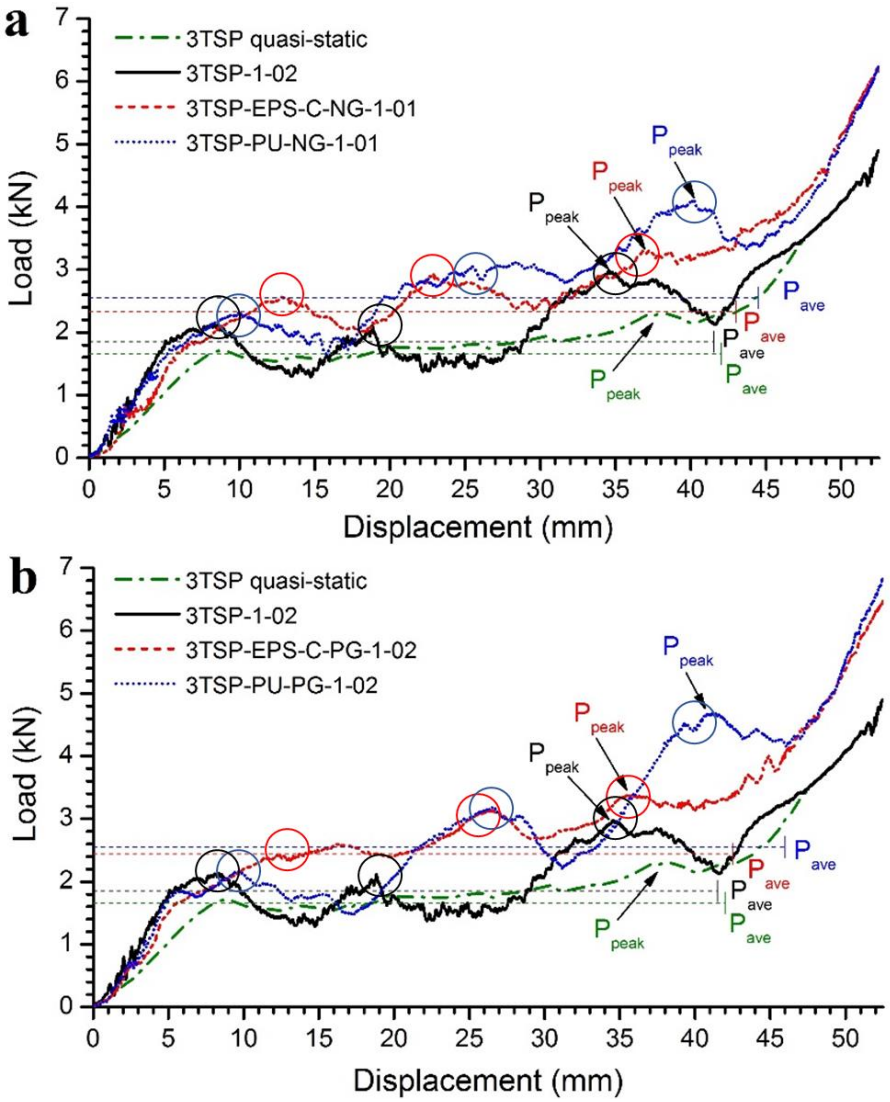

Figure 9-8. Load-displacement curves of uniform multi-layer TSP folded structure, (a) negatively graded folded structures; (b) positively graded folded structures under 1 m/s crushing; Marked out local peaks corresponds to initiation of buckling of the three layers

The load-displacement curves of multi-layer graded folded structures under 1 m/s crushing are shown in Figure 9-8. The average crushing forces are also calculated and indicated by the same coloured lines as the curves. The end bar of average force line represents the densification position of the structure where sudden and consistent rise of the crushing force occurs due to the compaction of the structure. The overall crushing response of the structures indicates good performances, with low fluctuations and a long plateau before reaching densification. The imperfections such as uneven levelling and existing gaps between foldcore and plates caused a decrease in the initial stiffness of the structure. This can be observed by the lower slope of curves before 1 to 2 mm displacement. However, the imperfections have little effect on energy absorption and overall crushing response of the multi-layer folded structures. It is also clear that the graded structures have a higher average crushing resistance than uniform folded structures without foam filler. As can be noted, the increment in compressive strength of the structure with added foam filler is greater than the compressive strength of the added foam itself. The great improvement in compressive strength to the folded structure by adding foam filler is due to the interaction effect between foam and the walls (98, 100). As marked out in circles in Figure 9-8, three local peaks can be observed for all graded and non-graded folded structures under this crushing speed. These peaks are associated with the initiation of buckling of the sidewalls in each layer. Under quasi-static loading, the load-displacement response is smoother due to simultaneous deformation on all layers. Furthermore, the foam filled graded structures have higher peak resistance than the case without foam fillers due to both added material and foam-sidewall interaction effect.

Table 9-2. Crushing responses of different graded structures under 1 m/s crushing speed

Graded configurations	P_{peak} (kN)	P_{ave} (kN)	$U= P_{peak} /P_{ave}$	ε_D	SEA (J/g)
3TSP-Quasi-static	2.30	1.66	1.386	0.70	2.50
3TSP-1-02	2.96	1.84	1.598	0.69	2.73
3TSP-EPS-C-NG-1-01	3.30	2.33	1.416	0.72	3.39
3TSP-PU-NG-1-01	4.12	2.55	1.616	0.74	3.67
3TSP-EPS-C-PG-1-02	3.37	2.44	1.381	0.71	3.50

3TSP-PU-PG-1-02	4.68	2.55	1.835	0.76	3.80

Structural responses of the graded structures are given in Table 9-2. The differences in the crushing response parameters of graded structures are minimal under low impacting speed. Both negatively graded and positively graded structures with the same set of foam fillers have similar crushing parameters. For instance, under 1 m/s crushing, negatively and positively graded structures with EPS foam filler show very similar peak, average crushing resistance, uniformity ratio, densification strain and specific energy absorption, although the crushing process is not the same as presented above. Similarly, negatively graded structure with PU foam filler has almost identical crushing parameters as the positively graded structure with PU foam filler. Significant enhancement in average crushing force (25% to 39%) is shown for foam filled graded structure as compared to uniform unfilled structure, while the mass of foam filler only increases between 5 and 10%. Excellent performances in energy absorption are shown for all folded structures with or without foam filler. The SEA varies between 2.50 J/g and 3.80 J/g, which is higher than 0.82-2.51 J/g of typical graded folded structures made of stronger sheet materials and higher core densities (e.g., brass, with Young's modulus 111.1 GPa and yield stress 142 MPa) (159).

Under crushing speed of 1 m/s, the graded structures have enhanced average crushing resistance and energy absorption capacity due to the added foam filler. However, difference in positively or negatively graded structure is minimal. For each foam filler configuration considered in this chapter, positively graded structures show similar crushing parameters as their negatively graded counterpart, due to the layer-by-layer deformation of the structure. Under low crushing speed, the deformation initiates at the weakest layer, followed by the collapsing of the second and then final layer, which are associated with three local peaks in the load-displacement curves as shown in Figure 9-8. The graded configuration changes the order of layer crushing but the compressive strength of each corresponded layer is the same. Therefore, the general trends of load-displacement curves between NG and PG under 1 m/s crushing are similar.

9.4.2 High-speed impact (10 m/s)

9.4.2.1 Damage mode comparison (10 m/s crushing)

Different from the low crushing speed cases, the graded configurations show significant influence on load-displacement responses under crushing speed of 10 m/s. Figure 9-9 (a) shows the crushing at the instant when the overall peak force of NG structure occurs at about 22 mm of displacement as shown in Chapter 9.4.2.2 (Figure 9-14 a), and Figure 9-9 (b) is at the same instant when the PG structure with PU foam fillers reaches the peak resistance. The NG structure has a significantly higher peak force than the PG structure with almost a 40% increase. This is because collision between the middle and bottom interlayer plates occurs on NG structure as shown in the figure, which results in higher force.

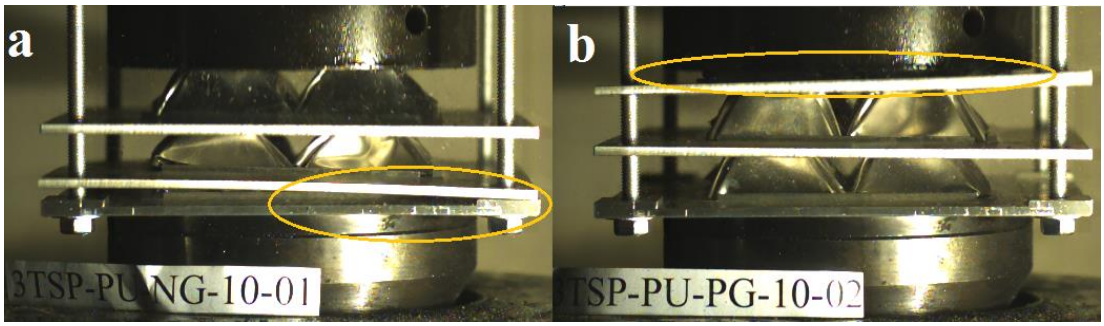

Figure 9-9. Complete collapsing of the first layer under 10 m/s crushing speed for (a) negatively graded; (b) positively graded structures with cubic EPS foam fillers.

The plates are larger than the foldcore, slight tilting may lead to collision on the edge of the plates. However, the primary reason behind the collision of the plates is the fully crushed foldcore layer. For graded structures, the strength difference between layers is amplified with graded structure due to inertia effect and extra stabilization by both the foldcore and the added foam. The weaker layer is first crushed and fully compacted. As shown in Figure 9-9 (a, b), the first deforming layer is completely crushed, resulting the contact between two plates. However, under 1 m/s crushing, the first deforming layer still has residual height for further deformation for both NG and PG structures as shown in Figure 9-5. The full compaction of the weaker layer leads to large rise in force being transmitted to the next layer. For NG structures, the foldcore of the first crushed layer is fully compacted (bottom layer), therefore, it leads to huge rise in the reaction force, i.e., the force being transmitted to the base where the load cell is located, as shown in Chapter 9.4.2.2 (Figure 9-14 a). For PG structures, the fully compacted

layer is at the top with two lower layers that further deform to absorb energy. Therefore the force transmitted to the base is still relatively small. Similar significant increase in transmitted force due to fully compacted layer subjected to dynamic loading were also reported in the previous analytical and experimental studies (18, 35).

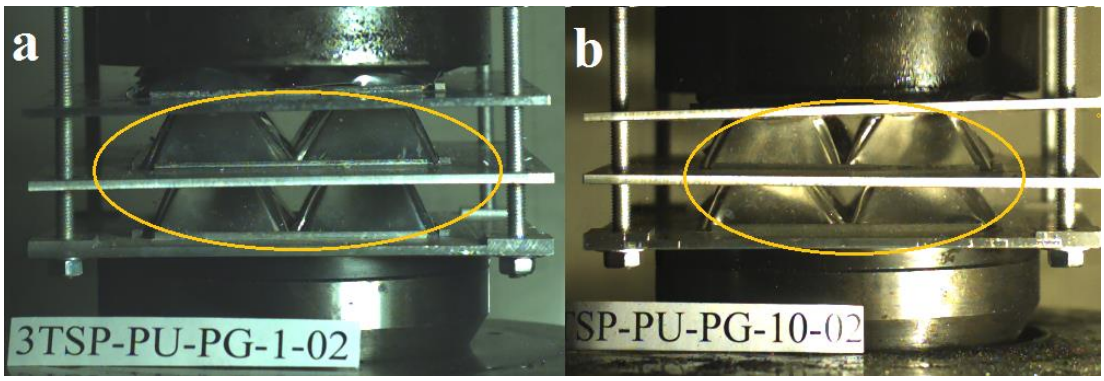

Figure 9-10. Deformation comparison of positively graded PU foam filled structure before first layer is completely crushed under (a) 1 m/s; (b) 10 m/s

Prior to layer-by-layer buckling, all three layers undergo slight deformation simultaneously under high speed crushing, which is slightly different from that under low speed crushing. As can be observed, there is almost no deformation on the middle and bottom layers when the top layer is fully crushed under 1 m/s impact as shown in Figure 9-10 (a). Under 10 m/s crushing, as shown in Figure 9-10 (b), both middle and bottom layers experience some slight deformation when the top layer is fully crushed. Due to simultaneous buckling initiation on all layers prior to layer-by-layer deformation, an increased crushing resistance at initial stage is observed. However, the crushing force at later stage is slightly reduced as compared to 1 m/s impacting case, as shown in Figure 9-16 of Chapter 9.4.2.2, which is due to the slightly deformed sidewalls of foldcores on middle and bottom layers prior to layer-by-layer crushing.

Damage modes of the two graded structures under 10 m/s crushing are show in Figure 9-11 and Figure 9-12. Similar damage modes are observed for foam filled layers due to foam-sidewall interactions. Comparing with 1 m/s crushing (Figure 9-7 b), larger residual opening and more buckled interconnections on the top layer (i.e. no foam filler) of 3TSP-PU-PG are observed under 10 m/s crushing as shown in Figure 9-11 (b). The change of damage mode with increasing crushing speed is due to the inertia effect and the geometry of the foldcore causing top portion of the foldcore to deform before the lower portion. As each corner of folded structure consists of two triangular

interconnections which strengthen the structure, the foldcore corners rotate about the base instead of buckling under low crushing speed. Under high crushing speed, the deformation of top layer is localized on the top edges of the sidewall where the top edges roll towards cell centre and the interconnections buckle instead of rotating. Therefore, the interconnection lines are no longer straight as observed under low speed crushing (marked out in Figure 9-7 (b) top layer), and the top openings are not closed as marked out on the top layer of Figure 9-11 (b).

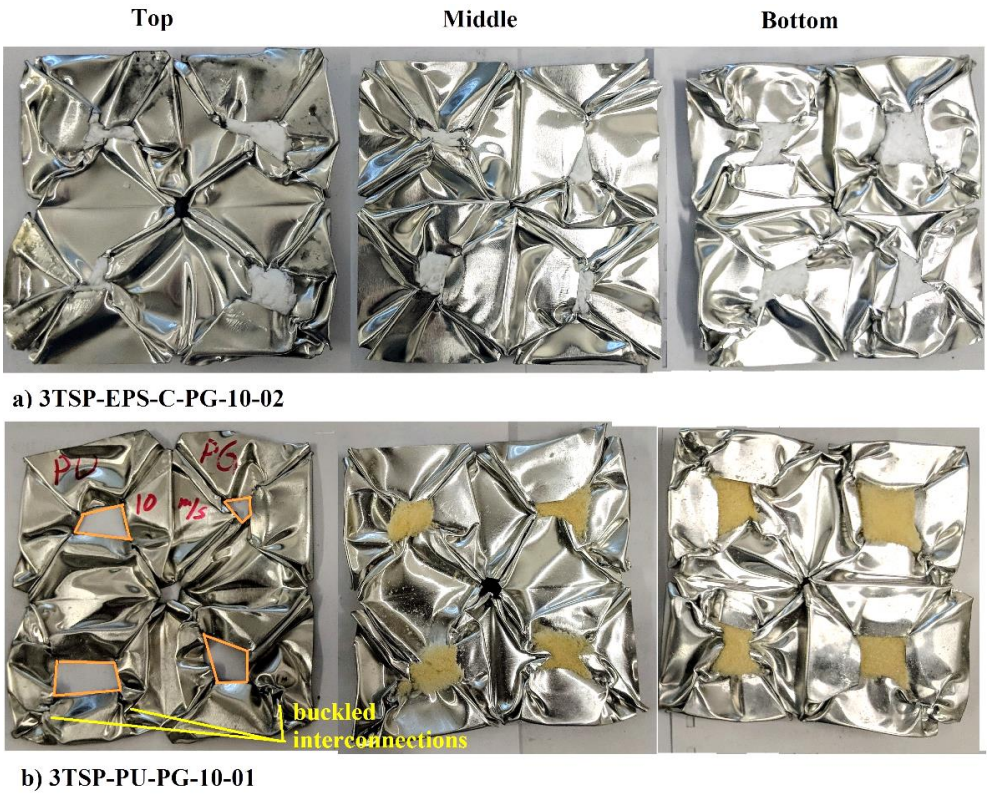

Figure 9-11. Damage modes of positively graded structure with (a) cubic EPS foam fillers; (b) PU foam fillers under 10 m/s crushing

To summarize the layer deformation of graded multi-layer folded structure under three graded configurations and two loading speeds, schematic diagrams are shown in Figure 9-13. Under low crushing speed, layer-by-layer deformation is observed for both graded configurations. The weakest layer deforms first followed by the second weaker layer. Under 10 m/s crushing, however, slight deformation on all three layers is observed prior to layer-by-layer crushing for both NG and PG structures. Different from that under low crushing speed, the weakest layer is completely crushed under 10 m/s impact before large crushing starts in the next weakest layer. The full compaction

of layer may result in a significant increase in force transmitted to the structure behind if the fully crushed layer is the bottom layer. It is also worth noting that the layer-by-layer deforming order for uniform TSP folded structure under 1 m/s impact starts from bottom layer. Random deforming order is observed for 10 m/s impacting case, as the impacting speed is not sufficiently high to cause the failure at impacting end while the interaction of reflected and propagating stress wave is not necessarily occurs at base end under this impacting speed.

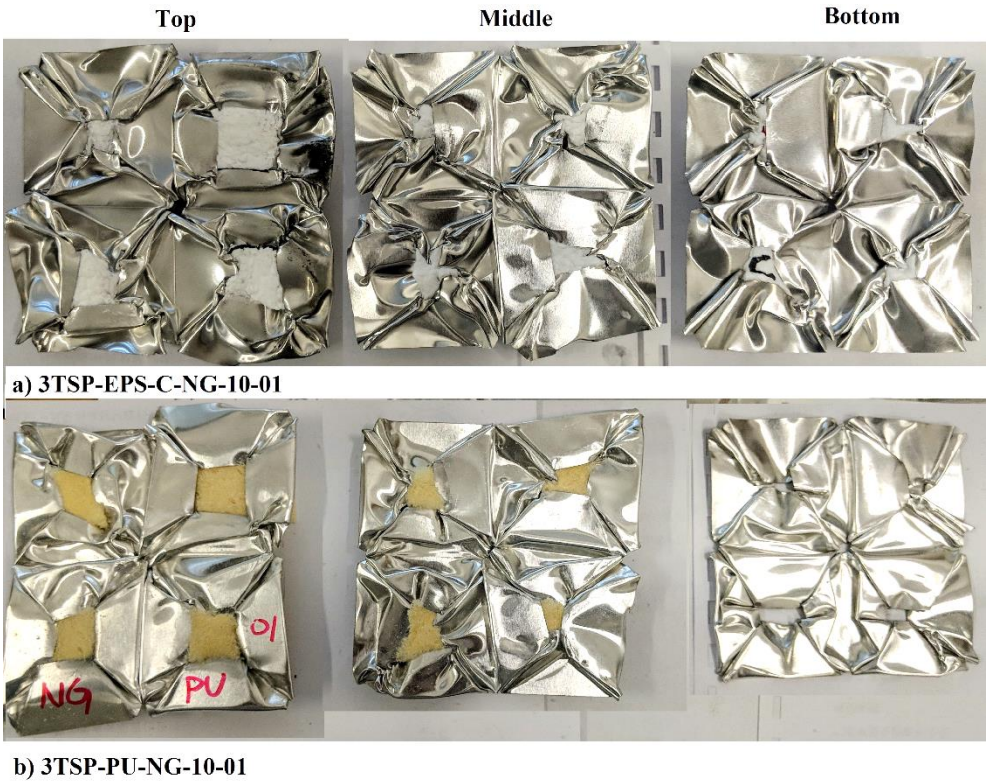

Figure 9-12. Damage modes of positively graded structure with (a) cubic EPS foam fillers; (b) PU foam fillers under 10 m/s crushing

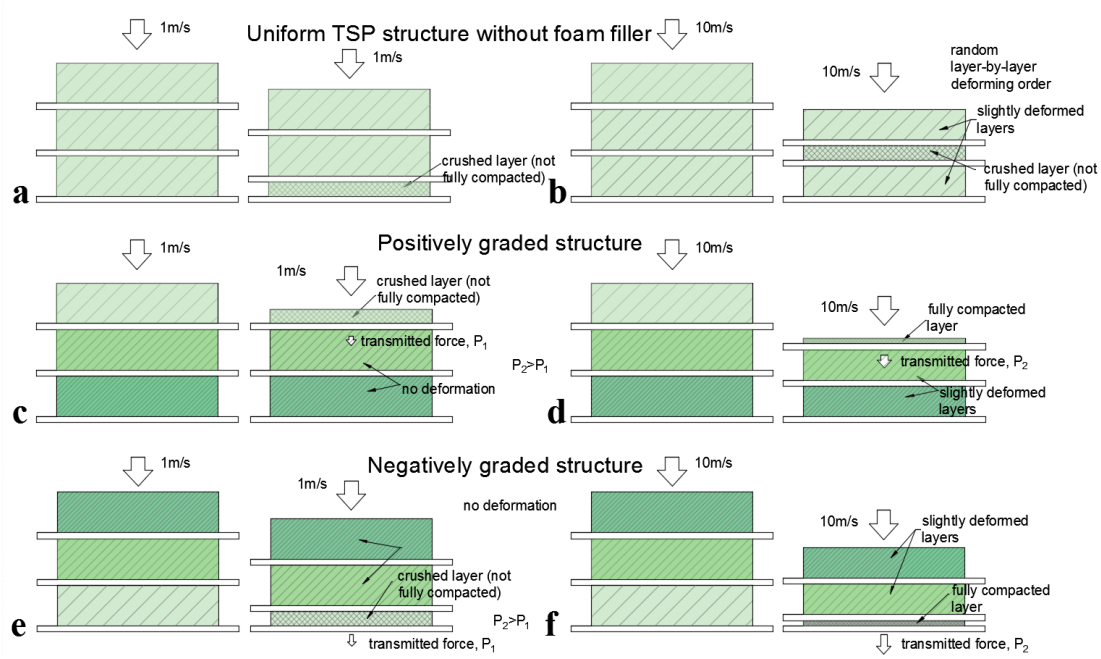

Figure 9-13. Schematic diagram of layer deformation under different loading and graded conditions; (a) No foam filled TSP folded structure under 1 m/s crushing; (b) No foam filled TSP folded structure under 10 m/s crushing; (c) PG structure under 1 m/s crushing; (d) PG structure under 10 m/s crushing; (e) NG structure under 1 m/s crushing; (f) NG structure under 10 m/s crushing; Note: denser lined layer represents the layer with higher compressive strength

9.4.2.2 Structural response and energy absorption (10 m/s crushing)

Load-displacement curves of the multi-layer graded structures under 10 m/s crushing are shown in Figure 9-14. Crushing responses of these graded folded structures under 10 m/s are very different, as compared to those under low crushing speed of 1 m/s. Fluctuation of the curves can be observed on both the negatively and positively graded cases. For negatively graded folded structures, three sudden rises can be identified on both EPS and PU foam filled NG structures. Out of which, the second peak at around 22 mm of crushed distance shows the highest rise and drop in force as marked out in Figure 9-14 (a). The peak value is almost twice than the average crushing resistance and almost 40% higher than that of PG counterparts. As previously explained, the collision of the middle and bottom plates as well as full compaction of the weakest layer, which is the bottom layer for NG structures, lead to large force transmitted to the structure behind. For the positively graded folded structure, the load fluctuates around the average line of the crushing force and the fluctuation is much smaller in amplitude, indicating a more uniform crushing response. Clear change in initial

stiffness can also be observed. For the first 2 to 3 mm of the crushing, the stiffness of all structures is much lower than that after initial stage, which is caused by the gap between foldcores and plates. Once the manual folding induced gaps are closed, the crushing stiffness rises quickly, which can be observed for PG and NG cases in Figure 9-14. The slopes of the initial stage of crushing after gap closing are much higher than those under 1 m/s crushing shown in Figure 9-8 due to inertia effect and stabilization effect of the cell walls.

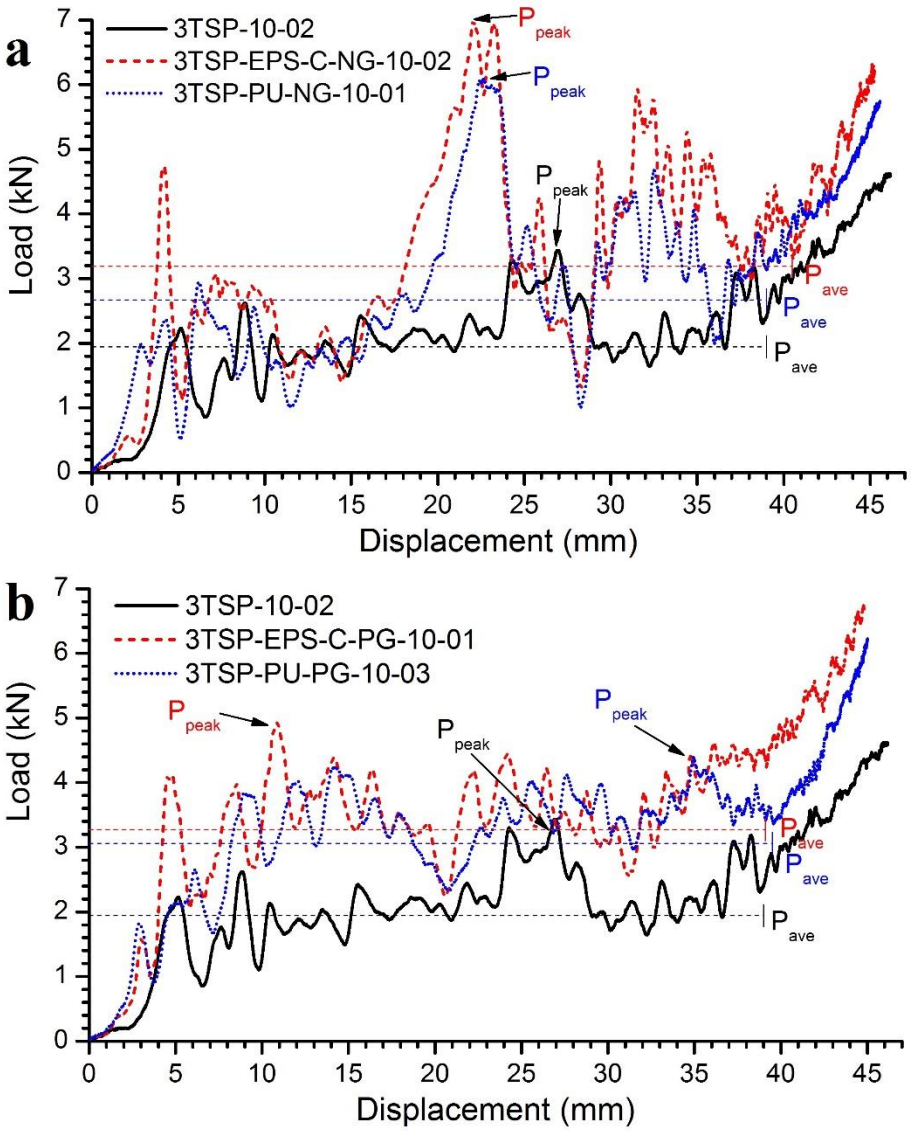

Figure 9-14. Load-displacement curves of uniform multi-layer TSP folded structure and (a) negatively graded folded structures; (b) positively graded folded structures, under 10 m/s crushing

Table 9-3. Crushing responses of different graded structures under 10 m/s crushing speed

Graded configurations	P_{peak} (kN)	P_{ave} (kN)	$U= P_{peak} /P_{ave}$	ε_D	SEA (J/g)
3TSP-10-02	3.44	1.94	1.773	0.65	2.70
3TSP-EPS-C-NG-10-02	6.97	3.19	2.206	0.68	4.37
3TSP-PU-NG-10-01	6.10	2.67	2.285	0.65	3.37
3TSP-EPS-C-PG-10-01	4.93	3.27	1.508	0.65	4.32
3TSP-PU-PG-10-03	4.40	3.06	1.438	0.66	3.91

The structural response and energy absorption of the graded structures under 10 m/s are listed in Table 9-3. The peak crushing forces for two configurations of negatively graded structures (3TSP-EPS-C-NG, 3TSP-PU-NG) are around 40% larger than their positively graded counterparts (3TSP-EPS-C-PG, 3TSP-PU-PG) under 10 m/s loading. On the other hand, the energy absorption and average crushing resistance of these NG structures are similar or lower than their PG counterparts. Both negatively graded structures (3TSP-EPS-C-NG, 3TSP-PU-NG) show less uniform crushing behaviour than the uniform and PG structures, by yielding a larger uniformity ratio. Positively graded structures, however, have smaller uniformity ratios than NG structures and uniform folded structures, demonstrating the improved crushing behaviour by adding positively graded foam fillers, which not only enhance the energy absorption but also lead to a more uniform crushing process.

Figure 9-15 shows the comparison of the peak and average crushing forces among the folded graded structures under low and high crushing speeds. With the increasing crushing speed, rises in average crushing forces can be observed for all graded configurations and the uniform foldcore without foam fillers. The increase of average crushing force is due to the structural stabilization and change of damage mode on some layers with the increasing crushing speed. With the increase of impacting speed from 1m/s to 10 m/s, the changes of the peak crushing forces are different for the two graded (PG/NG) configurations. As shown in Figure 9-15 (a), much higher rise of peak crushing force is shown for the negatively graded (NG) structure due to the quick full compaction of the bottom layer and impacting onto the base support where the load

cell is located. However, for the positively graded structure, the peak force increases slightly or even decreases (e.g. 3TSP-PU-PG as shown in Figure 9-15 b) when crushing speed increases from 1 to 10 m/s. Under 10 m/s impacting speed, all layers deform slightly before layer-by-layer deformation occurs, as shown in Figure 9-10. The slight deformation on all layer at initial stage will increase the initial peak force at early stage due to initiation of buckling on all layers, while the peak at later stage of the crushing is reduced as the layers are slightly buckled prior to layer-by-layer deformation.

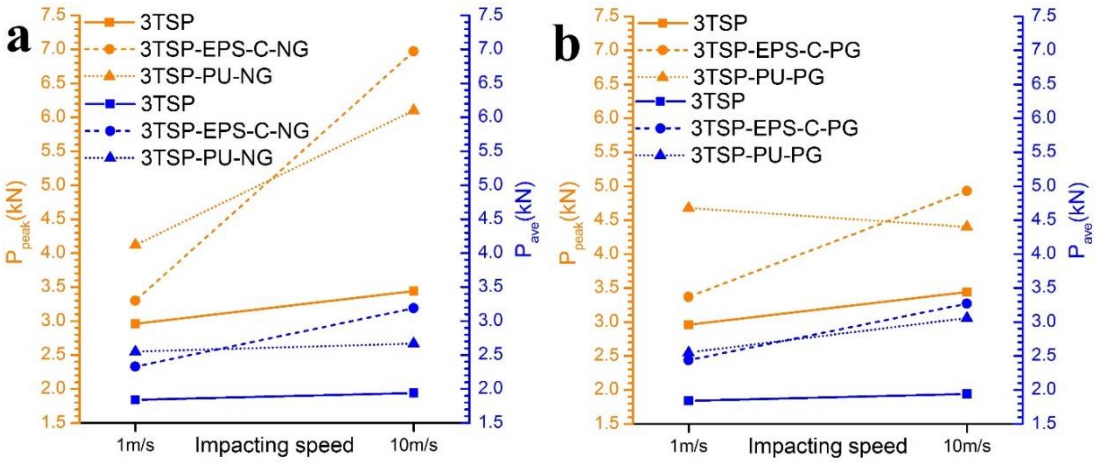

Figure 9-15. Peak and average crushing forces with the increase of impacting speed for (a) negatively graded structures; (b) positively graded structures

Under 10 m/s crushing, the overall peak force occurs at early stage of the deformation for EPS foam filled PG structure (Figure 9-14 b), different from low speed crushing where the peak force occurs at later stage of deformation (Figure 9-8 b). For PU foam filled PG structure, overall peak force occurs at later stage of the deformation under both crushing speeds. For both PG structures (EPS and PU), the deforming orders are the same, from top to bottom layer under both crushing speeds, whereas slight deformation occurs on all three layers before layer-by-layer deformation under higher crushing speed. The slight deformation on all layers leads to the increase in crushing force at early stage and reduction at later stage under higher crushing speed, as explained in the previous paragraph. Illustration of this change in crushing force at early and later stages under 1 and 10 m/s crushing is shown in Figure 9-16. It is worth noting that the illustration only shows the changes caused by the slight simultaneous buckling on all three layers before layer-by-layer crushing under 10 m/s loading, it

does not include other factors such as inertia effect and stabilization of the foam which result in a higher average crushing force under higher crushing speed as previously explained. For EPS foam filled PG structure, the difference in compressive strength from top to bottom layers (EPS 13.5, EPS19, EPS 28) is not significant. Therefore, with the increasing loading rate from 1 to 10 m/s, the appearance of peak force changes from later stage P2 (10 m/s) to early stage P1 (10 m/s) due to the increase of crushing force at early stage as shown in Figure 9-16 (a). For PU foam filled PG structure, the compressive strength from top to bottom layers is very different due to foam filler configuration (no foam, cubic foam and shaped foam from top to bottom layer). Therefore, under 10 m/s crushing, even with the increase in crushing force at early stage and decrease at later stage, the crushing force at early stage P1 (10 m/s) is still smaller than that at later stage P2 (10 m/s) where bottom layer with shaped foam is being crushed as shown in Figure 9-16 (b). Therefore, overall peak crushing force of PU foam filled PG structure occurs at later stage and its value is slightly reduced comparing to 1 m/s crushing case.

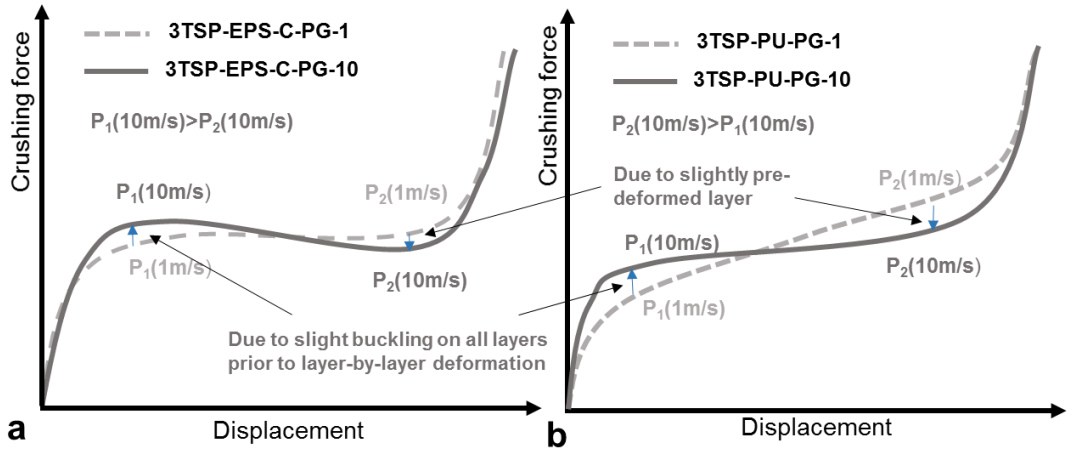

Figure 9-16. Illustration of changes in peak forces at early and later stage of crushing under 1 and 10 m/s impact for (a) EPS foam filled PG structure; (b) PU foam filled PG structure; note: this graph is only used to illustrate the changes in peak forces caused by the change of layer deformation mode under 1 and 10 m/s impact, does not represent the actual crushing responses

9.5 Summary

Two sets of negatively and positively graded TSP folded structures by varying foam filler configurations are experimentally studied. Their crushing behaviours including

peak and average crushing force, energy absorption, uniformity ratio and damage modes are compared under two different speeds. It is found that the structures with different graded configurations show similar crushing behaviors under low crushing speeds, indicating the graded configurations have minimum influences on the impact responses of the graded TSP folded structures. Under high crushing speed, however, significant advantages are obtained for positively graded structure where the core strength increases along the impacting direction. More uniform load-displacement responses with lower fluctuation, lower peak force and higher energy absorption are achieved for positively graded structures with two sets of foam filler configurations than their negatively graded counterparts. Different damage modes are observed for these graded structures as well. Layer-by-layer crushing with initiation on the weakest layer is observed on graded structure under low crushing rate. Under high crushing speed, all three layers undergo a slight simultaneous deformation prior to the layer-by-layer crushing. Due to foam-wall interaction effect, a better performance of graded structures can be achieved by inserting lightweight foam, which leads to up to 68.6% increase in average crushing force with only a 5.3% increase in structural mass. Furthermore, the graded configuration of this multi-layer TSP folded structure can be easily modified according to various scenarios by relocating the desired foam filler, as no permanent bonding between foldcores and plates is required. The interlayer plates of the set-up are also reusable, the core can be easily replaced after each use. Overall, with suitable graded configuration, this graded multi-layer TSP folded structure has superior energy absorption capacity than uniform TSP folded structure especially under dynamic loading conditions.

Chapter 10. Numerical study of sandwich panel with a new bi-directional Load-Self-Cancelling (LSC) core under blast loading

The related work in this chapter has been published in Thin-Walled Structures.

Li Z, Chen W, Hao H. Numerical study of sandwich panel with a new bi-directional Load-Self-Cancelling (LSC) core under blast loading. Thin-Walled Structures. 2018;127:90-101. DOI: doi.org/10.1016/j.tws.2018.02.003

10.1 Introduction

Apart from the folded structure studied in Chapter 3 to 9, a bi-directional load-self-cancelling blast resistant panel as new structural form is proposed and numerically investigated in this chapter.

To overcome the shortcomings of the uni-directional multi-arched panel previously developed(61, 75), a bi-directional LSC sandwich structure is proposed in this chapter, the core consists of an array of two-axis-symmetric square domes as shown in Figure 10-1. This new structural form is believed to have capability of cancelling load in both in-plane directions of the panel and therefore further reducing forces that would be transferred to the panel boundaries as compared to the uni-directional multi-arch panel. With the geometry similar to the proposed bi-directional LSC square dome structure, a modified structure named as “grid dome” is also numerically simulated in this chapter for comparison. It was originally proposed in (45), where the textile composite material and half sphere shape made it easy to deform and absorb energy. The grid of half spheres are placed with gaps between each other in the panel (45). The array of grid sphere is modified and placed next to each other in this study to make it similar to the bi-directional LSC structure proposed in this chapter, since the load can be cancelled at the intersection points of the adjacent sphere domes as well. However, the adjacent grids of sphere domes are only point connected while the proposed square dome structure are connected with intersection lines, which allow more forces to be self-cancelled. Therefore, a superior LSC capacity is expected for the proposed square dome structure.

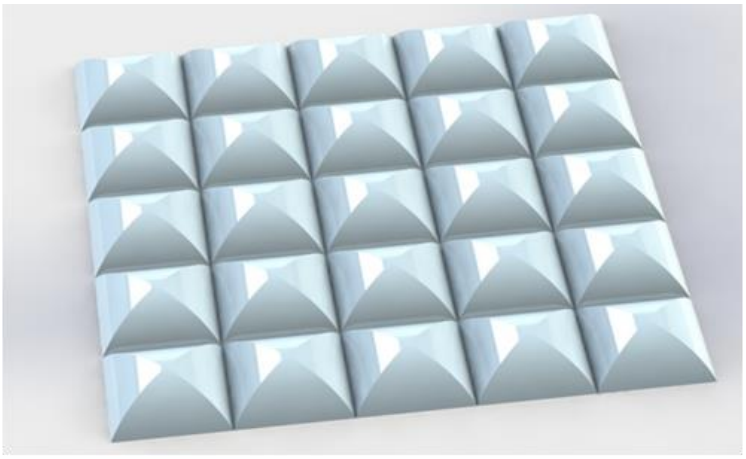

Figure 10-1. Proposed square dome as core of bi-directional load-self-cancelling structure

In this chapter, the effectiveness of the new form of LSC structure is numerically investigated and compared with an equivalent monolithic plate, and a uni-directional multi-arch structure (61) and a modified grid sphere dome structure (45). Finite element software LS-DYNA is employed to calculate and analyse energy absorption, back plate centre deflection and boundary reaction forces of these structures under blast loading. Existing blast test data of a flat plate from other researchers is used to validate the numerical model (165). The calibrated numerical model is then used to perform numerical simulations of the proposed structure to evaluate its energy absorption capacity, blast load resistance capacity and boundary reaction forces. A series of parametric studies are also conducted to investigate the effectiveness of sandwich panels with different core configurations on their blast loading resistance capacities.

10.2 Numerical model calibration

Finite element software LS-DYNA is used for numerical simulation. As a widely applied FEA tool based on explicit numerical methods, LS-DYNA is dedicated to highly nonlinear, dynamic finite element analysis subjected to impact and blast loads. To calibrate the accuracy and reliability of the numerical model, a steel plate which was tested and numerically modelled by DSTO (Defence Science and Technology Organization) of Australia is adopted (165). A series of blast tests were carried out to study structural response of a 5 mm thick mild steel plate. The charges of 250 g Pentolite (260 g TNT equivalent (61)) were applied with the alternating stand-off

distance of 250 mm, 400 mm, 500 mm directly above the centre of the steel plate with dimension of 1200 mm by 1200 mm. The steel plates were bolted on to a 1000 mm by 1000 mm rigid steel frame with 24 equally spaced high-strength bolts. The steel frame was simply supported by concrete stands on four sides with some openings. The schematic diagram of experimental setup of the steel plate is shown in Figure 10-2. Two Endevco 7255A piezoelectric accelerometers, two PCB Piezotronic 109A piezoelectric pressure gauges and a Novotechnik TI50 LVDT resistive displacement gauge were attached on the steel plate to record relevant data of the plate during and after the explosion. The test results are used to calibrate the numerical model in this chapter.

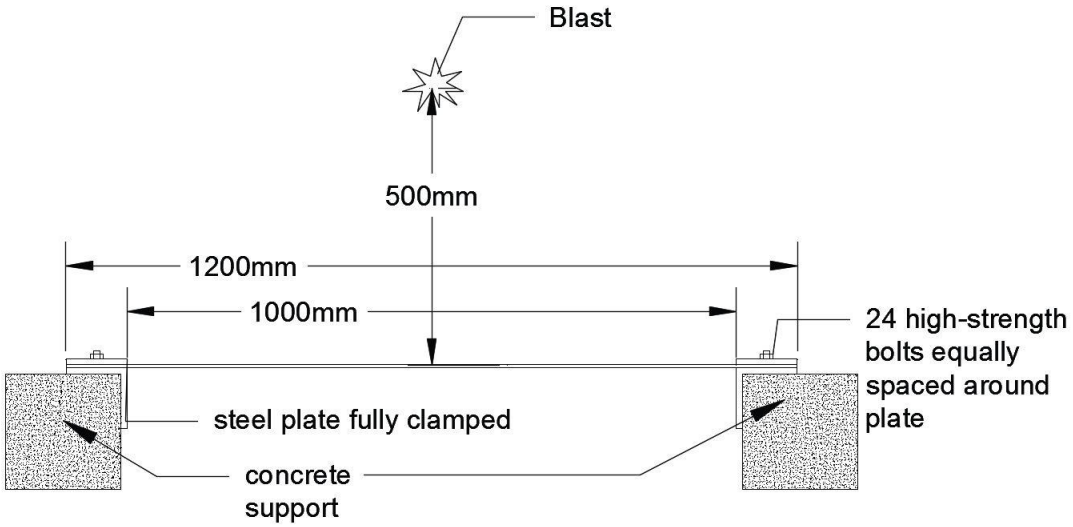

Figure 10-2. Experimental setup of a steel plate subjected to blast load

10.2.1 Element, mesh convergence test and boundary condition

The numerical model is constructed in Solidworks and LS-Prepost. The steel plate is modelled by using the fully integrated shell element to minimize hourglass energy in the simulations (128). As an important factor for determining both the computational time and simulation accuracy, mesh size convergence tests are carried out with the element sizes of 20 mm, 10 mm, 5 mm, and 2.5 mm. Mesh convergence test results are shown and discussed in Chapter 10.2.4.

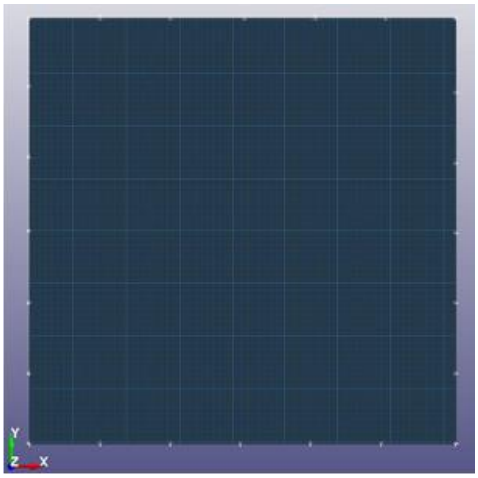

Figure 10-3. Boundary condition for finite element model of bolted steel plate subjected to blast loading

Boundary condition can be another critical factor for numerical simulation. In the model calibration and mesh convergence test, a simplified boundary condition for this steel plate subjected to blast loading is used to reduce computational time while representing the test conditions as closely as possible. In the simplified boundary condition, as shown in Figure 10-3, 24 nodes are modelled as fully fixed to represent the 24 bolts that connected the steel plate and steel frame in the test, other nodes along the plate edges are constrained in three degrees of freedom, UZ, Rot X and Rot Y by using *BOUNDARY SPC SET. This simplified approach was also adopted in Chen and Hao (61), and showed relatively good agreement with the test data.

10.2.2 Material model used in LS-DYNA

Table 10-1. Material properties of steel plate in Cowper and Symonds model (165)

Property	Young's modulus (GPa)	Poisson's ratio	Yield stress (MPa)	Tangent modulus (MPa)	Density (kg/m^3)	Hardening parameter, β	C (s^{-1})	P
Value	203	0.3	270	470	7850	1	40	6

The elastic-plastic material model *MAT 003 PLASTIC KINEMATIC is adopted for modelling the steel plate. This material model is commonly used for modelling metals with bi-linear elastic-plastic constitutive relationship and isotropic or kinematic hardening plasticity which is defined by a hardening parameter β equals to 1,

representing isotropic hardening. Material strain rate effect is also considered by applying Cowper-Symonds model in LS-DYNA which is defined by Eq. (10-1) (128) .

$$\frac{\sigma_d}{\sigma_s} = 1 + \left(\frac{\dot{\varepsilon}}{C}\right)^{\frac{1}{p}} \qquad (10\text{-}1)$$

where σ_d is the dynamic yield stress at plastic strain rate $\dot{\varepsilon}$, σ_s is the static yield stress. Strain rate parameters C and P are Cowper and Symonds constants, respectively. Material properties of steel used in this chapter are shown in Table 10-1. Failure strain of steel material is taken as 0.3 throughout this chapter.

10.2.3 Blast load modelling

*LOAD BLAST ENHANCED via the CONWEP feature in LS-DYNA is used to simulate blast load in numerical simulation (129). The enhancement of reflected waves in blast event is demonstrated in the blast model. Pressures on the plate are determined by the amount of TNT, standoff distance and incident angle as given in the equation (10-2) below:

$$P(\tau) = P_r cos^2\theta + P_i\left(1 + cos^2\theta - 2cos\theta\right) \qquad (10\text{-}2)$$

where *Pr* is the reflected pressure, *Pi* is the incident pressure and θ is the angle of incidence.

The keyword *LOAD BLAST SEGMENT in LS-DYNA is applied to define the loading face of the structure and the keyword *DATABASE BINARY BLSTFOR is used to export the blast pressure data. The scaled distance is defined by equation:

$$Z = \frac{R}{W^{\frac{1}{3}}} \qquad (10\text{-}3)$$

where *R* is the standoff distance in meter and *W* is the equivalent amount of TNT in kg.

10.2.4 Results and discussions of numerical model validation and mesh convergence test

Table 10-2. Experimental and numerical results of peak reflected pressure and peak displacement

Event	TNT equivalent (g)	Standoff (mm)	Experiment data (165)		Numerical simulation			
			P_r (MPa)	δ_{max} (mm)	P_r (MPa)	difference	δ_{max} (mm)	difference
E14	260	500	9.4	-33	9.3	1.0%	-31.2	5.4%
E16	260	400	16.4	-36	15.7	4.3%	-33.4	7.2%
E17	260	250	40.0	-35	44.5	-11.3%	-33.5	4.3%

The calculated reflected pressure-time histories from explosion at stand-off distances of 250 mm, 400 mm and 500 mm are shown in Figure 10-4. Numerical simulation results obtained using the model with mesh size of 5 mm and the experimental data under the same loading conditions are compared as listed in Table 10-2. The centre point peak displacement (δ_{max}) and the peak blast reflected pressure (P_r) of the three different stand-off distances are compared and a good agreement between the test data and numerical results is observed.

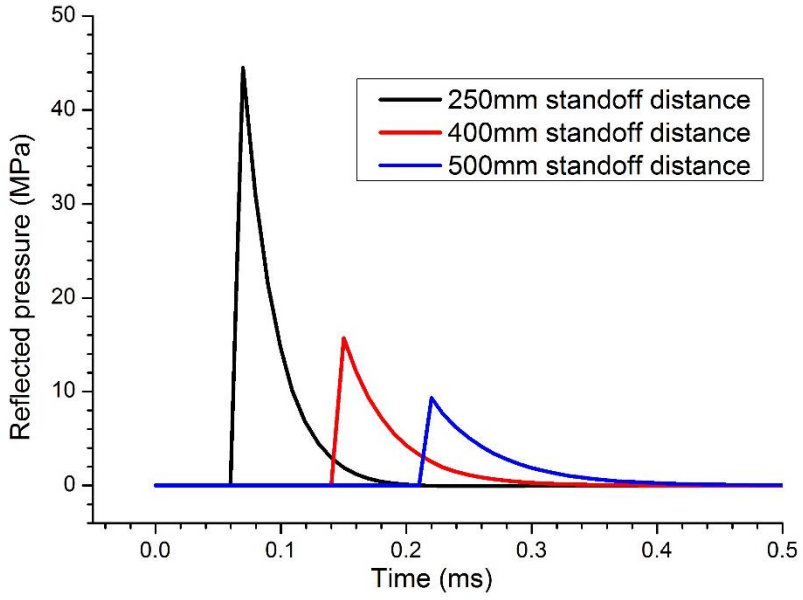

Figure 10-4. Reflected pressure time histories of steel plates with 250 mm, 400 mm and 500 mm stand-off distances

The results of mesh convergence test are shown in Figure 10-5. The discrepancy between the results corresponding to the mesh size of 20 mm from the rest are obvious while the results for the mesh size of 10 mm, 5 mm and 2.5 mm are close. It can be concluded that using the mesh size of 10 mm leads to reasonable numerical simulations as compared to the smaller mesh sizes, while the calculation on the model with finer mesh takes a substantially longer time. Therefore, the mesh size of 10 mm is acceptable. However, many structures simulated in this chapter contain different curvatures such as square dome, sphere dome, using 10 mm mesh leads to certain loss of geometry details. Therefore, 5 mm mesh size is employed in the subsequent analysis to ensure simulation accuracy and a reasonable computational time.

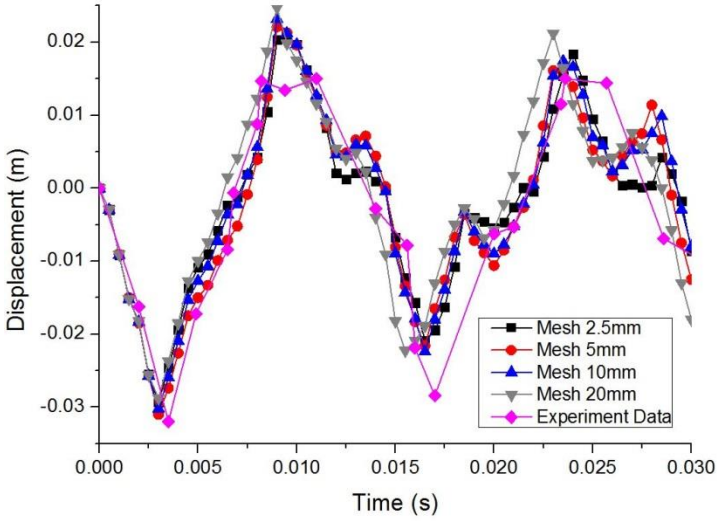

Figure 10-5. Displacement time histories with different mesh sizes and experimental data from event 14 (165)

10.3 Numerical simulations

The calibrated numerical model is used to perform simulations of dynamic response of monolithic plate, uni-directional LSC multi-arch sandwich panel, sphere dome sandwich structure and the proposed bi-directional LSC square dome sandwich panel under blast loading. The structural response quantities, i.e., the peak deflection at the centre of back plate, energy absorption and peak boundary reaction forces, are calculated and compared to evaluate their blast resistant performance.

10.3.1 Panel configuration

A flat plate with the size of 1000 mm by 1000 mm and the thickness of 5 mm is employed for comparison with the uni-directional and bi-directional LSC sandwich structures. The core of uni-directional LSC sandwich panel (A5) consists of five arches with the same length, width and arch height of 50 mm (H50) as shown in Figure 10-6. The proposed bi-directional LSC structure consists of five square domes along each horizontal direction (D5), with 25 domes in total. Each dome is 200 mm in length and width, 50 mm in arch height (H50). The whole panel has the size of 1000 mm by 1000 mm. As shown in Figure 10-7, the modified grid dome panel configuration is similar to that of the square dome panel, consisting of five sphere domes along each in-plane direction. Each dome has a 200 mm diameter and 50 mm height. Uni-directional LSC multi-arch, grid sphere dome and bi-directional LSC square dome sandwich structures have a 2 mm-thick top plate and a flat sheet attached at back with a thickness of 1.5 mm. The thickness of the core varies for each example in order to keep the overall mass of the panel the same. The schematic diagram of bi-directional LSC panel is shown in Figure 10-8. The interfaces between the core and the skins are treated as welded.

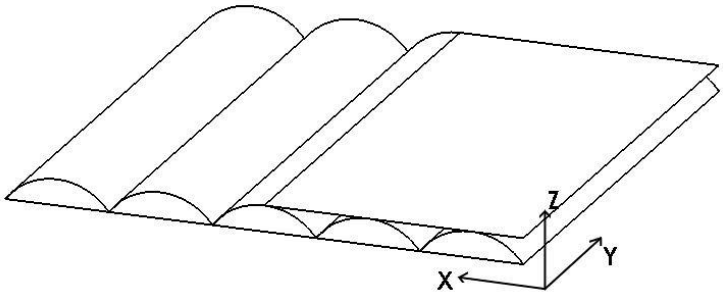

Figure 10-6. Five-arch uni-directional LSC sandwich panel with half of top plate removed for illustration.

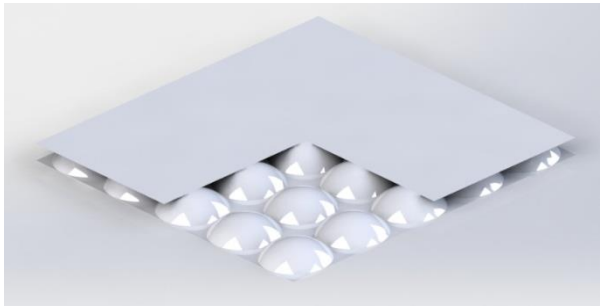

Figure 10-7. Grid sphere dome sandwich structure with top plate partially removed for illustration.

Four panels, i.e. flat plate (F1), uni-directional LSC multi-arch panel (A5-H50), grid sphere dome panel (S5-H50) and bi-directional LSC square dome panel (D5-H50) are analysed. Parametric simulations are presented in Chapter 10.4 to investigate the influences of size, geometry, material and loading condition of the square dome panel on its blast resistance capacity.

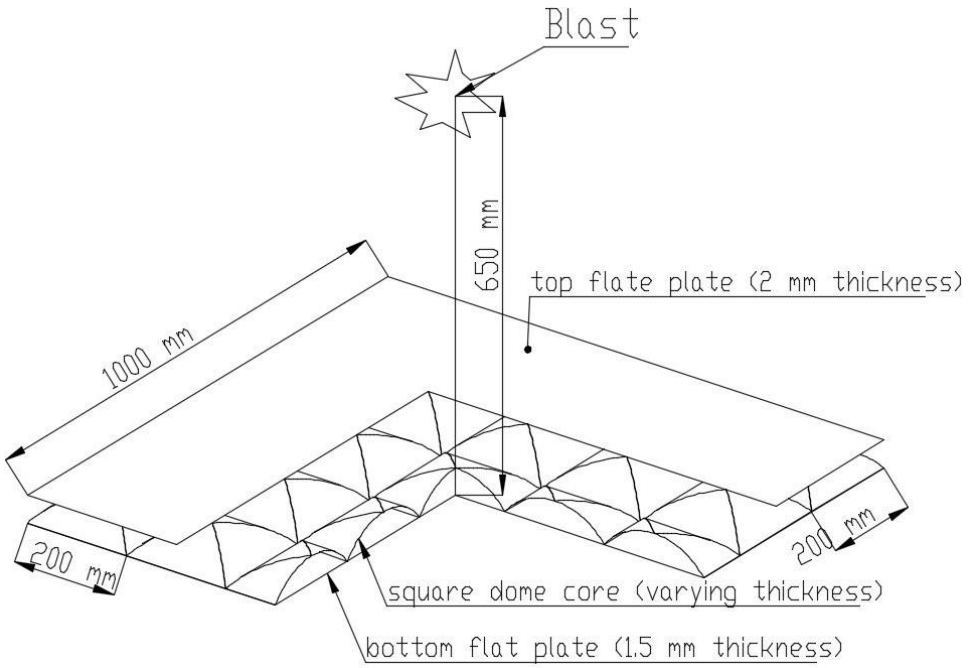

Figure 10-8. Schematic diagram of bi-directional LSC sandwich structure with five square domes in each direction

10.3.2 Finite element modelling

The fully integrated shell element with mesh size of 5 mm is used for numerical simulations. Boundaries of back plate of the panels are assumed to be fully fixed by constraining the nodes on four edges of the back flat plate in six degrees of freedom. The top face sheet and core are not constrained. Welded connection is applied for all the interfaces between layers using tied contact. The blast load applying onto the front flat sheet is simulated using *LOAD BLAST ENHENCED keyword, assuming 260 g TNT detonates directly above the centre of the panel at a 650 mm standoff distance measured from the back flat sheet centre point. The material model incorporating strain rate effect, i.e. Cowper-Symonds model is used. The material properties are the same as the ones in the model calibration given in Table 10-1. The peak reaction forces at the panel boundaries are calculated as the peak value of the sum of the nodal forces

on each edge by defining the keywords *SET NODE OPTION and *DATABASE NODAL FORCE GROUP. The termination of the simulations is set at 30 ms since the detonation of the explosive.

10.3.3 Results and Discussions

Table 10-3. Peak displacements, internal energy, boundary reaction forces of four forms of panels

Category	Layer thickness (mm)			Energy absorption by Core (kJ)	Peak displacement at centre of back plate (mm)	Peak boundary reaction force (10^5 N)		
	Top	Core	Back			F_x	F_y	$F_{vertical}$
F1	-	-	5	-	21.7	6.05	6.07	2.31
A5-H50	2	1.29	1.5	1.47	15.4	2.72	1.51	1.36
S5-H50	2	1.53	1.5	0.24	13.9	1.57	1.65	1.60
D5-H50	2	1.20	1.5	1.02	14.2	1.81	1.81	0.71

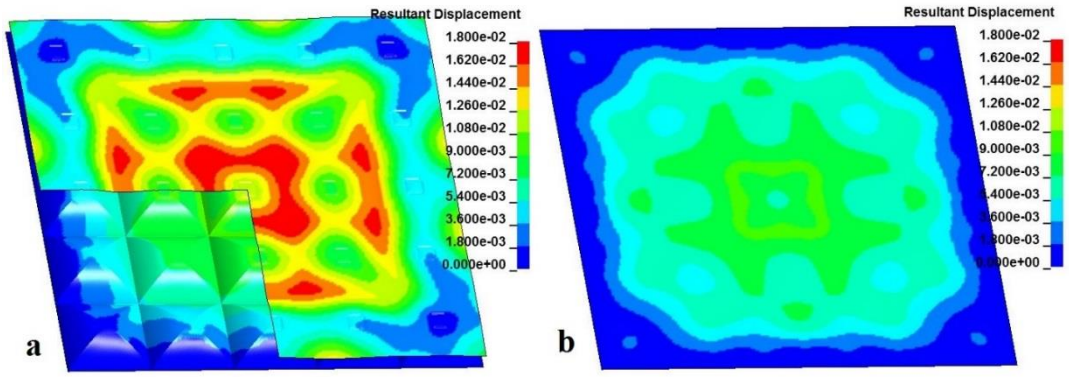

Figure 10-9. Contour of resultant displacement of D5-H50 square dome panel (a) Top layer and core, (b) Back layer, Unit: meter

Peak displacement contour plots of both the top and back plates of the D5-H50 panel are shown in Figure 10-9. Time history curves of displacement at the centre of back plate are shown in Figure 10-10. The structural responses of the panels including peak displacement, internal energy absorption of the top and back layers and peak boundary reaction forces are calculated and given in Table 10-3. To keep the total mass of each panel the same, the thicknesses of layers of each panel are calculated as given in Table 10-3 with a constant 2 mm and 1.5 mm thickness for the top and back layer respectively, and varying thickness for the core. The numerical results show that the peak displacements at the centre point of load-self-cancelling structures i.e. A5-H50,

S5-H50 and D5-H50 are reduced to 15.4 mm, 13.9 mm and 14.2 mm respectively as compared to the peak displacement of 21.7 mm of the flat plate. As shown, the S5-H50 yields the smallest peak displacement among these panels, followed by D5-H50. The minimal peak displacement is caused by the two-way symmetry of unit cells of S5 and D5 which results in a stiffer structure to deform comparing with the uni-directional multi-arch panel A5-H50, as can be seen in Figure 10-10 (a) where the vibration periods of S5 and D5 are much smaller than F1 and A5. The arches, as shown in Figure 10-6, can deform more easily along the x-axis than the y-axis because of the configuration of uni-directional arch. The deformation can also be confirmed from the internal energy absorption of the core, where the A5-H50 holds a much higher value than the other two types. Furthermore, S5-H50 has a thicker core than the other two panels, resulting in the smallest peak displacement at centre of the back plate.

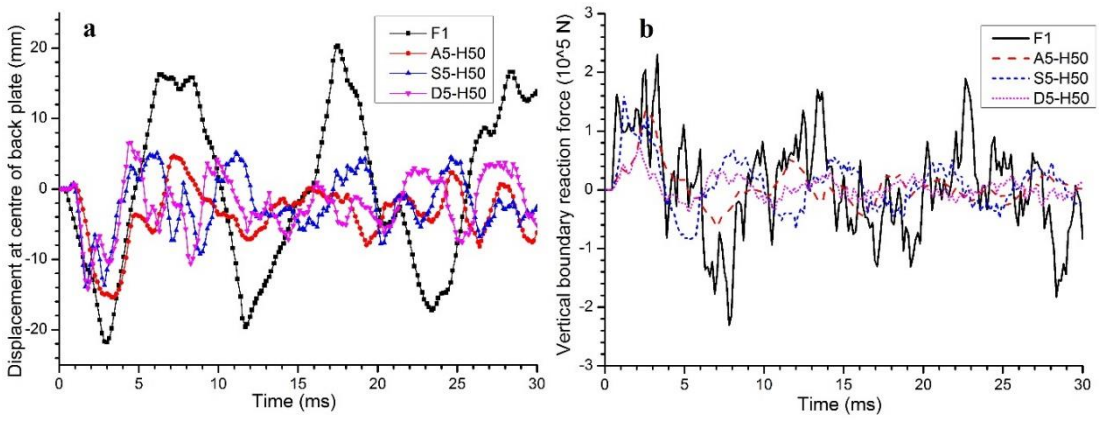

Figure 10-10. (a) Displacement time histories of centre point on back plate for four panels; (b) Time histories of vertical boundary reaction forces for four panels

As the numerical models including blast loading, boundary conditions, and geometries are symmetrical, the reaction forces Fx and Fy are taken as the sum of nodal forces on one edge only. Fz is the vertical reaction force which is taken as the sum of nodal forces in Z direction on all of four edges. Figure 10-11 shows the peak values of boundary reaction forces in three directions of four panels. Due to the geometrical symmetry of the panel F1, S5 and D5, the peak reaction forces along X and Y directions are very close in value. As given in Table 10-3, the reaction forces of A5-H50 uni-directional LSC structure in X and Y directions are 272 kN and 151 kN, respectively, which are around 55% and 75% less than the baseline F1 flat plate. The boundary reaction force in vertical direction is reduced by 41.1% to 136 kN. S5-H50

shows a similar LSC capacity, with a 72.7% reduction of boundary reaction forces in the in-plane directions and 30.7% reduction in the out-of-plane direction as compared to the flat plate F1. D5-H50 shows a more significant reduction with the reaction forces in the out-of-plane direction reducing to 71 kN, which is around 69.3% less than that of F1. The bi-directional LSC square dome panel (D5) achieves further 47.8% reduction in the out-of-plane boundary reaction force of the multi-arch structure (A5) and 55.6% less than that of the grid sphere dome (S5). The significant reduction in peak boundary reaction force on out-of-plane direction indicates the bi-directional square dome panel (D5) performs the best in cancelling blast loads, since the out-of-plane boundary reaction force of D5 is the smallest.

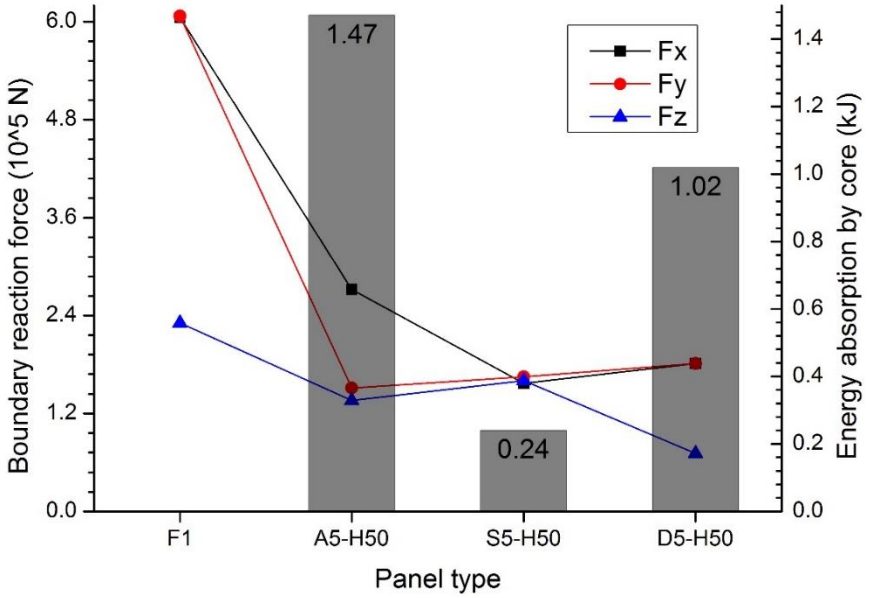

Figure 10-11 Boundary reaction forces in X, Y, Z directions and energy absorption by the core of four types of panels

It is worth noting that the boundary reaction force in out-of-plane direction is the most critical among those in three principal directions for many blast resistance applications such as blast resistant door, shield and sacrificial cladding, where the panels are simply supported at the boundary or placed directly on top of the protected structure. An example of blast resistant door is shown in Figure 10-12. Under blast loading, the door panel tends to bend inwards with reaction force exerting on the door frame mostly in the out-of-plane direction rather than the in-plane directions. The load-self-cancelling mechanism is shown in Figure 10-13. The blast loading with extremely short duration (less than 1 ms in this chapter) is applied onto the front plate. The loading is then

transmitted along the arch and to the intersections of the arches where part of the loading is cancelled out by adjacent arches before it reaches the panel supports. Therefore it reduces the loading transmitted to the back plate and support in the out-of-plane direction. All LSC structures (A5, S5 and D5) cancelling out partial blast loading at the intersections of arches or domes, lead to less blast loads being transmitted to the support. The longer and more evenly spread out of the intersections between arches or domes can lead to a higher LSC capacity, therefore the square dome panel (D5) has higher efficiency in reducing vertical boundary reaction force than the sphere domes (S5), in which the intersections between adjacent unit cells are points instead of lines.

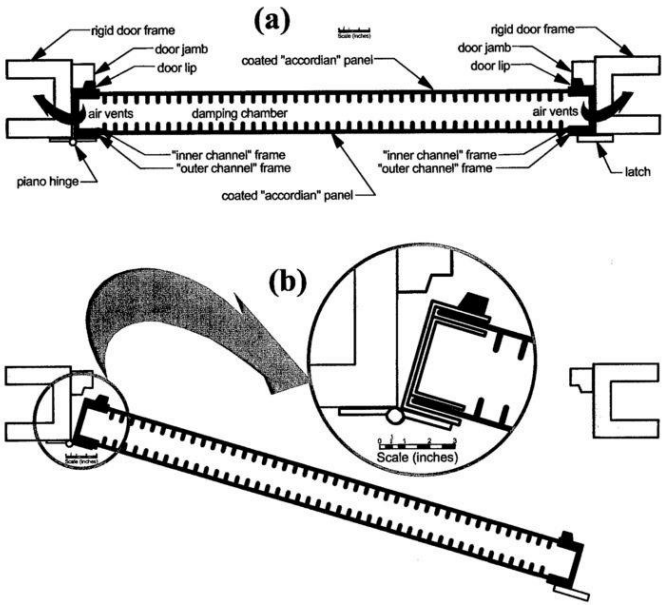

Figure 10-12. Schematic diagram of a typical blast resistant door panel (166)

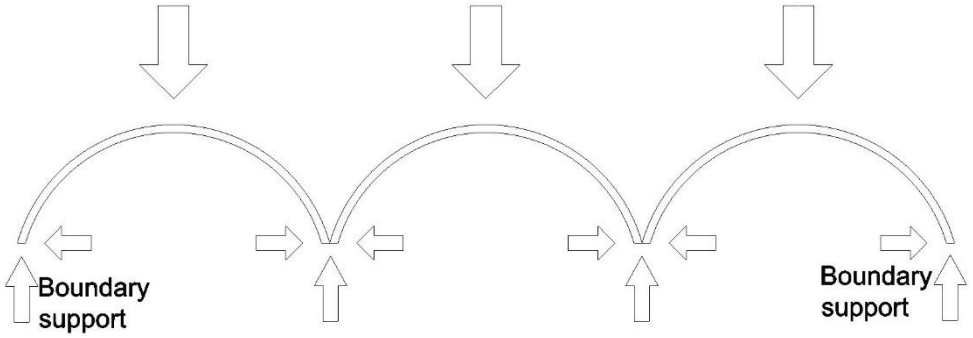

Figure 10-13. Schematic diagram of load-self-cancelling mechanism using arch or dome structure

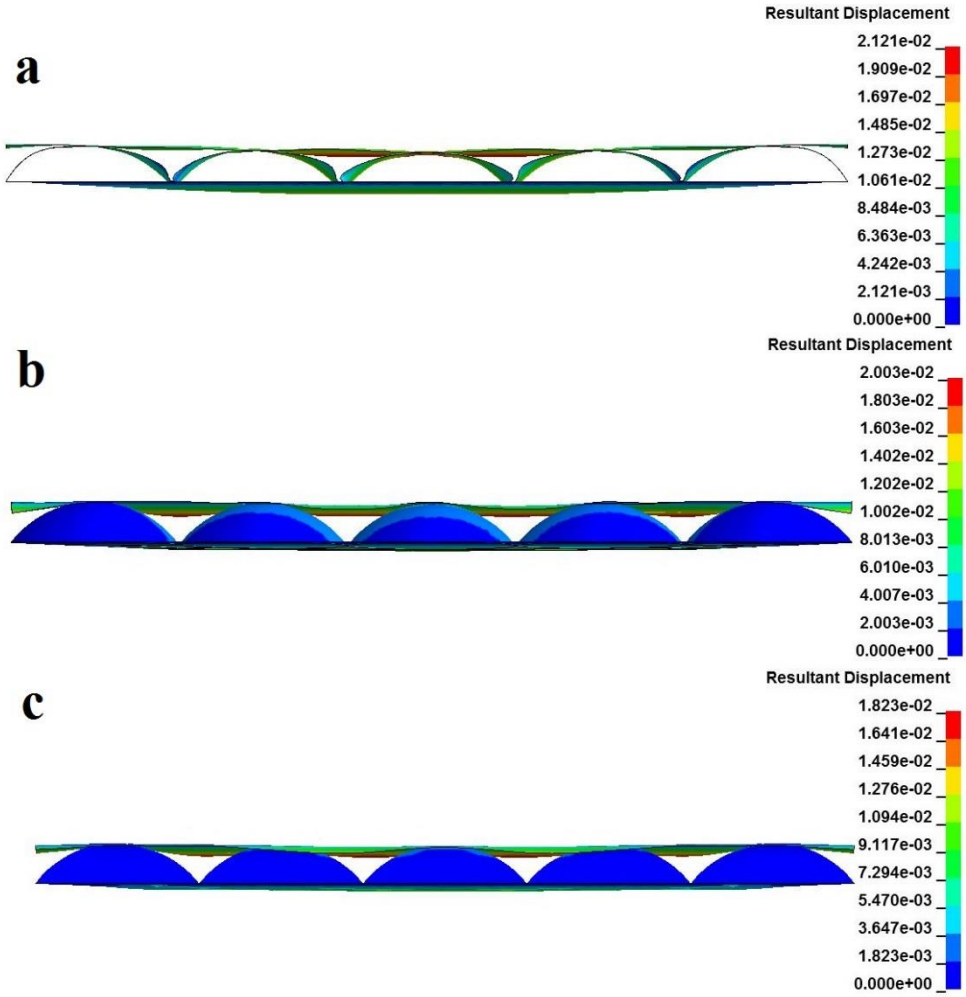

Figure 10-14. Front view of three panels' contour plots at their maximum back plate centre displacements (a) A5-H50; (b) S5-H50; (c) D5-H50; unit: meter

Figure 10-14 shows the deformation mode of three LSC panels at their maximum displacement level. The uni-directional multi-arch panel (A5) has the largest displacement for both the top plate and the core, obvious bending deformation can be spotted for the individual arch especially those at the middle of the panel. The bi-directional LSC panels (S5 and D5) show a different damage mode due to the increase in crushing resistance of individual unit. The peak displacement at the back face plate is smaller and the individual unit cell is more intact. This can be also confirmed from the energy absorption by the core listed in Table 10-3, where the core of A5 absorbs more energy than the core of the other two panels (S5 and D5), indicating larger plastic deformation of the core. With a 25% thicker wall of the core, S5 shows a slightly lower peak displacement of the back plate and a smaller energy absorption than the square

dome panel D5. However, the square dome panel (D5) has better performance in terms of reducing vertical boundary reaction force than the sphere domes (S5).

10.4 Parametric studies

In this section, performances of the LSC square dome panels with different configurations and parameters are investigated to evaluate their blast resistance capacities. These parameters include the number of square dome, dome height, layer material. Unless otherwise noted, the panel considered is 1 m by 1 m with 50 mm arch height subjected to 260 g of TNT equivalency detonated at 650 mm directly above the centre point of back flat layer, which is the same as the previous section. The top and back layer thickness is kept constant while the thickness of the core is varied in order to maintain the same overall mass of the panels. To examine the performances, the peak displacement, internal energy absorption and peak boundary reaction forces are extracted and compared.

10.4.1 Effect of dome number

The panels with different numbers of square domes are discussed in this section. D3, D4, D5, D6 and D7 represent the number of domes along one horizontal direction, therefore the total numbers of domes for these panels are 9, 16, 25, 36 and 49, respectively, as listed in Table 10-4. The results indicate that in general the peak deflection at the centre of the back layer decreases with the increase in the number of domes, except the panel D4 and D6, as more dome numbers lead to more connections between the layers. The panel thus becomes stiffer to bend, even though the thickness of the core decreases slightly with the increasing dome number. The displacement time histories of the panels are shown in Figure 10-15.

Table 10-4. Peak displacements, internal energy, boundary reaction forces of square dome panels with varying dome numbers

Category	**Layer thickness (mm)**			**Energy absorption by core (kJ)**	**Peak displacement at centre of back plate (mm)**	**Peak boundary reaction force (10^5 N)**		
	Top	Core	Back			F_x	F_y	F_z
D3-H50	2	1.38	1.5	1.22	21.3	1.39	1.4	0.88
D4-H50	2	1.29	1.5	1.12	12.2	2.13	2.13	0.75
D5-H50	2	1.20	1.5	1.02	14.2	1.81	1.81	0.71

D6-H50	2	1.10	1.5	1.16	9.6	2.10	2.10	0.70
D7-H50	2	1.01	1.5	1.29	10.1	2.10	2.11	0.71

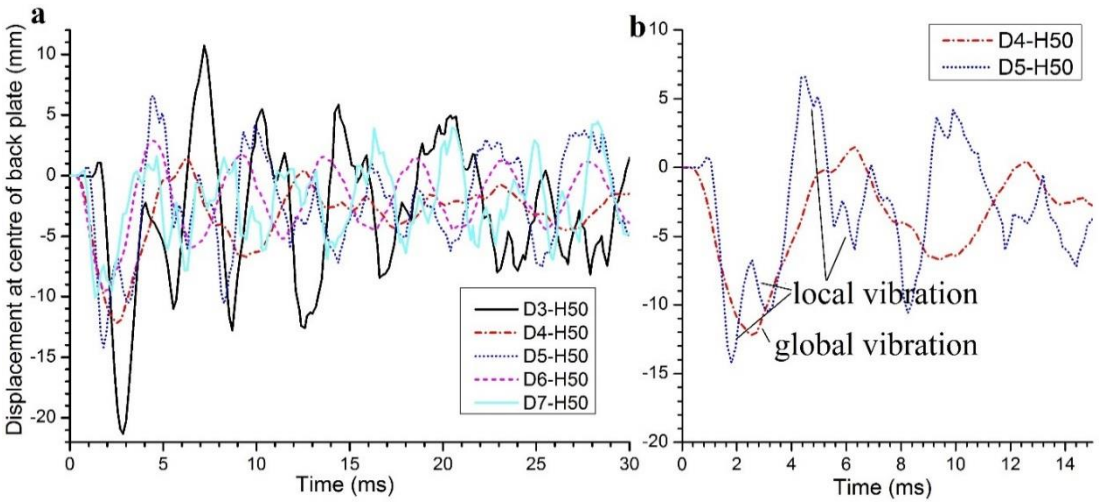

Figure 10-15. Displacement time histories of centre point of the back plate (a) for the panels with different dome numbers; (b) zoomed in for D4-H50 and D5-H50

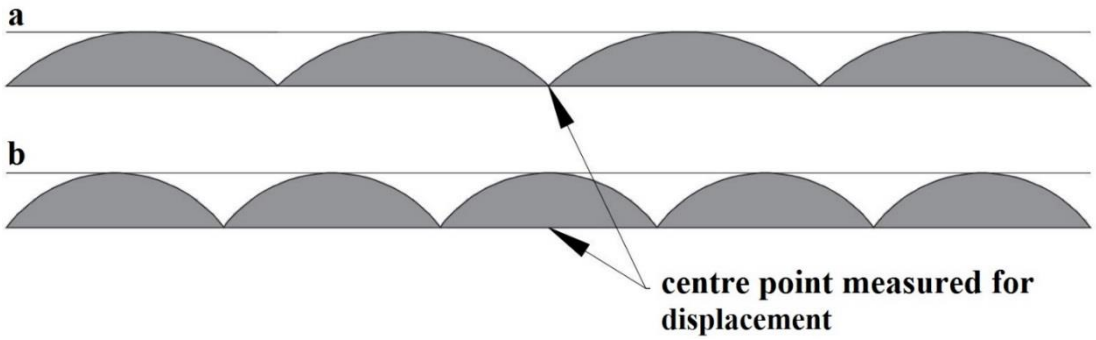

Figure 10-16. Illustration of the centre point location relative to the dome core connections (a) even and (b) odd number of square domes

The panels with an even number of dome core, i.e., D4 and D6, show smaller deformation at the centre point of the back layer as compared to those with odd number of dome core, because the centre point locates at the interactions between the adjacent domes as shown in Figure 10-16. The local stiffness is higher at centre point where four adjacent dome intersects, therefore leads to relatively smaller deformation of the point. Whereas the centre point of the panel with odd number of dome core locates at the centre of a dome, hence there is no local stiffening effect at the point. Moreover, after short duration of blast loading (less than 1ms in this chapter), free vibration occurs. As shown in Figure 10-15, only global vibration of the back plate contributes to the centre point displacement response when the core has an even number of domes,

but both the global response and local response modes, i.e., vibration modes between intersection points, contribute to the displacement responses of the centre point when the core has an odd number of domes. These are the reasons why the centre point of panels with odd number of domes experiences relatively smaller deformations. Nonetheless increasing the number of domes makes the panel stiffer and hence reduces the global panel deformations.

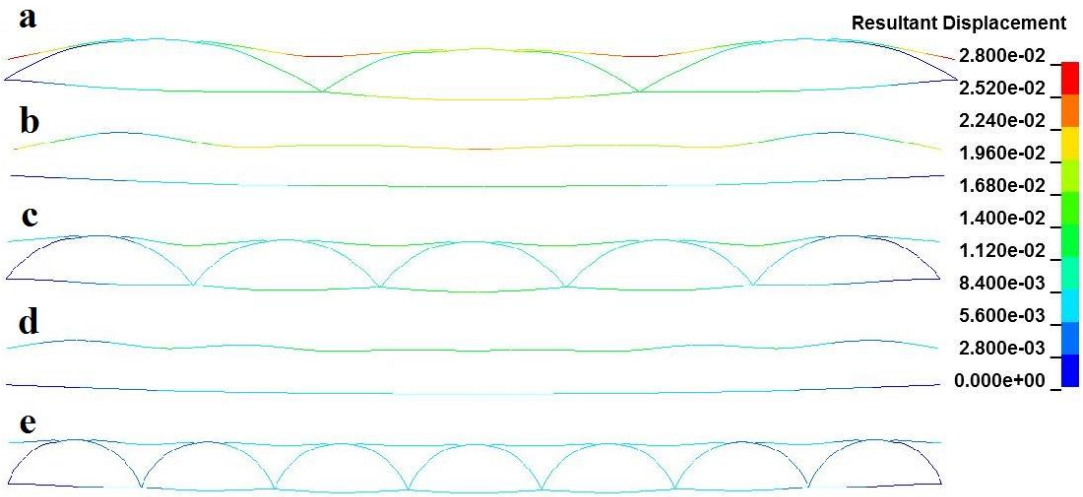

Figure 10-17. Middle plane cross-section views of square dome panels at their peak back plate centre deflection, (a) D3-H50; (b) D4-H50; (c) D5-H50; (d) D6-H50; (e) D7-H50; units: meter, note domes are not cut through for (b) and (d) where the centre planes are located at the intersection of domes, only top and back plates are shown

The cross-section view of deformation modes of the panels are shown in Figure 10-17. The peak boundary reaction forces for D4 to D7 along the both in-plane directions are similar in value, as given in Table 10-4 and Figure 10-18. D3 square dome panel has the lowest peak boundary reaction forces in the in-plane directions among the panels, which might be caused by the large deformation and energy absorption of the top plate and the core as shown in Figure 10-17 (a). Since the peak reaction force in the out-of-plane direction is more critical in the design as discussed in Chapter 10.3.3, it is of more interests in this chapter. As shown, the peak out-of-plane reaction force decreases around 20.5% to 70 kN with the increasing number of domes from D3 to D6, but increases slightly to 71 kN from D6 to D7. As explained in in Chapter 10.3.3 regarding the mechanism of using arch for load-self-cancelling, the more uniformly distributed loads on the adjacent domes increase the effectiveness of cancellation and decrease the peak reaction forces at the boundaries of panels. With the increasing

number of square domes, the load can be distributed more evenly onto the adjacent domes, resulting in a better LSC performance. However, further increasing the number of domes cannot lead to more effective load-self-cancelling of the panel. As the dome height is set to be fixed, with the increasing number of domes, the arches of domes are becoming closer to a half circle shape as shown in Figure 10-17. The loads transferred to the intersections of the arches decreases, which leads to a reduction in load cancellation. Another reason is that increasing the number of domes increases the surface area of core, and its thickness has to be thinned to maintain the same overall mass, which might decrease the bending stiffness of the whole panel. It can be concluded that increasing the number of square domes lowers the boundary reaction forces in the out-of-plane direction. However, this trend is no longer true when the dome base dimension approaches to the dome height, i.e., the dome shape approaches to a semi sphere. Among the configurations considered in the present study, D6-H50 has the best performance, with the smallest peak displacement at the back face and the smallest out-of-plane peak reaction force.

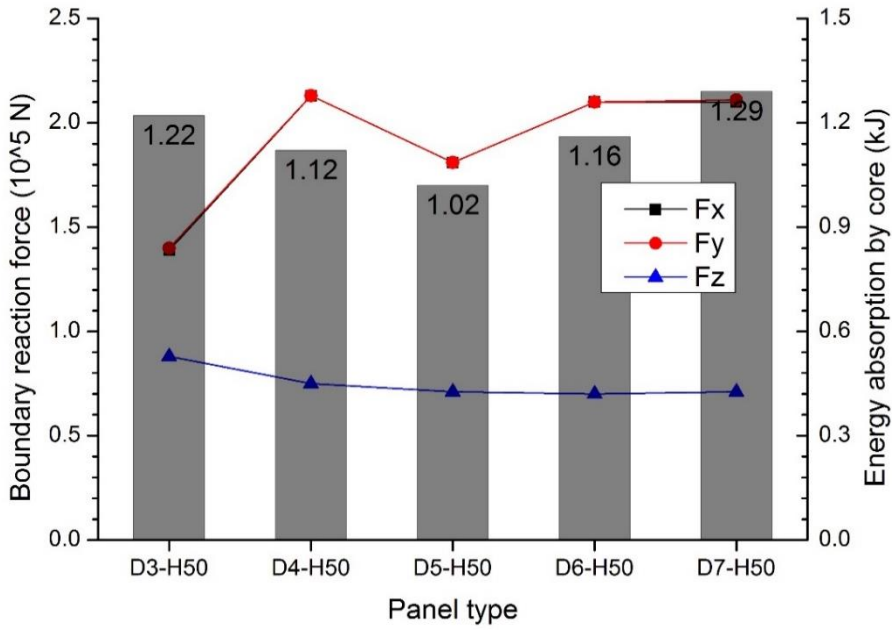

Figure 10-18. Boundary reaction forces in X, Y, Z directions and energy absorption by core of panels with varying numbers of square domes

10.4.2 Effect of dome height

The dome height varies from 30 mm to 70 mm with 10 mm interval. The peak responses of the panels are given in Table 10-5, and illustrated in Figure 10-19. It is

found that the peak displacement at the back decreases with the increasing height of the domes even though the blast load acting on the panel increases owing to the reduced stand-off distance from the explosion centre to the panel. The panel D5-H30 has a similar peak displacement as the baseline F1 flat plate (i.e. 21.9 mm). A relatively limited load-self-cancelling effect can be observed when comparing with other square dome structures. As compared with F1, the peak displacement of square dome panel reduces by 25%, 32%, 35%, 37% and 39% for the panels with different dome heights varying from 30 mm to 70 mm, respectively. The reduction in peak displacement is because the bending stiffness of the panel increases with the height of the domes.

Table 10-5. Peak displacements, internal energy, boundary reaction forces of square dome panels with varying heights

Category	**Layer thickness (mm)**			**Energy absorption by core (kJ)**	**Peak displacement at centre of back plate (mm)**	**Peak boundary reaction force (10^5 N)**		
	Top	Core	Back			F_x	F_y	F_z
D5-H30	2	1.41	1.5	0.83	16.2	2.36	2.36	0.73
D5-H40	2	1.34	1.5	0.91	14.7	1.88	1.88	0.73
D5-H50	2	1.20	1.5	1.02	14.2	1.81	1.81	0.71
D5-H60	2	1.10	1.5	1.12	13.6	1.40	1.40	0.66
D5-H70	2	1.01	1.5	1.43	13.3	1.12	1.11	0.69

The peak values of boundary reaction forces also decrease with the increase in the dome height from 30 mm to 60 mm. However further increase the dome height to 70 mm leads to a slight increase in the boundary reaction forces in the out-of-plane direction as compared with D5-H60 which can be explained by the dome geometries. The angle of dome at intersection edge can be calculated as 53 degree, 62 degree and 70 degree for the panel D5-H50, D5-H60 and D5-H70, respectively. The highest dome H70 has the largest angle at the intersection, which leads to less effective load cancelling performance. Similar to the results presented in Chapter 10.4.1, the more critical vertical component of boundary reaction force first decreases and then increases slightly with the increasing number of domes, which is also associated with the change of the angle at dome intersections. Moreover, the LSC panels with higher domes experience higher overpressure due to the reduction of the distance from the front plate to the detonation. Furthermore, the panels with higher domes have a larger

surface area of the dome shaped layer, which leads to a reduction on the thickness of the core. These combined factors affect the LSC capacity of the structure. Similarly, the energy absorption by the core increases with the rising height of the core as shown in Figure 10-19. With higher cores, the bending stiffness of the panel is higher, but the crushing of each individual dome becomes easier due to thinner dome wall thickness and larger crushing distance. Therefore, less bending of the panel but more deformation of the core is observed for the panels with higher domes. It is found that D5-H60 performs the best among the panels considered in the present study in terms of the effectiveness of load-self-cancelling of the structure using the out-of-plane peak reaction force as criteria.

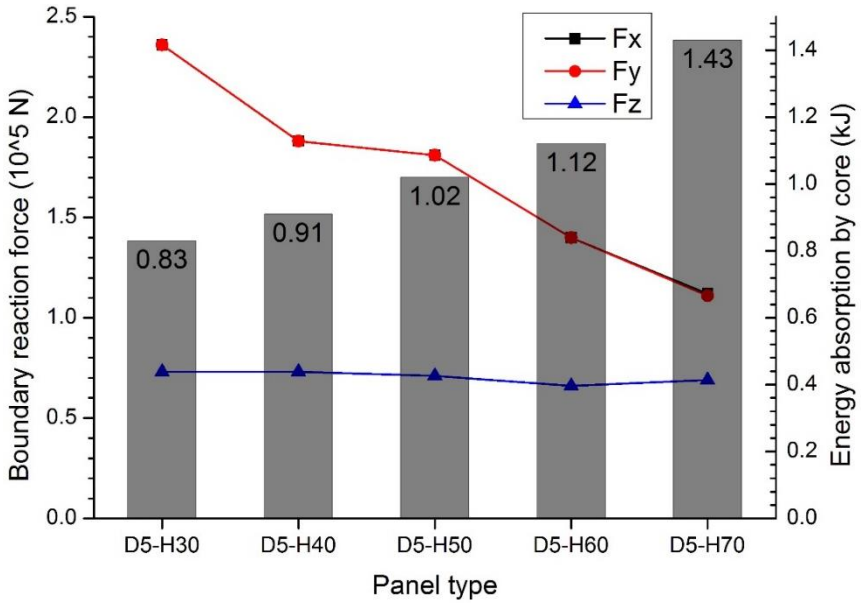

Figure 10-19. Boundary reaction forces in X, Y, Z directions and energy absorption by the core of panels with varying heights of square domes

10.4.3 Effect of blast intensity

Four different explosive weights are considered to study the effect of blast intensities. Four TNT weights of 260 g, 0.5 kg, 1 kg and 4 kg are set to examine blast resistance capacity of the proposed bi-directional LSC panel. Scaled distance is calculated based on the equation (10-3) and listed with structural responses in Table 10-6. Peak reflected pressure and positive phase impulse exerted on the front plate are calculated based on the centre element of the panel. The peak displacement, boundary reaction forces on the three axes increase with the increment of blast intensity as expected.

Increasing trend of energy absorption by the core with the increase of blast intensities can be also observed.

Table 10-6. Peak displacements, internal energy, boundary reaction forces of square dome panels under different blast intensities

Category	Scaled distance ($m/kg^{1/3}$)	Peak reflected pressure at centre (MPa)	Positive phase impulse (Ns)	Energy absorption by core (kJ)	Peak displacement at centre of back plate (mm)	Peak boundary reaction force (10^5 N)		
						F_x	F_y	F_z
D5-H50-0.26kg	0.94	5.8	389	1.02	14.2	1.81	1.81	0.71
D5-H50-0.5kg	0.76	10.4	646	3.04	21.8	1.98	1.95	1.35
D5-H50-1kg	0.60	18.4	1096	8.67	46.1	4.94	4.95	3.23
D5-H50-4kg	0.38	50.7	3448	51.7	146	8.39	8.39	11.7

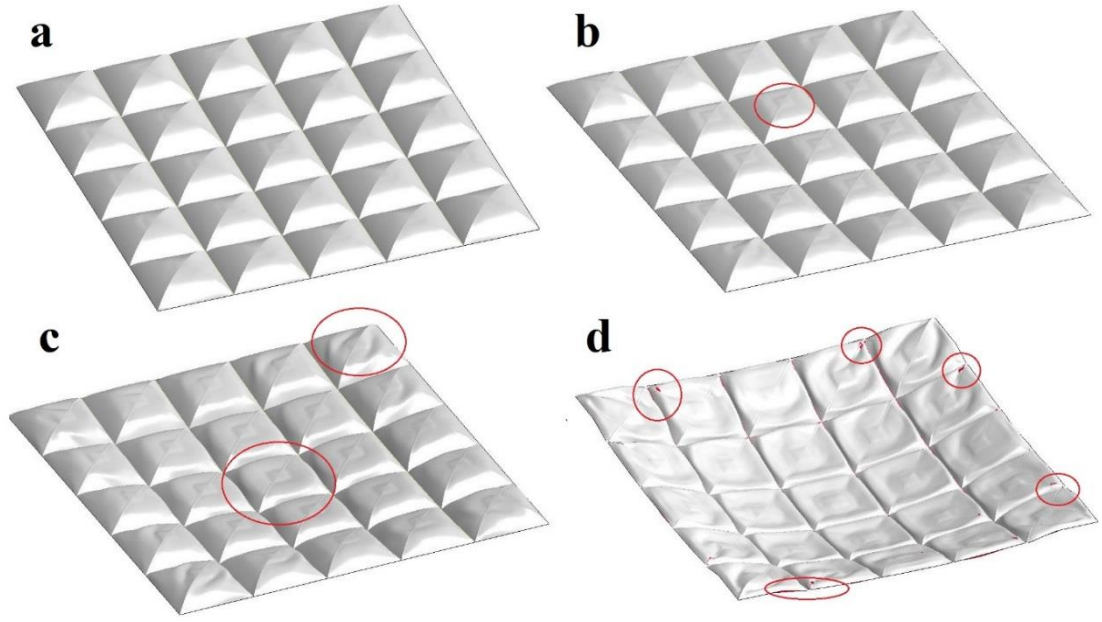

Figure 10-20. Damage modes of (a) D5-H50-0.26kg; (b) D5-H50-0.5kg; (c) D5-H50-1kg; (d) D5-H50-4kg at their maximum deflections, top plate removed for illustration

Damage modes of square dome panel under different blast intensities are shown in Figure 10-20. Both global damage of the panel and localized damage of individual square dome can be observed for the cases with higher blast intensities. For D5-H50-

0.26kg and D5-H50-0.5kg, only slight global deformation of the panels can be observed. The panel subjected to the blast loads from the other two cases experience severe localized damage of individual square domes at the centre and corners, as well as global deformation. The localized deformation near the corner under 4kg detonation (Figure 10-20 d) is caused by the global deformation of the panel when the panel bends along the in-plane directions. All the domes are crushed under blast load from 4 kg explosion, tearing and breakage of the panel appear near the corners of some individual domes as shown in Figure 10-20 (d) marked in circles. The plastic strain of back plate under blast loading of 4kg explosion is shown in Figure 10-21, where high plastic strain of elements at the outer edges and intersections of domes are captured. The line of elements at the outer edges are eroded due to stress concentration as circled. An increase in the damage of individual square domes and the whole panel can be observed with the increase of blast intensity.

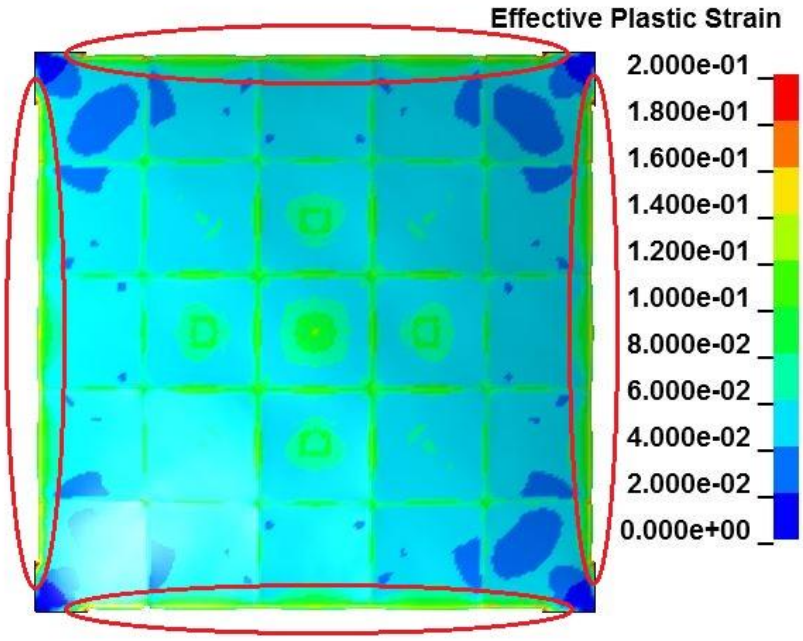

Figure 10-21. Plastic strain of back flat plate of D5-H50-4kg, eroded edge elements are circled

10.4.4 Effect of different materials

The layers made of different materials are considered in this section. Aluminium alloy Al-2024-T3 is used to replace the core made of steel. Since aluminium alloy shows less evident strain rate effect (65), strain rate effect is not considered in the material

model and the rest of the parameters used in the material model are given in Table 10-7.

Table 10-7. Material properties of Aluminium alloy Al-2024-T3 (65)

Property	Young's modulus (GPa)	Poisson's ratio	Yield stress (MPa)	Tangent modulus (MPa)	Density (kg/m^3)
Value	72	0.33	318	737	2680

Structural responses are summarized in Table 10-8 and shown in Figure 10-22 and Figure 10-23. The centre point peak deflection of back layer increases from 14.2 mm to 16.5 mm by replacing steel with aluminium alloy core. Similarly, the internal energy absorption of the core made of aluminium alloy increases 70.6% and the internal energy absorption of back flat layer increases as well. It is found that the out-of-plane boundary reaction forces increase 42.3% by using aluminium alloy core. It is because Aluminium alloy is less stiff than steel and it is easier to deform under the same load, which reduces the load-self-cancelling capability.

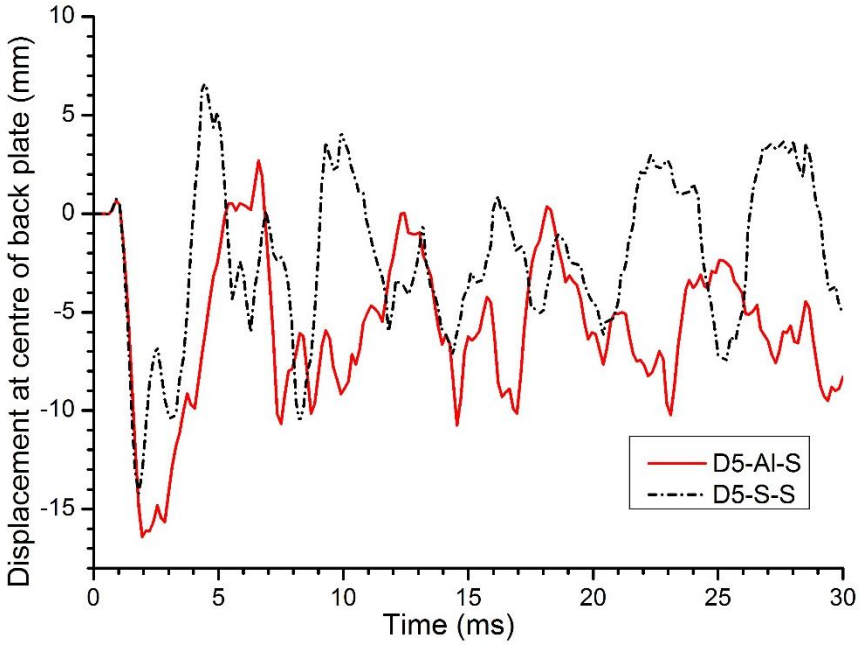

Figure 10-22. Displacement history of centre point on back plate for panel with different core materials

Table 10-8. Peak displacements, internal energy, boundary reaction forces of square dome panels with different core materials

Category	Layer thickness (mm)			Energy absorption by core (kJ)	Peak displacement at centre of back plate (mm)	Peak boundary reaction force (10^5 N)		
	Top	Core	Back			F_x	F_y	F_z
D5-S-S	2 (steel)	1.2 (steel)	2.5 (steel)	1.02	14.2	1.81	1.81	0.71
D5-Al-S	2 (steel)	1.2 (Al)	2.5 (steel)	1.80	16.5	1.39	1.39	1.01

Energy absorption is usually achieved by plastic deformation (2), fracture and friction of structure (124) during blast or impact event. In this study, the load-self-cancelling structure is functioned by the arching geometry of the structure and stress propagation after the loading. The excessive deformation of the core leads to the change of arch shape, which might undermine load-self-cancelling capability. As illustrated in Figure 10-23, the panel with aluminium core experiences a much more severe deformation than the one with steel core. Hence, the locations with stress concentration and large deformation are suggested to be strengthened to maintain load-self-cancelling function by using stiffer material or stiffened structure such as stiffened multi-arch double layer panels (75).

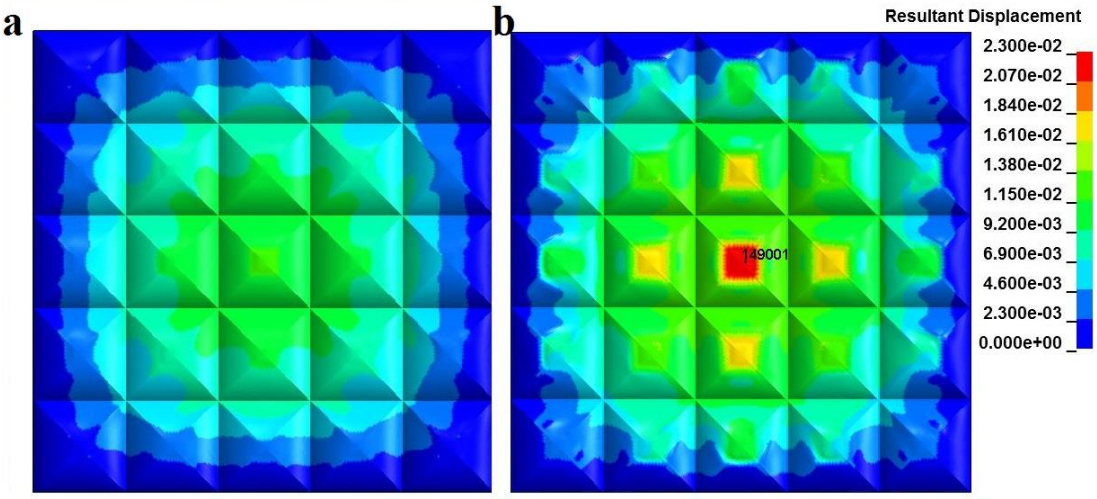

Figure 10-23. Contour plots of resultant displacement of D5-H50 square dome panel (a) with steel core, (b) with aluminium core, Unit: meter

10.5 Summary

A bi-directional load-self-cancelling (LSC) square dome sandwich panel is proposed in this chapter and its blast LSC effectiveness is numerically demonstrated in the most critical direction (i.e. out-of-plane direction), after comparing with the flat plate, uni-directional LSC multi-arch structure and sphere dome structure of the same mass. Up to around 69% reduction in boundary reaction force is observed as compared with the flat panel. Parametric studies on the number of square domes, dome height, blast intensity and material are also carried out. It is found that the panel with more numbers of domes and stiffer domes has better load-self-cancelling capability. Blast resistance capacity of the panel also enhances with the increase of dome height. However, further increasing the number and height of domes may reduce the blast resistance performance of the panel. The proposed new structural form might find applications to fabrication of sandwich panels to resist blast loadings.

Chapter 11. Conclusion and recommendations

11.1 Main findings

In this thesis, folded structures with different geometries, base shapes, layer configurations, foam infill configurations, and graded structures are numerically and experimentally investigated under various loading conditions, including quasi-static, dynamic crushing and blast loads. Due to the in-directly connected sidewalls of the folded structure, the folded structures show superior crushing behaviour and energy absorption over conventional core of sandwich panels. It has a high crushing resistance without inducing peak force throughout crushing process. The proposed folded structure also shows consistent crushing response over various loading conditions, thus it is ideal for the applications as energy absorbers. The multi-layer setup has been verified as reusable and its layer number can be easily adjusted to provide different energy absorbing capacities. Light weight foam infills can greatly enhance the energy absorption of the folded structures without introducing initial peak force, due to foam-wall interaction effect. Furthermore, graded configurations show significant influence on crushing responses of the multi-layer folded structures under high crushing speed. The proposed bi-directional load-self-cancelling panel demonstrates significant reduction in boundary reaction force in out-of-plane direction, comparing to other panels under blast loading, indicating potential application as blast resistant panels.

Chapter 3 presents the geometry effect of truncated square pyramid (TSP) kirigami folded structures on crushing behaviours. All four TSP foldcores show uniform crushing behaviour under quasi-static loading as compared to the existing cube strip kirigami structure. Under dynamic crushing, however, the TSP foldcores with higher sidewall slope have a huge increase in initial peak force. Similar observation has been also made with closed-top design, due to inertial stabilization effect provided to the sidewalls. Open-top TSP foldcore with slightly lower sidewall slope demonstrates ideal crushing response comparing with other geometries and the cube strip kirigami foldcore.

Chapter 4 presents the effects of base shape and boundary condition on the static and dynamic crushing behaviours of truncated pyramid folded structure. Three base shapes, triangle, square and pentagon are considered, which results in different slope angle of

sidewalls, size of interconnections, and folded number per unit area. Two boundary conditions (fixed and simple boundary) are considered as well. Under quasi-static loading condition, boundary condition shows great influence on crushing responses of the TSP and TPP but not so much for TTP and Miura type foldcore. TSP shows the best energy absorption performance over other three truncated pyramid folded structures and Miura type foldcore.

Chapter 5 and Chapter 6 present the blast mitigation capacity of sacrificial cladding with TSP folded structure as core. The TSP foldcore shows similar consistent collapsing resistance as aluminium foam but with higher average crushing resistance. Therefore, the TSP folded structure is able to absorb higher energy than aluminium foam of similar density. However, the density of TSP foldcore has the upper limit due to the folding process of the structure limiting its wall thickness. Thus, rigid polyurethane foam is added inside the TSP foldcore without increasing the thickness of the TSP cell walls, this is to further increase the energy absorption and blast mitigation under higher blast intensities. The foam infill greatly increases the energy absorption capacity of the structure due to foam-wall interaction effect. Furthermore, SDOF analysis is carried out. For each blast intensity, the required height of cladding can be calculated based on the blast parameters and cladding properties, which could be used as a designing tool for sacrificial cladding.

Chapter 7, Chapter 8 and Chapter 9 present the experimental study on multi-layer folded structures and the effects of different foam infill configurations under impact loads. In Chapter 7, reusable multi-layer set-up is proposed, the dynamic crushing behaviours of TTP, TSP and the influence of wall thickness are investigated. Foam-like consistent crushing behaviour with no initial peak force and low fluctuation is demonstrated for TSP foldcore under various dynamic crushing conditions, as compared to conventional sandwich structures. Different foam infill configurations including foam material, density, shape, and graded foam filler are considered. Foam infill greatly enhances the crushing resistance of the structure without inducing the initial peak during the deformation. With less than 20% increment in mass of the foam filler, the average crushing resistance of the structure increases up to 82%. Graded foam infill shows little influence on crushing response under low speed impact. Under higher speed impact, positively graded structure (i.e. increase density from impacting end) shows an enhanced and much more uniform crushing resistance than negatively

graded structure. It is also worth noting that the factors such as foam filler configurations and crushing speeds, could greatly affect the damage mode and the deforming order of the multi-layer TSP folded structure.

Chapter 10 presents the blast resistance performance of a new bi-directional load-self-cancelling panel. Its blast resistance is compared with other panels including one-directional multi-arch panel, grid sphere dome panel and flat plate. The proposed panel consists of array of square domes, each dome is two-way symmetrical along both in-plane directions. Owing to this geometry, the blast loading applying to the arch is cancelled out near the intersection of the adjacent arches, resulting in a greatly reduced reaction force at the boundary of the panel. Up to 69% reduction in out-of-plane boundary reaction force is observed as compared to the flat plate with the same weight. This design could be used as blast resistant door panel to reduce the reaction force acting on the door frame in the blast event.

Overall, two types of thin-walled structures are proposed and investigated in this thesis. Excellent energy absorption capability with low initial peak force, high average crushing force and low sensitivity to loading rate is observed for single and multi-layer truncated pyramid folded structures. This indicates the great potential of such structures to be used in energy absorbing applications such as highway or bridge impact attenuators, sacrificial claddings, helmets, etc. to protect personnel, vehicles and structures under impact and blast loads. For the other type of bi-directional load-self-cancelling structure, a significant reduction in boundary reaction force is shown under blast loads. This proposed structure can be used as lightweight blast resistant panel or door, which is capable to reduce load transferred to the supporting frames in the blast event.

11.2 Recommendations for future work

Parametric studies have been carried out in this thesis for both truncated pyramid folded structures and bi-directional load-self-cancelling square dome panels. Topological optimization could be conducted to optimize the geometries of these structures and enhance the crushing resistance of the proposed structures in the future.

Furthermore, blast tests can be carried out to verify and examine blast mitigation performance of the proposed TSP folded structures. Different blast intensities and

stand-off distances can be applied to evaluate the blast mitigating performance of the proposed structures. The proposed structure may be compared with current protective sacrificial cladding structures such as aluminium foam with similar density by comparing the peak force transmitted to the protected structures behind the claddings under different blast scenarios.

The damage mode of the proposed TSP foldcore is investigated numerically and experimentally under various loading speeds. The change in damage mode is observed with the increasing crushing speed. Further investigations on the transition of the damage mode and the associated loading rates could be conducted. Analytical study on the crushing process of the TSP foldcore could be carried out based on different damage modes under different loading speeds.

Reference

1. Hao H. Predictions of Structural Response to Dynamic Loads of Different Loading Rates. International Journal of Protective Structures. 2015;6(4):585-606.

2. Lu G, Yu T. Energy Absorption of Structures and Materials. Cambridge England: Woodhead publishing limited; 2003.

3. van Oorschot N. Deformable and energy absorbing protection against ship collision. 2017.

4. Sun G, Li G, Hou S, Zhou S, Li W, Li Q. Crashworthiness design for functionally graded foam-filled thin-walled structures. Materials Science and Engineering: A. 2010;527(7-8):1911-9.

5. Chatys R, Panich A, Jurecki RS, Kleinhofs M, editors. Composite materials having a layer structure of "sandwich" construction as above used in car safety bumpers. Automotive Safety, 2018 XI International Science-Technical Conference; 2018: IEEE.

6. Levadnyi I, Awrejcewicz J, Zhang Y, Goethel MF, Gu Y. Finite Element Analysis of Impact for Helmeted and Non-helmeted Head. Journal of Medical and Biological Engineering. 2017.

7. Hanssen A, Enstock L, Langseth M. Close-range blast loading of aluminium foam panels. International Journal of Impact Engineering. 2002;27(6):593-618.

8. Li Z, Chen W, Hao H. Blast resistant performance of multi-layer square dome shape kirigami folded structure,. 6th International Conference on Design and Analysis of Protective Structures; 29th Nov-1st Dec; Melbourne, Australia2017.

9. Li Z, Chen W, Hao H. Blast mitigation performance of cladding using Square Dome-shape Kirigami folded structure as core. International Journal of Mechanical Sciences. 2018;145:83-95.

10. Li Z, Chen W, Hao H. Blast resistant performance of cladding with folded open-top truncated pyramid structures as core. 7th International Meeting on Origami in Science, Mathematics, and Education; September 5-7; Oxford, UK2018.

11. Radford DD, McShane GJ, Deshpande VS, Fleck NA. Dynamic Compressive Response of Stainless-Steel Square Honeycombs. Journal of Applied Mechanics. 2007;74(4):658.

12. Wierzbicki T. Crushing analysis of metal honeycombs. International Journal of Impact Engineering. 1983;1(2):157-74.

13. Zhang J, Ashby M. The out-of-plane properties of honeycombs. International Journal of Mechanical Sciences. 1992;34(6):475-89.

14. Becker W. Closed-form analysis of the thickness effect of regular honeycomb core material. Composite structures. 2000;48(1):67-70.

15. Hazizan MA, Cantwell WJ. The low velocity impact response of an aluminium honeycomb sandwich structure. Composites Part B: Engineering. 2003;34(8):679-87.

16. Côté F, Deshpande VS, Fleck NA, Evans AG. The out-of-plane compressive behavior of metallic honeycombs. Materials Science and Engineering: A. 2004;380(1-2):272-80.

17. Xue Z, Hutchinson JW. Crush dynamics of square honeycomb sandwich cores. International Journal for Numerical Methods in Engineering. 2006;65(13):2221-45.

18. Ousji H, Belkassem B, Louar MA, Reymen B, Martino J, Lecompte D, et al. Air-blast response of sacrificial cladding using low density foams: Experimental and analytical approach. International Journal of Mechanical Sciences. 2017;128-129:459-74.

19. Gardner N, Wang E, Shukla A. Performance of functionally graded sandwich composite beams under shock wave loading. Composite Structures. 2012;94(5):1755-70.

20. Ouellet S, Cronin D, Worswick M. Compressive response of polymeric foams under quasi-static, medium and high strain rate conditions. Polymer Testing. 2006;25(6):731-43.

21. Banhart J, Schmoll C, Neumann U, editors. Light-weight aluminium foam structures for ships. Proceedings of the Conference on Materials in Oceanic Environment (Euromat'98); 1998.

22. Andrews E, Sanders W, Gibson LJ. Compressive and tensile behaviour of aluminum foams. Materials Science and Engineering: A. 1999;270(2):113-24.

23. Deshpande VS, Fleck NA. Isotropic constitutive models for metallic foams. Journal of the Mechanics and Physics of Solids. 2000;48:1253-83.

24. Nieh T, Higashi K, Wadsworth J. Effect of cell morphology on the compressive properties of open-cell aluminum foams. Materials Science and Engineering: A. 2000;283(1):105-10.

25. Paul A, Ramamurty U. Strain rate sensitivity of a closed-cell aluminum foam. Materials Science and Engineering: A. 2000;281(1):1-7.

26. Deshpande VS, Ashby MF, Fleck NA. Foam topology bending versus stretching dominated architectures. Acta Materialia. 2001;49(6):1035-40.

27. Ashby MF, Evans A, Fleck NA, Gibson LJ, Hutchinson JW, Wadley HNG. Metal foams: a design guide. Materials & Design. 2002;23(1):119.

28. Ruan D, Lu G, Chen F, Siores E. Compressive behaviour of aluminium foams at low and medium strain rates. Composite Structures. 2002;57(1):331-6.

29. Tan PJ, Harrigan JJ, Reid SR. Inertia effects in uniaxial dynamic compression of a closed cell aluminium alloy foam. Materials science and technology. 2002;18(5):480-8.

30. Chan KC, Xie LS. Dependency of densification properties on cell topology of metal foams. Scripta Materialia. 2003;48(8):1147-52.

31. US Army Corps of Engineers, Naval Facilities Engineering Command. Air Force Civil Engineer Support Agency. Unified Facilities Criteria: Structures to Resist the Effects of Accidental Explosions. UFC 3-340-022008.

32. Schaedler TA, Ro CJ, Sorensen AE, Eckel Z, Yang SS, Carter WB, et al. Designing Metallic Microlattices for Energy Absorber Applications. Advanced Engineering Materials. 2014;16(3):276-83.

33. Ma J, You Z. Energy Absorption of Thin-Walled Square Tubes With a Prefolded Origami Pattern—Part I: Geometry and Numerical Simulation. Journal of Applied Mechanics. 2013;81(1):011003--11.

34. Ma J, Hou D, Chen Y, You Z. Quasi-static axial crushing of thin-walled tubes with a kite-shape rigid origami pattern: Numerical simulation. Thin-Walled Structures. 2016;100:38-47.

35. Ma GW, Ye ZQ. Analysis of foam claddings for blast alleviation. International Journal of Impact Engineering. 2005;34(1):60-70.

36. Schwingel D, Seeliger H-W, Vecchionacci C, Alwes D, Dittrich J. Aluminium foam sandwich structures for space applications. Acta Astronautica. 2007;61(1-6):326-30.

37. Herrmann AS, Zahlen PC, Zuardy I. Sandwich structures technology in commercial aviation. Sandwich structures 7: Advancing with sandwich structures and materials: Springer; 2005. p. 13-26.

38. Banhart J. Aluminium foams for lighter vehicles. International Journal of vehicle design. 2005;37(2-3):114-25.

39. McShane GJ, Radford DD, Deshpande VS, Fleck NA. The response of clamped sandwich plates with lattice cores subjected to shock loading. European Journal of Mechanics - A/Solids. 2006;25(2):215-29.

40. Mines RAW, McKown S, Tsopanos S, Shen E, Cantwell W, Brooks W, et al. Local Effects during Indentation of Fully Supported Sandwich Panels with Micro Lattice Cores. Applied Mechanics and Materials. 2008;13-14:85-90.

41. Kooistra GW, Deshpande V, Wadley HN. Hierarchical corrugated core sandwich panel concepts. Journal of applied mechanics. 2007;74(2):259-68.

42. Rubino V, Deshpande VS, Fleck NA. The dynamic response of clamped rectangular Y-frame and corrugated core sandwich plates. European Journal of Mechanics - A/Solids. 2009;28(1):14-24.

43. Kılıçaslan C, Güden M, Odacı İK, Taşdemirci A. Experimental and numerical studies on the quasi-static and dynamic crushing responses of multi-layer trapezoidal aluminum corrugated sandwiches. Thin-Walled Structures. 2014;78:70-8.

44. Xue P, Yu T, Tao X. Effect of cell geometry on the energy-absorbing capacity of grid-domed textile composites. Composites Part A: Applied Science and Manufacturing. 2000;31(8):861-8.

45. Yu T, Tao X, Xue P. The energy-absorbing capacity of grid-domed textile composites. Composites science and technology. 2000;60(5):785-800.

46. Zupan M, Chen C, Fleck NA. The plastic collapse and energy absorption capacity of egg-box panels. International Journal of Mechanical Sciences. 2003;45(5):851-71.

47. Haldar A, Guan ZW, Cantwell WJ, Wang QY. The compressive properties of sandwich structures based on an egg-box core design. Composites Part B: Engineering. 2018;144:143-52.

48. Imbalzano G, Tran P, Ngo TD, Lee PV. Three-dimensional modelling of auxetic sandwich panels for localised impact resistance. Journal of Sandwich Structures and Materials. 2015.

49. Qi C, Remennikov A, Pei L-Z, Yang S, Yu Z-H, Ngo TD. Impact and close-in blast response of auxetic honeycomb-cored sandwich panels: Experimental tests and numerical simulations. Composite Structures. 2017;180:161-78.

50. Fleck NA, Deshpande VS. The Resistance of Clamped Sandwich Beams to Shock Loading. Journal of Applied Mechanics. 2004;71(3):386.

51. Mohsenizadeh M, Gasbarri F, Munther M, Beheshti A, Davami K. Additively-manufactured lightweight Metamaterials for energy absorption. Materials & Design. 2018;139:521-30.

52. Wang Z, Tian H, Lu Z, Zhou W. High-speed axial impact of aluminum honeycomb – Experiments and simulations. Composites Part B: Engineering. 2014;56:1-8.

53. Ozdemir Z, Hernandez-Nava E, Tyas A, Warren JA, Fay SD, Goodall R, et al. Energy absorption in lattice structures in dynamics: Experiments. International Journal of Impact Engineering. 2016;89:49-61.

54. Zhu F, Lu G, Ruan D, Wang Z. Plastic deformation, failure and energy absorption of sandwich structures with metallic cellular cores. International Journal of Protective structures. 2010;1(4):507-41.

55. DoS U. Country reports on Terrorism 2012. Bureau of Counterterrorism, US DoS. 2013.

56. Hao H. Predictions of Structural Response to Dynamic Loads of Different Loading Rates. International Journal of Protective structures. 2015;6(4):585-605.

57. Hao H, Hao Y, Li J, Chen W. Review of the current practices in blast-resistant analysis and design of concrete structures. Adv Struct Eng. 2016;19(8):1193-223.

58. Alghamdi A. Collapsible impact energy absorbers: an overview. Thin-walled structures. 2001;39(2):189-213.

59. Wang Y, Liew JYR. Blast performance of water tank with energy absorbing support. Thin-Walled Structures. 2015;96:1-10.

60. Wang Y, Zhou H. Numerical study of water tank under blast loading. Thin-Walled Structures. 2015;90:42-8.

61. Chen W, Hao H. Numerical study of a new multi-arch double-layered blast-resistance door panel. International Journal of Impact Engineering. 2012;43:16-28.

62. Zhu F, Lu G. A review of blast and impact of metallic and sandwich structures. EJSE Special Issue: Loading on Structures. 2007.

63. Yuen SCK, Nurick G. The Use of Tubular Structures as Cores for Sandwich Panels Subjected to Dynamic and Blast Loading: A Current "State of the Art". Blast Mitigation: Springer; 2014. p. 229-48.

64. Radford DD, McShane GJ, Deshpande VS, Fleck NA. The response of clamped sandwich plates with metallic foam cores to simulated blast loading. International Journal of Solids and Structures. 2006;43(7-8):2243-59.

65. Zhu F, Zhao L, Lu G, Wang Z. Structural response and energy absorption of sandwich panels with an aluminium foam core under blast loading. Advances in Structural Engineering. 2008;11(5):525-36.

66. Jing L, Wang Z, Zhao L. The dynamic response of sandwich panels with cellular metal cores to localized impulsive loading. Composites Part B: Engineering. 2016;94:52-63.

67. Liu XR, Tian XG, Lu TJ, Liang B. Sandwich plates with functionally graded metallic foam cores subjected to air blast loading. International Journal of Mechanical Sciences. 2014;84:61-72.

68. Zhang L, Hebert R, Wright JT, Shukla A, Kim J-H. Dynamic response of corrugated sandwich steel plates with graded cores. International Journal of Impact Engineering. 2014;65:185-94.

69. Jasion P, Magnucka-Blandzi E, Szyc W, Magnucki K. Global and local buckling of sandwich circular and beam-rectangular plates with metal foam core. Thin-Walled Structures. 2012;61:154-61.

70. Jing L, Xi C, Wang Z, Zhao L. Energy absorption and failure mechanism of metallic cylindrical sandwich shells under impact loading. Materials & Design. 2013;52:470-80.

71. Jing L, Wang Z, Zhao L. Response of metallic cylindrical sandwich shells subjected to projectile impact—Experimental investigations. Composite Structures. 2014;107:36-47.

72. Shen J, Lu G, Wang Z, Zhao L. Experiments on curved sandwich panels under blast loading. International Journal of Impact Engineering. 2010;37(9):960-70.

73. Shen J, Lu G, Zhao L, Qu Z. Response of Curved Sandwich Panels Subjected to Blast Loading. Journal of Performance of Constructed Facilities. 2011;25(5):382-93.

74. Chen W, Hao H. Experimental investigations and numerical simulations of multi-arch double-layered panels under uniform impulsive loadings. International Journal of Impact Engineering. 2014;63:140-57.

75. Chen W, Hao H. Numerical simulations of stiffened multi-arch double-layered panels subjected to blast loading. International Journal of Protective Structures. 2013;4(2):163-88.

76. Li Z, Chen W, Hao H. Numerical study of sandwich panel with a new bi-directional Load-Self-Cancelling (LSC) core under blast loading. Thin-Walled Structures. 2018;127:90-101.

77. Schenk M, Guest SD, McShane GJ. Novel stacked folded cores for blast-resistant sandwich beams. International Journal of Solids and Structures. 2014;51(25-26):4196-214.

78. Pydah A, Batra RC. Crush dynamics and transient deformations of elastic-plastic Miura-ori core sandwich plates. Thin-Walled Structures. 2017;115:311-22.

79. Miura K. Zeta-core sandwich-its concept and realization. title ISAS report/Institute of Space and Aeronautical Science, University of Tokyo. 1972;37(6):137.

80. Heimbs S, Middendorf P, Kilchert S, Johnson AF, Maier M. Experimental and Numerical Analysis of Composite Folded Sandwich Core Structures Under Compression. Applied Composite Materials. 2008;14(5-6):363-77.

81. Gattas JM, You Z. Quasi-static impact of indented foldcores. International Journal of Impact Engineering. 2014;73:15-29.

82. Heimbs S. Foldcore sandwich structures and their impact behaviour: an overview. Dynamic failure of composite and sandwich structures: Springer; 2013. p. 491-544.

83. Gattas JM, You Z. Miura-Base Rigid Origami: Parametrizations of Curved-Crease Geometries. Journal of Mechanical Design. 2014;136(12):121404--10.

84. Gattas JM, You Z. The behaviour of curved-crease foldcores under low-velocity impact loads. International Journal of Solids and Structures. 2015;53:80-91.

85. Du Y, Song C, Xiong J, Wu L. Fabrication and mechanical behaviors of carbon fiber reinforced composite foldcore based on curved-crease origami. Composites Science and Technology. 2019;174:94-105.

86. Nojima T, Saito K. Development of newly designed ultra-light core structures. JSME International Journal Series A Solid Mechanics and Material Engineering. 2006;49(1):38-42.

87. Fathers RK, Gattas JM, You Z. Quasi-static crushing of eggbox, cube, and modified cube foldcore sandwich structures. IJMS. 2015;101-102:421-8.

88. Wierzbicki T, Abramowicz W. On the crushing mechanics of thin-walled structures. Journal of Applied mechanics. 1983;50(4a):727-34.

89. Abramowicz W, Jones N. Dynamic axial crushing of square tubes. International Journal of Impact Engineering. 1984;2(2):179-208.

90. Abramowicz W, Jones N. Dynamic progressive buckling of circular and square tubes. International Journal of Impact Engineering. 1986;4(4):243-70.

91. Abramowicz W, Wierzbicki T. Axial Crushing of Multicorner Sheet Metal Columns. Journal of Applied Mechanics. 1989;56(1):113-20.

92. Abramowicz W, Jones N. Transition from initial global bending to progressive buckling of tubes loaded statically and dynamically. International Journal of Impact Engineering. 1997;19(5-6):415-37.

93. Guillow S, Lu G, Grzebieta R. Quasi-static axial compression of thin-walled circular aluminium tubes. International Journal of Mechanical Sciences. 2001;43(9):2103-23.

94. Jones N. Structural impact: Cambridge university press; 2011.

95. Aktay L, Toksoy AK, Güden M. Quasi-static axial crushing of extruded polystyrene foam-filled thin-walled aluminum tubes: Experimental and numerical analysis. Materials & Design. 2006;27(7):556-65.

96. Yuen SCK, Cunliffe G, du Plessis MC. Blast response of cladding sandwich panels with tubular cores. International Journal of Impact Engineering. 2017;110:266-78.

97. Santosa SP, Wierzbicki T, Hanssen AG, Langseth M. Experimental and numerical studies of foam-filled sections. International Journal of Impact Engineering. 2000;24(5):509-34.

98. Chen W, Wierzbicki T. Relative merits of single-cell, multi-cell and foam-filled thin-walled structures in energy absorption. Thin-Walled Structures. 2001;39(4):287-306.

99. Hanssen AG, Langseth M, Hopperstad OS. Static and dynamic crushing of circular aluminium extrusions with aluminium foam filler. International Journal of Impact Engineering. 2000;24(5):475-507.

100. Sun G, Li S, Liu Q, Li G, Li Q. Experimental study on crashworthiness of empty/aluminum foam/honeycomb-filled CFRP tubes. Composite Structures. 2016;152:969-93.

101. Cheng Y, Liu M, Zhang P, Xiao W, Zhang C, Liu J, et al. The effects of foam filling on the dynamic response of metallic corrugated core sandwich panel under air blast loading – Experimental investigations. International Journal of Mechanical Sciences. 2018.

102. Yazici M, Wright J, Bertin D, Shukla A. Experimental and numerical study of foam filled corrugated core steel sandwich structures subjected to blast loading. Composite Structures. 2014;110:98-109.

103. Cheng Y, Zhou T, Wang H, Li Y, Liu J, Zhang P. Numerical investigation on the dynamic response of foam-filled corrugated core sandwich panels subjected to air blast loading. Journal of Sandwich Structures & Materials. 2017:109963621770035.

104. Yoo SH, Chang SH, Sutcliffe MPF. Compressive characteristics of foam-filled composite egg-box sandwich panels as energy absorbing structures. Composites Part A: Applied Science and Manufacturing. 2010;41(3):427-34.

105. Zhang G, Wang B, Ma L, Wu L, Pan S, Yang J. Energy absorption and low velocity impact response of polyurethane foam filled pyramidal lattice core sandwich panels. Composite Structures. 2014;108:304-10.

106. Wang Y, Liew JYR, Lee SC, Wang W. Experimental and analytical studies of a novel aluminum foam filled energy absorption connector under quasi-static compression loading. Engineering Structures. 2017;131:136-47.

107. Wang Y, Zhai X. Dynamic Crushing Behaviors of Aluminum Foam Filled Energy Absorption Connectors. International Journal of Steel Structures. 2018.

108. Su P-B, Han B, Yang M, Wei Z-H, Zhao Z-Y, Zhang Q-C, et al. Axial compressive collapse of ultralight corrugated sandwich cylindrical shells. Materials & Design. 2018;160:325-37.

109. Zhang X, Hao H, Shi Y, Cui J. The mechanical properties of Polyvinyl Butyral (PVB) at high strain rates. Construction and Building Materials. 2015;93:404-15.

110. Li Z, Chen W, Hao H, Cui J, Shi Y. Experimental study of multi-layer folded truncated structures under dynamic crushing. International Journal of Impact Engineering. 2019;131:111-22.

111. Li Z, Chen W, Hao H. Dynamic crushing and energy absorption of foam filled multi-layer folded structures: Experimental and numerical study. International Journal of Impact Engineering. 2019;133:103341.

112. Zhu F, Lu G. A review of blast and impact of metallic and sandwich structures. EJSE Special Issue: Loading on Structures. 2007:92-101.

113. Nurick G, Martin J. Deformation of thin plates subjected to impulsive loading—a review part II: experimental studies. International Journal of Impact Engineering. 1989;8(2):171-86.

114. Langdon GS, Karagiozova D, Theobald MD, Nurick GN, Lu G, Merrett RP. Fracture of aluminium foam core sacrificial cladding subjected to air-blast loading. International Journal of Impact Engineering. 2010;37(6):638-51.

115. Guruprasad S, Mukherjee A. Layered sacrificial claddings under blast loading Part II—experimental studies. International Journal of Impact Engineering. 2000;24(9):975-84.

116. Wu C, Huang L, Oehlers DJ. Blast Testing of Aluminum Foam–Protected Reinforced Concrete Slabs. Journal of Performance of Constructed Facilities. 2011;25(5):464-74.

117. Codina R, Ambrosini D, de Borbón F. New sacrificial cladding system for the reduction of blast damage in reinforced concrete structures. International Journal of Protective Structures. 2017:204141961770157.

118. Palanivelu S. Energy absorption of crushable tubes for protective structures under static, impact and blast loading: Ghent University; 2011.

119. Ousji H, Belkassem B, Louar MA, Kakogiannis D, Reymen B, Pyl L, et al. Parametric Study of an Explosive-Driven Shock Tube as Blast Loading Tool. Experimental Techniques. 2016;40(4):1307-25.

120. Radford DD, Deshpande VS, Fleck NA. The use of metal foam projectiles to simulate shock loading on a structure. International Journal of Impact Engineering. 2005;31(9):1152-71.

121. Remennikov A, Uy B, Chan E, Ritzel D. The Australian national facility for physical blast simulation. 2019.

122. Zhu F, Zhao L, Lu G, Gad E. A numerical simulation of the blast impact of square metallic sandwich panels. International Journal of Impact Engineering. 2009;36(5):687-99.

123. Liu X, Tian X, Lu TJ, Zhou D, Liang B. Blast resistance of sandwich-walled hollow cylinders with graded metallic foam cores. Composite Structures. 2012;94(8):2485-93.

124. Chen W, Hao H. Numerical Study of Blast-Resistant Sandwich Panels with Rotational Friction Dampers. International Journal of Structural Stability and Dynamics. 2013;13(06):1350014.

125. Schwer L, editor A brief introduction to coupling load blast enhanced with Multi-Material ALE: the best of both worlds for air blast simulation. LS-DYNA Forum Bamberg; 2010.

126. Hanssen A, Hopperstad O, Langseth M, Ilstad H. Validation of constitutive models applicable to aluminium foams. International journal of mechanical sciences. 2002;44(2):359-406.

127. Croop B, Lobo H, DatapointLabs N, editors. Selecting material models for the simulation of foams in LS-DYNA. Proceedings of the 7th European LS-DYNA conference, Dynamore Gmbh, Salzburg, Germany; 2009.

128. Hallquist JO. LS-DYNA theory manual. Livermore software Technology corporation. 2006;3:25-31.

129. Hallquist JO. LS-DYNA keyword user's manual. Livermore Software Technology Corporation. 2007;970.

130. Russell B, Deshpande V, Wadley H. Quasistatic deformation and failure modes of composite square honeycombs. Journal of mechanics of materials and structures. 2008;3(7):1315-40.

131. Goldsmith W, Sackman JL. An experimental study of energy absorption in impact on sandwich plates. International Journal of Impact Engineering. 1992;12(2):241-62.

132. Caspar DL, Fontano E. Five-fold symmetry in crystalline quasicrystal lattices. Proceedings of the National Academy of Sciences. 1996;93(25):14271-8.

133. ASTM. E8M-04 Standard Test Methods for Tension Testing of Metallic Materials (Metric) 1: ASTM international; 2004.

134. Abbasi M, Reddy S, Ghafari-Nazari A, Fard M. Multiobjective crashworthiness optimization of multi-cornered thin-walled sheet metal members. Thin-Walled Structures. 2015;89:31-41.

135. Zhou X, Wang H, You Z. Mechanical properties of Miura-based folded cores under quasi-static loads. Thin-Walled Structures. 2014;82:296-310.

136. Li Z, Chen W, Hao H. Crushing behaviours of folded kirigami structure with square dome shape. International Journal of Impact Engineering. 2018;115:94-105.

137. Yang K, Xu S, Shen J, Zhou S, Xie YM. Energy absorption of thin-walled tubes with pre-folded origami patterns: Numerical simulation and experimental verification. Thin-Walled Structures. 2016;103:33-44.

138. Ma GW, Ye ZQ. Energy absorption of double-layer foam cladding for blast alleviation. International Journal of Impact Engineering. 2005;34(2):329-47.

139. CYMAT. Technical Manual for CYMAT SmartMetal™. CYMAT Technologies Ltd. 2009:5-1-17.

140. Hao H, Li Z, Chen W. Performance of sandwich panel with square dome shape folded kirigami core under blast loading. 13th International Conference on Steel, Space and Composite Structures; Perth, Australia2018.

141. Wu C, Zhou Y. Simplified analysis of foam cladding protected reinforced concrete slabs against blast loadings. International Journal of Protective Structures. 2011;2(3):351-65.

142. Hao H, Stewart MG, Li Z-X, Shi Y. RC column failure probabilities to blast loads. International Journal of Protective Structures. 2010;1(4):571-91.

143. Hou S, Han X, Sun G, Long S, Li W, Yang X, et al. Multiobjective optimization for tapered circular tubes. Thin-Walled Structures. 2011;49(7):855-63.

144. Zhang Y, Xu X, Sun G, Lai X, Li Q. Nondeterministic optimization of tapered sandwich column for crashworthiness. Thin-Walled Structures. 2018;122:193-207.

145. Wang Z, Liu J, Lu Z, Hui D. Mechanical behavior of composited structure filled with tandem honeycombs. Composites Part B: Engineering. 2017;114:128-38.

146. Li Z, Chen W, Hao H. Numerical study of open-top truncated pyramid folded structures with interconnected side walls against flatwise crushing. Thin-Walled Structures. 2018;132:537-48.

147. Li Z, Chen W, Hao H. Numerical study of blast mitigation performance of folded structure with foam infill. Structures. 2019;20:581-93.

148. Hou S, Shu C, Zhao S, Liu T, Han X, Li Q. Experimental and numerical studies on multi-layered corrugated sandwich panels under crushing loading. Composite Structures. 2015;126:371-85.

149. Li Z, Chen W, Hao H. Numerical study of folded dome shape aluminium structure against flatwise crushing. 12th International Conference on Shock & Impact Loads on Structures; June 14-16 Singapore2017.

150. Avallone E, Baumeister T. Mark's standard handbook for mechanical engineers: McGraw-Hill; 2017.

151. ASTM. B209M-14: Standard Specification for Aluminum and Aluminum-Alloy Sheet and Plate (Metric). ASTM International West Conshohocken; 2014.

152. Schneider M, Liewald M. Development of a Folding Tool for Miuri-Structures. IOP Conference Series: Materials Science and Engineering. 2018;418:012120.

153. Dharmasena KP, Wadley HNG, Xue Z, Hutchinson JW. Mechanical response of metallic honeycomb sandwich panel structures to high-intensity dynamic loading. International Journal of Impact Engineering. 2008;35(9):1063-74.

154. Zhang X, Cheng G. A comparative study of energy absorption characteristics of foam-filled and multi-cell square columns. International Journal of Impact Engineering. 2007;34(11):1739-52.

155. Chen W, Hao H, Hughes D, Shi Y, Cui J, Li Z-X. Static and dynamic mechanical properties of expanded polystyrene. Materials & Design. 2015;69:170-80.

156. Yu T, Qiu X. Introduction to impact dynamics: John Wiley & Sons; 2018.

157. Li S, Wang Z, Wu G, Zhao L, Li X. Dynamic response of sandwich spherical shell with graded metallic foam cores subjected to blast loading. Composites Part A: Applied Science and Manufacturing. 2014;56:262-71.

158. Shen CJ, Lu G, Yu TX. Dynamic behavior of graded honeycombs – A finite element study. Composite Structures. 2013;98:282-93.

159. Ma J, Song J, Chen Y. An origami-inspired structure with graded stiffness. International Journal of Mechanical Sciences. 2018;136:134-42.

160. Maskery I, Hussey A, Panesar A, Aremu A, Tuck C, Ashcroft I, et al. An investigation into reinforced and functionally graded lattice structures. Journal of Cellular Plastics. 2016.

161. Xiao L, Song W. Additively-manufactured functionally graded Ti-6Al-4V lattice structures with high strength under static and dynamic loading: Experiments. International Journal of Impact Engineering. 2017.

162. Pham TM, Chen W, Kingston J, Hao H. Impact response and energy absorption of single phase syntactic foam. Composites Part B: Engineering. 2018;150:226-33.

163. Pham TM, Chen W, Hao H. Failure and impact resistance analysis of plain and fiber-reinforced-polymer confined concrete cylinders under axial impact loads. International Journal of Protective Structures. 2018;9(1):4-23.

164. Wang Z, Liu J. Mechanical performance of honeycomb filled with circular CFRP tubes. Composites Part B: Engineering. 2018;135:232-41.

165. Boyd SD. Acceleration of a plate subject to explosive blast loading-trial results. DTIC Document; 2000.

166. Anderson M, Dover D. Lightweight, blast-resistant doors for retrofit protection against the terrorist threat. Applied Research Associates Inc Panama City FL; 2003.

Appendix I

STATEMENTS OF CONTRIBUTION OF CO-AUTHORS

To whom it may concern

I, Zhejian Li, conducted numerical, experimental investigations, data processing & analysis and wrote manuscripts of the papers titled as follows, which were revised and edited by the second and the third co-authors. They also provided insights on experimental preparation, data processing and data analysis.

1. Crushing behaviours of folded kirigami structure with square dome shape

2. Numerical study of open-top truncated pyramid folded structures with interconnected side walls against flatwise crushing

3. Blast mitigation performance of cladding using Square Dome-shape Kirigami folded structure as core

4. Numerical study of blast mitigation performance of folded structure with foam infill

5. Dynamic crushing and energy absorption of foam filled multi-layer folded structures: Experimental and numerical study

6. Functionally graded truncated square pyramid folded structures with foam filler under dynamic crushing

7. Numerical study of sandwich panel with a new bi-directional Load-Self-Cancelling (LSC) core under blast loading

(…….)

I, as a co-author, endorse that this level of contribution by the candidate indicated above is appropriate.

(Dr. Wensu Chen) (…….)

(Prof. Hong Hao) (…….)

To whom it may concern

I, Zhejian Li, conducted experimental investigations, data processing & analysis and wrote manuscript of the paper titled "**Experimental study of multi-layer folded truncated structures under dynamic crushing**" which was revised and edited by the second and the third co-authors. They also provided insights on experimental preparation, data processing and data analysis. The fourth and the fifth co-authors provided assistances including set-up, data recording throughout the dynamic tests.

(…….)

I, as a co-author, endorse that this level of contribution by the candidate indicated above is appropriate.

(Dr. Wensu Chen)	(……..)
(Prof. Hong Hao)	(…….)
(Dr. Jian Cui)	(…….)
(Prof. Yanchao Shi)	(…….)

Appendix II

Copyright Clearance

The proof of the rights, granted by publisher for the publication that form the chapters of this thesis are attached below.

Chapter 3. Li Z, Chen W, Hao H. Crushing behaviours of folded kirigami structure with square dome shape. International Journal of Impact Engineering. 2018;115:94-105.

DOI: 10.1016/j.ijimpeng.2018.01.013

Chapter 4. Li Z, Chen W, Hao H. Numerical study of open-top truncated pyramid folded structures with interconnected side walls against flatwise crushing. Thin-Walled Structures. 2018;132:537-48.

DOI: 10.1016/j.tws.2018.08.023

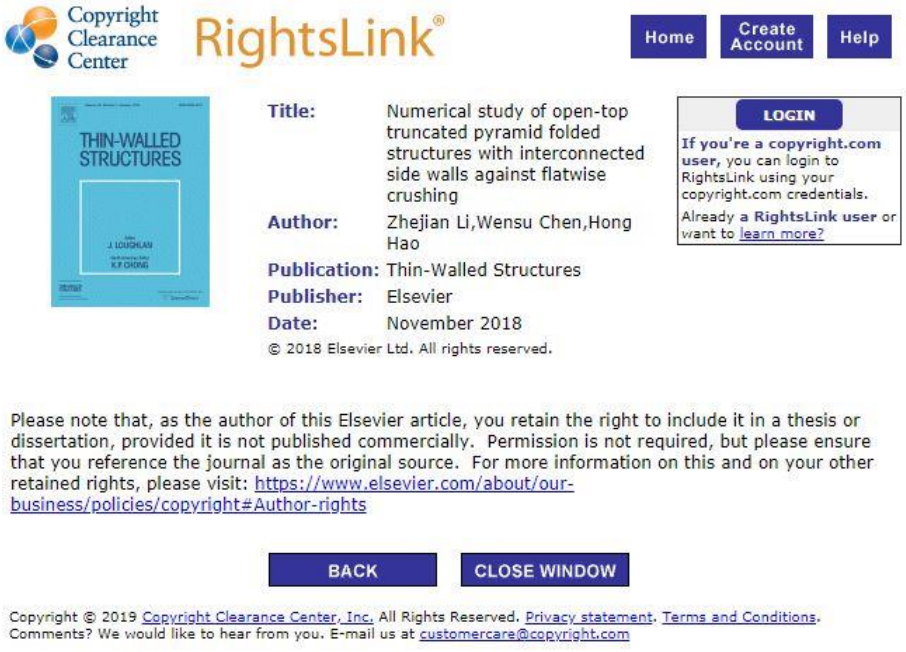

Chapter 5. Li Z, Chen W, Hao H. Blast mitigation performance of cladding using Square Dome-shape Kirigami folded structure as core. International Journal of Mechanical Sciences. 2018;145:83-95.

DOI: 10.1016/j.ijmecsci.2018.06.035

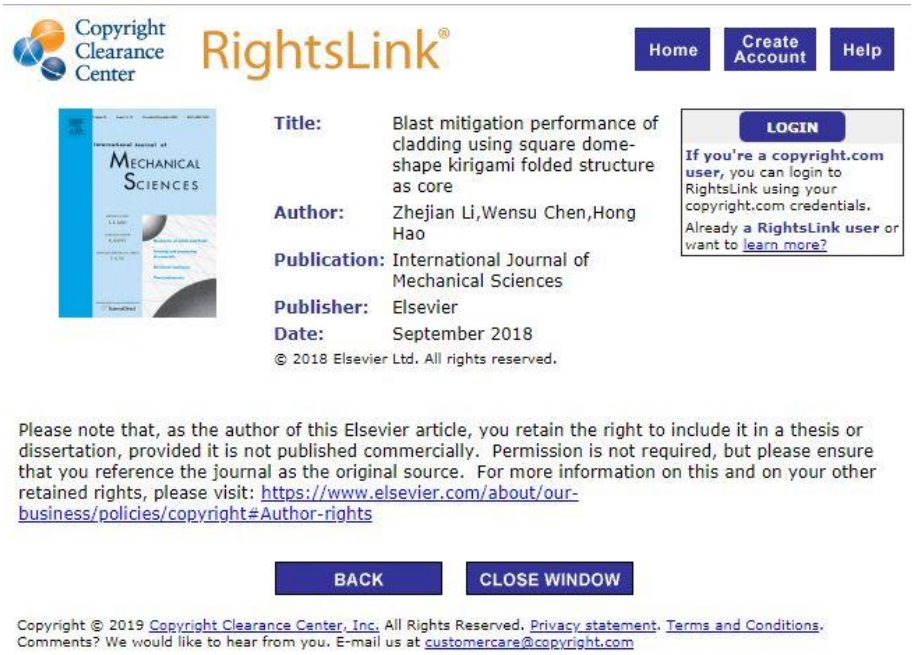

Copyright Clearance Center RightsLink®

Home | Create Account | Help

Title: Blast mitigation performance of cladding using square dome-shape kirigami folded structure as core

Author: Zhejian Li,Wensu Chen,Hong Hao

Publication: International Journal of Mechanical Sciences

Publisher: Elsevier

Date: September 2018

© 2018 Elsevier Ltd. All rights reserved.

LOGIN

If you're a copyright.com user, you can login to RightsLink using your copyright.com credentials.

Already a RightsLink user or want to learn more?

Please note that, as the author of this Elsevier article, you retain the right to include it in a thesis or dissertation, provided it is not published commercially. Permission is not required, but please ensure that you reference the journal as the original source. For more information on this and on your other retained rights, please visit: https://www.elsevier.com/about/our-business/policies/copyright#Author-rights

BACK | CLOSE WINDOW

Copyright © 2019 Copyright Clearance Center, Inc. All Rights Reserved. Privacy statement. Terms and Conditions.
Comments? We would like to hear from you. E-mail us at customercare@copyright.com

Chapter 6. Li Z, Chen W, Hao H. Numerical study of blast mitigation performance of folded structure with foam infill. Structures. 2019;20:581-93.

DOI: 10.1016/j.istruc.2019.06.012

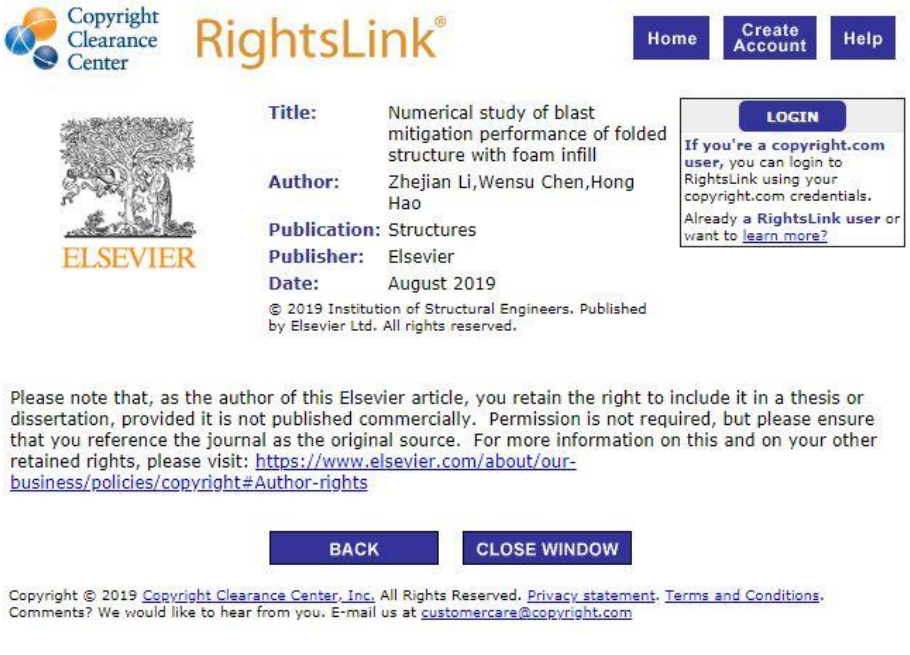

Copyright Clearance Center RightsLink®

Home | Create Account | Help

ELSEVIER

Title: Numerical study of blast mitigation performance of folded structure with foam infill

Author: Zhejian Li,Wensu Chen,Hong Hao

Publication: Structures

Publisher: Elsevier

Date: August 2019

© 2019 Institution of Structural Engineers. Published by Elsevier Ltd. All rights reserved.

LOGIN

If you're a copyright.com user, you can login to RightsLink using your copyright.com credentials.

Already a RightsLink user or want to learn more?

Please note that, as the author of this Elsevier article, you retain the right to include it in a thesis or dissertation, provided it is not published commercially. Permission is not required, but please ensure that you reference the journal as the original source. For more information on this and on your other retained rights, please visit: https://www.elsevier.com/about/our-business/policies/copyright#Author-rights

BACK | CLOSE WINDOW

Copyright © 2019 Copyright Clearance Center, Inc. All Rights Reserved. Privacy statement. Terms and Conditions.
Comments? We would like to hear from you. E-mail us at customercare@copyright.com

Chapter 7. Li Z, Chen W, Hao H, Cui J, Shi Y. Experimental study of multi-layer folded truncated structures under dynamic crushing. International Journal of Impact Engineering. 2019;131:111-22.

DOI: 10.1016/j.ijimpeng.2019.05.010

Chapter 8. Li Z, Chen W, Hao H. Dynamic crushing and energy absorption of foam filled multi-layer folded structures: Experimental and numerical study. International Journal of Impact Engineering. 2019;133:103341.

DOI: 10.1016/j.ijimpeng.2019.103341

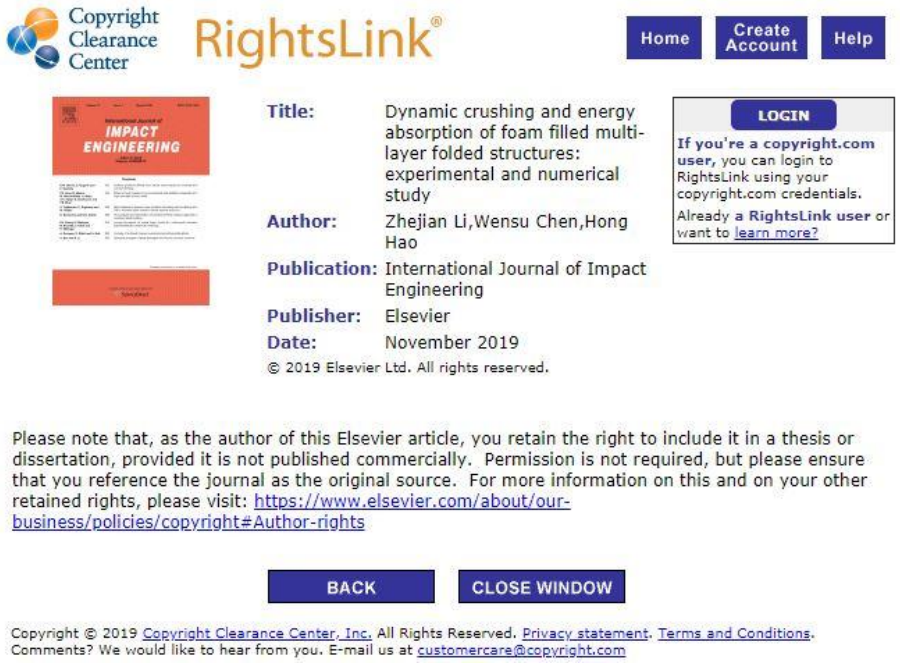

Chapter 9. Li Z, Chen W, Hao H. Functionally graded truncated square pyramid folded structures with foam filler under dynamic crushing. Composites Part B: Engineering. 2019:107410.

DOI: 10.1016/j.compositesb.2019.107410

Chapter 10. Li Z, Chen W, Hao H. Numerical study of sandwich panel with a new bi-directional Load-Self-Cancelling (LSC) core under blast loading. Thin-Walled Structures. 2018;127:90-101.

DOI: 10.1016/j.tws.2018.02.003